# Contribution to the development of the Micro-Vertex detector of the CBM experiment and feasibility study of open charm elliptic flow measurements

Sélim Seddiki

UMR 7178

Thèse

# Thèse .

*Présentée par*

Sélim SEDDIKI

*pour l'obtention du grade de*
*Docteur de l'Université de Strasbourg*

*Spécialité : Physique Nucléaire*

# Contribution au développement du détecteur de vertex de l'expérience CBM et étude de faisabilité des mesures du flot elliptique des particules à charme ouvert

**Contribution to the development of the Micro-Vertex Detector of the CBM experiment and feasibility study of open charm elliptic flow measurements**

**En cotutelle avec l'Université Goethe de Francfort**

**Soutenue publiquement le 12 septembre 2012**

***Membres du jury :***

| | |
|---|---|
| Janos POLONYI | Président |
| Nicole BASTID | Rapporteur |
| Alwin SCHEMPP | Rapporteur |
| Marcus BLEICHER | Examinateur |
| Fouad RAMI | Co-directeur de thèse |
| Joachim STROTH | Co-directeur de thèse |

**Institut Pluridisciplinaire Hubert Curien – Département de Recherches Subatomiques**
23 rue du Loess
BP 28
F-67037 Strasbourg cedex 2
Tél. : +33 (0) 3 88 10 6656
Fax : +33 (0) 3 88 10 6292
http://iphc.in2p3.fr/

# Remerciements

J'aimerais d'abord remercier mon co-directeur de thèse Fouad Rami, pour son immense disponibilité, pour ses suggestions nombreuses et avisées concernant les études menées dans ce travail, et enfin pour son soutien dans les moments difficiles. J'aimerais également exprimer mes remerciements à mon co-directeur de thèse Joachim Stroth pour m'avoir permis de faire ma thèse dans son équipe, pour s'être assuré que je puisse vivre confortablement à Francfort, et pour m'avoir fait profiter de sa grande expérience de la recherche et de ses connaissances.

Je suis également reconnaissant aux membres de mon jury de thèse, pour s'être intéressés à mon travail, pour s'être déplacés (certains de bien loin) afin d'assister à ma soutenance, et pour m'avoir jugé digne du titre de docteur.

Je remercie la collaboration CBM, au sein de laquelle il m'a été donné d'effectuer mes premiers pas dans la recherche, de rencontrer nombre de personnes de cultures très différentes, ayant toutes pour point commun la passion de la physique. A cet égard, je tiens tout particulièrement à mentionner Peter Senger, porte-parole de la collaboration, pour son soutien et ses conseils qui m'ont été très précieux.

Mention spéciale également à l'école "Helmholtz Research School for Quark Matter Studies", et par la même, à son directeur Harald Appelshäuser et à son coordinateur Henner Büsching. Les nombreux cours, donnés en des lieux idylliques, m'ont permis d'apprendre et d'approfondir mes connaissances dans la bonne humeur.

Je tiens tout particulièrement à rendre grâce à Michal Koziel, Christian Müntz et Ingo Fröhlich pour les corrections et les suggestions qu'ils ont apporté au manuscrit, ainsi qu'à Marianne Frey et Samir Amar-Youcef pour leur aide apportée en maintes occasions dans les démarches administratives.

Parmis les nombreuses personnes qui m'ont apporté leur savoir sur divers sujets, je tiens tout particulièrement à témoigner ma reconnaissance à Marc Winter et son équipe de l'IPHC de Strasbourg, à Florian Uhlig, Volker Friese, Sebastian Ratschow et Christoph Schrader.

Merci enfin à ma famille pour son indéfectible confiance en ma réussite, et à mes amis, scientifiques et non-scientifiques, pour la vie partagée à Francfort.

# Contents

# List of Figures

# List of Tables

# Résumé

## Introduction

Le sujet de cette thèse s'inscrit dans le cadre de l'expérience CBM (Compressed Baryonic Matter). Cette dernière est l'une des expériences majeures du nouvel accélérateur international FAIR (Facility for Antiproton and Ion Research), actuellement en cours de construction au GSI à Darmstadt (Allemagne). Le programme scientifique de CBM a pour but d'explorer le diagramme des phases de la matière nucléaire dans la région, peu connue jusqu'à présent, des hautes densités baryoniques nettes et des températures modérées. Il compte parmi ses objectifs principaux la recherche de signatures d'une transition de phase de première ordre du gaz hadronique vers le plasma de quarks et de gluons (PQG), la recherche du point critique du diagramme des phases de la matière nucléaire, l'étude des effets de milieu dans la matière baryonique dense et leur possible lien avec la restauration partielle de la symétrie chirale, et l'élaboration de l'équation d'état de la matière nucléaire. Les progrès dans ce domaine de recherche sont d'une importance cruciale pour comprendre la structure et les propriétés de la matière fortement interagissante à haute densité baryonique, et pour en élaborer une description théorique dans le contexte de la théorie fondamentale de l'interaction forte, la chromodynamique quantique (QCD). De plus, la matière produite dans ces conditions extrêmes de densité baryonique est particulièrement intéressante pour l'étude d'objets astrophysiques compacts tels que les étoiles à neutrons.

L'étude de la production et de la propagation des particules à charme ouvert, i.e. particules contenant un quark charmé et un ou plusieurs quarks légers, dans les collisions d'ions lourds est l'un des principaux thèmes de physique de l'expérience CBM. Plusieurs modèles prédisent que les observables physiques liées au charme ouvert sont sensibles à la transition de phase vers le plasma de quarks et de gluons. Par exemple, la production relative des mésons à charme ouvert (ou mésons D) et du charmonium a été proposée récemment comme observable sensible à la transition de phase vers le PQG : une diminution soudaine dans la fonction d'excitation du rapport du taux de production des mésons D à celui du charmonium est prédite à une énergie correspondant au seuil de formation du PQG. Cette transition de phase peut également être mise en évidence en mesurant le flot elliptique des mésons D. L'amplitude de cet effet dépend fortement des degrés de liberté du milieu chaud et dense produit durant les premiers instants de la collision. Dans un scenario purement hadronique, les particules à charme ouvert ont un faible taux d'interactions et, conséquemment, on s'attend à ce que l'amplitude de leur flot soit très faible. L'observation d'un flot elliptique important pour les mésons D aux énergies de FAIR

indiquerait l'apparition d'un milieu partonique. L'étude des hadrons à charme ouvert peut aussi fournir des informations précieuses sur les effets de milieu nucléaire et leur possible lien avec la restauration de la symétrie chirale. En effet, plusieurs modèles théoriques prédisent que la masse de ces particules devrait être modifiée dans un milieu nucléaire dense et chaud. On s'attend donc à une modification de leur taux de production dans les collisions noyau-noyau. Cet effet doit être particulièrement prononcé près du seuil cinématique de production de ces particules qui se situe dans le domaine d'énergie de FAIR.

La mesure des particules à charme ouvert dans les collisions noyau-noyau est un défi expérimental, particulièrement aux énergies de FAIR où ces particules sont produites, près de leur seuil cinématique, avec des sections efficaces très faibles. Cette mesure impose des taux de collisions nucléaires très importants, ce qui sera possible pour la première fois à FAIR en utilisant des faisceaux à très haute intensité, jusqu'à $10^9$ ions/seconde pour un faisceau d'ions Au, et une nouvelle génération de détecteurs rapides et radio-résistants.

## Défi expérimental

L'expérience CBM mesurera les particules à charme ouvert à travers leur désintégration en hadrons chargés (e.g. pions et kaons). La reconstruction de ces particules s'appuie sur la détermination de la masse invariante de leurs particules filles. Cette tâche est particulièrement difficile dans l'environnement des collisions d'ions lourds aux énergies de FAIR du fait que les multiplicités des hadrons à charme ouvert sont beaucoup plus petites (de plusieurs ordres de grandeur) que celles des hadrons chargés. Comme la méthode de la masse invariante combine toutes les particules chargées d'un événement en multiplets, selon le canal de désintégration choisi pour détecter les particules à charme ouvert, cette méthode produit un bruit de fond combinatoire colossal, constitué principalement de multiplets de particules non-corrélées. La stratégie employée pour discriminer le signal du bruit de fond combinatoire repose sur la topologie de désintégration des particules à charme ouvert et, en particulier, le déplacement caractéristique de leur vertex de désintégration par rapport au point d'interaction.

La reconstruction du vertex décalé des particules à charme ouvert est une tâche délicate en raison de la durée de vie très courte de ces particules (de l'ordre de la picoseconde). Leur distance de désintégration moyenne dans le référentiel du laboratoire est d'environ 1 mm. Cela requiert un détecteur de vertex extrêmement précis, capable de séparer le vertex de désintégration secondaire des particules à charme ouvert du vertex primaire de la collision.

Le détecteur de vertex de l'expérience CBM, appelé "Micro Vertex Detector" (MVD), doit par conséquent offrir la grande précision requise pour la mesure du vertex décalé de désintégration des particules à charme ouvert. Cela impose des contraintes fortes sur sa conception. Le MVD doit être très granulaire et aussi mince que possible de manière à réduire l'effet des diffusions multiples qui peut dégrader la précision de reconstruction de l'impulsion des hadrons chargés et du vertex secondaire. De plus, il doit être placé très près du point d'interaction, et doit donc être très résistant aux radiations émises. Cette contrainte est particulièrement forte du fait des taux de

collisions très élevés nécessaires pour mesurer le charme ouvert près de son seuil cinématique de production. De telles conditions exigent, par ailleurs, l'utilisation d'un détecteur extrêmement rapide pour limiter l'effet d'empilement de plusieurs collisions.

Les capteurs monolithiques à pixels actifs, "Monolithic Active Pixel Sensors" (MAPS), sont actuellement considérés comme étant la technologie la plus prometteuse pour équiper le détecteur MVD. Ces capteurs peuvent être amincis jusqu'à une épaisseur de 50 $\mu$m et offrent des résolutions spatiales typiquement meilleures que 5 $\mu$m. Des progrès substantiels ont été accomplis ces dernières années pour améliorer leur résistance aux radiations et leur temps de lecture. Les performances actuelles de ces capteurs MAPS sont les suivantes : un temps de lecture d'environ 100 $\mu$s et une tolérance à une dose de radiations non-ionisantes (ionisantes) supérieure à $10^{13}$ $n_{eq}/cm^2$ (0.3 Mrad). Des améliorations sont encore attendues dans les années à venir, avant la phase de construction du détecteur prévue à partir de 2015. Le temps de lecture pourrait être réduit d'un facteur 2-4, jusqu'à environ 25-50 $\mu$s. La tolérance aux radiations ionisantes pourrait également être améliorée en implémentant des capteurs MAPS à base de composants plus petits (0.18 $\mu$m au lieu de 0.35 $\mu$m) : un facteur de gain de 10 est attendu en suivant cette stratégie. A plus long termes, cette nouvelle technologie permettrait par ailleurs de réduire le temps de lecture des capteurs MAPS en deça de 10 $\mu$s.

La construction du détecteur MVD sera synchronisée avec la disponibilité des accélérateurs de FAIR. Dans la première phase de la réalisation de FAIR, le faisceau de particules sera délivré par le synchrotron SIS100 (à partir de 2017) à des énergies d'environ 10 AGeV pour les ions Au et à peu près 30 GeV pour les protons. A SIS100, CBM mesurera le charme ouvert dans les collisions proton-proton et proton-noyau. Ces mesures sont importantes pour comprendre les mécanismes de production du charme à des énergies de collisions faibles et serviront de référence pour l'interprétation des données sur le charme dans les collisions noyau-noyau. Le MVD pourra aussi être utilisé à SIS100 pour améliorer la précision de mesure des mésons vecteurs de faible masse et des particules multi-étranges (contenant plusieurs quarks étranges) dans les collisions noyau-noyau. Dans la seconde phase de la réalisation de FAIR, le faisceau délivré par le synchrotron SIS300 (attendu quelques années plus tard) atteindra des énergies jusqu'à 35 AGeV pour les ions Au et 89 GeV pour les protons. Cela permettra à CBM de compléter son programme de physique en mesurant le charme ouvert dans les collisions noyau-noyau.

La présente thèse est une contribution à la conception et au développement du détecteur MVD de l'expérience CBM. Elle inclut trois parties principales. La première porte sur la définition du cahier des charges du détecteur MVD de première génération destiné aux expériences lors de la phase 1 de CBM auprès du synchrotron SIS100. La seconde partie concerne des études de simulations détaillées ayant pour but d'évaluer les performances de l'expérience CBM pour la reconstruction des particules à charme ouvert dans les collisions noyau-noyau. Finalement, la troisième partie est une étude de faisabilité de la mesure du flot elliptique du charme ouvert dans CBM.

# Cahier des charges du MVD de première génération

Lors de la première phase de l'expérience CBM, auprès du synchrotron SIS100, le détecteur MVD servira à mesurer le charme ouvert dans les collisions proton-proton et proton-noyau à des énergies incidentes allant jusqu'à 30 GeV. Dans les collisions noyau-noyau, le MVD pourra aussi être utilisé pour améliorer les performances de l'expérience pour la mesure des mésons vecteurs de faible masse ($\rho$, $\omega$, $\phi$) et des particules multi-étranges (e.g. $\Xi$, $\Omega$) à des énergies incidentes allant jusqu'à 10 AGeV pour les ions Au. Des taux de collisions très élévés sont envisagés pour mener ces mesures, typiquement de l'ordre de $2 \times 10^6$ collisions/seconde pour les collisions p(30 GeV) + Au et de l'ordre de $2 \times 10^4$ collisions/seconde pour les collisions Au(10 AGeV) + Au.

Pour évaluer les taux de données générées dans le capteur MAPS qui équipera le détecteur MVD à SIS100, nommé MIMOSIS-1, des simulations Monte Carlo détaillées ont été menées dans l'environnement logiciel de l'expérience CBM (CBMRoot). Deux aspects importants des conditions d'opération, qui étaient absents dans les études précédentes, ont été inclus dans ces simulations : les fluctuations d'intensité des faisceaux de particules de FAIR et leur emittance. Il a été observé que l'émittance des faisceaux à SIS100, extrapolée à partir de celle mesurée auprès du synchrotron SIS18, a peu d'effet sur les densités de hits (point d'impact d'une particule) dans les stations du détecteur MVD. L'empilement de plusieurs collisions dans les capteurs MIMOSIS-1 a été simulé, en tenant compte de leur temps de lecture (de 25 $\mu$s), et en se fondant sur deux hypothèses concernant les fluctuations d'intensité du faisceau à SIS100 : un rapport maximum-sur-moyenne égal à 3 (en s'appuyant sur les mesures effectuées auprès du synchrotron SIS18) et 10 en tant qu'hypothèse conservatrice pour les faisceaux de protons et d'ions Au. Les fluctuations d'intensité du faisceau ont pour effet de générer des fluctuations importantes des taux de hits dans les capteurs MIMOSIS-1. Cet effet est particulièrement critique dans le cas des capteurs situés dans la région des stations MVD où les densités de hits sont maximales. Dans les collisions Au + Au, cette région est dominée par la contribution des électrons $\delta$, crées dans la cible de CBM par les ions Au du faisceau. Il a été demontré que la contribution des électrons $\delta$ au nombre total de hits reçus par le MVD peut être réduit substantiellement en ajoutant des absorbeurs en dehors de l'acceptance du détecteur. Cependant, cette stratégie a un effet mitigé sur la densité maximale de hits, du fait que cette dernière est dominée par la contribution des électrons $\delta$ qui impactent le détecteur avant d'atteindre les absorbeurs.

Le cahier des charges en termes de taux de données a été évalué pour les capteurs du MVD situés dans la région aux densités maximales de hits, et en se fondant sur différentes hypothèses sur la distance entre la station MVD et la cible. En comparant ce cahier des charges avec les performances attendues des circuits de sparsification des données du capteur MIMOSIS-1, il a été établi que ce capteur pourra tolérer des fluctuations d'intensité du faisceau importantes, tout en étant placé très près de la cible, jusqu'à une distance de 5 cm. Il a été constaté que la bande passante de sortie du capteur MIMOSIS-1, de 400 MHz ou de 800 MHz, est la contrainte dominante en ce qui concerne la distance minimale à laquelle la première station MVD peut être placée. Un capteur avec une bande passante de 400 MHz peut être placé à une distance comprise entre 5 et 10 cm (10 et 15 cm) de la cible pour les collisions p + Au (Au + Au),

en fonction de l'hypothèse faite sur les fluctuations de l'intensité du faisceau. Des études de faisabilité menées au sein de la collaboration CBM ont demontré que de telles distances pour la première station MVD sont appropriées pour les différentes mesures envisagées à SIS100. De surcroît, une bande passante de 800 MHz permettrait d'opérer le capteur dans des conditions de fluctuations d'intensité du faisceau importantes avec des marges de sécurité. Ces résultats montrent que les performances attendues de MIMOSIS-1 (en termes de capabilité à traiter les taux de données) satisfont pleinement le cahier des charges du détecteur MVD à SIS100.

Le travail présenté ci-dessus a également permis d'évaluer le cahier des charges en termes de bande passante pour les différents composants du système de lecture des données du détecteur MVD. Ce système de lecture est constitué de plusieurs chaînes de lecture identiques devant transmettre l'information délivrée par plusieurs (jusqu'à cinq) capteurs MIMOSIS-1. Le cahier des charges s'appuie sur la bande passante de sortie de MIMOSIS-1 : de 400 MHz ou de 800 MHz. Il a été montré que chaque chaîne de lecture doit comporter une bande passante totale de 5 GHz, ce qui impose des contraintes importantes sur le design de ses différents composants.

## Reconstruction des particules à charme ouvert dans les collisions noyau-noyau

Nous avons étudié les performances attendues du détecteur CBM pour la reconstruction des particules à charme ouvert dans les collisions noyau-noyau, à partir de leur désintégration en hadrons chargés. Pour ce faire, des simulations Monte Carlo ont été menées en utilisant une géométrie réaliste du détecteur MVD et en prenant en compte les performances des capteurs MAPS : une résolution spatiale de 3 $\mu$m, un temps de lecture de 10 $\mu$s, et une résistance à des doses de radiations de 3 Mrad et $3 \times 10^{13}\ n_{eq}/cm^2$ pour les radiations ionisantes et non-ionisantes, respectivement. Les simulations ont été effectuées dans le cas des collisions centrales Au + Au (paramètre d'impact b = 0 fm) à une énergie incidente de 25 AGeV, ce qui représente un environnement typique pour la reconstruction du charme ouvert dans les collisions noyau-noyau aux énergies de FAIR. Les mésons $D^+$ se désintégrant en $\pi^+\ \pi^+\ K^-$ ont été choisis pour évaluer les performances du détecteur. Ce choix était motivé par le fait que la reconstruction de ce canal de désintégration, impliquant trois particules filles, est particulièrement difficile étant donné que le signal doit être extrait d'un bruit de fond combinatoire très important (de plusieurs ordres de grandeur supérieur au signal). L'identification des particules a été prise en compte en supposant que l'information provenant du détecteur TOF permet de rejecter tous les protons.

La résolution obtenue sur le vertex secondaire est de 72 $\mu$m. Cette excellente résolution est due principalement à la très bonne résolution spatiale et le faible budget de matière du détecteur MVD. La résolution obtenue sur l'impulsion des hadrons chargés est comprise entre $1.2\%$ et $1.6\%$ pour les particules avec une impulsion supérieure à 1 GeV/c. Pour reconstruire les mésons $D^+$ via leur désintégration en triplets ($\pi^+$, $\pi^+$, $K^-$), plusieurs critères de sélection ont été utilisés afin de réduire le bruit de fond combinatoire (constitué principalement de triplets de particules chargées non-corrélées). Les critères s'appuient principalement sur la topologie singulière de

désintégration du méson $D^+$ et, en particulier, son vertex de désintégration décalé par rapport au point d'interaction. Après avoir optimisé les coupures de sélection sous-jacentes, un rapport signal sur bruit de 1.5 (3.0) a été obtenu dans la région de la masse invariante du méson $D^+$, en employant le modèle HSD (SHM) pour estimer sa multiplicité. Cela a été obtenu avec une efficacité de reconstruction totale (incluant l'acceptance géométrique) de $2\%$. Les performances de reconstruction ont également été déterminées pour le méson $D^-$ se désintégrant en triplets ($\pi^-\ \pi^-\ K^+$) dans les mêmes conditions (système, énergie et centralité) que pour le méson $D^+$ : un rapport signal sur bruit de 3.7 (12.0) a été obtenu en employant le modèle HSD (SHM), avec une efficacité de reconstruction de $1.4\%$.

Les statistiques en particules attendues après deux mois de prise de données (durée typique d'une campagne de prises de données) ont été évaluées pour un taux de collisions de 400 kHz. Il a été montré que l'expérience sera capable de mesurer $1.5 \times 10^4$ $D^+$ et $2.3 \times 10^4$ $D^-$ particules durant cette période (en supposant les multiplicités prédites par HSD). En combinant ces résultats avec ceux obtenus dans d'autres études menées au sein de la collaboration, il a été montré que le nombre total de mésons D mesurables après deux mois de prise de données est d'au moins 6.9 $\times 10^4$ particules. De telles statistiques devraient permettre d'effectuer des études détaillées de plusieurs observables physiques (e.g., taux de production, abondance relative, distributions en impulsion transverse et en rapidité) liées à la production du charme ouvert aux énergies de FAIR.

## Faisabilité des mesures du flot elliptique des particules à charme ouvert

La faisabilité des mesures du flot elliptique des mésons à charme ouvert a été étudiée. Ces mesures sont très difficiles aux énergies de FAIR où les particules à charme ouvert sont produites avec des sections efficaces très faibles (production au seuil). Elles ne sont pas seulement exigeantes en termes de statistiques en particules mais reposent également sur la possibilité de mesurer avec précision l'orientation azimutale du plan de réaction des collisions noyau-noyau.

Des simulations Monte Carlo ont été menées afin d'évaluer les capacités du détecteur CBM pour ces mesures du flot elliptique des particules à charme ouvert. Ceci a été effectué dans le cas des collisions Au + Au à une énergie incidente de 25 AGeV. Dans cette étude, nous nous sommes restreint au cas des collisions semi-périphériques, pour lesquelles on s'attend à ce que l'amplitude du flot elliptique soit maximale.

Dans un premier temps, la résolution attendue sur le plan de réaction a été évaluée en utilisant l'environnement de simulation CBMRoot et le code de transport UrQMD (utilisé comme générateur d'événements). Dans CBM, le plan de réaction peut être déterminé de manière indépendante au moyen de deux sous-détecteurs (couvrant deux régions différentes en rapidité) : le calorimètre PSD et le trajectomètre STS. Les performances de chacun de ces détecteurs ont été étudiées au moyen de la méthode standard, appelée "Event Plane" (EP). Il a été montré que l'analyse du flot elliptique peut être menée avec précision dans CBM, en utilisant le plan de réaction reconstruit avec le PSD à partir de la première harmonique (n=1) dans la méthode EP ou celui reconstruit

avec le STS à partir de la seconde harmonique (n=2). Les résultats indiquent que les deux sous-détecteurs PSD et STS offrent des résolutions très similaires pour la reconstruction du plan de réaction dans les collisions semi-périphériques (un paramètre d'impact compris entre 5 et 9 fm). La résolution obtenue, exprimée en termes du facteur <$\cos(2\times(\Psi_n-\Psi_R))$> (utilisé pour corriger l'effet des fluctuations du plan de réaction), est de 0.4 pour les collisions semi-périphériques, ce qui correspond à une résolution sur l'angle azimutal d'environ 40 degrées.

Pour l'étude du flot elliptique des mésons D, nous avons adopté une procédure Monte Carlo simple où une asymétrie azimutale a été introduite lors de la génération des particules. Pour prendre en compte les fluctuations du plan de réaction dues au nombre fini de particules et au différents biais introduits par le détecteur, une composante tirée au hasard selon une loi gaussienne de largeur $\sigma(\Psi_R)$= 40 degrées a été ajoutée à l'angle azimutal des mésons D. La distribution azimutale résultante, définie par rapport au plan de réaction, a ensuite été analysée pour extraire le paramètre de flot elliptique $v_2$ en fonction de l'impulsion transverse.

Les incertitudes statistiques sur le paramètre $v_2$ ont été évaluées pour un échantillon d'événements correspondant aux statistiques annuelles attendues dans les collisions semi-périphériques Au(25 AGeV) + Au. Cela a été fait en se fondant sur deux hypothèses concernant l'amplitude du flot des mésons D : i) un "faible flot", comme le prédit le modèle HSD (du fait de la faible section efficace d'interaction hadronique des mésons D) et ii) un "fort flot", qui est attendu dans le cas où les interactions partoniques sont suffisamment fréquentes. Comme l'on s'y attendait, les incertitudes statistiques sont plus petites dans le cas d'un "fort flot". En supposant que le paramètre $v_2$ est plus grand d'un facteur deux que celui prédit par le modèle HSD, une incertitude statistique relative d'environ $10\%$ a été obtenue pour le flot elliptique intégré de l'ensemble des mésons D. Cette erreur relative est comprise entre $16\%$ et $24\%$ pour chaque espèce individuelle.

Les résultats de cette étude montrent que même de petites valeurs de flot elliptique des mésons D peuvent être mesurées en un an de prise de données avec CBM et que la sensitivité de l'expérience devrait être suffisante pour départager les modèles purement hadroniques (e.g. HSD) et ceux incluant des degrées de liberté partoniques (e.g. PHSD, AMPT). Si le flot elliptique des mésons D est important, ce qui est fort probable aux énergies maximales accessibles à FAIR (25-35 AGeV), alors l'expérience CBM sera capable de mesurer avec précision son amplitude intégrée en fonction de l'énergie du faisceau. Cependant, les mesures du flot elliptique différentiel nécessiteraient des statistiques en particules plus élevées. Ceci pourrait être réalisé avec des capteurs MAPS plus rapides et plus tolérants aux radiations, permettant des mesures à des taux de collisions plus élevés.

# Conclusion et perspectives

Ce travail de thèse a apporté d'importantes contributions à la conception du détecteur de vertex de l'expérience CBM, l'une des expériences majeures du futur accélérateur FAIR.

Il a été démontré que la capacité en termes de flot de données à traiter par les circuits de lecture

embarqués des capteurs MAPS, destinés à équiper le détecteur de vertex, est approprié pour mener le programme de physique envisagé par CBM auprès du synchrotron SIS100. Le cahier des charges en termes de bande passante des différents composants du système de lecture a été évalué. Ces spécifications sont désormais incluses dans le design technique du système de lecture du détecteur de vertex, ce qui constitue une étape importante vers sa réalisation.

D'autre part, des études de simulation détaillées ont été menées pour évaluer les performances attendues de l'expérience CBM pour la mesure du charme ouvert dans les collisions noyau-noyau. Il a été démontré que la reconstruction des particules à charme ouvert via leur désintégration hadronique dans les collisions Au(25 AGeV) + Au est faisable avec une efficacité de reconstruction de $\sim 2\%$. La statistique estimée par année de mesure (i.e. deux mois effectifs de prise de données) à un taux de collisions de 400 kHz est de 1.5 $\times$ $10^4$ pour $D^+ \rightarrow \pi^+ \, \pi^+ \, K^-$ et au moins 6.9 $\times$ $10^4$ si l'on inclut tous les canaux de désintégration reconstructibles des mésons D. En s'appuyant sur ces résultats, la possibilité de mesurer le flot elliptique des mésons D a été étudiée, en tenant compte d'une estimation réaliste de la résolution attendue sur le plan de réaction. Il a été établi que le paramètre de flot elliptique intégré peut être déterminé avec une bonne précision statistique pour plusieurs espèces de mésons D. Cependant, les mesures détaillées de sa dépendance en $p_T$ requerrait plus de statistiques en particules et donc des taux de collisions plus élevés, au-delà de la limite tolérable des capteurs MAPS.

Il est important de noter que le développement des capteurs MAPS progresse de manière prometteuse et plus rapidement que prévu. Il est donc possible que, dans les années à venir, des capteurs plus performants (comparés à ceux considérés dans les simulations menées dans ce travail) puissent être disponibles. En particulier, l'émergence récente d'architectures d'intégration 3D promet des améliorations substantielles dans les performances des capteurs MAPS : un temps de lecture de quelques microsecondes et une tolérance à une dose de radiations non-ionisantes au-delà de $10^{14}$ $n_{eq}/cm^2$ et à une dose de radiations ionisantes supérieure à 30 Mrad. Cela augmenterait grandement les capacités de l'expérience pour la mesure des mésons D et pourrait offrir, en sus, la possibilité de mesurer également le baryon $\Lambda_c$, qui est plus difficile à reconstruire du fait de sa durée de vie extrêmement courte ($c\tau$ = 59.9 fm).

# Zusammenfassung

## Einleitung

Der Gegenstand dieser Arbeit ist Teil des „Compressed Baryonic Matter“ (CBM) Experiments. Dies ist eines der geplanten Experimente an der Anlage FAIR (Facility for Antiproton and Ion Research), die sich derzeit bei der GSI (Helmholtzzentrum für Schwerionenforschung) in Darmstadt/Deutschland im Bau befindet. Zielsetzung dieses Experiments ist die Untersuchung des Phasendiagramms von Kernmaterie bei hohen Netto-Baryonendichten und moderaten Temperaturen, welche durch Schwerionenkollisionen bei Strahlenergien im Bereich von 2 bis 45 AGeV erzeugt werden wird. CBM wird dabei insbesondere nach dem Phasenübergang von hadronischer zu partonischer Materie und nach dem kritischen Endpunkt des vorhergesagten Phasenübergangs erster Ordnung suchen. Desweiteren werden In-Medium-Effekte in dichter baryonischer Materie und ihr möglicher Zusammenhang mit der teilweisen Wiederherstellung der chiralen Symmetrie, sowie die Zustandsgleichung der dichten Kernmaterie studiert werden. Dies ist essentiell für das Verständnis der Struktur und der Eigenschaften von stark-wechselwirkender Materie bei hohen Netto-Baryonendichten und deren theoretischer Beschreibung im Rahmen der fundamentalen Theorie der starken Wechselwirkung, der Quantenchromodynamik (QCD). Außerdem ist diese unter extremer Netto-Baryonendichte entstandene Materie interessant für das Studium astrophysikalischer Objekte, wie zum Beispiel Neutronensterne.

Eines der Hauptthemen des CBM-Experiments ist die Untersuchung der Produktion und Propagation von „Open-Charm“-Teilchen in Schwerionenkollisionen. Dies sind Teilchen, die ein Charm-Quark und zusätzlich eines oder mehrere leichtere Quarks enthalten. Observablen, die mit Open-Charm in Zusammenhang stehen, sind - so die Vorhersage - besonders sensitiv für den Deconfinement-Phasenübergang und In-Medium-Modifikationen der Eigenschaften von Hadronen in dichter baryonischer Materie. Man erwartet, dass die relative Häufigkeit von D-Mesonen und Charmonium eine empfindliche Observable für den Deconfinement-Phasenübergang ist. Für den Energiebereich in dem das Quark-Gluon-Plasma (QGP) einsetzt, wird ein plötzlicher Abfall in der Anregungsfunktion des J/$\psi$-D Verhältnisses vorhergesagt. Zusätzlich kann die Vermessung des elliptischen Flusses von Open-Charm-Teilchen einen Hinweis auf den Deconfinement-Phasenübergang geben. Die Stärke dieses Effektes hängt eng mit der Zahl von Freiheitsgraden im heißen und dichten Medium zusammen, wie es in der frühen Phase der Kollision entsteht. Open-Charm-Teilchen haben in einem hadronisch dominierten Zustand eine moderate Wechselwirkungsrate, was zu einem schwachen kollektiven Fluss führt. Die Beobachtung eines stark

ausgeprägten elliptischen Flusses von Open-Charm-Teilchen bei FAIR-Energien hingegen würde auf die Existenz von partonischer Materie hindeuten. Die Untersuchung von Open-Charm-Hadronen kann auch Informationen zu In-Medium-Effekten liefern, da man davon ausgeht, dass sich ihre effektive Masse im heißen und dichten nuklearen Medium aufgrund der teilweise Wiederherstellung der chiralen Symmetrie ändert. Experimentell äussert sich dies in der änderung der Produktionsquerschnitte in Schwerionenkollsionen im Vergleich zu denen in elementaren Reaktionen. Im FAIR-Energiebereich wird eine hohe Sensitivität erwartet, da Open-Charm-Teilchen hier seltene Proben darstellen, die nahe an der kinematischen Schwelle produziert werden.

Die Messung von Open-Charm-Teilchen in Kern-Kern-Stössen stellt insbesondere bei FAIR-Energien, aufgrund der kleinen Produktionsquerschnitte nahe am kinematischen Limit, eine große Herausforderung dar. Um signifikante physikalische Aussagen treffen zu können, ist eine große Statistik erforderlich. Die wird durch hohen Kollisionsraten erzielt, wie sie durch die Kombination von Strahlen hoher Intensität an FAIR (bis zu $10^9$ Ionen/Sekunde für Gold-Strahlen) erreicht werden. Hierbei ist die Verwendung von strahlungsharten und ratenfesten Detektoren der neusten Generation und neuen Konzepten in der Datenaufnahme notwendig.

## Experimentelle Herausforderungen

Das CBM-Experiment wird Open-Charm-Teilchen mittels ihres schwachen Zerfalls in geladene Hadronen (Pionen und Kaonen) identifizieren. Die Rekonstruktion dieser Teilchen basiert auf der Bestimmung der invarianten Masse ihrer Tochterteilchen. Dies ist in Schwerionenkollisionen eine Herausforderung, da die Multiplizität von Open-Charm-Hadronen um viele Größenordnungen kleiner ist verglichen zu den häufig produzierten Hadronen (wie zum Beispiel die prompt emittierten Pionen und Kaonen). Die invariante Masse der Mutterteilchen wird, für den gewählten Zerfallskanal, über die Kombination aller in Frage kommenden geladenen Teilchen einer Reaktion bestimmt. Dies führt zu einem großen kombinatorischen Untergrund aus Multiplets unkorrelierter Teilchen. Um das Open-Charm-Signal zu identifizieren, muss die Zerfallstopologie des Mutterteilchens und der charakteristische Abstand des Zefallsvertex zum primären Wechselwirkungspunkt im Target, bekannt sein.

Die Rekonstruktion des Zerfallsvertex von Open-Charm-Teilchen ist aufgrund der kurzen Lebensdauern dieser Teilchen (im Bereich von Pikosekunden) schwierig. Ihre mittlere Zerfallslänge im Laborsystem liegt typischerweise im Bereich von 100 $\mu$m. Dies erfordert einen hochpräzisen Vertexdetektor, der in der Lage ist, den sekundären Zerfallsvertex von Open-Charm-Teilchen vom primären Wechselwirkungspunkt zu separieren.

Der Vertexdetektor des CBM-Experiments, der sogenannte „Micro-Vertex-Detector“ (MVD), muss deswegen eine hohe Genauigkeit haben, die eine Vermessung des sekudären Zerfallsvertex von Open-Charm-Teilchen erlaubt. Dies bedeutet stringente Bedingungen hinsichtlich seines Designs. Der MVD muss hochgranular sein und minimale Dicke besitzen, um Effekte aufgrund von Vielfachstreuung zu reduzieren, die die Genauigkeit der Vertex- und Impulsbestimmung einschränken. Hinzu kommt, dass der MVD unmittelbar am Wechselwirkungspunkt positioniert

sein muss, was eine hohe Strahlentoleranz voraussetzt. Außerdem muss die Signalverarbeitung des Detektors schnell sein, um die hohen Kollisionsraten verarbeiten zu können.

Monolithische Aktive Pixel Sensoren (MAPS) werden derzeit als die vielversprechenste Technologie zur Ausstattung des CBM-MVD betrachtet. Sie zeichnet ein geringes Material Budget (unter 0.05 % der Strahlungslänge $X_0$) kombiniert mit einer Ortsauflösung präziser als 5 $\mu$m aus. In den letzten Jahren wurden deutliche Fortschritte in der Strahlenhärte und Auslesegeschwindigkeit erzielt. Derzeit liegt die Auslesegeschwindigkeit von MAPS bei etwa 100 $\mu$s und die Strahlenhärte gegen nicht-ionisierende (ionisierende) Strahlung bei $10^{13} n_{eq}/cm^2$ (oberhalb von 0.3 MRad). Noch vor der Konstruktionsphase des MVD (Beginn 2015) wird erwartet, die Auslesezeit um einen Faktor 2 bis 4 zu verkürzen (etwa 25 bis 50 $\mu$s). Die Strahlenhärte wird durch die weitere Reduktion der sogenannten „Feature Size“ der MAPS-Chips auf 0.18 $\mu$m gesteigert werden können. Dadurch erwartet man eine Steigerung der Strahlenhärte gegen ionisierende Strahlung um eine Größenordnung. Die Verwendung von hochohmigen Epitaxalschichten verspricht, wie neuste Messungen nahelegen, eine substantielle Steigerung der Strahlenhärte gegen nicht-ionisierende Strahlung, zu Dosen deutlich oberhalb von $10^{13} n_{eq}/cm^2$.

Die Konstruktion des MVD wird parallel zum Aufbau des FAIR Beschleunigerkomplexes verlaufen. In der ersten Ausbauphase von FAIR wird das Synchrotron (SIS100, geplant für 2017) Strahlen mit Energien bis 10 AGeV für Gold-Ionen und 30 GeV für Protonen liefern. CBM wird am SIS100 Open-Charm in Proton + Proton und Proton + Kern Kollisionen untersuchen. Diese Messungen sind für das Verständnis des Charm-Produktionsmechanismus bei niedrigen Energien wichtig. Die Ergebnisse werden als Referenz für die Analyse der Charm-Daten in Kern-Kern-Stössen dienen. Bei SIS100 wird der MVD eingesetzt werden, um die Rekonstruktion von leichten Vektormesonen und von seltsamen Teilchen in Kern-Kern-Stössen zu verbessern. In der zweiten Phase des FAIR-Ausbaus werden mit Hilfe des SIS300-Synchrotrons Strahlen mit Energien von 35 AGeV (89 GeV) für Gold-Ionen (Protonen) zur Verfügung stehen. Dies wird das Physik Programm, und insbesondere das Studium von Open-Charm-Produktion in Kern-Kern-Kollisionen, von CBM hin zu höheren Energien vervollständigen.

Diese Arbeit stellt eine Beteiligung am Design und der Entwicklung des MVDs für das CBM-Experiment dar. Sie setzt sich aus drei Hauptteilen zusammen. Der erste Teil beschäftigt sich mit Monte-Carlo-Simulationen, die die Randbedingungen für das Design der ersten Generation des MVD, wie er am FAIR/SIS100 zum Einsatz kommen wird, festlegen. Der zweite Teil konzentriert sich auf detaillierte Simulationsstudien zur Leistungsfähigkeit des CBM-Experiments bezüglich der Rekonstruktion von Open-Charm-Teilchen in Kern-Kern-Stößen. Im dritten Teil wird schließlich ein Machbarkeitsstudie zum elliptischen Fluss von Open-Charm vorgestellt.

## Anforderungen an das Design des MVD der ersten Generation

Bei SIS100 wird Open-Charm in Proton + Proton und Proton + Kern Stössen mit Strahlenergien bis 30 GeV vermessen. In Kern-Kern-Stössen wird der MVD die Eigenschaften von CBM für leichte Vektormesonen und Multi-Strange-Hyperonen verbessern. Für diese Messungen sind

hohe Kollisionsraten vorgesehen, typischerweise in der Größenordnung von $2 \times 10^6$ Kollisionen/Sekunde für Proton(30 GeV)+ Gold Reaktionen und $2 \times 10^4$ Kollisionen/Sekunde für Gold(10 AGeV)+ Gold Reaktionen.

Um die erwarteten Datenraten in den MAPS-Chips MIMOSIS-1 für den mit SIS100 verwendeten CBM-MVD zu simulieren, wurden mit Hilfe des CBMRoot Simulationspakets detaillierte Monte-Carlo-Studien ausgeführt. Insbesondere wurden zwei Aspekte, die in den bisherigen Studien unberücksichtigt blieben, in die Simulationen integriert: Fluktuationen der Strahlintensität und die Strahlemittanz. Diese hat, ausgehend von der SIS18 Strahlemittanz, offensichtlich wenig Einfluss auf die Trefferdichte in den MVD Stationen, wie die Simulationen zeigen. Der Kollisions-„Pile-Up„ in MIMOSIS-1 Sensoren wurde unter Berücksichtigung ihrer erwarteten Auslesezeit von 25 $\mu$s ebenfalls simuliert. Dies geschah unter der Annahme von zwei Szenarien zu Fluktuationen der Strahlintensität bei SIS100: Das Verhältnis von maximaler zu mittler Strahintensität ist gleich 3 (motiviert durch Messungen am SIS18 Synchrotron), und gleich 10 als Sicherheitsmarge für Proton- und Gold-Strahlen bei SIS100. Diese Fluktuationen der Strahlintensität bedingen signifikante Fluktuationen der Trefferraten in den MIMOSIS-1 Sensoren. Dies ist insbesondere für Regionen mit maximalen Trefferdichten in den MVD-Stationen kritisch. In Gold + Gold Kollisionen sind diese Bereiche durch den Anteil der $\delta$-Elektronen dominiert, die im Targetmaterial durch Gold Strahlteilchen produziert werden. Es konnte gezeigt werden, dass der Anteil der $\delta$-Elektronen zur Gesamtzahl der Treffer im MVD substantiell durch das Hinzufügen von Absorbermaterial außerhalb der Detektorakzeptanz reduziert werden kann. Diese Strategie hat jedoch nur einen kleinen Einfluss auf die maximale Trefferdichte, da diese durch den Anteil von $\delta$-Elektronen dominiert wird, welcher den Detektor vor Erreichen des Absorbers trifft.

Die Anforderungen bezüglich der Datenrate werden von den MVD Sensoren bestimmt, die der maximalen Trefferdichte ausgesetzt sind, unter Berücksichtigung der unterschiedlichen Abstände zwischen MVD Station und CBM Target. Durch den Vergleich dieser Anforderungen mit der zu erwartenden Leistungsfähigkeit der Schaltungen im MIMOSIS-1 zur Nullunterdrückung wurde gezeigt, dass diese Sensoren signifikante Fluktuationen der Strahlintensität tolerieren können. Die gilt insbesondere unmittelbar am Target (5 cm Abstand in Strahlrichtung), sowohl für Proton + Gold als auch für Gold + Gold Reaktionen. Es konnte gezeigt werden, dass die erwartete Bandbreite von MIMOSIS-1 am Ausgang von 400 MHz oder 800 MHz die wesentliche Limitierung des minimalen Abstands der ersten MVD Station zum Target darstellt. Ein Sensor mit 400 MHz Bandbreite am Ausgang kann beispielsweise in einem minimalen Abstand von 5 bis 10 cm (10 bis 15 cm) für Proton + Gold (Gold + Gold) Reaktionen platziert werden, abhängig von der Größe der Strahlfluktuationen. Machbarkeitsstudien, ausgeführt von der CBM Kollaboration, haben gezeigt, dass diese Abstände für die Durchführung des Messprogramms von CBM bei SIS100 ausreichend sind. Eine Ausgangsbandbreite von 800 MHz würde darüber hinaus das Betreiben der Sensoren unter großen Fluktuationen der Strahlintensität, selbst mit ausreichenden Reserven, ermöglichen. Zusammenfassend kann festgestellt werden, das der MIMOSIS-1 Sensor die Anforderungen der hohen Datenraten bei SIS100 verarbeiten kann.

Die vorliegende Arbeit erlaubte zugleich, die Anforderungen an die Bandbreite der unterschiedlichen Komponenten des MVD Auslesesystems zu evaluieren, ausgehend von den Operations-

moden am SIS100. Diese Anforderungen basieren auf den von MIMOSIS-1 zur Verfügung gestellten Ausgangsbandbreiten von 400 beziehungsweise 800 MHz. Es stellt sich heraus, dass das Auslesesystem eine totale Bandbreite von 5 GHz bieten muss, was hohe Anforderungen an das Design der unterschiedlichen Komponenten des MVD Auslesesystems stellt.

# Untersuchungen über die Rekonstruktionseffizienz von CBM für Open-Charm-Teilchen in Kern-Kern-Stößen

Im Rahmen dieser Arbeit wurde die Rekonstruktionseffizienz des CBM-Detektors von Open-Charm-Teilchen (über deren schwachen hadronischen Zerfall) untersucht. In diesem Zusammenhang wurden Simulationen mit einer möglichst realistischen MVD-Detektor-Geometrie (bestückt mit MAPS-Sensoren) durchgeführt, nämlich einer Ortsauflösung von 3 $\mu$m, einer Auslesegeschwindigkeit von 10 $\mu$s und einer Strahlendosistoleranz von bis zu 3 Mrad und $3 \times 10^{13}\ n_{eq}/cm^2$ (jeweils für ionisierende und nichtionisierende Strahlung). Für die Teilchenidentifikation wurde dabei vorausgesetzt, dass die Information des TOF-Detektors ausreichend ist, um alle Protonen zu unterdrücken. Diese Simulationen wurden für zentrale Au+Au-Kollisionen bei einer Strahlenergie von 25 AGeV durchgeführt, was ein typisches Szenario für eine Open-Charm-Rekonstuktion bei FAIR darstellt. Um dabei die Detektor-Performance zu studieren, wurden $D^+$-Mesonen mit dem Zerfallskanal $\pi^+\ \pi^+\ K^-$ als Benchmark herangezogen. Diese Wahl wurde deshalb getroffen, da, wie oben beschrieben, die Rekonstruktion und die Trennung vom Untergrund von drei Töchterteilchen eine besondere Herausforderung darstellt.

Als Ergebnis wurde dabei festgestellt, dass die Auflösung des Sekundärvertex 72 $\mu$m beträgt, was insbesondere der geringen Materialbelegung und die hohe Ortsauflösung des MVD geschuldet ist. Für Teilchen mit Impulsen größer als 1 GeV/c beträgt die Impulsauflösung 1.2% bis 1.6%. Um die $D^+$-Mesonen über ihre Zerfallsprodukte ($\pi^+$, $\pi^+$, $K^-$) zu rekonstuieren, wurden mehrere Selektionsbedingungen gewählt, um den Untergrund durch zufällige 3-Teilchen-Kombinationen zu unterdrücken. Dabei basieren diese Kriterien im Wesentlichen auf der besonderen Topologie des $D^+$-Meson-Zerfalls mit dem charakteristischen Zerfallsvertex. Nachdem die Selektionsbedingungen weiter optimiert wurden, um das Signal zu extrahieren, wurde das HSD-Modell (bzw. SHM-Modell) verwendet, um das Signal-zu-Untergrund-Verhältnis zu bestimmen. Dieses beträgt 1.5 für das HSD-Modell, bzw. 3.0 für das SHM-Modell. Das Resultat ist eine gute Rekonstruktionseffienz (einschlieÃŸlich der geometrischen Akzeptanz) von 2%. Unter den gleichen Bedingungen wie für das $D^+$-Meson (d.h. Kollisionssystem, Energie und Zentralität) wurde ebenfalls die Rekonstuktionseffizienz des Zerfalls $D^- \rightarrow \pi^-\ \pi^-\ K^+$ untersucht: Hier wurde ein Signal-zu-Untergrundverhältnis von 3.7 (12.0) und eine Rekonstuktionseffizienz von 1.4% erreicht.

Die erwartete Statistik wurde sodann auf ein ganzes „CBM-Jahr“ hochgerechnet (d.h. auf 4 Monate Experimentzeit bei einer durchschnittlichen Auslastung von 50% und einer Kollisionsrate von 400 kHz, was für den MVD-Detektor noch akzeptabel ist). Das Ergebnis dieser Untersuchungen ist, dass man mit CBM in der Lage sein wird, $1.5 \times 10^4\ D^+$ und $2.3 \times 10^4\ D^-$-Teilchen

per Jahr nachzuweisen (die Multiplititäten wurden dabei mit HSD abgeschätzt). Kombiniert man dieses Resultat mit anderen Untersuchungen, kann man die totale Anzahl der produzierten D-Mesonen pro Jahr auf 6.9 $\times$ $10^4$ abschätzen. Diese Anzahl ist ausreichend, um diverse für die FAIR-Physik wichtige Open-Charm-Verteilungen zu untersuchen, wie z.B. Multiplitäten, Produktions-Verhältnisse, und pT-Verteilungen bei mittlerer Rapidität.

# Untersuchungen zur Messung des elliptischen Flusses von Open-Charm mit dem CBM-Spektrometer

In der vorliegenden Arbeit wurde ebenfalls untersucht, inwieweit man mit dem CBM-Spektrometer den elliptischen Fluss von D-Mesonen messen kann. Dies stellt bei FAIR-Energien wegen der Nähe zur Produktionsschwelle eine besondere Herausforderung dar. Insbesondere kommt es dabei nicht nur auf die Statistik an, sondern auch auf die Fähigkeit des Spektrometers, die azimuthale Lage der Reaktionsebene zu messen.

Die vorliegende Arbeit konzentriert dabei auf die Untersuchung, welche Statistik benötigt wird, um den elliptischen Fluss von D-Mesonen mit dem CBM-Spektometer zu messen. Hierzu wurden Monte-Carlo-Simulationen für Gold-Gold-Kollisionen bei einer Strahlenergie von 25 AGeV durchgeführt. Für diese Simulationen wurden semi-periphäre Kollisionen gewählt, da für diesem Fall erwartet wird, dass der elliptische Fluss das Maximum erreicht.

In einem ersten Schritt wird zunächst untersucht, welche Auflösung man für die Lage der Reaktionsebene erwarten kann. Dabei kam das CBMRoot-Softwarepaket und das UrQMD-Modell als Ereignisgenerator für die Au + Au-Stöße zum Einsatz. Mit dem CBM-Spektrometer kann die Reaktionsebene durch zwei unabhängige Detektoren bestimmt werden, nämlich zum einen mit dem PSD-Kalorimeter, und zum anderen mit dem STS-Tracker. Beide Methoden wurden im Rahmen dieser Arbeit hinsichtlich der möglichen Performance studiert. Im Folgenden wurde daher die Auflösung der Reaktionsebene als Funktion der Zentralität der Kollision mittels der „event-plane“-Methode analysiert. Das Ergebnis dieser Untersuchungen ist, dass der Elliplic Flow mit CBM hinreichend genau gemessen werden kann, und zwar entweder mit der Rekonstruktion erster Ordnung (n = 1) vom PSD, oder zweiter Ordnung (n = 2) vom STS. Beide Detektoren liefern eine gleichwertige Rekonstruktionsgenauigkeit für die Reaktionsebene, insbesondere für semi-periphäre Kollisionen (mit einem Stoßparameter zwischen 5 bis 9 fm) wurden die höchsten Auflösungen erreicht. Die Auflösung des Faktors <$\cos(2 \times (\Psi_n - \Psi_R))$>, der nötig ist, um den $v_2$-Parameter um die Fluktuationen der Reaktionsebene zu korrigieren, wurde als 0,4 für semi-periphäre Ereignisse bestimmt, was einer Auflösung von 40 Grad für den Azimulathalwinkel entspricht.

Für die Bestimmung des Elliptic Flow der D-Mesonen kam eine adaptierte Monte-Carlo-Methode zum Einsatz, in welcher eine pT-abhängige azimuthale Anisotropie zu der flachen Winkelverteilung hinzuaddiert wurde. Um die Fluktuationen der Reaktionsebene aufgrund der endlichen Anzahl der Teilchen und der limitierten Detektoreigenschaften mit zu berücksichtigen, wurden die Azimuthalwinkel der D-Mesonen mit der erwarteten Auflösung der Reaktionsebene von

($\sigma(\Psi_R)$= 40 Grad gefaltet. Die so erhaltenen Azimuthalverteilungen relativ zur Reaktionsebene wurden dann weiter analysiert, um den $v_2$-Parameter als Funktion des Transversalimpulses zu erhalten.

Die statistischen Unsicherheiten des $v_2$-Parameters wurden für eine Anzahl von semi-zentralen Au+Au-Ereignissen untersucht, die (wie im zweiten Teil dieser Arbeit dargestellt) einer ganzen Jahresstatistik für CBM entsprechen. Dies wurde für zwei verschiedene Szenarien für den D-Mesonenflusses durchgeführt: i.) ein „schwacher Fluss“, wie er vom HSD-Modell vorhergesagt wird (wegen der dort angenommenen geringen hadronischen Wechselwirkung der D-Mesonen), und ii.) ein „starker Fluss“, welcher für den Fall erwartet wird, dass die Wechselwirkung der Partonen häufig passiert. Wie erwartet ist dabei die statistische Unsicherheit für das Szenario mit dem „starken Fluss“ geringer. Unter der Annahme, dass der Effekt um einen Faktor von 2 höher ist als von HSD vorhergesagt, beträgt die relative statistische Unsicherheit ca. $10\%$ für den Elliptic Flow für alle D-Mesonen zusammen, und zwischen $16\%$ und $24\%$ für die einzelnen D-Mesonen-Arten.

Dieses Ergebnis zwigt, dass man mit CBM mit einem Jahr Messzeit in der Lage sein wird, auch einen elliptischen Fluss von D-Mesonen mit einer geringen Amplitude zu messen, und zwischen rein hadronischen Modellen (wie z.B. HSD) und Modellen mit partonischen Freiheitsgraden (wie z.B. PHSD oder AMPT) zu unterscheiden. Für den Fall, dass der elliptische Fluss sehr ausgeprägt sein wird, wie es für die höchsten FAIR-Energien (25-35 AGeV) erwartet wird, wird man in der Lage sein, deren Stärke als Funktion der Kollisionszentralität und Strahlenergie zu bestimmen. Eine detailliertere, nach pT differenzierte Messung wird hingegen nur möglich sein, wenn man die Summe aller D-Mesonen nimmt. Möchte man jedoch solche Untersuchungen getrennt nach D-Mesonen-Typen durchführen, braucht man eine höhere Statistik, was wiederum eine höhere Kollisionsrate benötigt, und damit strahlenhärtere MAPS-Sensoren.

# Zusammenfassung und Ausblick

Die vorliegende Arbeit liefert einige wichtige Beiträge für das Design des Micro-Vertex-Detektors, einer der wesentlichen Komponenten des CBM-Experimentes, der am zukünftigen FAIR-Komplex installiert werden wird.

Es konnte gezeigt werden, dass die zu erwartenden Datenraten der MAPS-Sensoren der ersten Generation des MVD ausreichend ist, um das angestrebte Physikprogramm des CBM-Detektors durchzuführen. Die benötigte Bandbreite der einzelnen Komponenten des MVD-Auslesesystems konnten bestimmt werden. Diese Spezifikationen wurden nunmehr in das technische Design des MVD-Auslesesystems integriert, was ein wesentlicher Schritt hin zur Realisierung des Systems darstellt.

Des Weiteren wurden detaillierte Simulationen durchgeführt, um die zu erwartende Leistung des CBM-Experimentes hinsichtlich der Messung von Open-Charm-Teilchen in Kern-Kern-Stößen zu evaluieren. Hier konnte gezeigt werden, dass die Rekonstruktion dieser Teilchen über deren hadronsicher Zerfall in Gold-Gold-Stößen bei 25 AGeV mit einer guten Reinheit machbar

ist. Die zu erwartende Statistik pro laufendem Jahr bei einer Kollisionsrate von 400 kHz wurde auf 11.5 $\times$ $10^4$ für den Kanal $D^+ \rightarrow \pi^+ \pi^+ K^-$ geschätzt, und mindestens 6.9 $\times$ $10^4$ für alle D-Mesonen und alle Zerfallskanäle zusammen. Basierend auf diesen Resultaten wurde des weiteren untersucht, ob man in der Lage sein wird, den elliptischen Fluss von D-Mesonen zu messen. Hierbei wurde eine realistische Auflösung für den Azimutalwinkel der Reaktionebene angenommen. Es konnte gezeigt werden, dass der integrierte Parameter des elliptischen Flusses für die verschiedenen D-Meson-Typen präzise genug vermessen werden kann. Eine Messung von differentiellen pT-Verteilungen würde jedoch eine größere Statistik und damit höhere Kollisionsraten benötigen, dies ist derzeit aufgrund der limitierten Strahlenhärte der MAPS-Sensoren noch nicht möglich.

Andererseit sollte nicht unerwähnt bleiben, dass hier die Entwicklung der MAPS-Sensoren bisher sehr zügig und schneller als erwartet vorangeschritten ist. Daher ist es nicht ausgeschlossen, dass zu dem Zeitpunkt, wenn der MVD für SIS-300 entwickelt wird, die Entwicklung der Sensoren soweit abgeschlossen sein wird, dass auch diese Bedingungen erfüllt sind. Insbesondere die fortschreitende Weiterentwicklung der integrierten 3D-Schaltungstechnik verspricht weitere Durchbrüche für die MAPS-Sensoren: Hier könnte eine Auslesezeit von wenigen Mikrosekunden und eine Strahlentoleranz für nichtionisierende Strahlung von mehr als $10^{14}$ $n_{eq}/cm^2$ und für ionisierende Strahlung von mehr als 30 Mrad erreicht werden. Dies würde die Möglichkeiten des Experimentes für D-Mesonen enorm erhöhen. Hier wären dann sogar Messungen des $\Lambda_c$ Baryon denkbar, was mit einer Lebenszeit von $c\tau$ = 59.9 fm eine Herausforderung darstellt.

# Chapter 1

# Introduction

The subject of this thesis lies within the framework of the Compressed Baryonic Matter (CBM) experiment. The latter is one of the major experiments planned at the new international accelerator Facility for Antiproton and Ion Research (FAIR), which is currently under construction at GSI in Darmstadt, Germany. The research program of this new experiment aims at exploring, by means of heavy ion collisions at beam energies in the range from 2 to 45 AGeV, the high net baryon density and moderate temperature region of the nuclear matter phase diagram, which is only poorly explored so far. This research program includes the search for the onset of the phase transition from hadronic to partonic matter, the search for the critical endpoint of the first order phase transition, the study of in-medium effects in dense baryonic matter and their possible relation to the partial restoration of chiral symmetry, and the investigation of the equation of state of dense nuclear matter. Progress in this research field is of crucial importance in understanding the structure and the properties of strongly interacting matter at high net baryon densities and its theoretical description within the fundamental theory of the strong interaction, the Quantum ChromoDynamics (QCD). Furthermore, the matter produced under these extreme conditions of net baryon densities is of particular interest for the study of compact astrophysical objects such as neutron stars.

The study of the production and propagation of open charm particles, i.e. particles containing one charm quark and one or several light quarks, in heavy ion collisions is one of the major physics topics of the CBM experiment. Physics observables related to open charm are predicted to be particularly sensitive to the deconfinement phase transition and to in-medium modifications of hadron properties in dense matter. For example, the relative yield of open charm mesons (D-mesons) and charmonium has been suggested recently as an observable sensitive to the deconfinement phase transition: a sudden drop in the excitation function of the J/$\psi$ over D yield ratio is predicted in the beam energy range corresponding to the onset of the Quark Gluon Plasma (QGP). Another evidence for the deconfinement phase transition can be obtained from the measurement of the elliptic flow of open charm particles. The magnitude of this effect depends strongly on the degrees of freedom of the hot and dense medium created in the early stage of the collision. In a purely hadronic scenario, open charm particles have a moderate interaction

rate and, hence, the magnitude of their flow is expected to be very weak. The observation of a strong elliptic flow of open charm at FAIR energies would indicate the creation of a partonic medium. The study of open charm hadrons can also provide valuable information on in-medium effects as their effective mass is expected to be modified in the hot and dense nuclear medium, possibly due to the effect of chiral symmetry restoration. This can be observed experimentally as a modification of their production cross section, in particular at FAIR energies where open charm is produced close to the kinematical threshold.

The measurement of open charm particles in nucleus-nucleus collisions is very challenging, in particular at FAIR energies because of their very low production cross section (close to the kinematical threshold). This measurement requires high collision rates, which will be possible for the first time thanks to the combination of the high intensity beams of FAIR, up to $10^9$ ions/second for Au beams, and the use of new generation high rate and radiation hard detectors.

The CBM experiment will measure open charm particles through their weak decay into charged hadrons (pions and kaons). The reconstruction of these particles is based on the determination of the invariant mass of their decay daughters. This task is particularly difficult in heavy ion collisions at FAIR energies due the fact that the multiplicity of open charm hadrons is much smaller (by several orders of magnitude) than that of abundant hadrons (such as promptly emitted pions and kaons). Since the invariant mass method consists in combining all charged particles of an event into multiplets, according to the decay channel chosen to detect the open charm signal, this method leads to a tremendous combinatorial background of uncorrelated particle multiplets. The strategy to discriminate the signal from the combinatorial background is based on the topology of open charm particle decays and, in particular, their characteristic displaced decay vertex relative to the interaction point.

The reconstruction of the decay vertex of open charm particles is very delicate due to the very short lifetime of these particles (on the order of a picosecond). Their mean decay length is typically on the order of several 100 $\mu$m. This calls for a very precise vertex detector, capable of separating the secondary decay vertex of open charm particles from the primary collision vertex.

The vertex detector of the CBM experiment, called Micro Vertex Detector (MVD), must therefore provide the high precision necessary for the measurements of the displaced vertices of open charm particles. This imposes strong constraints on its design. The MVD detector must be very granular to provide a high spatial resolution, and must be as thin as possible in order to reduce multiple scattering effects which can deteriorate the precision on the vertex and on the momentum reconstruction. Moreover, it must be placed very close to the interaction point and should be, therefore, highly radiation tolerant. The detector must be also fast enough to operate at the high collision rates needed for open charm measurements close to the kinematical threshold.

Monolithic Active Pixel Sensors (MAPS) are considered as the most promising technology for equipping the CBM-MVD. They are really thin (a thickness below 0.05% of the radiation length $X_0$) and can provide a spatial resolution below 5 $\mu$m. Substantial progresses have been made over the last years mainly in improving their radiation tolerance and their read-out speed. The current performances of MAPS sensors are a read-out time of about 100 $\mu$s and a tolerance to a non-ionizing (ionizing) radiation dose of $10^{13}$ $n_{eq}/cm^2$ (above 0.3 Mrad). Further improvements

are expected in the coming years, before the construction phase of the detector which is planned to start in 2015. The read-out time is expected to be improved by a factor of 2-4, reaching $\sim$ 50-25 $\mu$s. The radiation tolerance will be also further improved. One expects a gain factor of about 10 in the tolerance to ionizing radiation, and a substantial enhancement of the tolerance to non-ionizing radiation (above $10^{13}$ $n_{eq}/cm^2$).

The construction of the MVD detector will be synchronized with the availability of the FAIR accelerators. In the first phase of the realization of FAIR, the beams will be delivered by the SIS100 synchrotron (planned for 2017) with energies up to about 10 AGeV for Au, and around 30 GeV for protons. At SIS100, CBM will measure open charm in proton-proton and proton-nucleus collisions. These measurements are important for understanding the charm production mechanism at low collision energy and will serve also as a reference for the interpretation of charm data in nucleus-nucleus collisions. The MVD will also be used at SIS100 to improve the measurement of other observables in CBM, in particular those related to low-mass vector mesons and strange particles. In the second phase of the realization of FAIR, the beams from the SIS300 synchrotron (expected a few years later) will be provided up to 35 AGeV for Au and 89 GeV for protons. This will allow CBM completing its physics program by measuring open charm in nucleus-nucleus collisions.

The present thesis is a contribution to the design and development of the MVD detector of the CBM experiment. It includes three main parts. The first part deals with Monte Carlo simulations carried out in order to define the design requirements for the first generation MVD which will operate at the FAIR/SIS100 synchrotron. The second part is a detailed simulation study aiming at assessing the expected performances of the CBM experiment for the reconstruction of open charm particles in nucleus-nucleus collisions. Finally, the third part is a feasibility study of open charm elliptic flow measurements in CBM.

At SIS100, due to the high collision rates foreseen in p + A and A + A collisions, the MVD sensors and front-end electronics are expected to be exposed to large and inhomogeneous hit rates. This is a critical issue since the read-out electronics embedded in MAPS sensors and located in the front-end electronics is limited in terms of data rate capability (due to the fact that these electronic circuits must be confined into small volumes, inside or close to the sensors). This motivated a detailed evaluation of the data rate requirements for MAPS sensors. To do so, the particle flux in the MVD detector has been simulated for p(30 GeV) + Au and Au(10 AGeV) + Au collisions under realistic running conditions, accounting for: the beam emittance, the beam intensity fluctuations expected at SIS100 and several sources of background particles including, in particular, $\delta$-electrons knocked out by beam ions out of the CBM target. The characteristics of the MAPS sensor expected in 2015 for equipping the MVD detector, namely MIMOSIS-1, were accounted for: active area, read-out time, response to the passage of charged particles, fake hit rate, and data formatting.

To be able to read out MVD sensors, a high and inhomogeneous data flow will have to be handled by the read-out system. An other aspect of the design of the MVD addressed in this thesis concerned the design of the read-out system, for which the requirements in terms of bandwidth were assessed.

The purpose of the second part of the thesis was to study the reconstruction of open charm particles in nucleus-nucleus collisions with the CBM detector. Detailed Monte Carlo simulations were performed taking into account the geometry of the MVD detector stations and the anticipated performances of MAPS sensors composing the stations. These studies were done for central Au + Au collisions at an incident energy of 25 AGeV, which represent a typical environment for open charm particle reconstruction in nucleus-nucleus collisions in the FAIR energy range. The expected performances for open charm particle reconstruction were evaluated using as a benchmark the $D^+$ meson decaying into $\pi^+$ $\pi^+$ $K^-$. This choice was motivated by the fact that the reconstruction of such decay channel (involving three daughter particles) is particularly challenging due to the very large combinatorial background. The simulations allowed us estimating the efficiency with which this decay channel can be reconstructed in CBM and the corresponding signal-to-background ratio. Based on this, we evaluated the expected statistics during a typical running period.

In the last part of the thesis, we investigated the possibility of measuring the elliptic of open charm D-mesons. This has been done through Monte Carlo simulations for semi-peripheral Au + Au collisions at a beam energy of 25 AGeV. The extraction of the elliptic flow requires the reconstruction of the reaction plane. The latter will be measured with two sub-detector components in CBM: the Silicon Tracking System (STS) and the Projectile Spectator Detector (PSD). The first step of this work consisted in assessing the resolution with which the reaction plane can be determined with each of these two detectors. To this end, detailed studies were carried using the so-called "event plane" method. In a second step, based on the results of these studies, we performed a simple simulation study to investigate the capability of the experiment for measuring the elliptic flow component of D-mesons. For this purpose, we evaluated the expected statistical accuracy on the elliptic flow ($v_2$) of these particles for a typical CBM run period. This was done for two different assumptions on the magnitude of the elliptic flow.

The organization of this thesis is the following:

Chapter 2 gives an introduction to the physics of high energy heavy-ion collisions. A short overview of the current status of the knowledge about the nuclear matter phase diagram is presented with a focus on the high baryon density region which is of particular interest in the context of this thesis. The last part of this chapter is focused on the importance of measuring open charm particles in nucleus-nucleus collisions at FAIR energies regarding, in particular, the deconfinement and chiral phase transitions.

Chapter 3 acts as an introduction to the CBM experiment and its main physics goals together with a description of the overall layout of the detector setup and its different sub-components.

Chapter 4 is dedicated to the Micro-Vertex Detector. First, the conceptual design of the detector is described. Then, the status of the R&D on MAPS sensors and the performances presently achieved are summarized. Finally, the improvements expected in the forthcoming years are discussed.

Chapter 5 deals with the design of the first generation MVD detector at the FAIR/SIS100 synchrotron with a focus on the determination of the data rate requirements for the MAPS sensors

and their read-out system. The simulation studies carried out for this purpose are presented. Then, the results are reported and their implications on the MVD detector design are discussed.

Chapter 6 concerns the simulation study carried out in order to investigate the reconstruction of open charm particles in heavy-ion collisions. First, the simulation procedure is described in detail. Then the method used to reconstruct $D^+$-mesons, used as a benchmark, is presented along with the strategy employed to separate the signal from the combinatorial background. The results are reported in terms of the signal reconstruction efficiency and the signal-to-background ratio. Finally, an estimate of the expected statistics per running year is given for different D-meson species.

Chapter 7 concentrates on the feasibility of measuring the elliptic flow of open charm mesons. The procedure used to simulate the D-meson elliptic flow is described. This is followed by a detailed study of the resolution with which the reaction plane can be determined in CBM. Finally, the expected performances of CBM for D-meson elliptic flow measurements are presented and their implications and limitations are discussed.

# Chapter 2

# High energy heavy ion collisions

Heavy ion collisions offer the unique opportunity to create and investigate extreme states of strongly interacting matter under controlled laboratory conditions. By colliding two nuclei at high energy, one can deposit a large amount of energy in a small region of space for a short duration of time. In this region, the achieved energy density can be very large, of the order of several GeV/$fm^3$, which is one order of magnitude higher than the energy density of nuclear matter in its ground state. Under such conditions, a deconfined state of matter called the Quark Gluon Plasma (QGP) may be formed. The occurrence of this new form of matter is related to fundamental properties of the strong interaction.

This chapter is organized as follows. We begin with a brief reminder about the theory of the strong interaction, namely the quantum chromodynamics (Section 2.1). Next, we discuss the main features of the nuclear matter phase diagram and its exploration by means of heavy-ion experiments. Then, we give a short review of the main results from previous and current experiments. Finally, in the last part of the chapter, we emphasize the importance of investigating open charm production in nucleus-nucleus collisions and in particular at FAIR energies.

## 2.1 The Quantum chromodynamics

**Quark and gluons**

The Quantum ChromoDynamics (QCD) [1] is the theory describing the interactions between colored objects, i.e. quarks, by the exchange of color field quanta, the gluons. This theory emerged as an extension of the quark model of hadrons * [2]. The latter was incomplete in the sens that the Pauli exclusion principle would not allow the existence of a particle like the $\Delta^{++}$ baryon made of three quarks of same flavor (up) and same spin (spin up). One had to postulate the existence of another quantum number, or degree of freedom, characterizing the quark quantum states, namely the color. The structure of QCD emerges, similarly as in Quantum ElectroDy-

*Bound states of quarks and anti-quarks

namics (QED), from the requirement of local gauge invariance of the QCD Lagrangian, i.e. the dynamics of QCD must be invariant under rotations of the quark fields in color space [*]. One has to introduce, following the familiar case of QED, the gauge field of gluons for QCD to exhibit such an exact internal symmetry with respect to the color degrees of freedom of quarks or, in technical terms, for the gauge invariance of the QCD Lagrangian to be realized under such transformations.

**The strong coupling constant**

QCD exhibits unique features: gluons are color charged and can therefore emit other gluons and interact among themselves[†]. As a result, the strong coupling constant ($\alpha_S$), quantifying the strength of the strong interaction, decreases logarithmically at short distances, or equivalently for large energy-momentum transfers ($Q^2$), i.e. for $Q^2 \gg \Lambda^2_{QCD}$[‡]. In this regime, quarks and gluons are weakly coupled, leading to the so-called asymptotic freedom of the strong interaction [8]. At large distances, or for $Q^2 \sim \Lambda^2_{QCD}$, $\alpha_S$ becomes strong, which leads to the confinement of colored objects[§]. Indeed, isolated quarks are not observed in nature, but only in hadronic and colorless bound states like mesons and baryons. The rising of $\alpha_S$ might also lead to the spontaneous breaking of chiral symmetry.

The next two sections give a qualitative understanding of the phenomena of color confinement and spontaneous breaking of chiral symmetry, both characterizing hadronic matter.

### 2.1.1 Confinement of colored objects

QCD, calculated on the lattice (see Section 2.3), indicates that when the distance scale is comparable to the size of a hadron, quarks interact with a potential energy which goes approximately linearly with the distance. This observation supports the idea that the interaction between quarks can be modeled by using a so-called string [3], i.e. a simplified picture where pairs of quarks are elastically linked to each other by a color electric field $\vec{\epsilon}$ contained in a flux tube, as pictured in Figure 2.1. Here we choose to discuss the case of a quark interacting with an anti-quark. $\vec{\epsilon}$ is assumed constant and finite inside the flux tube linking the two quarks, while null outside this tube. The energy contained inside the flux tube is then equal to:

$$E = \frac{1}{2}\epsilon^2 \times A \times L \tag{2.1}$$

$$E = \kappa \times L \tag{2.2}$$

where $\kappa$ is the linear energy density in the tube, referred to as the string tension, $\epsilon$ is the magnitude of the color electric field, A is the cross-section area of the tube, and L is its length (i.e. the

[*] Keeping in mind that while there is only one electric charge in QED, there are three color charges in QCD

[†] QCD is thus a non-Abelian gauge field theory, coupled with the color quantum number

[‡] $\Lambda_{QCD}$ is a typical energy scale, of $\sim$ 200 MeV, at which colored objects interact strongly

[§] Note that $\alpha_S$ is determined experimentally as a function of $Q^2$ from a variety of processes [7]

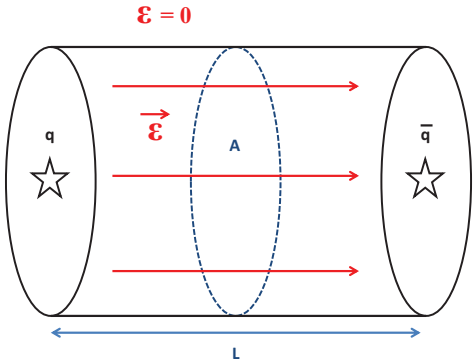


**Figure 2.1:** *Sketch of a string [3], modeling the interaction between a quark and an anti-quark. The color electric field in between them is assumed constant and finite inside the tube of radius A and length L separating the two quarks, and null outside.*

distance separating the quark and the anti-quark). Equation (2.2) gives the potential energy carried by gluons exchanged by the two quarks. As the separation between the quark and the anti-quark becomes large, it becomes energetically more favorable to produce another quark - anti-quark pair at a point along the tube such that the produced quark is connected to the original anti-quark and vice-versa. Thus, quarks remain confined inside colorless bound states or hadrons.

For example, one has the following condition for the creation of a new quark - anti-quark pair to be allowed inside the original string:

$$E > 2 \times m_T \tag{2.3}$$

with the transverse mass $m_T$ equal to $\sqrt{m^2 + p_T^2}$*. The factor 2 accounts for both the quark and the anti-quark newly created. Combining the relations (2.2) and (2.3) one obtains the following condition:

$$L > \frac{2 \times m_T}{\kappa} \tag{2.4}$$

If we assume for quarks confined inside hadrons to have a constituent mass (see next section) and a transverse momentum of around 300 MeV each, and considering a string tension of around 1 GeV/fm †, the distance at which the formation of a new quark-antiquark pair is energetically more favorable, is approximately equal to the size of the hadrons, i.e. 1 fm.

### 2.1.2 Spontaneous breaking of chiral symmetry and the origin of the mass of hadrons

In the limit of vanishing quark masses (or relativistic velocity) the spin of a fermion is aligned either parallel or anti-parallel to its momentum, independently of the reference frame. In such

*By convention for the units, we take the speed of light c = 1

†Phenomenological constant estimated using hadron spectroscopy [4]

a case, this fermion has a Lorentz invariant, right-handed or left-handed chirality. Fermions of opposite chiralities, or chiral parters, are transformed into each other under a parity transformation. For vanishing quark masses, the QCD Lagrangian is invariant under chiral transformation of the quark fields. This is the so-called chiral symmetry. Several evidences exist which support that chiral symmetry is partially realized in nature [5]. This is due to the fact that the bare mass of light quarks ($\sim$ 5 - 10 MeV for the up and down quarks, respectively), generated through the weak interaction by the Higgs mechanism, is small compared with the typical energy scale of QCD (as mentioned earlier, $\Lambda_{QCD} \sim 200$ MeV).

One of the most puzzling features of QCD is that, if the chiral symmetry was realized in nature, even partially, fermions with opposite parities, i.e. chiral partners, would have the same mass, at least up to a few MeV. This symmetry in the mass spectrum between chiral parters is not observed in nature. For example, the mass of the chiral partners $\rho$ and $a_1$ mesons is of 770 MeV and 1260 MeV, respectively. This asymmetry is however successfully described by the mechanism of spontaneous breaking of chiral symmetry [5]. This phenomenon is the expression of the fact that the QCD vacuum (see below) does not have the symmetry which the QCD Lagrangian has under chiral transformation of the quark fields. Due to the rising coupling constant of the strong interaction at large distances, the lowest energy state of QCD matter, i.e. its ground state or vacuum, is reached through the condensation of quark- antiquark pairs, or q-$\bar{q}$ condensate. The q-$\bar{q}$ condensate thus has a finite expectation value <q-$\bar{q}$> in the QCD vacuum [6], and characterizes the low energy structure of QCD. q-$\bar{q}$ states have the same quantum numbers as the $\sigma$ meson. The latter is one representative only of the chiral partner doublet $\sigma$ - $\pi$. Thus, the vacuum state of QCD is not chirally symmetric, being essentially populated with the q-$\bar{q}$ condensate. Since in quantum field theory, particles are elementary excitations of the vacuum, a chirally asymmetric vacuum leads to different masses between chiral partners. Hence, the spontaneous breaking of chiral symmetry is consistent with the observed asymmetry in the mass spectrum between chiral parters. Note that the spontaneous symmetry breaking is a well known phenomenon for spin systems e.g. the rotational symmetry of the ground state of ferromagnets is spontaneously broken, through spin alignment at temperatures below the Curie temperature.

Another important feature of QCD is the generation of hadron masses. For example, for nucleons (mass $\sim$ 1 GeV), the sum of the bare mass of their constituent u and d quarks, of a few MeV, is far below 1 GeV. In the context of simplified models assuming spontaneous breaking of chiral symmetry (e.g. the linear sigma model [5]), it can be shown that the mass of the nucleon is dynamically generated through its interaction with the QCD vacuum, i.e. with the q-$\bar{q}$ condensate. This dynamics then results into a constituent mass for u and d quarks of about 330 MeV*. Figure 2.2 shows the relative contribution to the constituent mass of quarks, resulting from the spontaneous breaking of chiral symmetry and from the Higgs mechanism. The heavier the quark is, the most of its constituent mass is generated through the Higgs mechanism. In particular, while the mass of the top quark is entirely generated through the Higgs mechanism, the mass of the u and d quarks originates mostly from the spontaneous breaking of chiral symmetry (close to 99 $\%$). Hence, if the spontaneous breaking of chiral symmetry is the proper mechanism for the

*Since nucleons are constituted with three valence quarks, this is just one third of the nucleon mass

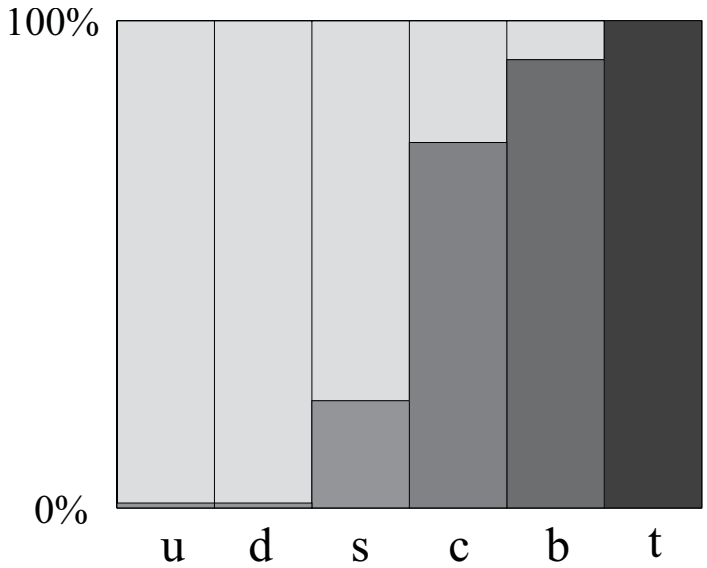


**Figure 2.2:** *Contributions to the constituent quark mass due to the spontaneous breaking of chiral symmetry (light grey) and the Higgs mechanism (dark grey).*

mass generation of hadrons, almost all of the mass in the visible universe originates from the low energy structure of QCD (i.e. the q-$\bar{q}$ condensate).

## 2.2 The phase diagram of nuclear matter

A schematic picture of the phase diagram of nuclear matter is presented in Figure 2.3. This diagram displays the phases of nuclear matter, as a function of thermodynamic state parameters: the temperature (T) and baryon chemical potential ($\mu_B$). In the ground state (T $\sim$ 0, $\mu_B \sim$ 1 GeV), nuclei behave like a Fermi liquid. At higher temperatures, when the (average) kinetic energy of nucleons becomes higher than their binding energy inside nuclei, the latter dissolve into nucleons, leading to a first order phase transition from a liquid to a dilute gas of nucleons*. At moderate temperatures above the liquid-gas phase transition, nucleons are excited into short-lived baryon resonances and pairs of (light) hadron and anti-hadron (mostly pions) are created. This mixture of nucleons, baryon resonances and mesons is called hadronic matter. More related to the present thesis is the presence in this diagram of another phase transition from hadronic matter to a deconfined phase of quarks and gluons, the Quark Gluon Plasma (QGP), which appears at very high temperatures and/or baryon chemical potentials. The existence of this transition is predicted by lattice QCD calculations [23] (see Section 2.3).

The transition to a color deconfined matter can be intuitively understood in this way: by increas-

*Experimental evidence of this phase transition has been observed at intermediate beam energies. The critical temperature is estimated to be of about 5 MeV [10]

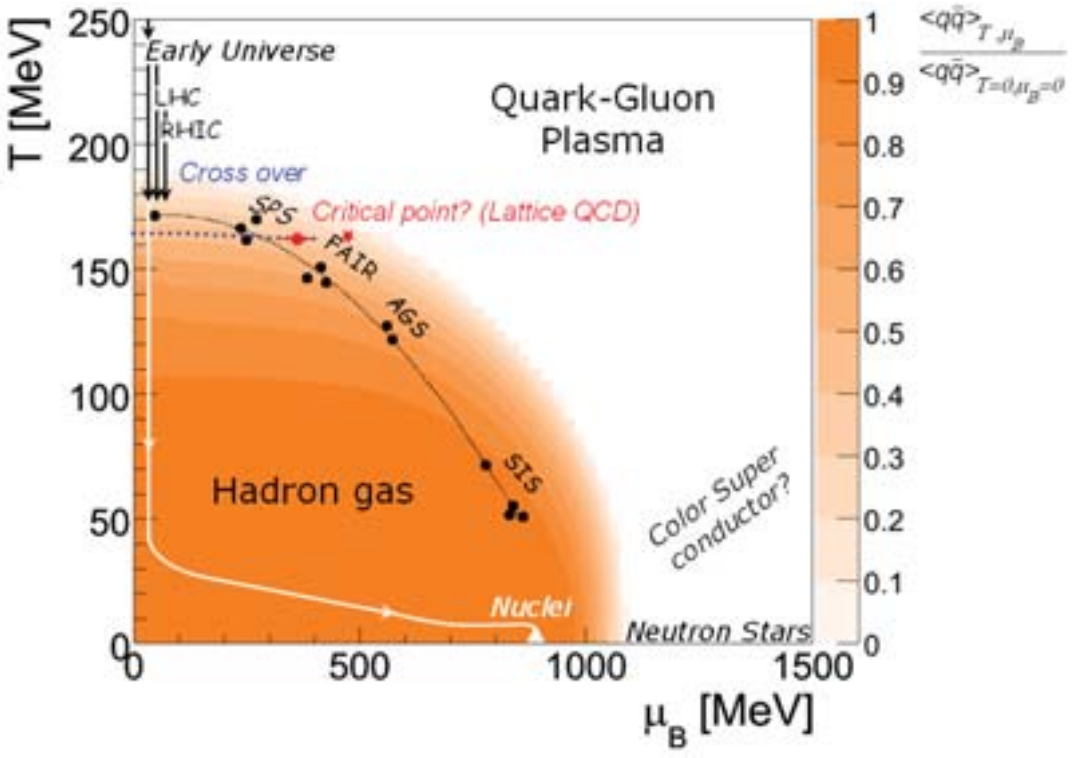


**Figure 2.3:** *Phase diagram of nuclear matter as a function of temperature (T) and baryon chemical potential ($\mu_B$). It is strongly believed that the hadronic and partonic phases are separated by a smooth crossover phase transition at vanishing $\mu_B$, whereas a first-order phase transition may take place at larger values of $\mu_B$. The crossover and first-order lines must then be separated by a critical endpoint. The state of nuclear matter with large baryon chemical potential and small temperature is believed to exist at the interior of dense neutron stars. The black points correspond to the chemical freeze-out conditions in heavy ion collisions at beam energies in the range from SIS to RHIC energies, obtained from a statistical fit of measured hadron yield ratios [13]. Also shown is the chiral condensate (third axis), as a function of temperature and baryon chemical potential, calculated with the Nambu and Jona-Lasinio model [6].*

ing the temperature, light hadrons (mostly pions) are thermally created. Their spatial extension fills the QCD vacuum. At increasing baryon chemical potential ($\mu_B$), or equivalently, at increasing net baryon density ($\rho_B$)*, most of the nucleons originating from the impinging ions deposit their baryonic content in the small, Lorentz contracted, overlap region of the two ions. At high T or high $\rho_B$, the wave functions of hadrons begin to overlap. A simplified, classical picture is drawn in Figure 2.4 (lower part). In the ground state ($\rho_0$ = 0.17/$fm^3$), the average distance between hadrons is about 1.8 fm. This distance is larger than their typical size ($r_h \sim 0.8$ fm). At such densities, hadrons are thus distinct objects in space. At $\rho_B \simeq 8 \times \rho_0$, the average distance between hadrons is of the order of their size, and their wave functions start to overlap. As the density of the color charges (quarks and gluons) surrounding each quark is increasing, the binding potential between quarks is dynamically screened. As an illustration, the upper part of Figure 2.4 shows the shape of the quark-antiquark potential as a function of the inter-quark distance. As explained in Section 2.1.1, in the hadronic phase (i.e. confined quarks in the QCD vacuum), this potential increases linearly with the distance between the quarks. In the deconfined phase, the screening effect mentioned above increases with the distance between the quarks, as more color charges are present in between them. The screening of color charges results into a quark-antiquark potential which saturates at long inter-quark distances. The long-range interaction between quarks (for a distance above R in the figure) does not depend on their relative distance, and quarks can move freely. In such deconfined plasma of quarks and gluons, the effective degrees of freedom associated with the strong interaction at large distances (or low energy-momentum transfers) are quarks and gluons, in contrast with that in the hadronic phase†. It is important to stress that the color screening effect is supported by lattice QCD [21] (see Section 2.3.1).

Additionally, the region of extreme temperatures and net baryon densities is also characterized by a restoration of chiral symmetry. The chiral condensate is shown as the third axis of Figure 2.3. Its expectation value is predicted by the Nambu and Jona-Lasinio model [6]. While it is non-vanishing in the hadronic phase, it melts at high temperatures or net baryon densities. This leads to a restoration of chiral symmetry. These predictions are supported by lattice QCD [20].

A phase transition is characterized by its order, i.e how rapidly the properties of the system are changing in response to a change of temperature or net baryon density. At high T and low $\rho_B$, it is generally accepted that the transition from a hadron gas to a QGP is a smooth cross-over without discontinuity in the thermodynamic state variables, e.g. pressure, energy density or entropy density. The cross-over phase transition in the high temperature region of the phase diagram is predicted by lattice QCD (see Section 2.3.1). At high $\rho_B$ and low T, recent lattice results predict a first order phase transition‡ (see Section 2.3.2). A coexistence between hadronic and QGP phases is expected to exist at the phase transition line, usually referred to as mixed phase. The cross-over and first order phase transitions, predicted at high temperatures and large net baryon

*$\mu_B$ and $\rho_B$ are directly related, i.e. $\rho_B \propto e^{\frac{\mu_B - m}{T}}$ - $e^{\frac{-\mu_B - m}{T}}$. Increasing the net baryonic content of the system increases the baryon chemical potential in the system, i.e. the energy required to produce one additional baryon

†Note that the high energy dynamics of QCD is governed by interactions between partons in either, confined or deconfined, phases of the nuclear matter, due to the asymptotic freedom of the strong interaction

‡A phase transition of $n^{th}$ order is characterized by a discontinuity in the $n^{th}$ derivative of state variables as a function of temperature and baryon chemical potential

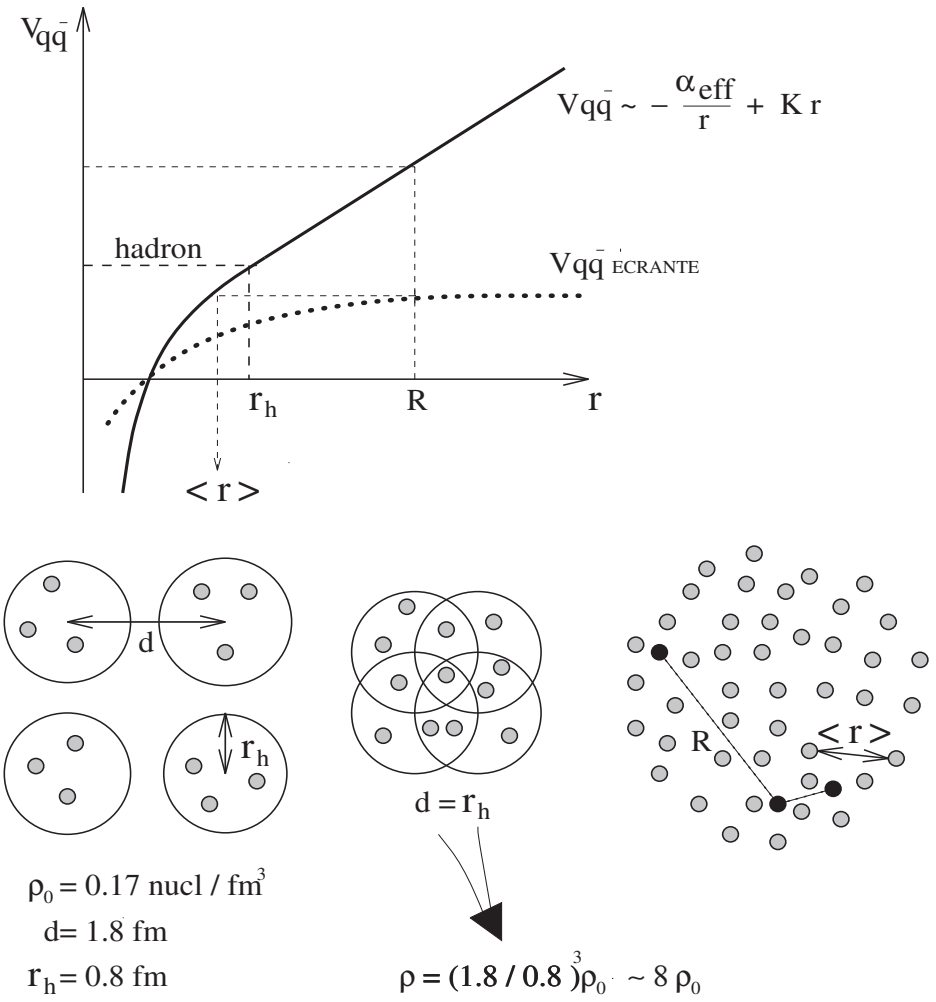


**Figure 2.4:** *Top: Illustration of the quark-antiquark potential as a function of their relative distance. In the ground state of nuclear matter ($\rho_0$ = 0.17/$fm^3$), the potential increases approximately linearly with the distance, leading to the confinement of quarks. Bottom: at net baryon densities $\rho_B \sim 8\ \rho_0$, hadron wave functions begin to overlap, leading a screening of the quark-antiquark potential at large distances. As a result, quarks can move freely in the so-called Quark Gluon Plasma. Taken from [12].*

densities, respectively, suggest the existence of a critical point where the nature of the phase transition changes [22]. Note that it could also be that the transition is continuous at large $\mu_B$, in which case no critical endpoint would exist. There are lattice QCD calculations which favor one scenario or the other [14, 15]. It is thus of particular importance to explore experimentally the high $\mu_B$ region of the nuclear phase diagram.

The knowledge of the structure of the nuclear phase diagram has strong implications in cosmology. The quark gluon plasma is believed to have existed during the first 10 microseconds after the Big Bang, and it may exist today in the cores of neutron stars.

Additionally, the nuclear phase diagram is likely to exhibit more complex structures as depicted in Figure 2.3. For example, the deconfinement and chiral phase transitions are linked to each other, since they are both related to the low energy regime of QCD and to the structure of the QCD vacuum. However, they do not necessarily take place at equal critical temperatures and densities. From lattice QCD calculations, both phase transitions occur at nearly the same temperature at vanishing baryon chemical potential [23]. This may not be the case at high $\mu_B$. It has been suggested that a color confined, chirally symmetric nuclear matter could exist at high net baryon densities, referred to as quarkyonic matter [16]. At very high $\mu_B$, one also expects a color super-conductor phase, characterized by the condensation of quarks into quark-antiquark pairs (similarly as the Cooper mechanism in electromagnetic super-conductors) [17].

## 2.3 Predictions from lattice QCD

Processes involving high energy transfers can be studied with high accuracy in the realm of perturbation theory, as an expansion in powers of the (weak) coupling constant of strong interaction [9]. By contrast, the regime of low energy transfers, at which the coupling constant is strong, can not be treated perturbatively. This regime is referred to as non-perturbative regime. As mentioned earlier, the non-perturbative regime of QCD governs processes like the confinement of quarks and the dynamical generation of hadron masses. There is currently no exact solution of the QCD equations in the non-pertubative regime. Thus, these two mechanisms, among others, cannot be formulated analytically from first principles with present theoretical tools. However, the non-perturbative regime can be addressed with the help of QCD-based models* and lattice QCD calculations (lQCD) [18, 19]. lQCD consists in solving the complex QCD equations on an simplified, discrete and finite, euclidean space-time lattice.

The current predictions of lQCD for the conditions in which color deconfinement occurs are briefly addressed in Section 2.3.1. The possible locations of the QCD critical point in the nuclear phase diagram are presented in Section 2.3.2.

*For example, at low temperature and low baryon chemical potential, chiral pertubation theory can be successfully used to describe low energy pion physics [5], using expansions in powers of the pion mass

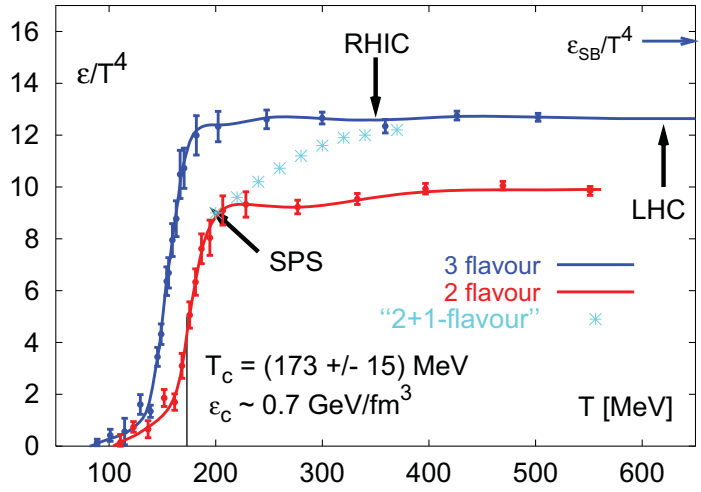


**Figure 2.5:** *The energy density in units of $T^4$ as a function of temperature from lattice QCD calculations at vanishing baryon chemical potential [20]. The results are obtained for various number of quark flavors. The blue arrow indicates the Stefan Boltzmann ideal gas limit for the energy density.*

### 2.3.1 Deconfinement phase transition

Phase transitions are characterized by a discontinuity in the change of thermodynamic state variables with temperature or net baryon density. For example, the liquid-gas phase transition of nuclear matter is of first order [11], and exhibits a significant change in particle density at constant temperature. The particle density is thus a good order parameter for such phase transition, i.e. its value is significantly different in the two phases. In the case of the hadronic-partonic matter phase transition, the relevant order parameters are the energy density, the pressure, and the entropy density.

Thermodynamic quantities like the energy density, the pressure, and the entropy density can be computed by lattice QCD as a function of temperature. Reliable informations are available from lattice calculations at vanishing baryon chemical potential. Figure 2.5 shows the energy density as a function of temperature, at vanishing baryon chemical potential [20]. It is divided by $T^4$ to get rid of its trivial dependence with temperature. One can see a rapid rise of the energy density in a narrow temperature range, from 150 to 200 MeV. This reflects the phase transition from a hadron gas to QGP phase: this increase in energy density is due to the liberation of quark and gluon degrees of freedom. Note that this increase is smooth, i.e. there is no singularity at any order of the derivatives of the energy density with temperature. In this sense, one refers to this phase transition as a rapid cross-over.

Note that the value for the critical temperature ($T_c$) in the vicinity of which the transition occurs, depends on basic parameters of QCD, i.e. the number of quark flavors ($n_f$) and the quark masses ($m_q$) (see for example [21, 22, 23]). As an example, for $n_f = 2$ (up and down quarks), and at the

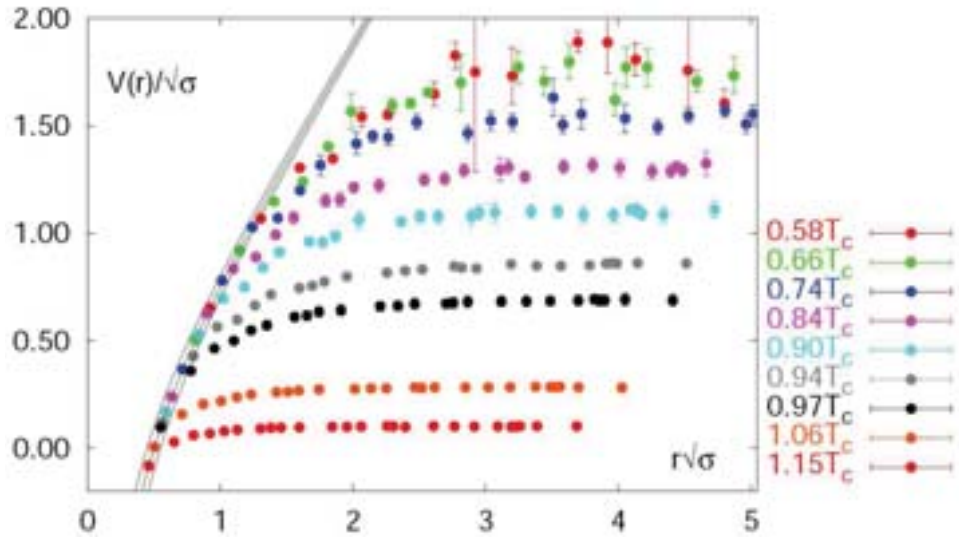


**Figure 2.6:** *Quark binding potential calculated by lattice QCD as a function of distance for different values of the temperature in the vicinity of the critical temperature where the phase transition occurs (see text) [21]. The potential is expressed in units of* $\sqrt{\sigma}$ *(*$\sigma$ *is the string tension).*

chiral limit ($m_q \to 0$), one gets $T_c \sim 173$ MeV [20]. This corresponds to a critical energy density of around 0.7 GeV/$fm^3$, which is about four times the energy density in ordinary nuclei (0.17 GeV/$fm^3$).

Note also that the cross-over nature of the phase transition is supported by measurements performed in high energy heavy ion collisions at the RHIC* and SPS† facilities.

The deconfinement of quarks above the critical temperature is illustrated in Figure 2.6. The latter shows lattice QCD results for the quark binding potential as a function of the inter-quark distance and for different values of the temperature in the vicinity of $T_c$ [21]. This potential is divided by the square root of the string tension ($\sqrt{\sigma}$), defined in Section 2.1.1. The band of black lines gives the effective Cornell-potential [24], which includes a repulsive Coulomb term dominating at small distances and a linear confining term dominating at long distances. In the low temperature regime (T $\leq 0.8 \times T_c$), the potential starts to deviate from the Cornell-type confinement potential for r$\sqrt{\sigma} \sim 1.2$ and reaches a plateau for r$\sqrt{\sigma} \sim 3$. This corresponds to distances r of about 0.6 fm and 1.4 fm, respectively (i.e. the typical size of hadrons). Quarks are then confined in colorless hadrons due to the confining forces of strong interactions. At temperatures above the critical temperature, there is a strong screening of quark color charges, which significantly diminishes the quark binding potential and results into a distance-independent potential (the plateau) already at r$\sqrt{\sigma} \sim 1.2$ (corresponding to r $\sim 0.6$ fm). Confining forces are then unsufficient to confine quarks into hadronic bound states.

*Relativistic Heavy Ion Collider at BNL, Brookhaven
†Super Proton Synchrotron at CERN

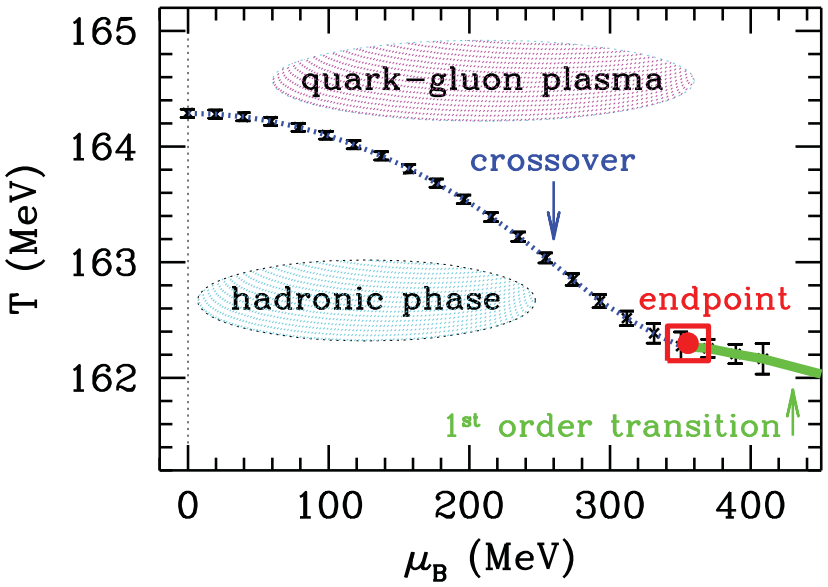


**Figure 2.7:** *Lattice QCD results for the phase diagram in the temperature versus baryonic chemical potential plane [22]. The box indicates the uncertainties on the location of the critical endpoint within these calculations.*

### 2.3.2 The QCD critical point

Recent lattice QCD calculations at finite baryon chemical potential predict the existence of a critical point in the nuclear matter phase diagram, where the phase transition changes from a first order one to a smooth cross-over [22]. An example of these calculations is shown in Figure 2.7. A critical point separating the first order region from the cross over region is predicted to occur at T = 162 $\pm$ 2 MeV and $\mu_B$ = 360 $\pm$ 40 MeV [22].

Note however that the exact location of the critical point suffers from large systematic uncertainties due to limitations in the present lQCD calculations, and even its existence itself is still a matter of debate [14, 15]. Figure 2.8 summarizes the results obtained from different lQCD calculations (green symbols) along with the predictions of other theoretical QCD-based models (black symbols). According to lQCD predictions, the critical point, if ever existing, should lie in a wide region in temperature and baryon chemical potential: 150 MeV < T < 200 MeV and 200 MeV < $\mu_B$ < 800 MeV. An experimental access to this high $\mu_B$ region of the nuclear phase diagram should help clarifying this issue.

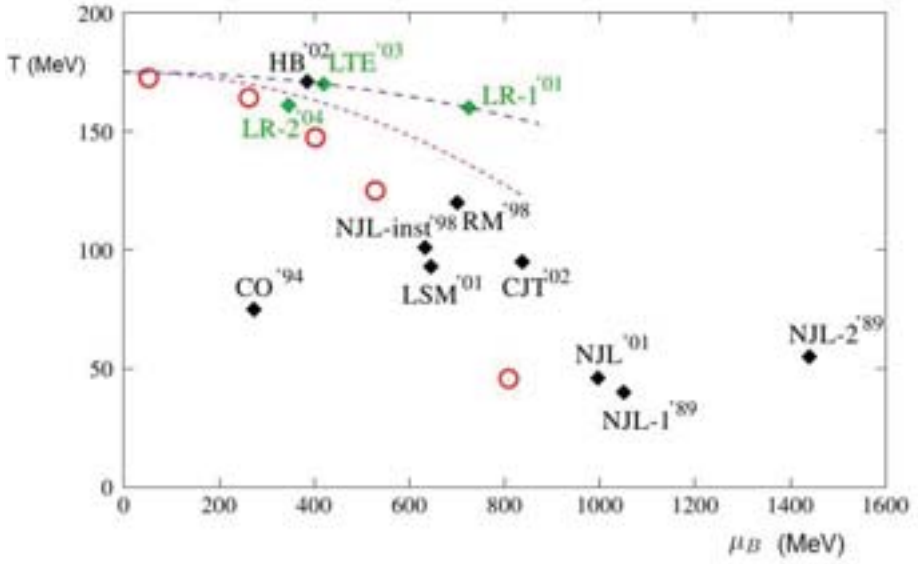


**Figure 2.8:** *Theoretical predictions for the location of the QCD critical point [25]. The green symbols are the results of the lattice simulations and the black symbols correspond to the predictions of different QCD-based models (see [26] for details). The red circles indicate the freeze-out points obtained at various collision energies.*

## 2.4 Exploration of the nuclear matter phase diagram with high energy heavy ion collisions

### 2.4.1 Evolution of high energy heavy ions collisions

When two nuclei collide with relativistic speeds, the overlap region is Lorentz contracted. In this overlap region, the so-called fireball, a large amount of energy is deposited in a short time. A sketch of the evolution of the collision is shown in Figure 2.9. Two scenarii are considered: in the first one (left-hand side of the figure), the effective constituents of the system are purely hadronic all over the collision history, while in the second one (right-hand side) the collision undergoes a phase transition to a QGP.

In the scenario without QGP formation, hadrons are formed early in the collision. Then, these hadrons interact inelastically until the system reaches the chemical freeze-out where inelastic collisions stop. At this point, the yields of the different species are fixed. The gas of hadrons, being still hot enough, continues to interact through elastic collisions as it further expands and cools. When the relative distance between hadrons becomes larger than the range of the strong interaction, elastic collisions among them cease to take place. At this moment, called kinetic freeze-out, the kinematical properties of the produced particles are fixed. The nuclear system evolves as free hadrons that fly towards the detection system.

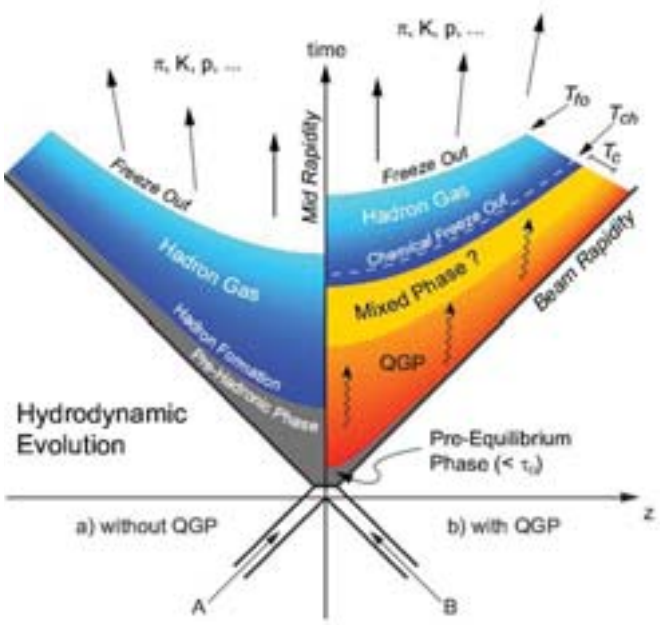


**Figure 2.9:** *Sketch of the space-time evolution of the fireball created in high-energy heavy ion collisions [27]. The left-hand side represents the case of a purely hadronic scenario, whereas the scenario pictured in the right-hand side includes the formation of a transient QGP phase.*

In the scenario with QGP formation, there is a pre-equilibrium phase when partons interact strongly. If this phase is long enough, a thermal equilibrium is established, forming the QGP phase. This is the region indicated in red color in Figure 2.9. In a further step, the QGP expands and cools down. When the temperature becomes close to the critical temperature, hadronization takes place and the system enters into a mixed phase (yellow shaded band) where deconfined quarks and hadrons co-exist. At the end of this mixed phase, the QGP has been converted into hadrons forming the hadron gas (blue color). Next, chemical freeze-out sets in when the particles cease inelastic collisions. Finally, the hadrons stream out from the collision region after the kinetic freeze-out, when they stop interacting elastically.

### 2.4.2 Bjorken estimate of the initial energy density reached in relativistic heavy ion collisions

The initial energy density reached in heavy ion collisions can be estimated in the so-called "Bjorken-scenario" [28]. It is based on the measured transverse energy density $dE_T/d\eta$ * [29], as follows:

$$\epsilon = \frac{1}{A_T} \times \frac{dE_T}{d\eta} \times \frac{1}{\tau} \tag{2.5}$$

*$\eta$ is the pseudo-rapidity, which is the limit of the rapidity for vanishing rest mass. It depends only on the angle $\theta$ between the particle momentum and the beam direction: $\eta$ = - $\ln[\tan(\theta/2)]$

| Machine | AGS* | SPS† | RHIC‡ | LHC§ |
|---|---|---|---|---|
| $\sqrt{s_{NN}}$ [GeV] | 4.9 | 17.3 | 200 | 2760 |
| $dE_T/d\eta$ [GeV] | 192 | 363 | 625 | 1600 |
| $\epsilon$ [GeV/$fm^3$] | 1.2 | 2.4 | 4.1 | > 10 |

**Table 2.1:** *Bjorken estimates for the initial energy density ($\epsilon$) reached in heavy ion collisions for various accelerator facilities at their maximal center-of-mass energy per nucleon pair ($\sqrt{s_{NN}}$) [29, 30].*

with $A_T$ the transverse area of the fireball*. The only unknown parameter in these calculations is the proper time $\tau$ needed for the equilibration of the medium to take place. $\tau$ is usually taken to be 1 fm/c (although it is expected to decrease as a function of the energy). The results are presented in Table 2.1 for heavy ion collisions in the energy range from AGS to LHC. One can see that the initial energy densities are above the critical energy density for color deconfinement predicted by lattice QCD ($\epsilon_c \sim 0.7$ GeV/$fm^3$, see Section 2.3.1), already at a center-of-mass energy per nucleon pair ($\sqrt{s_{NN}}$) of 4.9 GeV. The conditions for the formation of a QGP state are thus very likely to be achieved in relativistic heavy ion collisions. Note that the future FAIR facility will allow reaching $\sqrt{s_{NN}}$ up to 9.2 GeV.

### 2.4.3 Freeze-out conditions

By varying the energy of the colliding ions, one can probe experimentally different regions of the QCD phase diagram. This is illustrated in Figure 2.10, which shows the freeze-out conditions, in terms of temperature and baryon chemical potential, at different beam energies from the SIS energy range up to the highest RHIC energies. The experimental points in this figure are obtained from the analysis of the measured particle ratios within the statistical thermal model [13]. In the future, the high baryon density region will be further explored by FAIR experiments (CBM, HADES) and the MultiPurpose Detector (MPD) experiment at the NICA facility.

### 2.4.4 Expected dynamical trajectories in the nuclear phase diagram

The chemical freeze-out points (Figure 2.11) only give the conditions reached at the later stages of the collision. The dynamical trajectory (in the (T, $\mu_B$) plane) can not be measured by experiments, since we only detect particles after thermal freeze-out. However, these trajectories can be determined by means of theoretical models [32, 33]. Figure 2.11 shows an example of such

*$A_T$ = 154 $fm^2$ for central Au + Au collisions
*Alternating Grandient Synchrotron, BNL, Brookhaven
†Super Proton Synchrotron, CERN
‡Relativistic Heavy Ion Collider, BNL, Brookhaven
§Large Hadron Collider, CERN

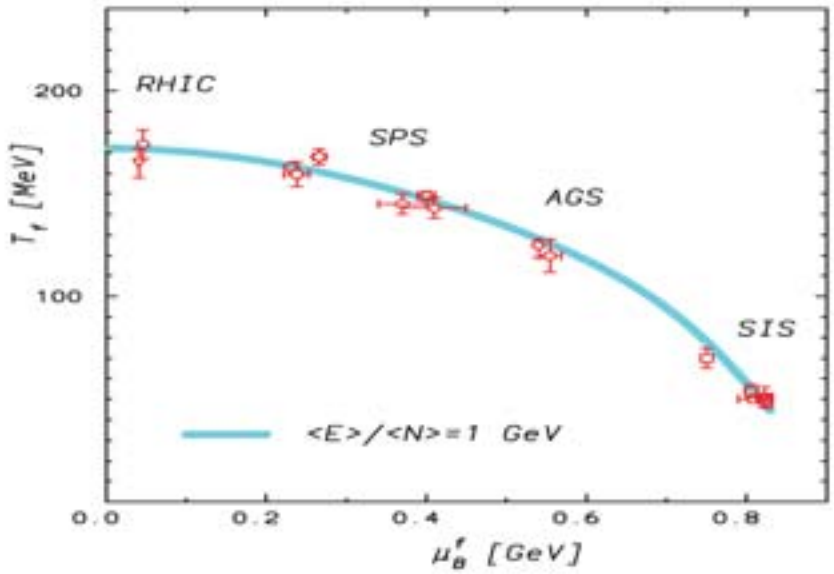


**Figure 2.10:** *Experimental values of the chemical freeze-out points in the nuclear phase diagram (temperature versus baryon chemical potential). They are obtained from a statistical model analysis of data at beam energies ranging from SIS to RHIC. The curve corresponds to a fixed energy per hadron of 1 GeV in the hadronic gas model. The figure is taken from reference [13].*

calculations in the case of the 3-fluid hydrodynamics model [31]. The calculations correspond here to central Pb + Pb collisions at different beam energies going from 5 to 158 AGeV (top SPS energy). In this model, the nuclear system reaches equilibrium after a certain time. This is indicated by the thick parts of the trajectory lines while the thin lines represent the pre-equilbrium phase of the collision. The time instants expressed in the center-of-mass frame of the colliding nuclei are indicated by the numbers near the trajectories. Also shown in the figure are the experimental freeze-out line (dotted line), the boundary of the phase transition from hadronic matter to the QGP (light grey shaded region) and the critical point (star symbol) predicted by lattice QCD [22].

It is interesting to notice in this figure that the deconfinement phase transition and the QCD critical point may be accessible at beam energies above 30 AGeV (corresponding to $\sqrt{s_{NN}} \sim$ 8 GeV). Note, however, that these calculations should be taken with caution since they strongly depend on the used equation of state, which in this case is purely hadronic.

## 2.5 Experimental exploration of the QCD phase diagram

The high temperature and small baryon chemical potential region of the phase diagram is accessible at the very high energies provided by the RHIC ($\sqrt{s_{NN}}$ up to 200 GeV) and LHC ($\sqrt{s_{NN}}$ up to 5.5 TeV) colliders, while the high $\mu_B$ and moderate T region can be explored at $\sqrt{s_{NN}}$ in

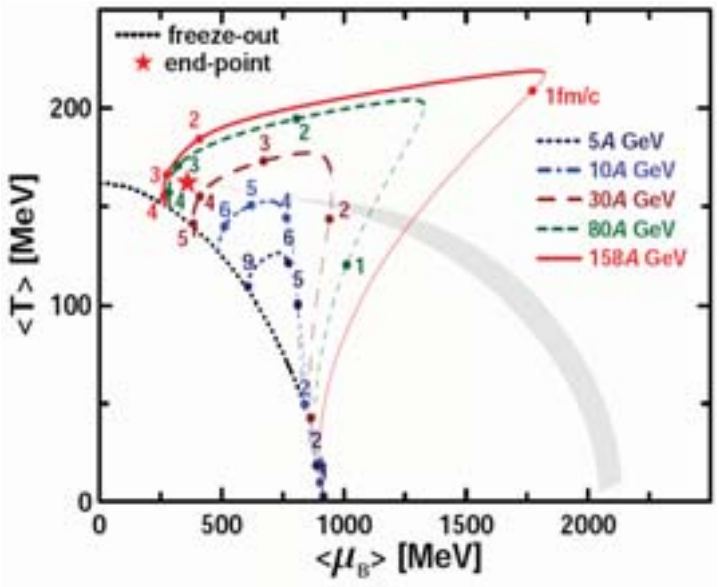


**Figure 2.11:** *Dynamical trajectories in the nuclear phase diagram (T, $\mu_B$) as obtained from the 3-fluid hydrodynamical model [31] for central Pb + Pb collisions at different beam energies from 5 to 158 AGeV.*

the range of 5 - 10 GeV. This latter energy range is presently reachable at SPS and RHIC, and will be also accessible at the future accelerators NICA and FAIR.

In the two following sections, we summarize briefly some of the important experimental results obtained so far from high energy heavy ion experiments mainly at SPS and RHIC. The purpose here is not to present an exhaustive review on the subject, but rather to give an idea of what has been learned to date from these studies at both low $\mu_B$ (Section 2.5.1) and high $\mu_B$ (Section 2.5.2).

### 2.5.1 The region of high temperatures and low baryon chemical potentials

The CERN/SPS experiments measured several potential signatures of the deconfinement phase transition [34]. The most striking one is the anomalous suppression of J/$\psi$ mesons (bound states of c-$\bar{c}$ quarks). Matsui [35] first predicted that the formation of a QGP state would screen the color binding potential (as a result of Debye screening of quark color charges), preventing c-$\bar{c}$ quarks to form bound states and leading to an observable suppression of J/$\psi$ yields in high energy heavy ion collisions. Such suppression was indeed observed by the NA50 experiment in central Pb + Pb collisions at an incident energy of 158 AGeV [36]. Figure 2.12 shows the J/$\psi$ production yield measured in different collision systems as a function of energy density. It is divided by the expected one considering an absorption in ordinary nuclear matter, extrapolated from p + A data [37]. As expected, this ratio is equal to 1 in p + A collisions and light systems (i.e. S + U collisions), while an anomalous J/$\psi$ suppression is observed in Pb + Pb collisions. Note that this

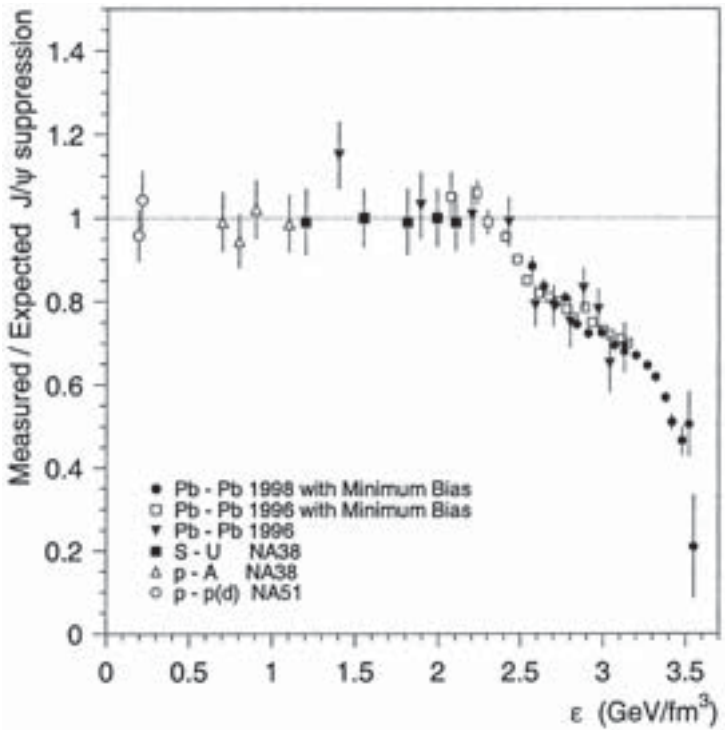


**Figure 2.12:** *J/$\psi$ production yield normalized to the expected yield assuming that the only source of suppression originates from the absorption in ordinary nuclear matter. The data obtained in different experiments at the CERN-SPS are shown as a function of the energy density reached in different collision systems [36].*

anomalous suppression of J/$\psi$ mesons has been confirmed by the NA60 experiment [38]. It is worthwhile to note that the interpretation of the suppression effect as a signature of the transition to the QGP is not yet settled. Indeed, other conventional mechanisms based on J/$\psi$ absorption by comoving hadrons might also contribute significantly to the observed suppression if the J/$\psi$ absorption cross-sections are on the order of a few mb [39, 40].

RHIC experiments reported several evidences that the QGP state formed in high energy heavy ion collisions is strongly interacting (referred to as sQGP) [41, 42, 43]. One of the most remarkable one is the jet quenching phenomenon. Jet events are showers of particles originating from parton fragmentation and thus emitted roughly in the same direction. Figure 2.13 shows an example of azimuthal angular correlations measured in p + p, d + Au and central Au + Au collisions at $\sqrt{s_{NN}}$ = 200 GeV [44]. This is obtained by triggering on high-$p_T$ particles, each of them being then associated with all other particles produced in the same collision. The difference in azimuthal angle ($\Delta_\phi$) between the trigger particles and associated particles is shown in the figure. At $\Delta_\phi$ = 0, the peak of the distribution corresponds to registered jet-like events. At $\Delta_\phi = \pi$, the peak of the distribution corresponds to registered di-jets events, i.e. hadrons originating from the fragmentation of two oppositely directed (back to back) partons. As one can see,

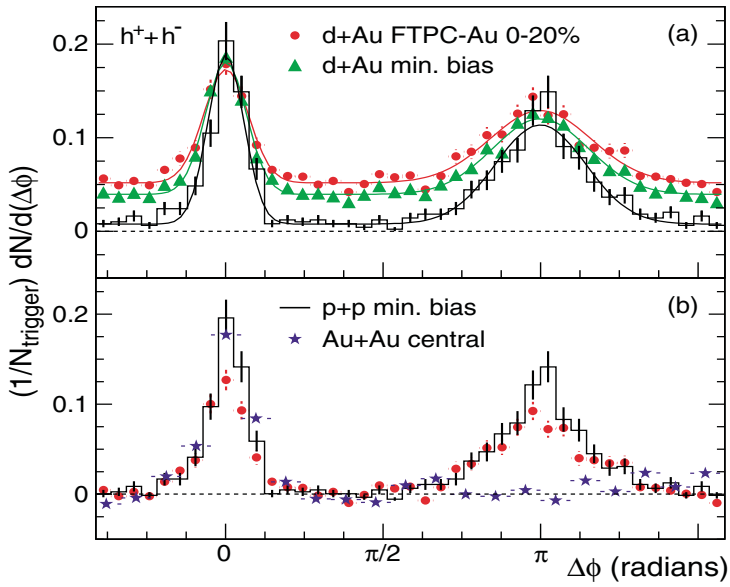


**Figure 2.13:** *Azimuthal angular correlations between a high-$p_T$ leading hadron (selected as a trigger particle) and particles produced in the same collision, measured in p + p and Au + Au central collisions (lower part) and d-Au collisions (upper part) at the RHIC maximal beam energy, i.e. $\sqrt{s_{NN}}$ = 200 GeV [44]. $N_{trigger}$ is the number of high-$p_T$ particles.*

jet-like events are present in all systems. In contrast, di-jet events are suppressed (with respect to p + p collisions) in central Au + Au collisions only (lower part of the figure). This is interpreted as follows: energetic partons produced near the surface of the fireball in central Au + Au collisions, and directed outward the fireball, are nearly undisturbed by the medium and fragment into detectable hadrons. On the contrary, the associated, oppositely directed partons loose a large amount of energy when traversing through the dense medium in the core of the fireball, leading to a suppression of observed di-jets events in central Au + Au collisions.

Other important observations have been made by RHIC experiments, demonstrating that the medium created in heavy ion collisions has partonic degrees of freedom. Among them, the observation of a strong elliptic flow, which is as large as the one predicted by ideal-fluid hydrodynamical models (which assume zero viscosity), suggests that the system is strongly collective as it must be in the case of an equilibrated system [45]. First results from LHC experiments confirm this effect [45]. Another important finding at RHIC is the quark number scaling of elliptic flow [46]. This is illustrated in Figure 2.14. As shown in the right panel, the elliptic flow normalized to the number of constituent quarks exhibits an universal scaling (for all species including baryons and mesons).

It is interesting to note that the excitation function of the various QGP signatures mentioned above do not show any singularities, which is consistent with a cross-over phase transition as predicted by lattice QCD in the high temperature, low net baryon density region of the nuclear phase diagram.

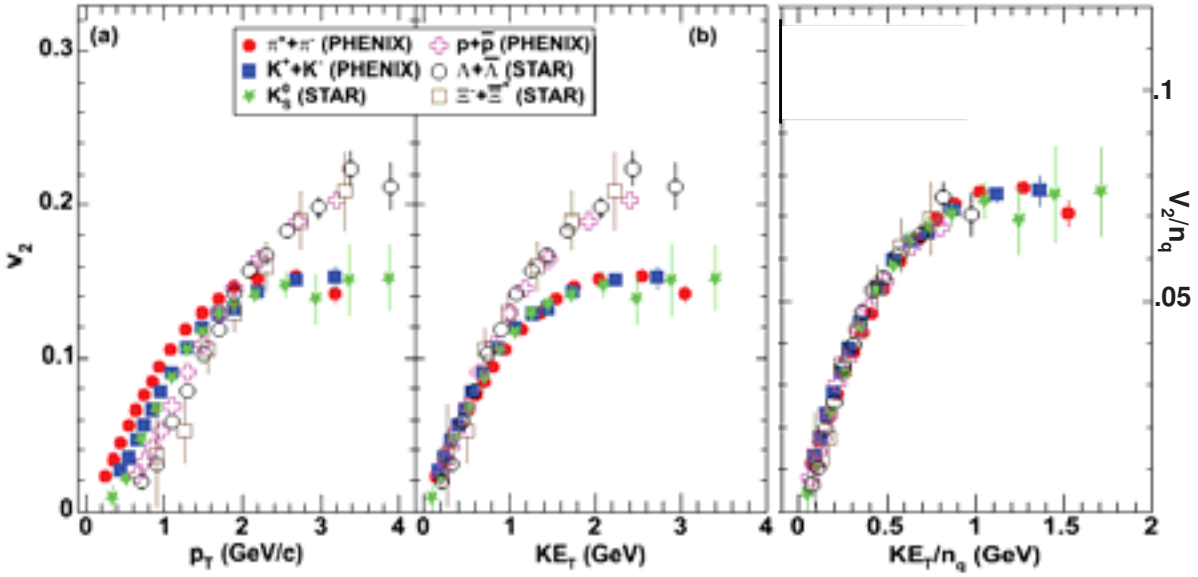


**Figure 2.14:** *Differential elliptic flow ($v_2$) of different hadron species measured at RHIC in minimum bias Au + Au collisions at a center-of-mass energy per nucleon pair of $\sqrt{s_{NN}}$ = 200 GeV. The left-, and middle panels show the elliptic flow as a function of the transverse momentum ($p_T$) and of the transverse kinetic energy ($KE_T$), respectively. The right panel shows the results obtained by scaling $v_2$ and $KE_T$ with the number of constituent quarks (n = 2 for mesons and 3 for baryons) [46].*

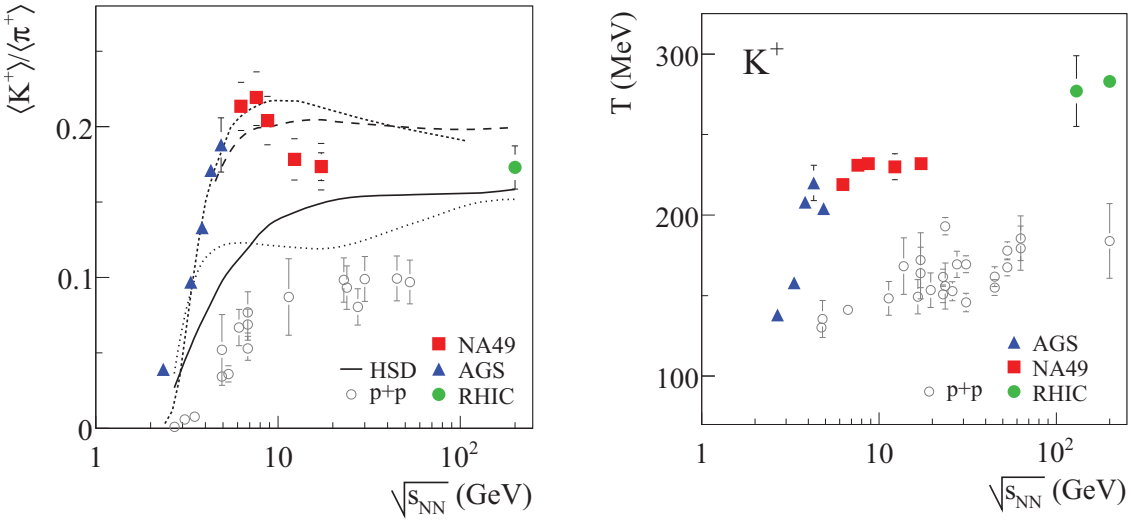


**Figure 2.15:** *Left panel: Ratio <$K^+$>/<$\pi^+$> as a function of the center-of-mass energy per nucleon pair ($\sqrt{s_{NN}}$) measured in proton-proton (open circles) and Pb + Pb collisions (full symbols). The curves correspond to the predictions of different theoretical models (see ref. [47] for details). Right panel: inverse slope parameter (T) of $K^+$ mesons as a function of $\sqrt{s_{NN}}$. The data are from different experiments carried out at the AGS, SPS (NA49) and RHIC accelerators.*

### 2.5.2 The high baryon-chemical potential region

Several anomalies have been observed at the CERN-SPS in the excitation functions of various observables measured in nucleus-nucleus collisions. They all appear around the same beam energy of 30 GeV/nucleon (corresponding to a center-of-mass energy per nucleon pair $\sqrt{s_{NN}} \sim 8$ GeV) [47]. These anomalies are not observed in proton-proton collisions and can not be reproduced by hadronic models. They are thus interpreted as signatures of the onset of deconfinement.

The presence of these anomalies in the experimental data is illustrated in Figure 2.15. The left side shows the excitation function of the relative strangeness production expressed in terms of the ratio <$K^+$>/<$\pi^+$> [47]. One can see clearly a non-monotonous behavior in Pb + Pb collisions: there is a steep increase of the ratio <$K^+$>/<$\pi^+$> with increasing energy, followed by a turn-over at $\sqrt{s_{NN}}$ of about 8 GeV. This structure is referred to as the horn structure. Other anomalies have also been observed at the same energy. For example, the right panel of the figure shows the chemical freeze-out temperature of $K^+$ mesons (obtained as the inverse slope parameter of their $p_T$ spectra) as a function of $\sqrt{s_{NN}}$. A clear saturation of this parameter is observed in Pb + Pb collisions at collision energies above 7 - 8 GeV.

The fact that the above anomalies are not observed in p + p collisions suggests that they are due to the dense medium created in heavy ion collisions. Additionally, they are not reproduced by hadronic models (details in [47]), indicating that the observed effect may be linked to the onset of deconfinement. All these facts support a scenario in which the onset of deconfinement is located at a beam energy of about 30 GeV/nucleon.

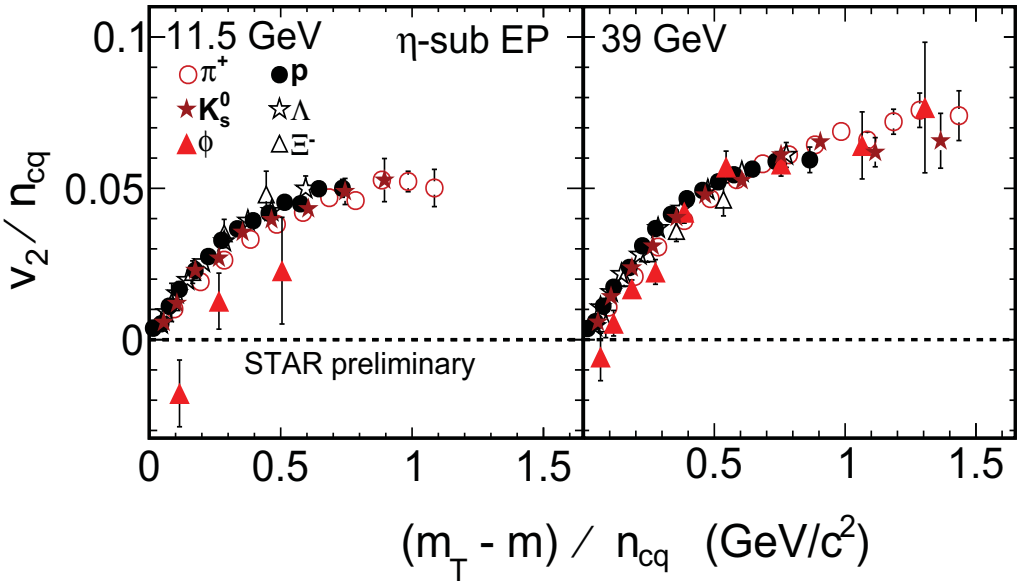


**Figure 2.16:** *Elliptic flow ($v_2$) measured by the STAR experiment [50] for various identified particles as a function of transverse kinetic energy ($m_T$ - m) in Au + Au (80 % most central) collisions at a center-of-mass energy per nucleon pair of 11.5 GeV (l.h.s.) and 39 GeV (r.h.s.). $v_2$ and ($m_T$ - m) are both scaled with the number of constituent quarks, i.e. $n_{cq}$ = 2 and 3 for mesons and baryons resp.*

It is important to stress that the recent STAR data from the low energy scan at RHIC [48] confirm the anomalies observed in the excitation functions of the observables mentioned above.

The STAR experiment performed systematic measurements of elliptic flow in the energy range of $\sqrt{s_{NN}}$ = 7.7 - 39 GeV (including the region where the anomalies mentioned above are observed). The main aim was to search for the disappearance of the quark number scaling ($n_q$-scaling) observed at higher energies (see right panel of Figure 2.14). Figure 2.16 shows the elliptic flow measured by the STAR experiment [50] for various identified particles as a function of the transverse kinetic energy in Au + Au collisions at $\sqrt{s_{NN}}$ = 11.5 GeV (l.h.s.) and 39 GeV (r.h.s.). At $\sqrt{s_{NN}}$ = 39 GeV, the $n_q$-scaling is clearly observed. In contrast, at the lower energy ($\sqrt{s_{NN}}$ = 11.5 GeV), the elliptic flow of $\phi$ mesons falls off, while the flow of other species still follows the $n_q$-scaling. This is interpreted as partonic interactions becoming less and less important with decreasing energy. This is consistent with the idea that the onset of deconfinement is located at $\sqrt{s_{NN}}$ of about 8 GeV. Note, however, that the error bars on the estimated elliptic flow of $\phi$ mesons are important, due to moderate statistics of measured particles.

It should be noted that the SPS results mentioned above are restricted mainly to bulk observables. More detailed investigations of this energy domain with penetrating probes are expected to provide further information on the properties of the dense nuclear matter created at the early stages of nuclear collisions. Several experimental programs, to a large extent complementary, are exploring the region of high $\mu_B$ of the nuclear phase diagram (see Table 2.2). All of them are able

| Accelerator | SPS | RHIC | NICA | FAIR |
|---|---|---|---|---|
| Experiment | NA61, SHINE | STAR, PHENIX | MPD | CBM |
| $\sqrt{s_{NN}}$ [GeV] | 4.5 - 17.3 | 5 - 200 | 3 - 9 | 2 - 9 |
| $\mu_B$ [MeV] | 220 - 580 | < 540 | 360 - 700 | 380 - 780 |
| Collision rate [Hz] | $10^2$ | 1 - $10^3$ | $10^4$ | $10^7$ |

**Table 2.2:** *Overview of present (NA61, SHINE, PHENIX, STAR) and future (CBM, MPD) experiments exploring the high $\mu_B$ region of the QCD phase diagram.*

to investigate abundant observables in more detail than has been done so far. Rare probes such as multi-strange hyperons, low-mass vector mesons and charm particles will only become accessible at FAIR where measurements at very high collision rates are foreseen (up to $10^7$ collisions/s). Open charm particles, in particular, are one of the most challenging measurements.

## 2.6 Open charm

The study of charm production in heavy ion collisions at FAIR energies is particularly interesting. Because of the large mass of charm quarks ($m_c \sim 1.5$ GeV / $c^2$), the latter can only be produced during the first instants of nuclear collisions, with a formation time of:

$$\tau \sim \frac{1}{2m_c} < 0.1 fm/c \tag{2.6}$$

Moreover, charm hadrons (containing at least one charm quark) are less affected by late hadronic interactions than lighter particles, due to their relatively small hadronic interaction cross section. Thus, observables related to charm particles are expected to carry important and nearly undisturbed information on the hot and dense nuclear matter formed at early stages of the collisions.

In the fireball, a large fraction of charm quarks is recombined into open charm hadrons, such as D-mesons (containing one light quark and one charm quark) and the $\Lambda_c$ baryon (made of two light quarks and a charm quark). This can be understood intuitively by considering that c-$\bar{c}$ pairs are most of the time produced back to back and fly away from each other. Given that light quarks are much more abundant than charm quarks, a charm quark has more chance to recombine with light quarks (producing an open charm hadron) than with another anti-charm quark (creating a hidden charm meson). Therefore, it is particularly crucial to measure open charm hadrons.

Before discussing the physics motivations for measuring open charm hadrons in heavy ion collisions at FAIR energies, we present some general considerations on the charm production cross-section.

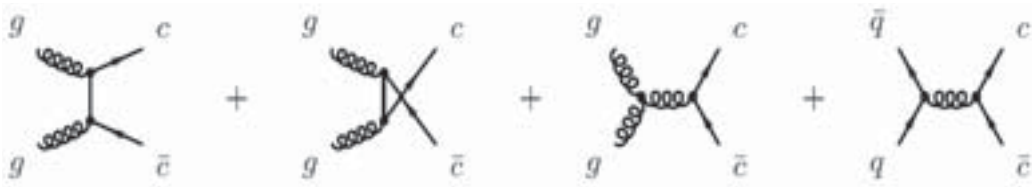


**Figure 2.17:** *Feynman diagrams for c-$\bar{c}$ pair production. The processes of gluon-gluon fusion and quark-antiquark annihilation are shown.*

### 2.6.1 Charm production cross-section

The charm production cross-section in parton-parton collisions can be calculated by perturabtive QCD (pQCD), since the mass of charm quark (of about 1.5 GeV / $c^2$) is a few times larger than the typical QCD energy scale $\Lambda_{QCD}$ (of around 0.2 GeV). There are several mechanisms to produce a pair of charm quark-antiquark (c-$\bar{c}$). Among them are those involving gluon fusion, which dominate at high energies, and q-$\bar{q}$ annihilation. The associated Feynman diagrams at leading order are shown in Figure 2.17.

Note that the available charm data can indeed be well described by pQCD calculations, over a broad energy range [58], only if next-to-leading (NLO) corrections are accounted for. This comes from the fact that the mass of charm quarks is not several orders of magnitude higher than $\Lambda_{QCD}$.

The above mentioned pQCD calculations allow to determine the parton induced c-$\bar{c}$ production cross-section. Once the latter is known, the charm cross-section in hadron-hadron collisions can be obtained from the convolution of the partonic cross-sections with the parton distribution functions (i.e. their momentum distributions) inside the hadrons [51]. The underlying dynamics of the latter is driven by the non-perturbative regime of QCD.

For p + A collisions, the charm production, being dominantly a hard process, is expected to depend on the number of binary nucleon-nucleon collisions. The scaling from p + p to p + A collisions is generally expressed as:

$$\sigma(pA \rightarrow c\bar{c}) = A^{\alpha} \times \sigma(pp \rightarrow c\bar{c}) \tag{2.7}$$

where A is the atomic mass number. The A dependence comes from the Glauber model calculation of the number of binary collisions, averaged over the collision impact parameter [52]. $\alpha$ = 1 corresponds to a perfect binary collision scaling, which means that there is no nuclear effect beyond the geometrical scaling.

For nucleus-nucleus collisions, one expects that the total charm cross-section will also scale as a function of the number of binary collisions, given that the collision process between the two nuclei can be described by a simple superposition of nucleon-nucleon interactions. In this case, the binary scaling can be expressed as:

$$\sigma(AB \rightarrow c\bar{c}) = AB \times \sigma(pp \rightarrow c\bar{c}) \tag{2.8}$$

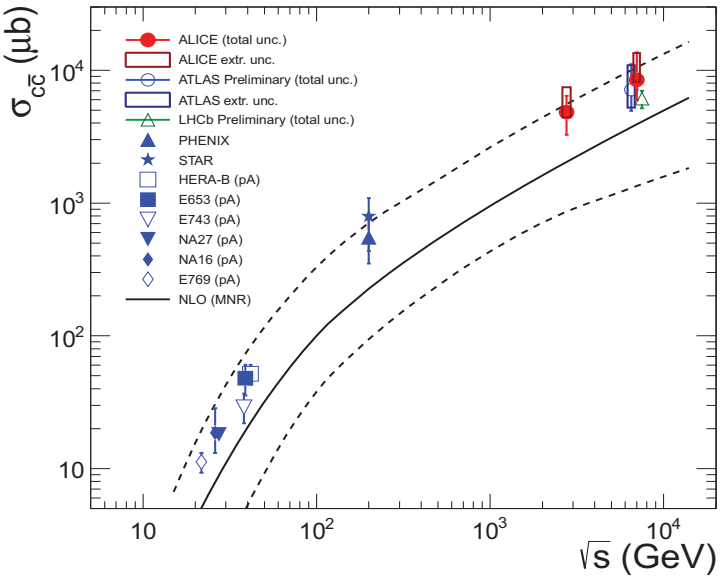


**Figure 2.18:** *Total charm production cross-section ($\sigma_{c\bar{c}}$) measured in various systems and at different center-of-mass energies [57]. The cross-sections measured in proton-nucleus and nucleus-nucleus collisions are divided by the number of binary nucleon-nucleon collisions. The solid line corresponds to NLO pQCD calculations and the dashed lines show the uncertainties of the calculations.*

### 2.6.2 Available data on the charm production

Figure 2.18 shows the total charm production, i.e. the production cross-section for c-$\bar{c}$ pairs ($\sigma_{c\bar{c}}$) in different collision systems and for a broad energy range. $\sigma_{c\bar{c}}$ is estimated from the measured cross-section of charm hadrons. To compare the data obtained in different systems, these cross-sections are divided by the number of binary collisions. Note that at energies below $\sqrt{s_{NN}} \simeq$ 20 GeV, there is no data on open charm production cross-section. As mentioned previously, NLO pQCD calculations (solid line) reproduce well the excitation function of the total charm production within the uncertainty of the calculations (represented by the dashed lines).

As can be seen in Figure 2.18, the data on p + A collisions seem to support a simple binary scaling with respect to p + p collisions. It should be mentioned, however, that those data were extracted using indirect methods and are, therefore, subject to large systematic uncertainties. Hence, more precise data from direct measurements are needed. Such measurements are also very important for understanding the contribution of initial state effects in nucleus-nucleus collisions (e.g. the Cronin effects [54] and the nuclear shadowing [55]). Such studies are currently carried-out at RHIC and LHC, and will be undertaken at lower energies at FAIR.

The charm production cross-section in nucleus-nucleus collisions has been evaluated so far mostly indirectly via semi-leptonic decays, by studying dilepton spectra (in the NA38/NA50 experiments at the SPS) [53] or single lepton spectra (in RHIC experiments) [56]. This kind of

indirect measurements requires subtracting all other sources of leptons, which is subject to large uncertainties. Here also, more accurate data are needed.

Direct measurements of open charm particles (via their hadronic decays) require the use of high precision vertex detectors. Such measurements is currently performed at LHC by the ALICE experiment, and will soon be possible at RHIC with the upgrades of STAR and PHENIX vertex detectors, and at the future FAIR facility with the CBM Micro-Vertex detector. The latter will allow open charm hadrons to be measured close to their production threshold, where their production cross-section is extremely low (see Figure 2.18). In the following section, we will discuss in more detail the perspectives for open charm physics in A + A collisions at FAIR with the CBM detector.

### 2.6.3 Open charm at FAIR energies

As mentioned earlier, open charm will be one of the major physics topics of the CBM scientific program. In CBM, open charm particles will be measured, through their hadronic decays, at beam energies close to their kinematical production threshold. This will be performed in nucleus-nucleus collisions but also in proton-proton and proton-nucleus collisions at different incident energies: up to 90 GeV for proton beams and up to 45 AGeV for heavy-ion beams. The experimental methods proposed for performing such challenging measurements will be presented in Chapter 4.

The CBM experiment will measure for the first time the total charm production cross-section at these relatively low energies. This is very important for a good understanding of how charm hadrons are produced at threshold energies. Such measurements will, in particular, allow testing pQCD calculations (Section 2.6.1) at low energy where their validity is questionable. They will also provide an important input in the theoretical models used in heavy-ion collisions for the interpretation of signatures of a possible deconfinement phase transition (e.g. J/$\Psi$ suppression).

Open charm particle measurements at FAIR energies are important not only for the total charm cross-section but also as sensitive probes of the dense and hot medium formed in heavy-ion collisions. Those measurements can, indeed, provide valuable information on the nature of this medium and on the deconfinement phase transition. In addition, the experimental study of open charm production at FAIR energies, close to the kinematical threshold, is greatly interesting for investigating the modifications of hadron properties in dense nuclear matter. In what follows, we will discuss in more detail the sensitivity of open charm observables to the deconfinement phase transition and to the in-medium modifications of hadron properties.

#### 2.6.3.1 Open charm as a sensitive probe of the state of matter in the early stage

As mentioned previously, the onset of the deconfinement phase transition is expected in the FAIR energy range. This transition can be investigated in the CBM experiment through the measurement of excitation functions of several observables. Among the latter, open charm hadrons are

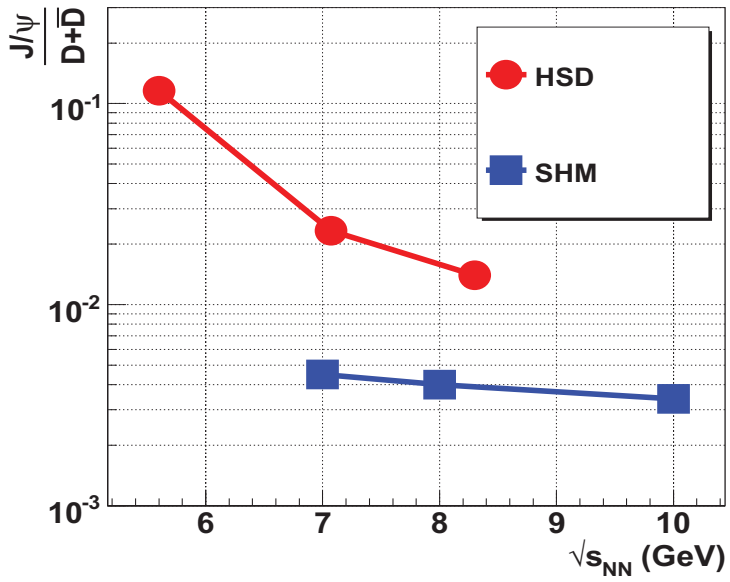


**Figure 2.19:** *Predictions for the ratio of J/Ψ over (D+$\bar{D}$) in central Au + Au collisions as a function of the center-of-mass energy per nucleon pair ($\sqrt{s_{NN}}$) [59]. FAIR will cover the energy region below 9.2 GeV.*

of particular interest as their production in nucleus-nucleus collisions depends strongly on the nature (whether partonic or hadronic) of the medium in which they are formed.

The sensitivity of open charm particles to the onset of the QGP is illustrated in Figure 2.19. The latter shows the predictions of two different theoretical models, HSD (purely hadronic) and SHM (assuming the formation of QGP), for the ratio of J/Ψ to (D+$\bar{D}$) in central Au + Au collisions as a function of $\sqrt{s_{NN}}$. A striking difference between the two theoretical predictions is clearly observed: the J/Ψ to (D+$\bar{D}$) ratio differs by a large factor of about 5 in the energy region where one expects the onset of deconfinement to take place, namely at $\sqrt{s_{NN}}$ of 7 - 8 GeV. This reflects the fact that these two models are based on two extreme scenarii. In HSD [60, 61, 62], the collision evolution is assumed to be driven by purely hadronic interactions, while in SHM [49] one assumes a complete dissociation of charmonium in the quark gluon plasma, followed by statistical production of J/Ψ-mesons and open charm particles during hadronization.

In the HSD model, the charm production mechanism proceeds through the creation of pairs of charm hadrons (e.g. $D^+$-$D^-$). A very different production mechanism is assumed in the SHM model: charm hadrons are produced by recombining the charm quarks created in the first hard collisions. The difference observed in Figure 2.19 between the predictions of HSD and SHM is due to the fact that these two mechanisms involve different production thresholds ($\sqrt{s_{th}}$). The production threshold for a c-$\bar{c}$ pair in a partonic medium is lower than the minimum energy needed to create a pair of charmed hadrons. For example, the lowest threshold for charm production in hadronic collisions is defined by the process p + p $\rightarrow$ $\bar{D}$ + $\Lambda_c$ + p resulting in a value of $\sqrt{s_{th}}$ = 5.07 GeV. In SHM, the lowest threshold is defined by the process p + p $\rightarrow$ p + p +

c-$\bar{c}$ resulting in a value of $\sqrt{s_{th}}$ = 4.5 GeV. Due to these different threshold definitions in the cross-section parameterizations, the abundance of c-$\bar{c}$ pairs in SHM is about 7 times higher than the abundance of D-$\bar{D}$ and D-$\Lambda_c$ pairs in HSD at a collision energy of $\sqrt{s_{NN}} = 7$ GeV.

According to the predictions discussed above, the excitation function of the J/$\Psi$ to (D+$\bar{D}$) ratio should exhibit a discontinuity in the energy range where the onset of deconfinement takes place. The CBM experiment will allow performing such measurements with good accuracy.

Another evidence for the deconfinement phase transition can be obtained from the measurement of the elliptic flow of open charm particles. The latter effect is expected to be particularly sensitive to the degrees of freedom of the hot and dense medium created in the early stage of the collision. In a purely hadronic scenario, open charm particles have a moderate interaction rate and, hence, the magnitude of their flow is expected to be very weak. This is illustrated in Figure 2.20, which shows the predictions of the HSD model for the elliptic flow in semi-peripheral collisions at a beam energy of 25 GeV/nucleon. As can be seen, D-mesons exhibit a substantially lower elliptic flow than do charged hadrons (predominantly pions, kaons and protons).

The presence of deconfined partons in the early stage of the collision is expected to enhance the pressure, and hence the magnitude of the elliptic flow. The effect of partonic interactions on the elliptic flow has been studied recently within the framework of the AMPT (A Multiphase Transport) model in semi-peripheral Au + Au collisions at 25 GeV/nucleon [130]. Figure 2.21 shows the results of AMPT with and without the inclusion of string melting, along with the predictions of several other hadronic models. Note that all hadronic models, including AMPT without string melting, predict similar strength for the $v_2$ of charged hadrons. The inclusion of string melting, i.e. assuming that the initially produced matter is entirely partonic, leads to a significant enhancement of the elliptic flow. Similar conclusions were drawn recently from the PHSD (Parton hadron String Dynamics) model [132]. These calculations illustrate the high sensitivity of the elliptic flow to partonic contributions in the early dynamics of heavy-ion collisions at FAIR energies. This sensitivity is expected to be particularly marked for open charm particles, since their scattering cross-section is small in the late hadronic phase. Measurements of open charm elliptic flow would, in addition, provide information on the degree of thermalization at the partonic level [63, 59].

Experimental information on open charm production can also help better understanding the origin of the anomalous suppression of charmonium in central heavy-ion collisions (see Section 2.5.1). This effect is considered as a potential signature for the QGP formation. However, other interpretations in terms of hadronic effects, e.g. absorption on hadronic comovers [39, 40], cannot yet be ruled out. Measurements of open charm particles can contribute to clarify this issue, since they are essential for an accurate estimate of the total charm cross-section. This would in turn give access to the number of c-$\bar{c}$ pairs created in the initial hard collisions, which is the natural reference for charmonium studies.

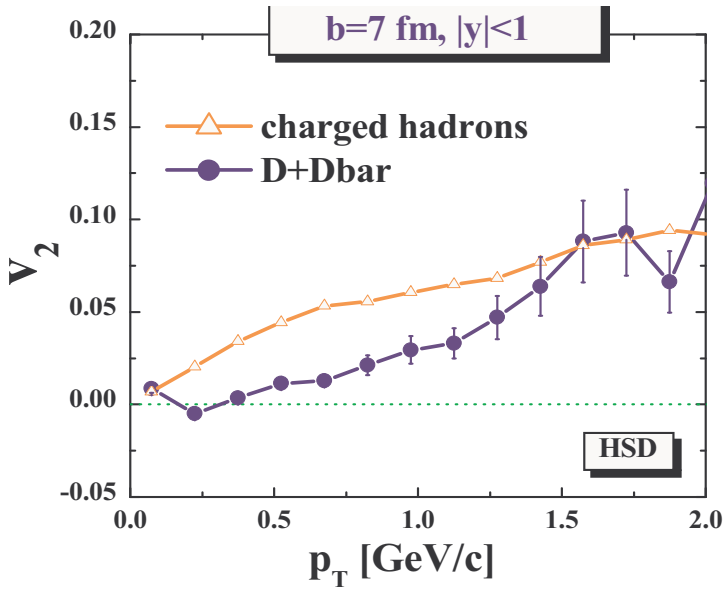


**Figure 2.20:** *Elliptic flow ($v_2$) as a function of transverse momentum ($p_T$), predicted by the transport code HSD for semi-peripheral Au + Au collisions at a beam energy of 25 GeV/nucleon (with an impact parameter equal to 7 fm). The solid lines with full dots and open triangles present the cases of D mesons and charged hadrons, respectively [61].*

#### 2.6.3.2 Sensitivity to in-medium effects and the restoration of chiral symmetry

In-medium modifications of hadron properties can provide valuable information on the chiral symmetry restoration. Their study is particularly interesting at FAIR energies, where very high net baryon densities can be reached during the early evolution of nucleus-nucleus collisions. The CBM experiment will measure several observables sensitive to these effects, among them are those related to open charm production. As discussed earlier, charm is produced very early in the collision, in particular at FAIR energies which lie in the region of the charm production threshold. One expects, therefore, open charm particles to carry information on the early phase of the collision, when the net baryon density is maximal.

As can be seen in Figure 4.1 (Chapter 4), the excitation function of open charm particle production is very steep in the threshold energy region. Therefore, a change in the effective mass of these particles would translate into a substantial modification of their yield. This is is illustrated in Figure 2.22, which shows the transverse mass spectra of (D+$\bar{D}$) mesons as calculated by the HSD transport model for central Au + Au collisions at 25 GeV/nucleon. The calculations are performed with (red) and without (blue) taking onto account in-medium effects. The latter are introduced as an attractive D-N potential, i.e. a mass shift of -50 $\times \rho/\rho_0$ MeV. As can be seen, the introduction of the mass shift leads to an enhancement of the D-meson yield by almost an order of magnitude as compared to the bare mass case.

It is important to stress that the amount of charm quarks produced initially in hard nucleon-

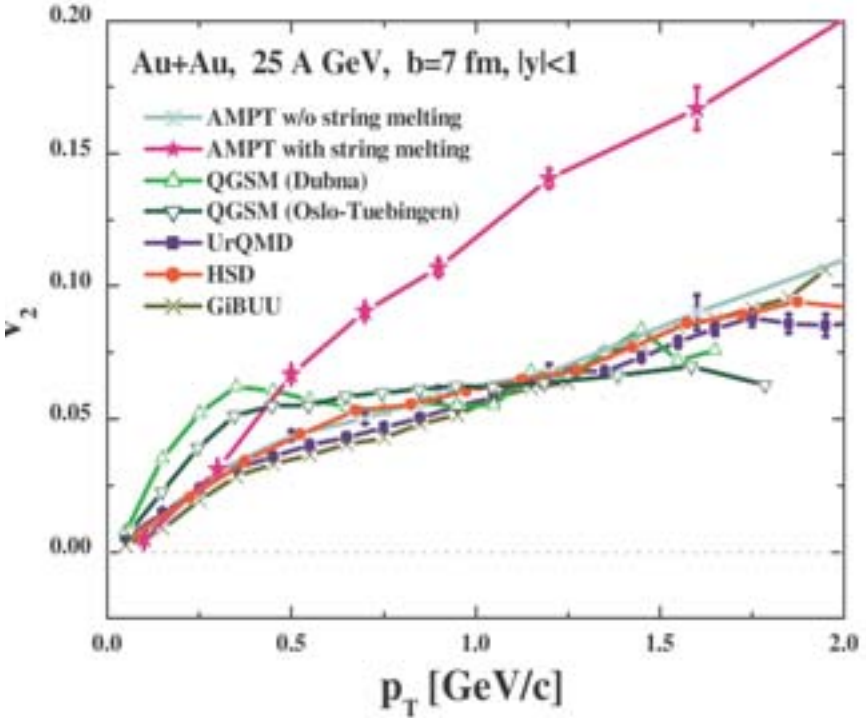


**Figure 2.21:** *Predictions of various transport models for the elliptic flow parameter $v_2$ of charged hadrons as a function of transverse momentum $p_T$. The calculations are performed at mid-rapidity |y| < 1 for mid-central Au + Au collisions (impact parameter b = 7 fm) at a bombarding energy of 25 GeV/nucleon. (see Ref. [59] for details).*

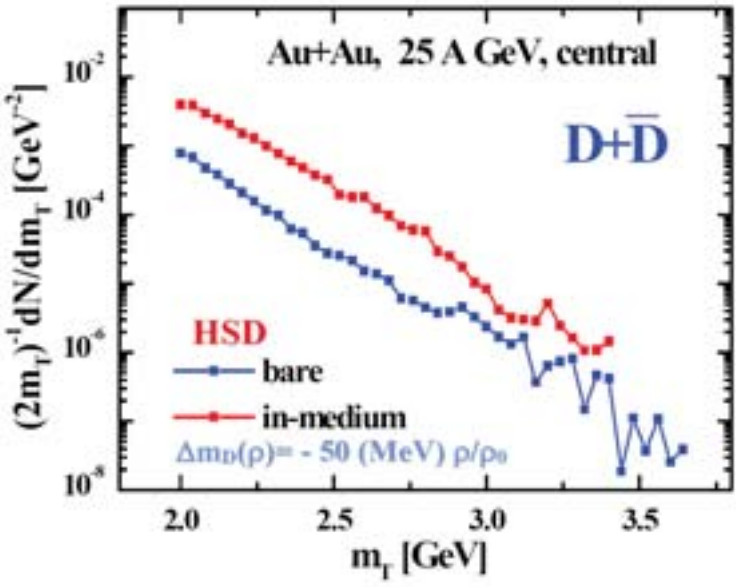


**Figure 2.22:** *Transverse mass spectra of D mesons in central Au + Au collisions at a beam energy of 25 GeV/nucleon, as predicted by the HSD model with (red curve) and without (blue curve) the inclusion of in-medium effects [62].*

nucleon collisions is conserved over the full collision evolution. Hence, the increase in yield of D mesons must be reflected in a decrease in the yields of other charm hadrons. It is thus particularly important to measure different charm hadron species. Additionally, the yield of D-mesons must be measured for different collision systems, to investigate the medium density dependence of in-medium effects.

To investigate the physics observables discussed above in this section, CBM will measure open charm particles at different beam energies in nucleus-nucleus collisions but also in proton-proton and proton-nucleus collisions. Measurements of elementary p + p collisions are needed to provide a baseline for A + A collisions, while p + A measurements are important for the evaluation of the contribution of initial state effects to the phenomena observed in A + A collisions.

# Chapter 3

# The Compressed Baryonic Matter experiment

The Compressed Baryonic Matter (CBM) experiment is one the main experiments which will operate at the future Facility for antiproton and Ion Research (FAIR), in Darmstadt. It aims at exploring the structure and properties of nuclear matter under extreme conditions of net baryon densities. The major topics which will be addressed are the search for the first order deconfinement phase transition, the search for the QCD critical point and the study of the modifications of hadron properties in dense nuclear matter.

In this chapter, we give a short description of the FAIR accelerator facility. Then we present the scientific program of the CBM experiment and its main objectives. The last part of the chapter is devoted to the description of the CBM detection set-up and its main sub-systems.

## 3.1 The future FAIR facility

The Facility for antiproton and Ion Research is a new accelerator facility under construction at the GSI Helmholtz Centre for Heavy Ion Research in Darmstadt, Germany. It will provide a large variety of beams from antiprotons to heavy nuclei with excellent quality and high intensities: up to $10^{13}$ protons/second and $10^{9}$ Au ions/second are foreseen. The blue and red parts of Figure 3.1 show schematically the current GSI and future FAIR facilities. FAIR will consist of two superconducting synchrotrons SIS100 and SIS300, placed in the same tunnel one above the other, and with a circonference of 1084 meters. The denomination of these two synchrotrons comes from the fact that they will provide beams with a magnetic rigidity of 100 Tm for SIS100 and 300 Tm for SIS300. The main goal for these two synchrotrons is the possibility of delivering beams for up to 4 research programs running in parallel, thus offering to each of them a large beam availability. SIS100 will provide an intensity of up to $5 \times 10^{11}$ uranium ($U^{28+}$) ions/second at a beam energy of 2.7 GeV/nucleon, and up to $4 \times 10^{13}$ protons per second at 29 GeV/nucleon. The high intensity proton beam, which is mandatory to produce intense antiproton beams, will

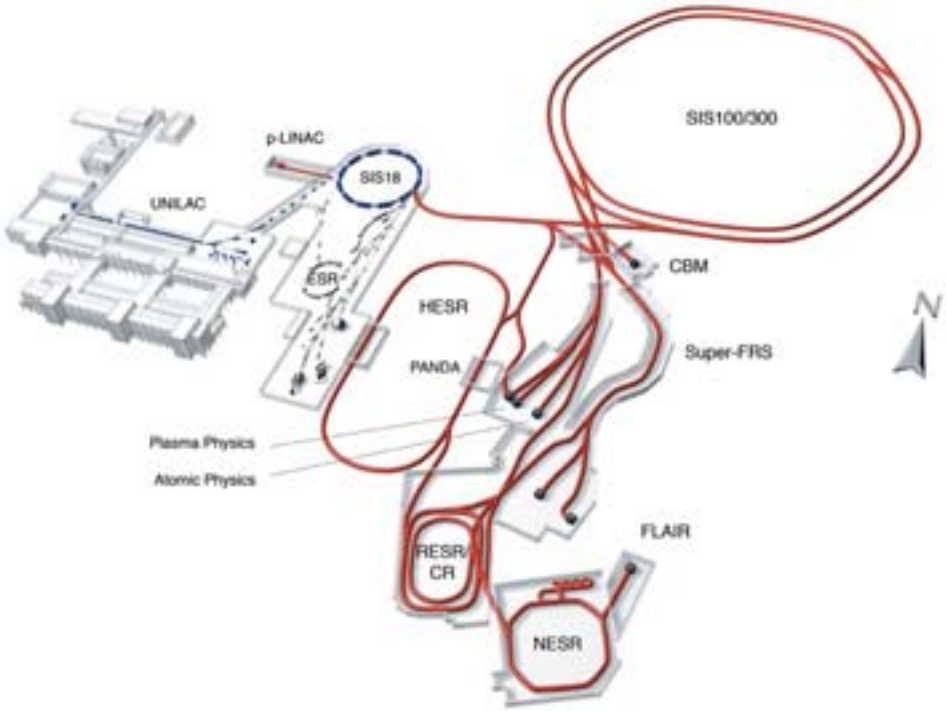


**Figure 3.1:** *Layout of the existing GSI facility (UNILAC,SIS-18, ESR) on the left and the planned FAIR facility on the right: the superconducting synchrotrons SIS-100 and SIS-300, the collector ring CR, the accumulator ring RESR, the new experimental storage ring NESR, the superconducting fragment separator Super-FRS, the proton linac (p-LINAC) and the high energy antiproton storage ring HESR. The location of the PANDA (antiproton annihilation at Darmstadt), the FLAIR (facility for low-energy antiproton research) and the CBM experiments are also shown.*

be supplied by the future separate proton linac which will serve as an injector for the current SIS18 synchrotron. SIS300 will provide up to $3 \times 10^{11}$ uranium ($U^{92+}$) ions per second at 34 GeV/nucleon. The beam energy per nucleon (E/A) which can be reached for each ion is given by:

$$\frac{E}{A} = \sqrt{(0.3 \times B \times \rho \times \frac{Z}{A})^2 + m^2} - m \tag{3.1}$$

with A the atomic mass of the ion, Z its charge number, m the nucleon mass, and $B \times \rho$ the beam rigidity. For Au ions (A/Z = 197/79), a beam rigidity of 100 and 300 Tm, at SIS100 and SIS300 respectively, allows reaching a beam energy of 11 and 35 GeV/nucleon. The existing accelerators (UNILAC and SIS18) will be upgraded to serve as an injector for SIS100 and SIS300. The beam will be extracted and delivered to experiments in a quasi-continuous mode, over periods of 10 - 100 second. A continuous beam is suitable for high rate experiments to avoid large fluctuations in the flux of beam particles.

Several research programs are foreseen at FAIR. They can be categorized in 5 main scientific areas: nuclear structure, astrophysics, atomic physics, plasma physics, and QCD and hadron

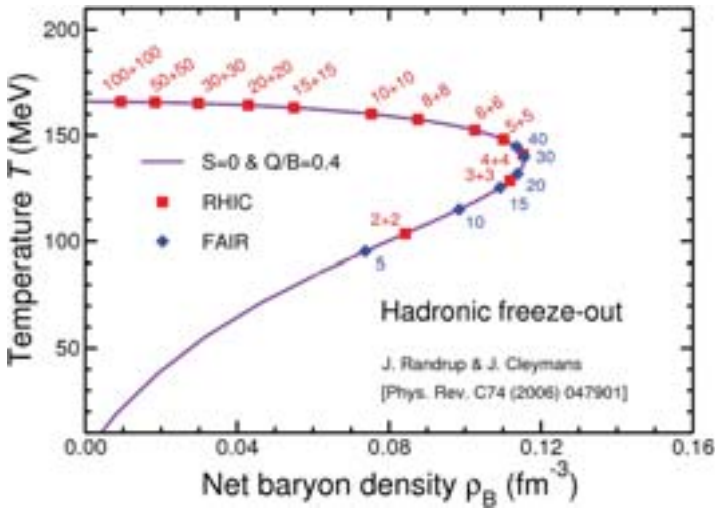


**Figure 3.2:** *The hadronic freeze-out line in the plane temperature (T) versus net-baryon density ($\rho_B$) as obtained in the statistical model with the values of baryon chemical potential and T that have been extracted from the experimental data in Ref. [66]. The curve corresponds to Au + Au collisions. The symbols represent beam energies (in A GeV) at either RHIC (total energy in each beam), or FAIR (kinetic energy of the beam for a stationary target). The figure is taken from [65].*

physics, in which CBM will contribute. For a more detailed description of the FAIR facility, see reference [64].

## 3.2 The CBM physics program: main goals and relevant observables

CBM is one of the major experiments foreseen at FAIR. It is a fixed-target experiment, aiming at exploring the region of high net baryon densities ($\rho_B$) of the nuclear phase diagram, which has been until now only poorly examined both experimentally and theoretically. This can be seen in Figure 3.2, which shows the chemical freeze-out conditions in heavy ion collisions. $\rho_B$ is maximal at beam energies between 20 - 40 GeV/nucleon *, which will be accessible at FAIR. The CBM research program is complementary to that of RHIC and LHC heavy ion experiments, which concentrate on the region of high temperatures and low net baryon densities.

As mentioned above, the depicted values of $\rho_B$ and T are those of the system at chemical freeze-out. Figure 3.3 shows predictions of the Parton-Hadron-String Dynamics (PHSD) model [33] for the phase space trajectory at the center of a central Au + Au collision at several beam energies in the FAIR energy regime. PHSD is a recent extended version of the HSD model, which includes

*This corresponds to a c. m. energy per nucleon pair $\sqrt{s_{NN}}$ in the range 6-10 GeV

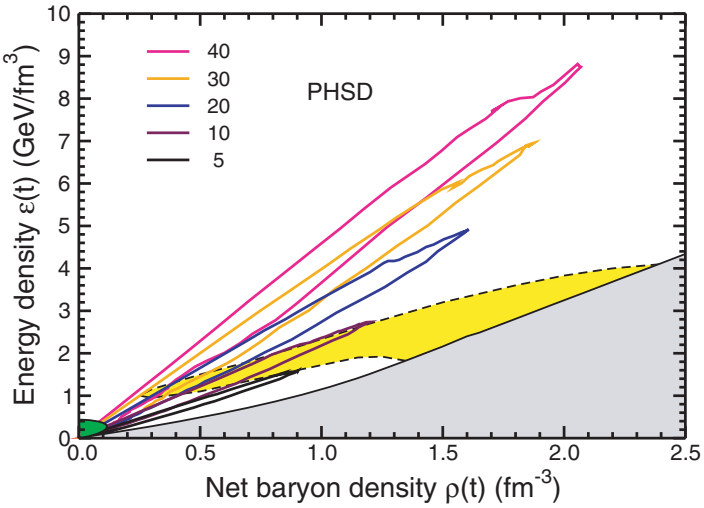


**Figure 3.3:** *Predictions of the Parton-Hadron-String Dynamics (PHSD) model for the phase space trajectory at the center of a central Au + Au collision at various bombarding energies in the FAIR energy regime. The trajectories are shown in the energy density ($\epsilon(t)$) versus net baryon density ($\rho_B(t)$) plane. For more details, see reference [33].*

an early partonic phase with an equation of state from lattice QCD and quasiparticle properties for quarks, antiquarks, and gluons that have been obtained from fits to lattice results. The figure shows that the energy density goes up to 8 - 9 GeV/$fm^3$ at a beam energy of 40 GeV/nucleon, far beyond the critical energy density for deconfinement predicted by lattice QCD [20]. Moreover, the maximal net baryon density achieved at this energy is of 2 $fm^{-3}$, which is about 10 - 12 times higher than the density of ordinary nuclear matter. Note that similar features are also predicted by several other dynamical models [33]. This suggests that heavy ion collisions at FAIR energies will allow investigating different phases of dense nuclear matter [16, 17].

CBM will search for the phase transition to deconfinement and the QCD critical point, and will study the in-medium modifications of hadron properties in dense baryonic matter (these modifications may be related to the chiral symmetry restoration). It will also investigate the Equation of State (EoS) of dense baryonic matter, which has strong implications for understanding neutron stars. To achieve these goals, CBM will measure a large variety of observables (see Ref. [59]), including those associated with charm particles. As mentioned in Section 2.6.2, charm particles have not been measured so far in heavy ion collisions at beam energies below 160 GeV/nucleon.

Some of the relevant observables that will be measured in the CBM experiment are briefly discussed below.

The chiral symmetry restoration in dense baryonic matter is expected to modify the mass of hadrons containing light (up and down) quarks. This would have a strong effect on the yield of D-mesons at FAIR energies since they are produced close to their kinematic production threshold. The yield of D-mesons is thus a promising observable to investigate the phenomenon of chiral symmetry restoration.

The suppression of hidden charm (J/$\Psi$) is considered as one of the most promising observables to probe the deconfinement phase transition. However, alternative interpretations within hadronic models have been suggested to describe the data observed so far [39, 40]. The measurement of this observable at FAIR energies where the onset of deconfinement is expected would help clarifying this issue. In this respect, the ratio J/$\Psi$/(D+$\bar{D}$) as a function of beam energy is of particular interest as we have seen in Section 2.6.3.1.

Strangeness production can also be used to investigate the phase transition to deconfinement. Several anomalies have been observed in heavy ion collisions at a beam energy of around 30 GeV/nucleon, and which are absent in proton-proton collisions. These anomalies cannot be reproduced by hadronic models and suggest that partonic interactions take place at the incident energy range 20-40 GeV/nucleon (see Section 2.5.2). This motivates further investigations at FAIR.

The presence of a critical point in the QCD phase diagram is predicted to be reflected by non-statistical event-by-event fluctuations of conserved quantities such as the baryon or strangeness quantum numbers. Detailed excitation functions of such observables at beam energies in the range 20-40 GeV/nucleon are of great importance. This will be measured accurately by the CBM experiment.

The collective motion (i.e., flow) of emitted particles in heavy-ion collisions is sensitive to the very early stage (possibly partonic) of the collision. The study of flow observables at FAIR energies will provide essential information on the effective degrees of freedom, either hadronic or partonic, in the system. In particular, hadronic models predicts that the elliptic flow of D-mesons in Au + Au collisions at a beam energy of 25 GeV/nucleon, is weaker than that of light hadrons (pions, etc). If partonic interactions participate to the build-up of elliptic flow at early stage of heavy ion collisions, the elliptic flow of D-mesons is expected to be significantly enhanced. It is thus a very sensitive probe of the phase transition to deconfinement. Moreover, this observable is sensitive to the pressure build up in the medium and can be used to investigate the equation of state of nuclear matter.

Direct photons are undisturbed probes of the hot and dense medium (they are not affected by strong interactions). Thermal photons emitted by a partonic medium are predicted to be the dominant source of direct photons at low transverse momenta in heavy ion collisions. CBM will be able to measure thermal photons with unprecedentedly high statistical accuracy.

CBM will be operated in two phases. The first phase will start in 2017 at the SIS100 synchrotron. At SIS100, CBM will measure p-p, p-A (at incident energies up to 29 GeV) and A-A collisions (11 GeV/nucleon for Au + Au and up to 14 GeV/nucleon for Ca-Ca). The second phase, planned at SIS300, will allow CBM completing its physics program by measuring A-A collisions (up to 35 GeV/nucleon for Au beams), and p-p and p-A collisions (at incident energies up to 89 GeV).

## 3.3 The CBM experimental set-up

In order to measure rare probes, the CBM experiment will have to sustain high beam intensities and long running periods. A collision rate of up to 10 MHz is foreseen in Au + Au collisions. Such a high collision rate results into a drastic particle flux (of the order of $10^{10}$ particles/second). To sustain this high particle flux and to provide good position accuracy, the detectors must have a high granularity.

This particle flux also imposes strong constraints for the detectors and their read-out system in terms of radiation tolerance and read-out speed. Additionally, the data acquisition system must be able to handle a large amount of data.

The track reconstruction algorithms should provide high precision and fast online tracking, with high track reconstruction efficiency and good momentum resolution.

The requirements mentioned above must be fulfilled for various systems (p-p, p-A and A-A) over a broad beam energy range (from 2 to 40 GeV/nucleon) in order to carry on the physics program of CBM.

A schematic view of the detector concept is given in Figure 3.4. Two detector configurations are envisaged: one is dedicated to the identification of electrons, while the other one is specialized in detecting muons. The second configuration must include absorbers which can efficiently absorb all particles except muons, and is thus not compatible with the first one. In both configurations, the detector comprises a high resolution Micro-Vertex Detector (MVD), a low mass Silicon Tracking System (STS), a Transition Radiation Detector (TRD), a Time-Of-Flight (TOF) detector and a Projectile Spectator Detector (PSD). The electron configuration additionally comprises a Ring Imaging Cherenkov (RICH) and an Electromagnetic CALorimeter (ECAL). As for the muon configuration, these two last sub-detectors must be replaced by a Muon Chamber (MUCH).

The MVD is meant to measure the collision vertex (or primary vertex) and the decay vertices of short lived particles with high accuracy. The STS must reconstruct the trajectories (or tracks) of charged particles and determine their momentum. The TOF is used to measure the time of flight of particles, which in combination with the STS provides the identification of charged hadrons. The TRD allows identifying electrons and positrons at high momenta, and can also be used to reconstruct the tracks of charged particles. The RICH must identify electrons and allow suppressing pions misidentified as electrons in the momentum range of electrons originating from the decay of low mass vector mesons. Finally, the ECAL is used for identifying electrons and photons.

The various detector components of CBM are designed to cover laboratory polar angles from 2.5 to 25 degrees (with full azimuthal coverage). This geometrical coverage has been chosen such that for central nucleus-nucleus collisions at 25 AGeV and a magnetic bending power of 1 Tm more than 60% of the emitted charged particles are accepted. Note that the geometrical acceptance varies only little as a function of the beam energy [68]. This is very important for performing an accurate scan of different observables, in particular those sensitive to the decon-

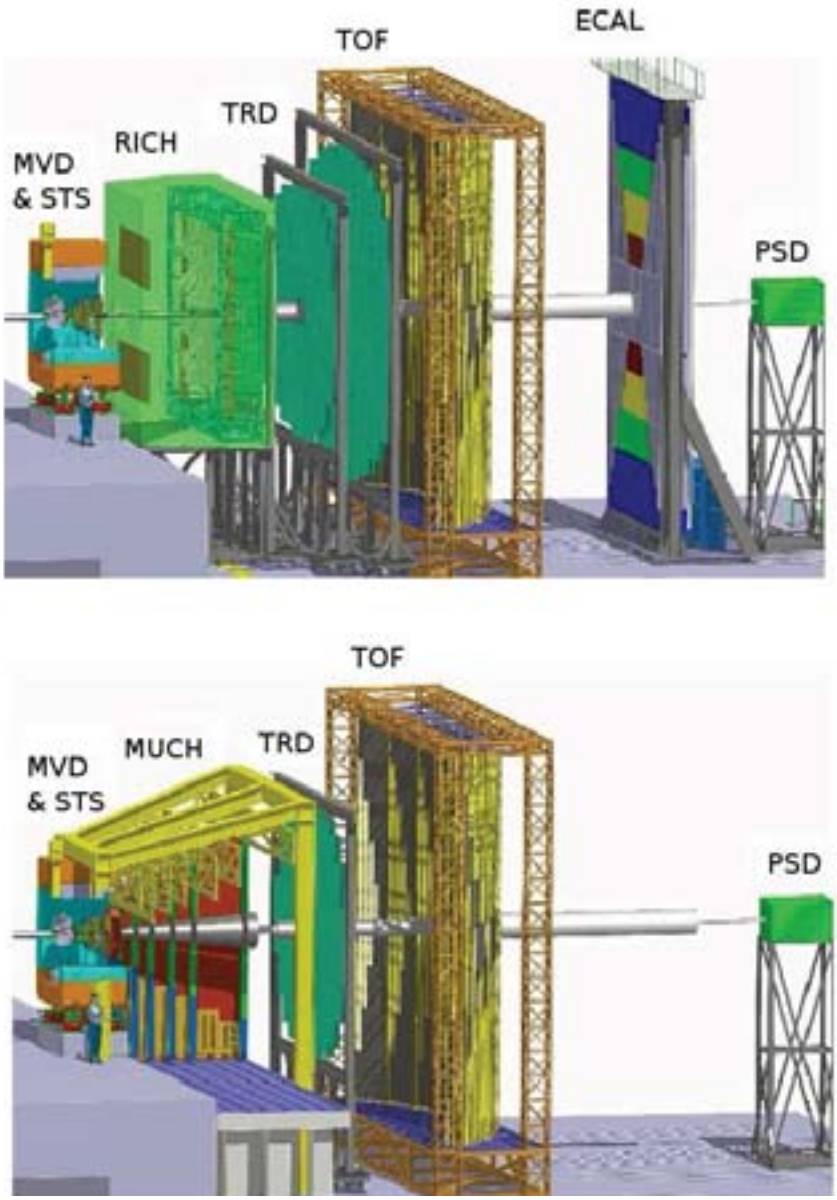


**Figure 3.4:** *Schematic view of the CBM experiment. The beam direction is from left to right. Following the target there are the Micro Vertex Detector (MVD) and the Silicon Tracking System (STS). Both are located inside the dipole magnet (orange). The electron configuration is shown in the top panel: the detectors situated more downstream are the Ring Imaging CHenrenkov (RICH), three Transition Radiation Detector (TRD) planes, a Time-Of-Flight (TOF) detector, an Electromagnetic CALorimeter (ECAL) and a Projectile Spectator Detector (PSD). The muon setup is shown in the bottom panel: in the place of the RICH, there is a Muon Chamber (MUCH) and the ECAL is not present.*

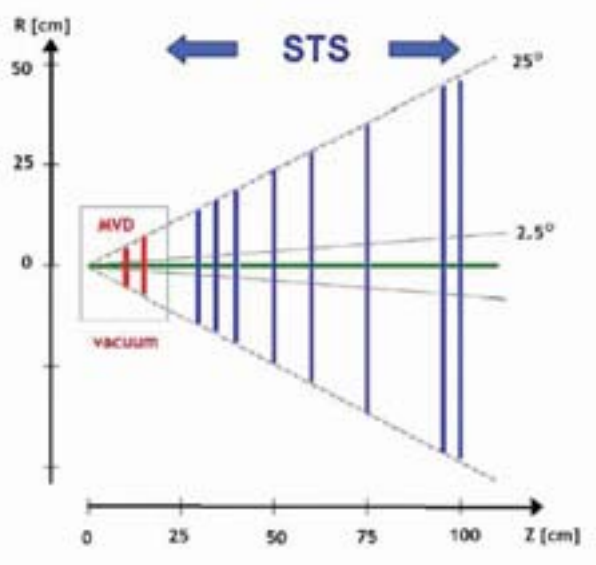


**Figure 3.5:** *Schematic side-view of the STS and MVD stations: their distances from the target and their acceptance in terms of laboratory polar angles are indicated.*

finement phase transition and to the critical endpoint.

### 3.3.1 The Micro-Vertex Detector

The Micro-Vertex Detector (MVD), along with the Silicon Tracking System, is the core components of CBM. The MVD must be located the closest to the collision point. Thus, it will have to tolerate particularly high particle fluxes and track densities (several times $10^8$ tracks/$cm^2$/s), which calls for a very highly granular silicon pixel detector. To insure a channel occupancy below $1\%$ and an excellent position resolution, the pixel size must be of about $20 \times 20$ $\mu m^2$ and the detector station must be very thin (of a few $0.1\%$ of the radiation length). Both requirements can be fulfilled by Monolithic Active Pixel Sensors (MAPS). However, the MVD must sustain very high radiation doses, up to $10^{15}$ $n_{eq}/cm^2$ per year for Au + Au collisions at a collision rate of 10 MHz. The speed and radiation hardness of MAPS sensors still need to be improved to fulfill the requirements of CBM. This is the goal of ongoing R&D activities [96]. A schematic cross-section of the MVD is shown in Figure 3.5. The current design consists presently in two stations (red color) covering polar angles from 2.5 to 25 degrees in the laboratory frame, and located in a vacuum vessel. A detailed description of the MVD and MAPS sensors is given in the next chapter.

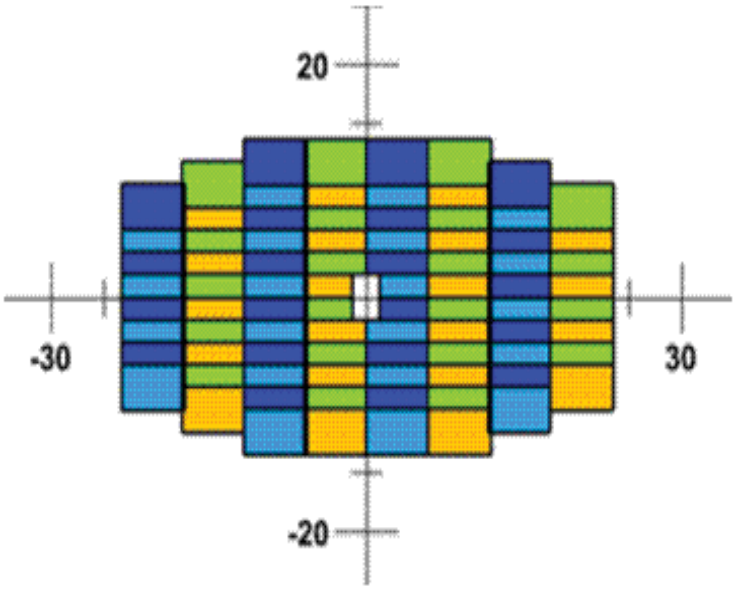


**Figure 3.6:** *Layout of the first STS station placed at 30 cm downstream the target (X/Y-axis in cm).*

### 3.3.2 The Silicon Tracking System

The Silicon Tracking System (STS) [69] is the central component of CBM. It aims at reconstructing the charged particle tracks and determining their momentum with high accuracy and good reconstruction efficiency. Considering the high particle flux crossing the detector (several times $10^9$ particles/s), these tasks put strong constrains on the detector, in terms of material budget, radiation tolerance and read-out speed. In Figure 3.5, a schematic view of the STS (blue color) is shown. The STS is constituted of 8 stations located at distances of 30, 35, 40, 50, 60, 75, 95, 100 cm from the target. This detector is based on low mass silicon micro-strip detectors of 60 $\mu$m pitch. Strips from the front and back sides of each station are titled with respect to each other (by a stereo angle of 15 degrees), which provides 2 dimensional information on the position of tracks. The stations are placed inside a dipole magnet which bends the particle trajectories and allows determining their momentum: for centripetal acceleration in a magnetic dipole field, one has the following equation:

$$\frac{p}{q} = B \times \rho \tag{3.2}$$

with p and q the momentum and charge of the particles, B the strength of the magnetic field, and $\rho$ the bending radius. Since B is known and $\rho$ can be obtained by the track reconstruction algorithm, p/q can be estimated (giving in addition the particle's charge). The bending power provided by the magnet, in combination with the good resolution of the STS must provide a momentum accuracy of about $\delta$p/p = 1%. Finally, the STS must have a time resolution of about 10 ns, to be able to distinguish collisions from one another at a collision rate of 10 MHz.

Note that the first two STS stations may be constituted of hybrid sensors to improve the tracking

performance. Hybrid sensors have higher granularity than strip sensors, and provide better time resolution than MAPS. However, they feature a larger thickness than the two other technologies. The issue of using hybrid stations is still under debate.

### 3.3.3 The superconducting dipole magnet

The dipole magnet must provide the bending power necessary for the STS to achieve good momentum resolution. For this purpose, a dipole field of 1 Tm is envisaged in the vicinity of the target. Such high magnetic rigidity can only be provided by superconducting magnets. The MVD and the STS must be placed inside the magnet. The latter must then be large enough to allow for the installation and the maintenance of these detectors (a cross-sectional area of at least $1.3 \times 1.3\ m^2$).

### 3.3.4 The Time-Of-Flight detector

The Time of Flight (TOF) detector measures the time ($\Delta$t) between a start signal provided by a fast diamond pixel (or micro-strip) detector and the stop signal. The velocity ($\beta$) of the particles can then be obtained as follows:

$$\beta = \frac{L}{c \times \Delta t} \tag{3.3}$$

with L the flight path length of the particles and c the speed of light. In combination with the momentum (p) information provided by the STS, the mass of the particles can be estimated by the following formula:

$$m = \frac{p}{\gamma \times \beta \times c} \tag{3.4}$$

The distance between the start detector and the TOF wall is approximately 10 meters, which results, for example, into a time difference between pions and kaons at p = 3 GeV/c of about 400 ps. The TOF wall consists in a large area (150 $m^2$) of Resistive Plate Chambers (RPC) comprising approximately 60 000 cells providing a time resolution of about 80 ps [70]. Due to the high particle flux, RPC chambers must handle hit rates of up to 20 kHz/$cm^2$. Figure 3.7 shows the reconstructed mass of protons, kaons and pions as a function of momentum [71]. One can see that the separation power between different particles degrades at high momentum, since the hits deposited in the TOF by fast particles are more difficult to separate in time. Pion and kaons can be distinguished up to 3.5 GeV/c, while protons are clearly separated up to 6 GeV/c.

### 3.3.5 The Transition Radiation Detector

The Transition Radiation Detector (TRD) aims at contributing to the identification of electrons and to the reconstruction of charged particle tracks. As for the first task, it must provide a suppression of pions misidentified as electrons by a factor of about 100 (while keeping an electron

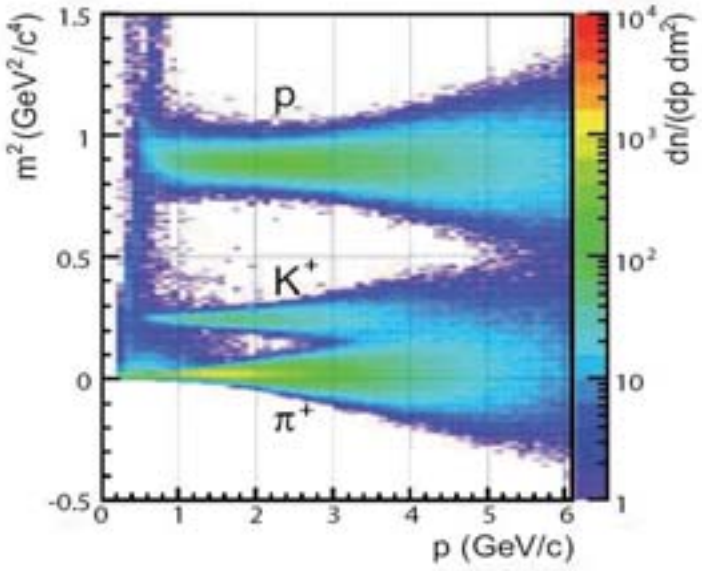


**Figure 3.7:** *Squared mass as a function of momentum of hadrons reconstructed by the TOF in central Au+Au collisions at a beam energy of 25 GeV/nucleon [71].*

reconstruction efficiency of at least 90%). Transition radiation is produced when a relativistic particle crosses an inhomogeneous medium, for example the boundary between materials with different dielectric constants. For particles emitted in relativistic heavy ion collisions, this type of radiation can only be produced by electrons and positrons (which have a Lorentz boost $\gamma$ higher than 1000). These particles can thus be distinguished from, e.g., pions. Currently, the TRD is composed of three stations constituted of three to four layers each, and located at distances of 5, 7.25, and 9.5 m from the target. The detector has a total active area of 600 $m^2$. Each layer comprises a radiator where the transition radiation is produced, and a gaseous detector measuring the energy deposited by charged particles and the transition radiation.

### 3.3.6 The Ring Imaging Cherenkov detector

The Ring Imaging CHerenkov (RICH) detector consists in a radiator and a photodetector. When charged particles cross through the radiator with a velocity higher than the speed of light in that medium, Cherenkov light is produced. The light is emitted under a constant angle ($\theta$) relative to the particle trajectory. This angle is given by:

$$cos(\theta) = \frac{1}{\beta \times n} \tag{3.5}$$

with $\beta$ the velocity of the particle and n the refractive index of the medium inside the radiator. This light cone is reflected by a mirror to the photodetector located at the focal plane of the mirror, thus producing rings of collected photons.

The RICH will be used to identify electrons with momenta up to 10 - 12 GeV/c. For this purpose, a suppression factor of pions mis-identified as electrons of $10^2$ - $10^3$ must be provided by the RICH [72]. It can also be used to identify pions for the sake of separating them from kaons. The latter last task is mandatory since when using the TOF information alone, the separation between pions and kaons becomes difficult at momenta above 4 GeV/c (see Figure 3.7). In the current detector layout, the RICH is placed behind the magnet and in front of the first TRD station. Since a global tracking has to connect tracks reconstructed in the STS and the TRD, the RICH should not be longer than 3 meters and should feature a material budget below 3 - 4 $\%$ of radiation length (to limit the effect of multiple scatterings).

### 3.3.7 The Electromagnetic Calorimeter

In the current design, the Electromagnetic CALorimeter (ECAL) is a "shashlik" type calorimeter dedicated to the measurements of photons and neutral mesons decaying into photons. The detector consists in 140 layers of 1 mm lead and 1 mm scintillator material. These layers are divided into modules which have an area of $3 \times 3$, $6 \times 6$ and $12 \times 12$ $cm^2$.

### 3.3.8 The Projectile Spectator Detector

The Projectile Spectator Detector (PSD) [125] is a compensated hadronic calorimeter designed to measure the collision centrality and the azimuthal angle of the reaction plane. It measures the energy carried by spectator projectile nucleons, which in turn allows determining, on an event-by-event basis, the amount of participant nucleons (in the overlap region of impinging ions) and thus the collision centrality. The task of measuring the reaction plane with the PSD has been addressed in this work, and is described in detail in Chapter 7. Currently, the detector consists in $12 \times 9$ modules of $10 \times 10$ $cm^2$, each composed of 60 layers with combined absorber and scintillator material. The photons produced in the scintillator are measured via WaveLength Shifting (WLS) fibers by Multi-Avalanche Photo-Diode (MAPD) featuring an active area of $3 \times 3$ $mm^2$ and a pixel density of $10^4/mm^2$.

### 3.3.9 The Muon Chamber

The MUon CHamber (MUCH) must measure low mass vector mesons ($\rho$, $\omega$, $\phi$) and J/$\psi$ mesons via their decay into dimuons. To do that, hadrons must be suppressed, which is the task of several absorber layers located behind the STS. Unlike hadrons, muons interact very little with matter and pass through the absorber layers. A matching between muons identified in the MUCH and tracks reconstructed in the STS must be performed to estimate the invariant mass of, e.g., J/$\psi$ mesons. This can be achieved by highly granular and fast detectors which are located in each gap between absorber layers. In the current design, 18 detector stations and 6 segmented iron absorbers are foreseen. Promising candidates for the fast and highly granular detectors are

gaseous detectors based on GEM technology [73], straw tubes, and one of the TRD stations. In this design, the total amount of material budget is of about 13.5 times the nuclear interaction length. The MUCH detector covers a total area of about 70 $m^2$.

### 3.3.10 The Data Acquisition system

The need to measure rare probes like J/$\Psi$ and open charm imposes the use of high collision rates. The design goal of the DAQ system of CBM is to operate the detector at a maximal collision rate of 10 MHz for Au + Au collisions. This motivated to design the DAQ of CBM as a free-streaming system without low level trigger. The last is replaced by self-triggered front-end electronics which recognize hits in the related sub-detectors. For the sake of event building, the hit information is complemented with time-stamps, which are generated from a central time distribution system. Hereafter, the data is streamed in a push mode towards the central DAQ. In the latter, high level operations (such as event building, real time tracking, and secondary vertex reconstruction) will presumably be performed by highly parallel multi-core computing systems.

The archiving rate will be of about 1 GBytes/s [59]. Considering an average event data volume* of about 50 kBytes†, the DAQ will accept an event rate of about 20 kHz. An online event selection is thus required to reject events that are not significant to the experiment. For example, at a collision rate of 10 MHz, a event suppression factor of about 500 has to be achieved to decrease the rate of events recorded down to 20 kHz. This has to be done through online hardware and software selection.

In the case of open charm measurements, a reduced collision rate in the order of $10^5$ collisions/s is foreseen (see next chapter). The online selection must then achieve an event suppression factor of about 10. The selection of events containing an open charm hadron will be performed through the reconstruction of secondary vertex candidates. This task requires fast tracking and event reconstruction in the STS and in the MVD.

*Volume of data obtained after event building for one collision

†In Au + Au minimum bias collisions at FAIR energies, assuming a very compact data format after event reconstruction. This number could get larger

# Chapter 4

# The CBM Micro-Vertex Detector

This chapter is devoted to the Micro-Vertex detector (MVD) of the CBM experiment. First, the strategy to measure open charm particles is presented (Section 4.1). The operating environment and the corresponding requirements for the MVD detector are discussed (Section 4.2). After a brief review on pixel silicon sensors, the choice of CMOS Monolithic Active Pixel Sensors (MAPS) for equipping the MVD is motivated (Section 4.3). The working principle of MAPS is introduced, the present status of the R&D developments is summarized, and the future performances of the CMOS sensor foreseen to equip the MVD are discussed (Section 4.4). The chapter ends with considerations on the technical design of the MVD detector (4.5).

## 4.1 Strategy to measure open charm particles

The major task of the CBM-MVD is to detect open charm particles in heavy ion collisions at FAIR energies. This thesis is devoted to the measurement of D-mesons, which contain most of the charm quarks. The ability to measure them is thus commonly considered as a benchmark for characterizing the physics potential of the experiment. Table 4.1 presents the main characteristics of D-mesons. Their mean decay length (c $\tau$) is typically of hundreds of micrometers. Considering that CBM is a fixed-target experiment, one has to account for the Lorentz boost ($\gamma\ \beta$) of particles into the direction of the beam. At a beam energy of 25 GeV/nucleon, $\gamma\ \beta \sim 3.8$. The mean decay length of D-mesons in the laboratory frame (equal to $\gamma\ \beta\ c\ \tau$) is thus of the order of 1 mm. One can see that their measurements must be done through their decay daughter particles.

The measurement of D-mesons is based on the invariant mass method (see Chapter 6), which consists in combining their daughter particles into multiplets. Table 4.1 also shows the main hadronic decay channels of D-mesons. In these channels, the decay products are pions and kaons. The experimental challenge to measure D-mesons comes from the fact that their multiplicity is extremely low at FAIR energies, below $10^{-3}$ in Au(25 AGeV) + Au collisions. Pions and kaons directly produced in these collisions (or primary pions and kaons) have much larger multiplicities, above $10^2$ and 10, respectively (see Figure 4.1). These primary pions and kaons are

| Particles | Quarks | Mass [MeV/$c^2$] | Mean decay length c $\tau$ [$\mu$m] | Decay channel | Branching ratio [%] |
|---|---|---|---|---|---|
| $D^+$ | c $\bar{d}$ | 1869.4 $\pm$ 0.5 | 311.8 | $K^-\pi^+\pi^+$ | 9.51 $\pm$ 0.64 |
| $D^-$ | $\bar{c}$ d | 1869.4 $\pm$ 0.5 | 311.8 | $K^+\pi^-\pi^-$ | 9.51 $\pm$ 0.64 |
| $D^0$ | c $\bar{u}$ | 1864.6 $\pm$ 0.5 | 122.9 | $K^-\pi^+$ | 3.8 $\pm$ 0.07 |
| $\bar{D^0}$ | $\bar{c}$ u | 1864.6 $\pm$ 0.5 | 122.9 | $K^+\pi^-$ | 3.8 $\pm$ 0.07 |

**Table 4.1:** *Characteristics of D-mesons [67]. Note that $\tau$ refers to their proper lifetime and c to the speed of light.*

thus responsible for a very large combinatorial background of uncorrelated particle multiplets.

The strategy to reduce this combinatorial background consists in using the displaced decay topology of D-mesons (displaced with respect to the collision vertex, or primary vertex). This is illustrated in Figure 4.2, in the case of a $D^+$ meson decaying into $K^-\pi^+\pi^+$. The distinction between $D^+$ mesons and the combinatorial background can be made by reconstructing the $D^+$ decay vertex. However, this task is complicated due to the fact that $D^+$ decay very close to the primary vertex (see above). Hence, to separate the decay vertex of $D^+$ from the primary vertex, the former must be measured with a really high accuracy, on the order of 100 $\mu$m for example.

In the following, the detection of $D^+ \rightarrow K^-\pi^+\pi^+$ in central Au + Au collisions at 25 AGeV will be considered as a representative benchmark for assessing the performance of the MVD. The choice of this particular decay channel was motivated by the fact that it features three daughter particles, which in turn leads to a drastic amount of combinatorial background. Additionally, the Au + Au system provides a typical limiting environment for the MVD (notably due the high expected hadron multiplicity per event in this system).

## 4.2 Detector environment and requirements

The precision needed to measure the decay vertex of open charm particles and the very high collision rates necessary to obtain a sufficient statistics of these particles create very constraining running conditions for the MVD. Those conditions and the requirements they impose to the MVD are the subject of the following section.

### 4.2.1 Expected hit densities

Figure 4.3 presents the hit density reached in the MVD station in Au + Au collisions at various beam energies (from 15 to 35 GeV/nucleon) and for typical distances between the MVD station and the target (from 5 to 15 cm) [74]. The hit density is normalized per Au + Au collision. First, it is important to mention that the hit density is highly inhomogeneous over the MVD area: it increases substantially while going closer to the beam axis. This effect comes from the fixed-

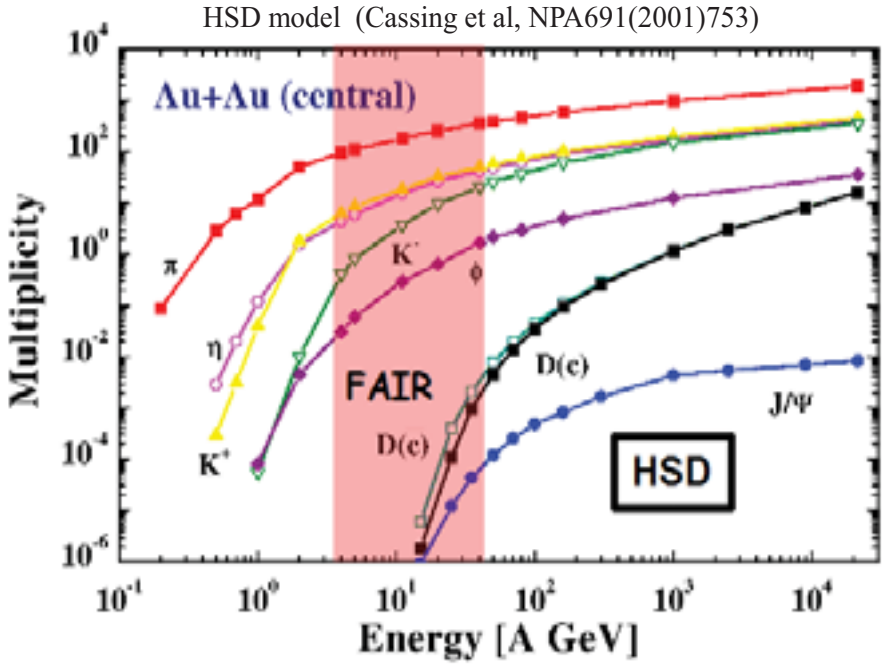


**Figure 4.1:** *Predictions of the HSD microscopic transport code [62] for the multiplicity of various hadrons, including D-mesons and J/$\psi$ mesons, in central Au + Au collisions as a function of beam energy.*

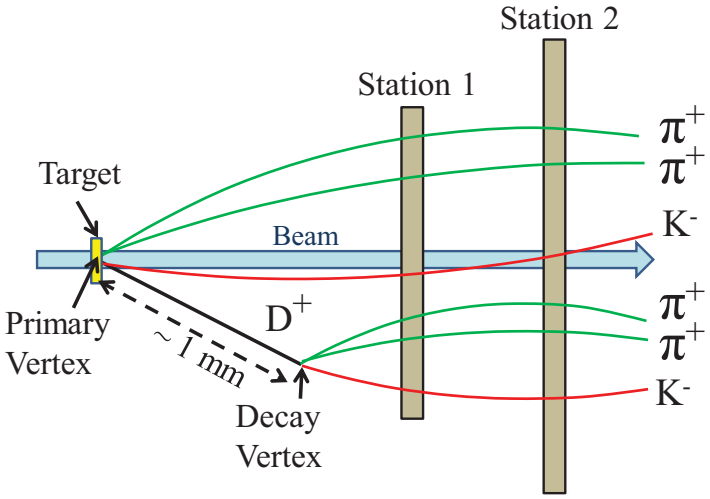


**Figure 4.2:** *Simplified sketch of the MVD (with two stations). As an illustration, one $D^+$ meson decaying into $K^-\pi^+\pi^+$ is pictured, along with pions and kaons created in the nuclear collision (or primary vertex). $D^+$ mesons have a mean decay length of 312 $\mu$m. At a beam energies of 25 GeV/nucleon, due to a Lorentz boost $\gamma$ of 3.8, they decay at a distance to the primary vertex of about 1 mm on average.*

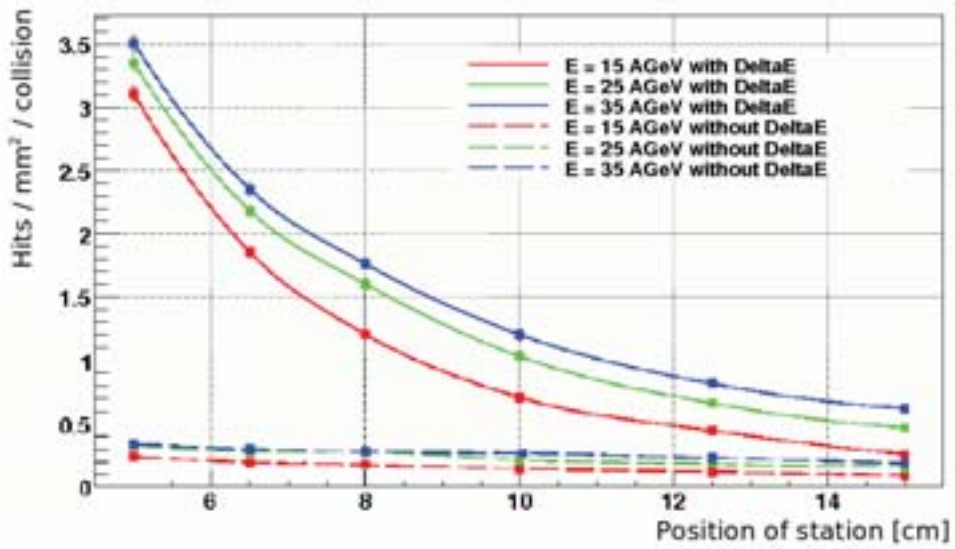


**Figure 4.3:** *Average hit density per $mm^2$ and per Au + Au collision as a function of the distance from the target and of the beam energy. The hit density is given for the most exposed part of the MVD. Two cases are shown: with (full lines) and without (dashed lines) the contribution of $\delta$-electrons (see text). Taken from [74].*

target topology of the CBM experiment: particles produced in nuclear collisions are Lorentz-boosted in the direction of the beam. Figure 4.3 presents the hit density reached in the most exposed part of the MVD. Note that a copious amount of $\delta$-electrons are produced in the target by beam ions (see Section 5.6.2). One can see that the hit density increases substantially while going closer to the target if the contribution of $\delta$-electrons is accounted for. This increase is particularly important going from 10 cm down to 5 cm, where they reach up to 3.5 hits/$mm^2$/collision.

To keep the average fraction of channels which receive a hit below, for example, $1\%$ per collision, a granularity of more than 300 channels/$mm^2$ is required. This imposes the use of highly granular pixel sensors.

### 4.2.2 Expected radiation doses

Table 4.2 presents the expected radiation doses received by the most exposed part of the MVD detector in Au(25 AGeV) + Au collisions. These results were estimated in [102] including the contribution of $\delta$-electrons produced by beam ions in the target. The radiation doses are shown for two typical distances: 5 and 10 cm downstream the target. For example at 5 cm from the target, the most exposed part of the MVD is expected to receive 6.7 $\times$ $10^{-6}$ rad/collision and 30.2 $n_{eq}/cm^2$/collision.

To obtain the requirements on the radiation hardness of the MVD, one has to normalize the radiation doses according to the collision rate. As discussed in the last chapter, the ambitioned

| Distance from target [cm] | | 5 | 10 |
|---|---|---|---|
| Ion. rad. dose [rad] | per collision | $6.7 \times 10^{-6}$ | $1.6 \times 10^{-6}$ |
| | per year | $> 3 \times 10^{6}$ | $8 \times 10^{5}$ |
| Non-ion. rad. dose [$n_{eq}/cm^2$] | per collision | 30.2 | 14.7 |
| | per year | $> 10^{13}$ | $7.3 \times 10^{12}$ |

**Table 4.2:** *Non-ionizing and ionizing doses received by the most exposed part of the MVD station in Au(25 AGeV) + Au collisions as a function of the distance from the target. These values were estimated in [102], including the contribution of $\delta$-electrons produced by beam ions in the target. The doses are given normalized to one nuclear collision, and accumulated over a run period (about two months beam on target per year).*

collision rate for charm measurements in nucleus-nucleus collisions is of 10 MHz. However, to measure open charm particles with high precision, the current concept of the MVD is based on Monolithic Active Pixel Sensors (MAPS) technology (see Section 4.3). Due to constraints in read-out speed and radiation hardness of MAPS, it seems reasonable to operate a first generation of the MVD with a collision rate on the order of $10^5$ collisions/s. Considering that CBM will have an effective time duration of measurements (i.e. beam on target) of about two months ($5 \times 10^6$ seconds) per year, the expected cumulative doses received by the most exposed part of the MVD are above 3 Mrad/year and $10^{13}$ $n_{eq}/cm^2$/year at 5 cm from the target.

### 4.2.3 Precision

The reconstruction of the secondary vertex of open charm particles imposes strong constraints on the vertex resolution. To reconstruct the secondary vertex, the tracks measured in the MVD and STS are extrapolated back to the collision vertex. The accuracy of such extrapolation is driven mostly by the spatial resolution of the most upstream MVD stations and the momentum vector resolution of the tracking detectors. Note that the momentum vector resolution depends on the thickness of the tracking stations (it is degraded by multiple scatterings).

Figure 4.4 shows the resolution achieved for the longitudinal position of the secondary decay vertex of $D^+$ mesons decaying into $\pi^+$ $\pi^+$ $K^-$, as a function of the spatial resolution and thickness of the first two MVD stations (see Figure 3.5). The detailed geometry of the MVD and STS stations considered here is presented later in Table 6.1. Note that the different thicknesses in Figure 4.4 are given in unit of $\mu$m of silicon equivalent. The simulations steps to reconstruct the decay vertex of $D^+$ mesons are presented in detail in Chapter 6.

As expected, the secondary vertex resolution deteriorates with increasing material thickness and degrading spatial resolution. To achieve, for example, a vertex resolution of 100 $\mu$m (see Section 4.1), a material budget per station of 300 $\mu$m (corresponding to approximately 0.3% of the radiation length) and a spatial resolution of 5 $\mu$m are appropriate. This ambitious spatial resolution imposes the use of very granular, pixelized sensors.

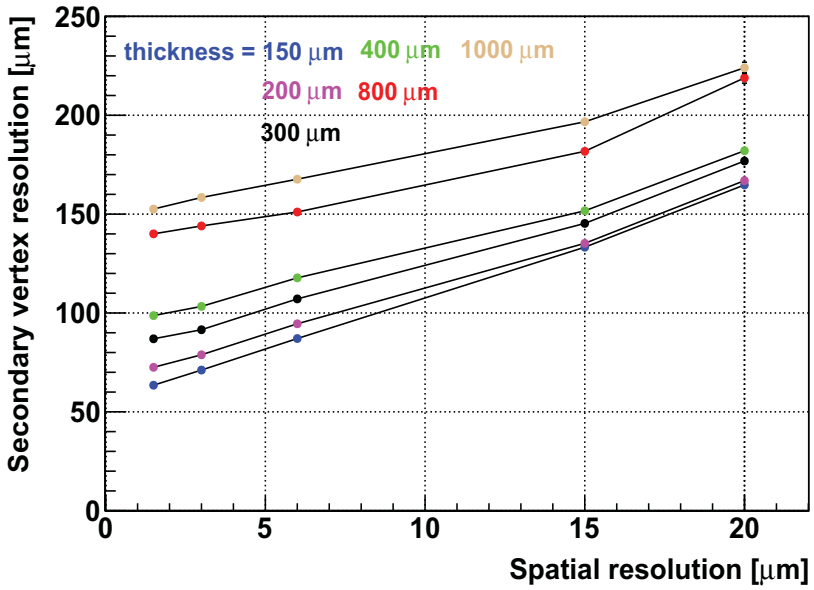


**Figure 4.4:** *Resolution on the position (along the beam axis) of the decay vertex of $D^+$ mesons decaying into $\pi^+$ $\pi^+$ $K^-$. The results are presented as a function of the spatial resolution and the thickness of the first two MVD stations.*

Additionally, the uncertainty on the track extrapolation mentioned above increases with the distance separating the collision vertex and the first MVD station. This is an issue since the latter cannot be located as close as wanted to the target, due to the high and steeply rising particle flux and radiation dose in this case, as seen in the previous two sections. Previous studies [75, 76] demonstrated that a first MVD station located at 5 cm downstream the target provides the necessary vertexing precision to measure open charm. In Chapter 6, we will see that the first MVD station can be placed further, at 10 cm downstream the target in order to reduce the hit densities and radiation doses received.

## 4.3 Silicon pixel sensors

Currently, there are several silicon based pixel sensor technologies: Hybrid Active Pixel Sensors (HAPS), Silicon On Insulator (SOI), Charge Coupled Devices (CCD), DEPleted Field Effect Transistor (DEPFET) and CMOS* pixel sensors. Among those, HAPS, CCD and CMOS technology seems to be currently mature enough to be considered to equip the CBM-MVD.

The detector requirements for pixel sensors equipping the CBM-MVD at SIS300 are summarized in Table 4.3. Apart from the previously mentioned requirements, a read-out time below 10 $\mu$s is mandatory to limit the collision pile-up in the MVD detector to a few collisions (at an average collision rate on the order of $10^5$ collisions/s). The table also gives the current performance of

*Complementary Metal Oxide Semi-conductor

| | MVD | Pixel sensor performance | | |
|---|---|---|---|---|
| | requirements | MAPS | HAPS | CCD |
| Spatial resolution [$\mu$m] | $\leq 5$ | < 5 | > 10 | < 5 |
| Material budget [$X_0$] | $\leq 0.3\%$ | $\leq 0.05\%$ | $0.6\%$ | $0.02\%$ |
| Ionizing radiation hardness [Mrad] | > 3 | > 0.3 | 50 | > 1 |
| Non-ionizing radiation hardness [$n_{eq}/cm^2$] | > $10^{13}$ | > $10^{13}$ | $10^{15}$ | $\lesssim 10^{10}$ |
| Time resolution [$\mu$s] | < 10 | $\sim 110^*$ | 0.025 | $11.5^*$ |

**Table 4.3:** *Detector requirements for the MVD at SIS300, given in the case of Au(25 AGeV) + Au collisions at a collision rate of $10^5$ collisions/s and for a station located at 5 cm from the target. The material budget is expressed in terms of percentages of the radiation length ($X_0$): the requirement accounts for a complete MVD station (including support structure, cables etc), while the performance accounts for the sensors alone. The main characteristics of pixel sensors are also shown. A comprehensive summary of the performance of HAPS and CCD can be found in [80] and [88].*

HAPS, CCD and CMOS sensors (see discussion below). Note that the mentioned thicknesses account for sensors alone. Additional material budget must be added to include the contributions, for example, of the mechanical support, the cooling structure, the read-out cables, the glue and wire bonds.

HAPS [81] are semi-conductor devices in which read-out electronics and sensing parts are implemented on separate silicon layers. Both parts are electrically connected using the bump bonding technique [83]. Each pixel has its own read-out chain including the signal amplification, discriminator circuits and the data buffering. These sensors thus feature an excellent time resolution (of about 25 ns*). Moreover, they are very radiation tolerant. The main reason is that they are fully depleted and provide a high charge collection efficiency. They can withstand a non-ionizing (ionizing) dose of $10^{15}$ $n_{eq}/cm^2$ (50 Mrad) [82]. Nonetheless, due to spatial constraints (originating mainly from the bump-bonding technique), the pixel size of HAPS is on the order of $100 \times 100$ $\mu m^2$. This limits their spatial resolution, typically to about 30 $\mu$m. Furthermore, due to the presence of separate layers, their material budget is high, on the order of $0.6\%$ of the radiation length. Table 4.3 shows that the performance of hybrid sensors does not match the MVD requirements in terms of spatial resolution and material budget.

In CCD [84], the charge generation takes place in typically 20 $\mu$m thick sensitive volume. Since this volume is very thin, CCD can be thinned down to $0.2\%$ of the radiation length. This type of sensor features low noise since the noise contribution from thermally generated carriers into the sensing volume is limited by the thickness of this volume. Additionally, CCD have a pixel pitch typically of about 10 $\mu$m, providing a high spatial resolution, below 5 $\mu$m. However, these devices are read out in a so-called "rolling shutter" mode. Their read-out time depends

*This number was derived assuming a column parallel read-out for CCD [86] and MAPS [90] and 576 pixels in a column for both sensors. See ref. [80] for details.

*Note that this is not a hard limit for the read-out electronics

on the sensor size (number of pixels) and it is mainly limited by the maximum frequency of signals applied to the transfer gates [88]. Even assuming a column-parallel read-out for CCD [86] (see also [80] for detailed computation) their time resolution is limited, of 11.5 $\mu$s. Another weak point of the currently available CCD is that they are rather sensitive to radiation damage. In particular, they can only withstand a non-ionizing dose of up to $\sim 10^{10}$ $n_{eq}/cm^2$ only [85]. Summarizing (see Table 4.3), CCD do not match the MVD requirements in terms of particle rate capability (time resolution and radiation tolerance).

CMOS sensors are also known as Monolithic Active Pixels Sensors (MAPS) [87]. This type of sensor will be described in more detail in the next section. MAPS provide a high spatial resolutions (below 5 $\mu$m) and feature a small material budget (below 0.05$\%$ of the radiation length). As one can see in Table 4.3, the material budget and the spatial resolution of MAPS match the MVD requirements. Also, the radiation tolerance and time resolution have been improved significantly over the past few years. MAPS have demonstrated a time resolution of about 110 $\mu$s, in combination with a tolerance to a non-ionizing dose higher than $10^{13}$ neq/$cm^2$, and to an ionizing dose above 0.3 Mrad [93]. Although their time resolution and ionizing radiation hardness do not match the MVD requirements yet, both parameters are expected to be improved in the near future [96]. Nowadays, MAPS offer the most promising performance in order to match all MVD requirements.

In the next section, the operation principle of MAPS is presented. Then, the status of the R&D on their achieved time resolution and radiation hardness is summarized. Finally, the projected achievements of the R&D on these two key parameters are discussed.

## 4.4 Monolithic Active Pixel Sensors

MAPS are fabricated using standard CMOS processes, for example the same as used for imaging devices. This makes them relatively inexpensive for prototyping and mass production. The CMOS process was proposed to be used for manufacturing particle tracking devices in 1999 by the IReS*-LEPSI† (Strasbourg) as detecting device for charged particles.

### Working principle

In MAPS [87], both particle sensing elements and read-out electronics are implemented on the same substrate. It is illustrated in Figure 4.5 (left part), which shows the cross-sectional view of a CMOS-sensor pixel (see [88] for a detailed description). The sensitive volume of these sensors is a p-type epitaxial layer (P-EPI), which is typically 10-20 $\mu$m thick. When a charged particle crosses this volume, pairs of electrons - holes are generated along its path. Regularly implanted N-Wells form P-N junctions (with the P-EPI), which serve as collecting diodes. In MAPS with undepleted P-EPI (hereafter referred as standard EPI), there is no electric field apart of a slight

*Institut de Recherches Subatomiques

†Laboratoire d'Electronique et de Physique des Systèmes Instrumentaux

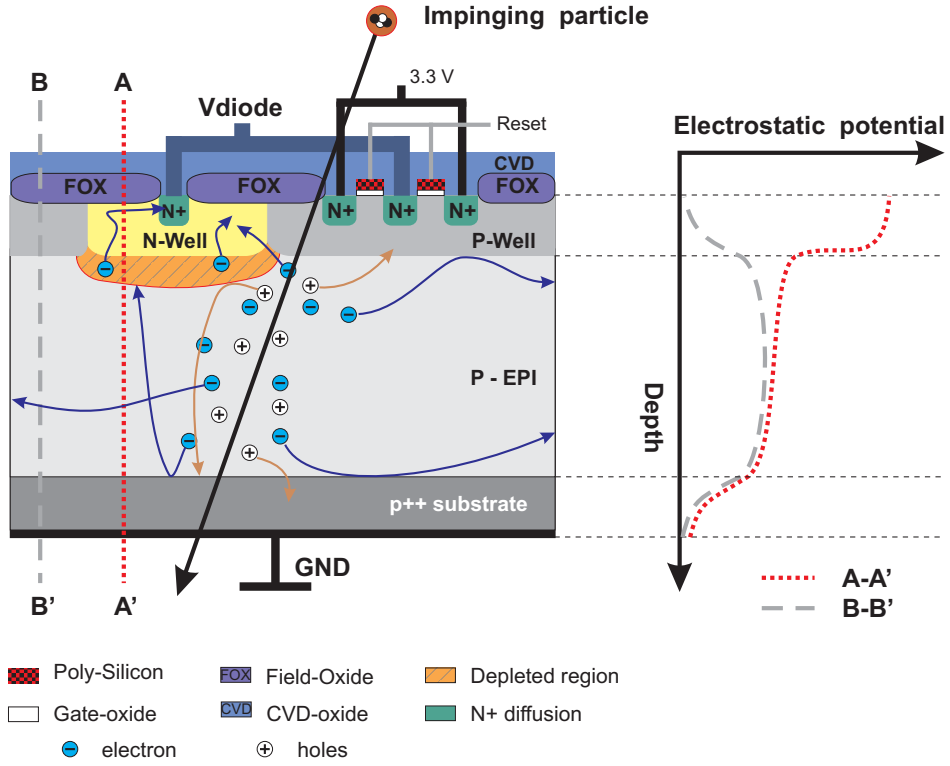


**Figure 4.5:** *Left: cross-sectional view of a Monolithic Active Pixel Sensor showing the basic sensing element (N-Well) and the reset transistor (formed by $N^+$ implants introduced in the P-Well), both implemented on the same substrate. The charge generated by a particle is diffused thermally inside the p-EPI layer towards the sensing element. Right: electrostatic potential through the sensor depth in two lines marked as A-A' (red dotted line) and B-B' (gray dashed line). Taken from [88].*

(<1 $\mu$m) depleted region underneath the N-Wells. The electrons created in the sensitive volume are thus diffused thermally. They are reflected back to the epitaxial layer by the P-EPI/$P^{++}$ and the P-well/p-EPI interfaces. The diffusion continues until the electrons are intercepted by an N-Well, where the electrostatic potential reaches its maximum (right side of Figure 4.5). Within the N-Wells, the electron charge is converted into a voltage on the collecting diode capacitance. This voltage is transferred to a source-follower implemented in each pixel, and it is read out.

The distance between collecting diodes defines the pixel pitch, typically in the range of 10-20 $\mu$m. The pixel pitch is the leading parameter which defines the spatial resolution of the sensor. The spatial resolution mentioned earlier, typically below 5 $\mu$m, is reached due to the combined high granularity and charge sharing in MAPS (several pixels can receive charges created by a particle). Due to the latter phenomenon, the hit position is usually obtained by performing a center of gravity of pixels which receive charges.

The charge collection occurs in the 10-20 $\mu$m epitaxial layer only. The rest of the substrate does

not participate in the charge collection. Hence, MAPS can be thinned down to 30-50 $\mu$m [89], i.e. below 0.05$\%$ of the radiation length.

These sensors feature a low noise, typically of about 10 ENC*†. The low noise allows achieving a signal-over-noise ratio in the range of 20-30 at room temperature (about 20°C). This results into a very good particle detection performance: a detection efficiency close to 100$\%$ with a low fake hit rate (below $10^{-4}$) [90, 91].

**Achieved time resolution**

CMOS sensors consist of thousands of individual pixels regularly distributed over the silicon surface. They form an "array of pixels". This array of pixels is scanned by read-out electronics located at the periphery of the sensor. Only a fraction of the pixels is read out simultaneously. This is done mostly to limit the area occupied by the read-out electronics and its power consumption. The whole pixel array is read out in rolling shutter mode: it is divided in sub-arrays of pixels, which are read out one after another. The time resolution ($T_p$) of MAPS is equal to the time needed to read out the whole array of pixels. Note that the time resolution of MAPS is equal to their read-out time. $T_p$ is inversely proportional to the frequency of the (externally delivered) clock signal (f), and it is directly proportional to the number of pixels read out serially ($N_{pix}$) as defined by the following expression:

$$T_p = N_{pix} \cdot \frac{n}{f} \tag{4.1}$$

where n is the number of clock cycles needed to read out a single pixel. For MAPS with fully sequential read-out (pixels read one by one), $T_p$ was typically of several milliseconds. In order to decrease $T_p$, MAPS can be organized in N columns read out in parallel. This approach reduces $N_{pix}$ in Equation (4.1) by a factor of N with respect to a fully sequential read-out.

However, decreasing $T_p$ has an effect of increasing the rate of data which has to be transmitted by the sensor. This data rate may become too large to be handled efficiently by the embarked read-out circuitry. In order to overcome this potential obstacle, a logic which selects only information related to hits was implemented in MAPS. This signal processing is referred as data sparsification. A simplified schematic of the sensor architecture containing the column-parallel read-out and the data sparsification block is shown in Figure 4.6. The pixel array (left side) is scanned row by row (X-axis). To select pixels which receive a hit, each column (Y-axis) is terminated by a comparator where the voltage signal from each pixel is compared with a reference voltage. The binary information provided by all comparators (of the type fired/unfired pixels) is processed by a data sparsification circuitry and saved (on local memory) in a compact format, containing only the (X, Y) position of fired pixels (or "1"s in binary logic). In this way, the binary information is zero-suppressed. Details about the data sparsification procedure can be found in Section 5.6.5. The hit information is then transmitted to the outside world.

*Equivalent Noise Charge. It is the number of electrons one would have to collect from a silicon sensor in order to create a signal equivalent to the noise of this sensor

†Most probable value

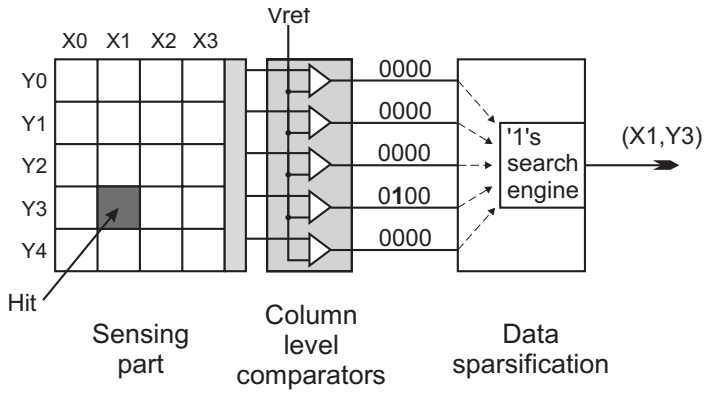


**Figure 4.6:** *Schematic view of the sensor pixel array (left side) equipped with a column-parallel read-out and data sparsification (right side). The column level comparators compare the charge signal provided by pixels with a common threshold ($V_{ref}$). The data sparsification logic stores the (X, Y) position of pixels with signal above the threshold. Taken from [88].*

It is important to mention that to provide binary output and data sparsification, the sensor must incorporate signal processing on the pixel level: signal amplification and pedestal correction through Correlated Double Sampling (CDS).

The first large-scale sensor with a column-parallel architecture and zero-suppressed binary output, called MIMOSA*-26 [90], was developed in the framework of the EUDET project [95]. MIMOSA-26 will also serve as a baseline for sensors equipping vertex detectors of several experiments, for example: the STAR Heavy Flavor Tracker upgrade [99] and the CBM-MVD. Figure 4.7 shows a picture (left side) and a schematic view (right side) of this sensor: MIMOSA-26 features a pixel array of 1152 $\times$ 576 pixels. The read-out circuitry is located on the bottom part (see Section 5.4.4 for details). This array is scanned row by row, so N = 1152. In MIMOSA-26, 16 clock cycles are needed to read out a single pixel, for signal processing (see below), and the clock frequency is of about 80 MHz. Thus, one has $N_{pix}$/N = 576, n = 16 and f = 80 MHz. As one can see from Equation (4.1), a time resolution of 115,2 $\mu$s is achieved with MIMOSA-26.

### Achieved radiation hardness

Radiation induced damages can be categorized into two types: bulk damages, induced by non-ionizing radiation, and surface damages, caused by ionizing radiation. Bulk damages are displacements of atoms from their places in the crystal lattice of the p-EPI layer (the p-EPI layer can be seen in Figure 4.5). This has an effect of creating new intermediate energy levels in the energy gap of the silicon material, which increase the probability for signal electrons to recombine before they could reach the collecting diode. Bulk damages thus reduces the charge collection efficiency, and in turn, decreases the signal-to-noise ratio of MAPS.

Surface damages are related to the accumulation of holes at the Si/Si-$O_2$ interfaces in electronic

*Minimum Ionizing particle MOS Active pixel sensor

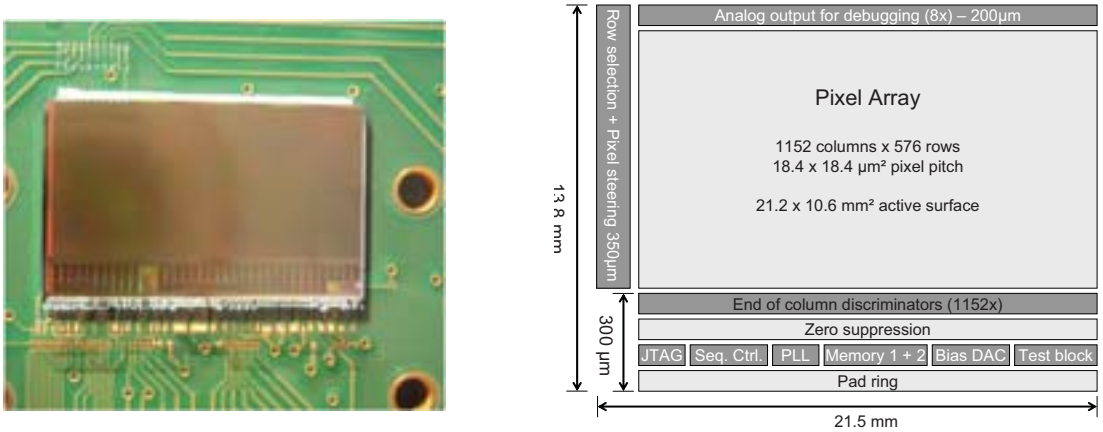


**Figure 4.7:** *Left: Picture of MIMOSA-26. Right: The pixel array is located on the upper part, while the read-out circuitry is situated on the bottom part. Taken from [93].*

devices. In CMOS transistors, the accumulation of positive charges in the oxide gate are responsible for threshold voltage shifts, which increases the leakage current flowing from the transistor drain to the source. This in turn increases the noise of the pixels and reduces the signal-to-noise ratio of MAPS. More details can be found in [88].

In both case, a reduced signal-to-noise ratio leads to a deteriorated detection performance of MAPS, in particular a lower detection efficiency and a higher fake hit rate.

MAPS based on a standard EPI layer are sensitive to non-ionizing radiation [92]. This is due to the fact that signal electrons propagate by thermal diffusion until they reach a collecting diode. Their path length before collection is thus relatively long, which increases the probability that they recombine in the p-EPI layer. In MIMOSA-26, the epitaxial layer features a low resistivity ($\sim 10\ \Omega \cdot$cm). This sensor has shown a moderate tolerance to non-ionizing radiation, to a dose of a few $10^{12}\ n_{eq}/cm^2$ [88].

One of the ideas to improve the tolerance of MAPS to non-ionizing radiation was to decrease the pixel pitch. This reduces the diffusion path length of electrons (see Fig. 3 in Ref. [93]). However, this approach has two drawbacks: the higher the pixel density is, the longer it takes to read out the pixel array (at fixed active area). Additionally, in MIMOSA-26, the presence of a complex signal processing circuitry (amplifier, CDS logic) implemented inside each pixel (imposed by the fast read-out, as mentioned above), does not allow decreasing the pixel pitch to the value which allows achieving a non-ionizing radiation tolerance above $10^{13}\ n_{eq}/cm^2$.

An other strategy to improve the tolerance of MAPS to non-ionizing radiation was to use a high-resistivity epitaxial layer. This has an effect of increasing the depletion region (see Figure 4.5) where the potential gradient sets in, which fasten the charge collection through the electrical drift of electrons. An evolved version of MIMOSA-26, named MIMOSA-26 AHR, was fabricated based on an EPI layer featuring a resistivity of 400 $\Omega \cdot$cm. The performance of MIMOSA-26 AHR was studied in 2011, and has demonstrated a tolerance to a dose higher than $10^{13}\ n_{eq}/cm^2$

[93].

The development of CMOS sensors in the last few years (including MIMOSA-26 and MIMOSA-26 AHR) was based on the 0.35 $\mu$m CMOS technology. This technology features a limited tolerance to ionizing radiation. MIMOSA-26 showed a relatively low tolerance, to a dose above 0.3 Mrad [88]. This relatively poor ionizing radiation tolerance remained with MIMOSA-26 AHR.

Current CMOS sensors meet already some of the MVD requirements, that is: a spatial resolution below 5 $\mu$m, a material budget below 0.3% of $X_0$ and a tolerance to a non-ionizing radiation dose above $10^{13}$ $n_{eq}/cm^2$. However, the time resolution and ionizing radiation tolerance must be improved to match the MVD requirements. The way in which these parameters are going to be improved is discussed below.

**Expected performance of future MAPS**

An evolved version of MIMOSA-26 AHR, named MIMOSIS-1 (expected in 2015), is foreseen to equip the MVD detector for CBM at SIS100 (phase 1, planned for 2017). To achieve a shorter read-out time, the number of pixels per column (read out serially) will be reduced by a factor of two with respect to MIMOSA-26 AHR. A possible layout includes an array of 1536 $\times$ 256 pixels with a pitch of 20 $\times$ 20 (see 4.8). This will allow improving its time resolution down to about 50 $\mu$s. A complementary approach would be to implement elongated pixels in the column direction. This would have the same effect of reducing the number of pixels to read out serially, while keeping the active area (of about 3 $\times$ 0.5 $cm^2$) unchanged. For example, an increase of the pixel pitch (in the column direction) by a factor of two is a possibility considered for MIMOSIS-1. Another conceivable layout includes an array of 1536 $\times$ 128 pixels with a pitch of 20 $\times$ 40 $\mu m^2$. With such a design, a time resolution of $\sim$ 25 $\mu$s would be reachable.

In 2011, the 0.18 $\mu$m technology has been made available for MAPS implementation [100], and future MAPS will be based on such a technology [96]. A smaller feature size will allow for example increasing the number of metal layers (with respect to the 0.35 $\mu$m CMOS process) and improving the interconnections between the pixels and the peripheral read-out electronics. This offers for instance the possibility to read out two rows of pixels at once *. The latter design is intended to improve the time resolution by a factor of two. The array of pixels could also be divided into sub-arrays (in the column direction) read out in parallel. These improvements should allow reaching a time resolution below 10 $\mu$s for the second phase of CBM at SIS300 (phase 2) which will take place a few years later. It is also important to mention that 3D integrated sensors [101] may be a possible solution for the MVD on longer terms, and would allow reaching even faster read-out.

CMOS devices implemented in 0.18 $\mu$m technologies (design plan for MIMOSIS-1) are intrinsically more tolerant to ionizing radiation (with respect to those based on the 0.35 $\mu$m technology). This comes from the fact that processes with smaller feature size use thinner gate oxides. Consequently, the accumulation of net positive charges introduced in the gate oxides by ionizing

*The sensor featuring two comparators ending each column

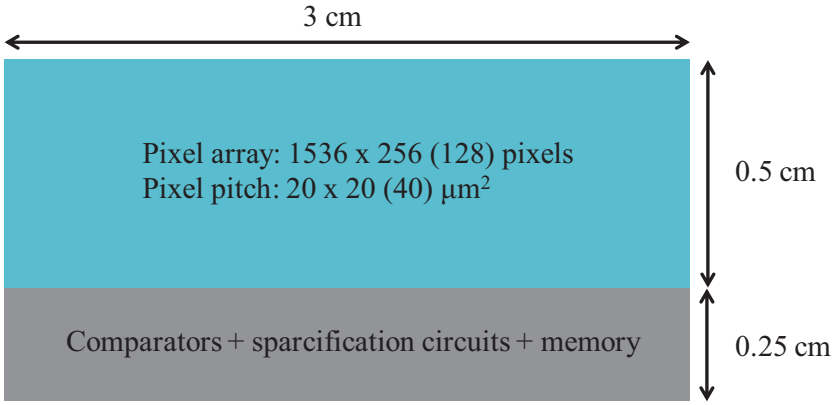


**Figure 4.8:** *Possible geometry of the CMOS sensor MIMOSIS-1, foreseen to equip the MVD. Its active area (blue area) is of* $\sim 3 \times 0.5\ cm^2$*. It has an array of 1536* $\times$ *256 (128) pixels with a pixel pitch of 20* $\times$ *20 (40)* $\mu m^2$*. The gray area indicates the embarked signal processing circuits. The number in parentheses refer to a possible design with elongated pixels (in the column direction).*

radiation is significantly reduced and ionizing radiation-induced effects become less important. It is expected that MIMOSIS-1 will be tolerant to a dose above 3 Mrad. For the phase 2 of the project, this tolerance is likely to be further improved. But as a conservative approach, we can assume that the next CMOS sensor intended to equip the MVD detector will feature a tolerance to an ionizing radiation dose above 3 Mrad. It is worthwhile noticing that the appearance of 3D integrated sensors may improve this tolerance by a factor 10.

As mentioned, the non-ionizing radiation tolerance of current MAPS already matches the CBM requirement: a tolerance to a dose above $10^{13}\ n_{eq}/cm^2$ achieved with MIMOSA-26 AHR. Nonetheless, further improvements are expected with future CMOS sensors. As a conservative approach one can assume that MIMOSIS-1 will be as radiation tolerant as MIMOSA-26 AHR (e.g., to a dose of $10^{13}\ n_{eq}/cm^2$), and a tolerance to a dose three times larger for CMOS sensors for the second phase of the experiment. The use of 3D integrated sensors on longer terms might also improve this tolerance above $10^{14}\ n_{eq}/cm^2$.

The future performance of MAPS sensors are summarized in Table 4.4. They are compared with the MVD requirements at the SIS100 and SIS300 synchrotrons. The operation of the first accelerator is scheduled for 2017. Note that at energies that will be reached at SIS100 (up to about 10 GeV/nucleon for impinging Au ions and about 30 GeV for impinging protons), open charm will be measured in p + p and p + A collisions. This measurement is crucial to serve as a reference for the charm data which will be collected in A + A collisions. Table 4.4 gives the detector requirements for p(30 GeV) + Au and Au(25 AGeV) + Au collisions.

For the p(30 AGeV) + Au case, the requirement in terms of spatial resolution and material budget are assumed to be the same as in the Au + Au case. The radiation doses received by the MVD were simulated with the transport code FLUKA [79]. At $10^6$ collisions/s [104], the most exposed parts of the MVD are expected to receive ionizing and non-ionizing doses of $10^4$ rad and 7 $10^{11}$

| | MVD requirements | | MAPS performance | |
|---|---|---|---|---|
| | SIS100 (2017) | SIS300 | 2015 | $\geq$ 2018 |
| Spatial resolution [$\mu$m] | $\leq 5$ | $\leq 5$ | < 5 | < 5 |
| Material Budget [$X_0$] | $\leq 0.3\%$ | $\leq 0.3\%$ | 0.05% | 0.05% |
| Ion. rad. hard. [Mrad] | $10^{-2}$ | > 3 | $\geq 3$ | $\geq 3$ |
| Non-ion. rad. hard. [$n_{eq}/cm^2$] | $7 \times 10^{11}$ | > $10^{13}$ | > $10^{13}$ | $\sim 3 \times 10^{13}$ |
| Time resolution [$\mu$s] | < 100 | < 10 | 25 - 50 | < 10 |

**Table 4.4:** *MVD requirements for the first phase of CBM at the SIS100 synchrotron (operation scheduled for 2017) and for the second phase at the SIS300 synchrotron. These requirements are given in the case of p + Au and Au + Au collisions at a collision rate of* $10^6$ *collisions/s and* $10^5$ *collisions/s respectively, and for a station located at 5 cm from the target. The material budget is expressed in terms of percentages of the radiation length ($X_0$): the requirement accounts for a complete MVD station (including support structure, cables etc), while the MAPS performance accounts for the sensor alone. The future performance of MAPS is also given.*

$n_{eq}/cm^2$, respectively. The requirement in terms of time resolution (below 100 $\mu$s) is intended to limit the collision pile-up below 100 collisions. This would be sufficient considering the much smaller hadron multiplicities with respect to those expected in Au + Au collisions [104].

On can see in Table 4.4 that the expected performance of MAPS in 2015 fulfills the MVD requirements at SIS100. The MAPS performance expected in 2018 or later also matches the MVD requirements for the second phase of the experiment at SIS300.

## 4.5 MVD design considerations

The integration of MAPS into a complete MVD is currently the object of intense activities carried out by the CBM-MVD Collaboration, involving in particular the Institut fuer Kernphysics (IKF) at the Goethe Universitaet/Frankfurt and the Institute Pluridisciplinaire Hubert Curien (IPHC) in Strasbourg. The integration of MAPS is driven by the following requirements: the MVD stations must have a sensing area fully covering the CBM acceptance, their material budget (in the CBM acceptance) must be low (below 0.3% of $X_0$) while featuring a sufficient stiffness (mandatory for high vertex accuracy), and they must operate in a vacuum of around $10^{-3}$ mbar (to limit the multiple scattering a charged particles with air molecules).

A detailed optimization of the MVD detection set-up is currently on-going [74]. Three typical locations are currently considered for the MVD stations: at 5, 10 or 15 cm downstream the target. Existing feasibility studies (see Ref. [75], [76], and Chapter 6 of the present thesis) have demonstrated that a first MVD station located at distances from 5 to 10 cm downstream the target, and a second one positioned from 10 to 20 cm, are suitable for open charm measurements in Au + Au collisions. The second station may be placed further than 10 cm away from the target

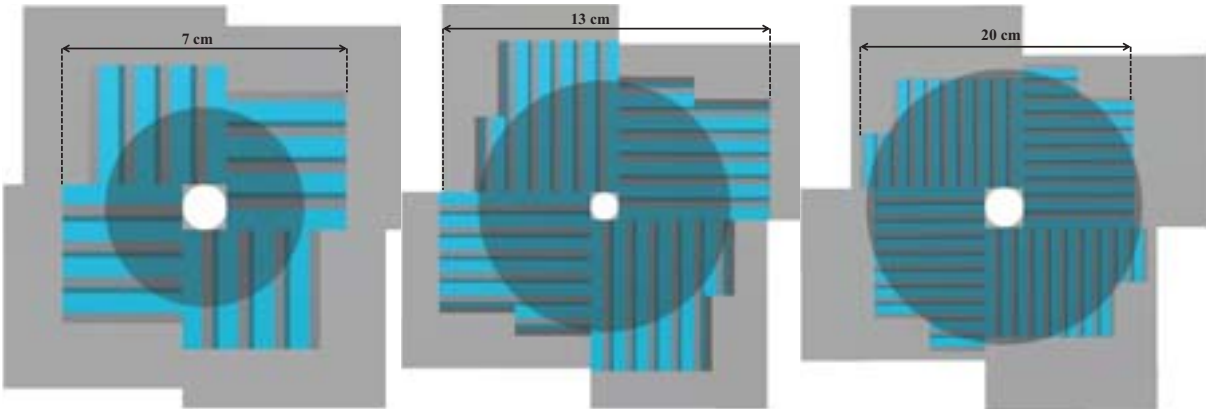


**Figure 4.9:** *Layouts of the MVD stations (front side) located at 5 cm (left), 10 cm (middle), and 15 cm (right) from the target [103]. The stations are equipped with the MIMOSIS-1 sensors (see Figure 4.8). The shaded disk area indicates the CBM acceptance. The gray area shows the support structure.*

| Distance from the target [cm] | 5 | 10 | 15 |
|---|---|---|---|
| Inner radius [cm] | 0.22 | 0.44 | 0.66 |
| Outer radius [cm] | 2.3 | 4.6 | 6.9 |

**Table 4.5:** *Inner and outer radii corresponding to the CBM acceptance (a laboratory polar angle in the range from 2.5 to 25 degrees), as a function of the distance from the target.*

to improve the track matching between the MVD and the STS [74], e.g., at a distance of 15 cm. Alternatively, this improvement could also be obtained by adding a third MVD station.

At each of these distances, the CBM acceptance can be represented by a disk. This disk is depicted in Figure 4.9 (shaded areas) for the three possible locations of the MVD station. The inner and outer radii of this disk are given in Table 4.5.

The design of the MVD foreseen at SIS100 is based on MIMOSIS-1 sensors. Figure 4.9 shows the layout of MIMOSIS-1 sensors for the three possible locations of the MVD station [103]. First, this layout allows covering the CBM acceptance. Note also that each station has sensors equipped on the front and back sides (see Figure 4.10). This is mandatory to cover 100% of the CBM acceptance, considering that a part of the sensor area is occupied by read-out electronic circuits (see Figure 4.8).

Cables are needed to transfer the data from the sensor to a front-end read-out board located outside the detector acceptance (also to power-up the sensors, etc). The sensors must be cooled to limit the radiation-induced increase of their leakage current. This, and the fact that they must operate in vacuum, calls for an efficient and compact cooling system. All these elements must be stabilized with a support structure. These requirements must be fulfilled while keeping the material budget of each station (including sensors, cables, cooling system and support structure)

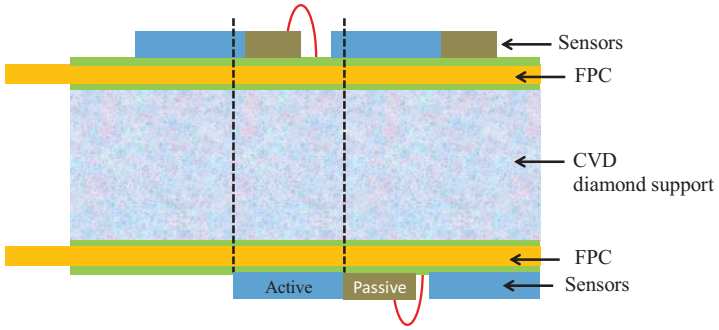


**Figure 4.10:** *Cross-sectional design of MVD stations [114]. The CVD based layer serves as mechanical and cooling support, on which read-out Flex Print Cables (FPC) and MIMOSIS-1 sensors are glued. The active (blue) and passive (gray) area of the latter are shown. The sensors are connected to FPC by wires (red lines).*

below 0.3% of $X_0$.

Figure 4.10 shows the cross-sectional view of one part of the MVD station [114]. The CVD* diamond is planned to be used as a material offering a solid mechanical support for the MVD sensors and the read-out Flex Print Cables (FPC). Moreover, due to an excellent heat conductivity, the CVD diamond will ensure the heat evacuation from the MVD sensors. The FPC and sensors will be glued on both sides on the CVD diamond support and wire-bonded to one another (red bow).

The material budget of the MVD stations has been derived accounting for the CVD diamond support, the FPC cables, the sensors, and the different layers of glue. For these estimations, it is considered that MAPS are thinned down to 50 $\mu$m (see Section 4.4). Note that, for stations located at 10 and 15 cm from the target (where more sensors are used) the thickness of the CVD diamond support is increased to improve the heat evacuation. Additionally, at these distances, the estimation of the material budget accounts for thicker FPC cables (embedding more metal traces for signal transmission in order to connect more sensors). In the detector acceptance, the estimated material budget of the MVD stations is of 320 $\mu$m, 545 $\mu$m and 730 $\mu$m of silicon equivalent at distances of 5, 10 and 15 cm from the target [80]. This corresponds to about 0.34%, 0.58%, and 0.78% of $X_0$, respectively.

The material budget of the present design does not match the detector requirements yet. The design of the MVD detector presented above is the first step of future developments aiming at reducing the thickness of MVD stations to meet the MVD requirement (a material budget per MVD station below 0.3% of $X_0$).

*CVD stands for Chemical Vapor Deposition type

# Chapter 5

# Hit rate and data rate capability of the MVD sensors and of their read-out system

The goal of the study is to estimate the hit rate and data flow that MVD sensors and the read-out system will have to sustain during CBM operation at the SIS100 synchrotron (operation scheduled for 2017). This will allow determining the requirements for the sensor which will equip the MVD at SIS100, namely MIMOSIS-1, in terms of hit * rate capability and output bandwidth for its embedded read-out electronics circuits. The requirements in terms of data rate capability for the read-out system is also addressed.

First, the motivations for using the MVD in CBM at the SIS100 synchrotron are briefly discussed (Section 5.1). The inputs needed for the present study are shortly introduced (Section 5.2), followed by a more detailed description of these prerequisites: the beam running conditions (Section 5.3), the expected features of MIMOSIS-1 (Section 5.4) and the current concept of the MVD read-out system (Section 5.5). The simulation procedure is presented in Section 5.6, followed by the definition of the observables (based on the output of the simulations) used to determine the data rate requirements for MIMOSIS-1 and for the MVD read-out system (Section 5.7). The detector setup, along with an optimization study aiming at reducing the contribution of background particles to the hit density in MVD stations, are presented in Section 5.8. The data rate requirements for MIMOSIS-1 and for the MVD read-out system are finally presented and discussed (Section 5.9).

## 5.1 Motivations

As seen in the previous chapter, open charm will be measured in p + p and p + A collisions at SIS100. In A + A collisions, at the maximal reachable beam energy (up to about 10 AGeV in Au + Au collisions), the predicted multiplicity of open charm particles is extremely small, likely be-

*A hit is defined as the intersection of a particle trajectory with the sensitive area of the detector

yond the detection capability of CBM. More abundant particles than open charm particles will be measured in A + A collisions at SIS100, in particular multi-strange hyperons ($\Xi$, $\Omega$, $\Lambda$) by reconstructing their weak decay vertex, and low-mass vector mesons ($\rho$, $\omega$, $\phi$) through their di-electron decay channels [104]. Note that for these measurements, the MVD detector may also be used: this could provide accurate vertexing for hyperon measurements (similarly as for open charm) and high accuracy impact parameter reconstruction for low-mass vector meson measurements to reduce the large background of electron-positron pairs (dominated by conversion of $\gamma$'s coming mostly from $\pi^0$ decays). The latter can be partly suppressed by removing electron-positron pairs with small opening angles [105].

The CBM physics program envisaged at the SIS100 synchrotron is an experimental challenge, since high and inhomogeneous hit densities are expected to be received by MIMOSIS-1 sensors, as it will be seen later. It is thus crucial to estimate the hit rate and data flow that their internal circuits will have to handle (in particular those of the most exposed sensors). Additionally, a large number of sensors will have to be read out by the read-out system, and a large and highly inhomogeneous data flow is expected to be delivered by MIMOSIS-1 sensors.

In this work, we investigated the cases of the heaviest p + A and A + A systems at the highest beam energies foreseen at SIS100: p(30 GeV) + Au and Au(10 AGeV) + Au collisions.

## 5.2 Inputs of the simulations

To simulate the hit rate and data flow in the MVD sensors and in their read-out system, one needs several inputs:

- the beam conditions: collision rates, beam emittance and intensity fluctuations;
- the sensor characteristics: active area, read-out time, response to charged particles, fake hit rate, and data sparsification performed by the on-chip electronics;
- the read-out system characteristics: data processing and data path.

These three items are developed in the next sections.

## 5.3 Beam conditions

The considered collision rates are presented and discussed. The beam emittance and intensity fluctuations expected at the SIS100 synchrotron have also been accounted for. These latter two features of the beam rely on those measured at the existing SIS18 facility (see Section 3.1).

### 5.3.1 Collision rates

In p + Au collisions, simulation studies suggest that a collision rate of a few $10^6$ collisions/s would allow reconstructing open charm particles with good statistics [104]. In this work, we considered a collision rate of, e.g., $2 \times 10^6$ collisions/s. In Au + Au collisions, the issue of the collision rate is less critical at SIS100, as compared with the very demanding one at SIS300 for open charm measurements. In the absence of trigger signature, hyperon measurements will be performed at the data archival rate of $2 \times 10^4$ collisions/s. This was the number we assumed in the present work. Such a collision rate is expected to allow measuring hyperons with high statistics [104].

At these collision rates, the radiation doses do not exceed the expected tolerance of MIMOSIS-1. The latter is expected to withstand non-ionizing and ionizing doses above $10^{13}$ $n_{eq}/cm^2$ and 3 Mrad, respectively (see previous Chapter). The radiation doses received by the MVD were simulated for p(30 AGeV)-Au and Au(10 AGeV) + Au collisions with the transport code FLUKA [79]. $\delta$-electrons produced by beam ions traversing the target were taken into account in the Au + Au case (similarly as explained in Section 4.2.1). CBM will have an effective run period (i.e. beam on target) of about two months per year (see Section 3.1), after which it is planned to replace the most exposed MVD sensors. At the collision rates mentioned above, the latter sensors are expected to be exposed to radiation doses (at 5 cm from the target) of $2 \times 10^4$ rad and $1.4 \times 10^{12}$ $n_{eq}/cm^2$ ($1.2 \times 10^5$ rad and $10^{12}$ $n_{eq}/cm^2$) in p + Au (Au + Au) collisions. One can see that the projected tolerance of MIMOSIS-1 to radiation offers very comfortable security margins.

Note, however, that in the p + Au case, the collision rate will be rather limited by the collision pile-up that the MVD can tolerate, considering the expected read-out time of MIMOSIS-1 sensors (of 25-50 $\mu$s, as discussed in Section 4.4).

### 5.3.2 Beam intensity fluctuations

The beam intensity fluctuations can cause large fluctuations of the collision pile-up in MVD sensors, which directly affects the hit densities reached in them.

Figure 5.1 presents the results of a beam diagnostic performed by the HADES experiment at the SIS18 synchrotron [110], using a beam of Argon (Ar) ions at a bombarding energy of 1.75 GeV/nucleon. The left-hand side panel shows the distribution of the number of ions crossing the detector per time interval of 1 ms. The right-hand side panel shows the dependence of such distribution with the time interval considered, in particular its ratio average-to-maximum (green squares). One can see that a ratio maximum-to-average equal to 3 is achieved with a time binning of 1 ms. At smaller time interval, a slight increase of this ratio is observed due to increased random fluctuations: up to 3.5 for a time binning of 10 $\mu$s. The random fluctuations depend on the average number of ions crossing the detector. As mentioned, a beam intensity of $2 \times 10^6$ Au ions/s is foreseen at SIS100. Considering a read-out time for MIMOSIS-1 of 25 $\mu$s, we thus expect that about 50 Au ions will cross the target on average, per sensor read-out cycle.

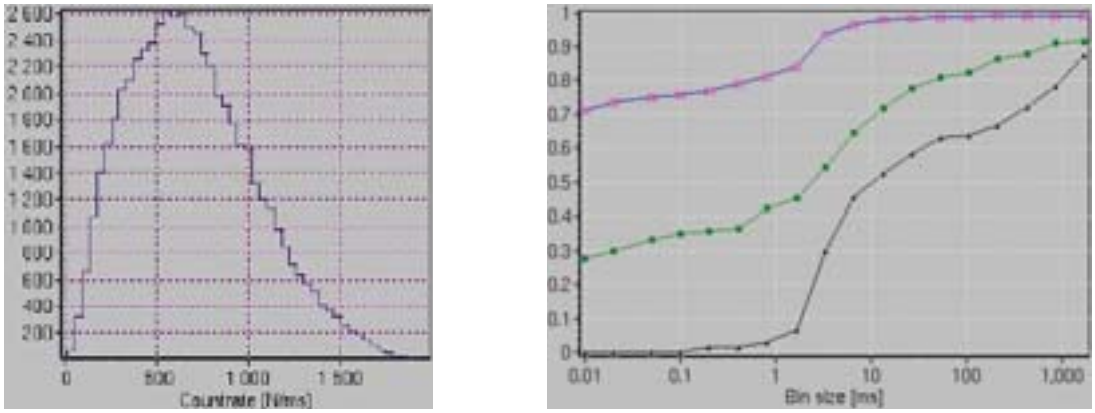


**Figure 5.1:** *HADES beam diagnostic performed at the synchrotron SIS18 with $Ar^{18+}$ at a beam energy of 1.75 GeV/nucleon [110]. Left-hand side: distribution of the number of particles crossing the detector per time interval of 1 ms. Right-hand side: minimum-to-average ratio (black triangles) and average-to-maximum ratio (green squares) of the distribution shown on the left-hand side, as a function of time binning (from 10 $\mu$s to 1s).*

Considering that an average particle flux of 7.5 $10^5$ Ar ions/s was used by HADES, the same average number of Ar ions crossing the detector is obtained for a time binning of $\sim$ 70 $\mu$s. At such time interval, the ratio maximum-to-average of the number of ion counts is of $\sim$ 3.

Beam diagnostics have also been performed by the HADES experiment for a proton beam at 3.5 GeV [111]. With a flux of $10^4$ particles/s and a time interval of 1 ms, a ratio maximum-to-average of the number of ion counts equal to 6 was observed. In such conditions, 40 protons on average were imping the detector per time interval. At a beam intensity of $2 \times 10^8$ protons/s (envisaged at SIS100), we thus expect that 5000 protons will cross the target on average per read-out cycle of MIMOSIS-1. In terms of beam intensity random fluctuations, the situation is thus favored at SIS100 compared with the HADES beam diagnostic running conditions.

There is currently no rigorous extrapolation of the beam intensity fluctuations from SIS18 to SIS100. According to [111], a ratio maximum-to-average of the beam intensity of 10 is a safe assumption for both proton and Au ion beams at SIS100. This is the number which we assumed in this work.

Note that the beam will be tuned to feature an intensity as homogeneous in time as possible, notably for the purpose of CBM. Furthermore, the envisaged slow extraction of the beam from SIS100 to the CBM beam line should improve its temporal homogeneity. Thus, the case of an improved homogeneity of the beam intensity was also investigated, assuming for it a ratio maximum-to-average of 3 for both proton and Au ion beams.

The implementation of the beam intensity fluctuations in the simulations is explained in Section 5.6.3.

### 5.3.3 Beam emittance

The beam emittance can cause an increase of the hit density in the MVD detector. It has been accounted for, based on the beam emittance measured at SIS18 (see Appendix A). Briefly, to extrapolate the beam emittance to beam energies reachable at SIS100, adiabatic damping of the beam is assumed. This allows the emittance to be scaled with the inverse of the beam rigidity. According to geometrical arguments (aperture of the focusing magnet and its distance to the CBM apparatus), the beam divergence will be very small at the CBM target, of about 2 mrad (in both X and Y directions). Given the estimated emittance of the beam at this point, the spatial spread of the beam in the X and Y directions is expected to be of about 1 mm and 0.33 mm, respectively, in the case of a Au ion beam (it is smaller in the case of a proton beam). This is much smaller than the inner hole of MVD stations, which size is currently of 5.5 mm [102]. In Appendix A, it is also shown that the beam emittance expected at SIS100 has a small effect on the number of hits created in the MVD.

For the sake of completeness, the beam divergence and spatial spread mentioned above were included in the simulations. This was done by distributing beam ions randomly in the (transverse) spatial-momentum phase space, according to the beam emittance (see Figure A.1). Note that beam particles have straight trajectories in the simulations, we thus neglected the effect of intra-beam scattering.

## 5.4 Sensor characteristics

The focus is made on the sensor characteristics which are relevant for data rate studies:

- the sensor active area and read-out time;
- the sensor response to the passage of charged particles and dark noise;
- the data sparsification strategy employed by of its embedded electronics to reduce the volume of data to transmit.

We assumed the characteristics of the sensor MIMOSIS-1 (see previous chapter). MIMOSIS-1 will be the successor of the existing, and validated, MIMOSA-26 sensor [90]. As a conservative approach, the first two characteristics (first item) are extrapolated from those of MIMOSA-26, assuming shorter columns of pixels and, as a result, faster read-out (as explained in the previous Chapter). The next two characteristics (second item) are based on the data collected with MIMOSA-26. Finally, we assumed the same data sparsification strategy for MIMOSIS-1 as performed by MIMOSA-26.

The issues listed in the first item are discussed in Section 5.4.1. The ones listed in the second item are addressed in Sections 5.4.2 and 5.4.3. Finally, Section 5.4.4 is devoted to the last issue.

### 5.4.1 Sensor active area and read-out time

In the study we assumed the expected features of MIMOSIS-1: an active area of about 3 $\times$ 0.5 $cm^2$ and a read-out time of 25 $\mu$s (see Section 4.4). Note that this read-out time would be reached by designing elongated pixels (in the column direction), with a pitch of 20 $\times$ 40 $\mu m^2$. A sensor with a pixel pitch of 20 $\times$ 20 $\mu m^2$ (thus having a read-out time of 50 $\mu$s) would experience the same constraint in terms of hit rate for its data sparsification circuits. To understand this, let us recall that the sparsification circuits read pixels row per row (see section 5.6.5), and the number of hits in one row of pixels is accumulated over the read-out time of the sensor. Thus, the number of hits read out by the sparsification circuits scales approximately with the area of one row of pixels ($A_{row}$) times the read-out time of the sensor ($T_p$). Decreasing the pixel pitch along a column by a factor of two has two compensating effects: an increase of $T_p$ and a decrease of $A_{row}$, both by the same factor. Additionally, both scenarii (pixel pitch of 20 $\times$ 40 or 20 $\times$ 40 $\mu m^2$) lead to the same requirement in terms of output bandwidth for the sensor: there are more hits accumulated in the sensor over a longer read-out time, but at the same time, there is more time to transmit the information on those hits outside the sensor. However, an increase of the read-out time by a factor of two requires about two times more memory cells embedded in the sensor. This aspect will be discussed later (see Section 5.9).

### 5.4.2 Sensor response to the passage of charged particles

The response of the sensor to the passage of charged particles is defined as the number of fired pixels * per particle hit. Hence, it affects the amount of information which has to be processed by the data sparsification circuits. It also impacts the data volume generated over the full sensor, and thus the required size of its embedded memory and its output bandwidth. The figure 5.2 shows the fired pixel multiplicity per hit (or cluster size) measured in the MIMOSA-26 sensor† [90]. Note that the higher the threshold applied to exclude unfired pixels (this threshold depends on the dark noise of pixels), the smaller the cluster size will be. The latter is observed to be equal to 3 or 4 fired pixels on average, whether a threshold equal to 6 or 5 times the noise is applied, respectively.

In this study, we assumed the same response for MIMOSIS-1 as measured for MIMOSA-26: an average cluster size of 4 fired pixels.

The results shown in Figure 5.2 are obtained for incident tracks (perpendicular to the detector plane). One must account for the many different impinging angles which particles can have, when crossing MVD sensors. They could cross and deposit charge in several pixels, which would have an effect of enlarging the average cluster size.

Figure 5.3 shows the probability of the number of pixels crossed per impinging particle in Au(10 AGeV) + Au collisions (simulation procedure described in Section 5.6.1). We assumed

*Pixels with a voltage signal above the applied threshold, see Section 4.4

†Unirradiated

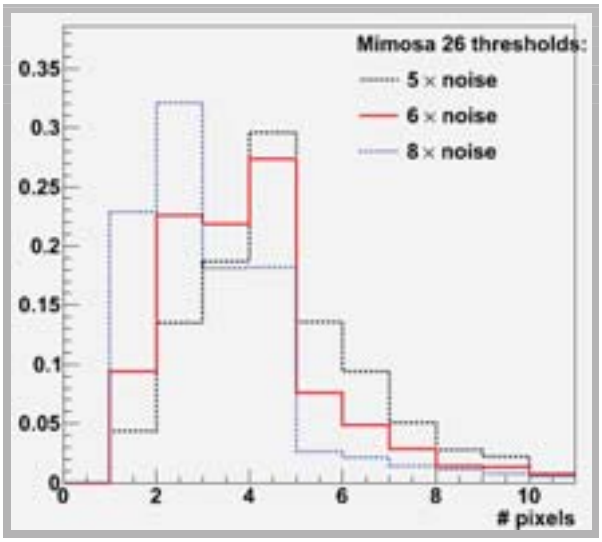


**Figure 5.2:** *Fired pixel multiplicity per hit (see text) measured in the MIMOSA-26 sensor [90].*

for MIMOSIS-1 an epitaxial layer thickness of 15 $\mu$m. The black histogram shows the contribution of Au + Au collisions, while the red one shows the contribution of $\delta$-electrons created in the target by beam ions (see Section 5.6.2). One can see that $\delta$-electrons cross on average more pixels than primary particles. This comes from the fact that most of them have low momenta and are strongly deviated by the magnetic dipole field of CBM. Note, however, the logarithmic scale on the vertical axis. Only 1.26 (1) pixels are crossed, on average, by $\delta$-electrons (primary particles). The reason is that the epitaxial layer of MIMOSIS-1 is assumed to be very thin. One can see that the finite angle of incident tracks can be neglected.

### 5.4.3 Fake hit rate

Fake hits are selected unfired pixels, i.e. their voltage signal is accidentally above the applied threshold (see Section 4.4) due to the presence of several sources of noise (thermal noise, capacitive noise of read-out electronics, etc). The fake hit rate has to be kept much below the rate of hits created by the passage of charged particles (or real hits). The average rate of real hits, defined as the number of hits received per pixel and per read-out cycle, is of the order of $\sim 10^{-3}$ at a distance of 5 cm from the target in Au(10 AGeV)-Au collisions (considering a collision rate of 20 kHz, see Section 5.9.1). Hence, the average fake hit rate (per pixel and per read-out cycle) must be kept typically below $10^{-4}$.

The figure 5.4 presents the detection efficiency (ratio between selected fired pixels and the total amount of fired pixels) as a function of the average fake hit rate (per pixel and per read-out cycle). These results were obtained for the sensor MIMOSA-26 AHR (featuring a high resistivity epitaxial layer, as explained in the previous Chapter) [94]. This sensor was tested while being either un-irradiated or irradiated, up to a non-ionizing (ionizing) dose of $10^{13}$ $n_{eq}/cm^2$ (300 kRad).

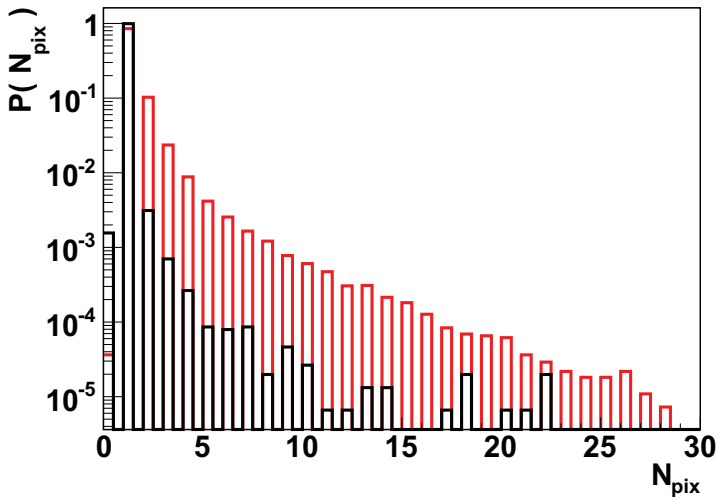


**Figure 5.3:** *Probability of the number of pixels crossed per impinging particle ($N_{pix}$) in Au(10 AGeV) + Au collisions, assuming a 15$\mu$m thick epitaxial layer for MIMOSIS-1. The black histogram shows the contribution of Au + Au collisions, while the red histogram shows the contribution of $\delta$-electrons knocked out of the target by beam ions.*

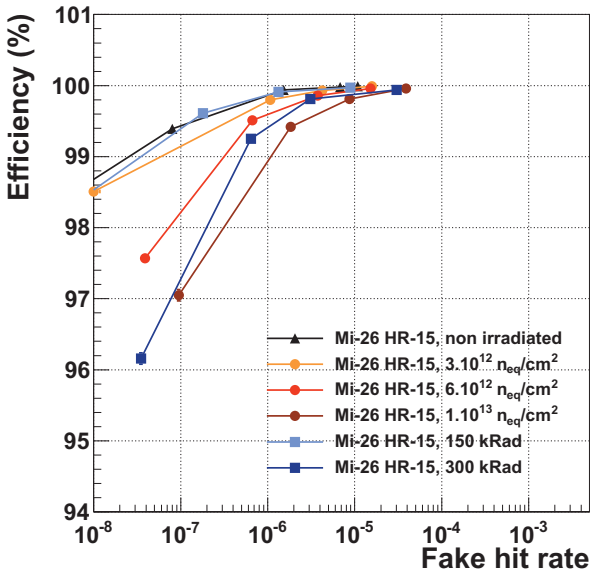


**Figure 5.4:** *Detection efficiency versus average fake hit rate (per pixel and per read-out cycle), measured in the MIMOSA-26 AHR sensor (featuring a high resistivity epitaxial layer), after several irradiation doses: up to $10^{13} n_{eq}/cm^2$ or 300 kRad [94]. The different points obtained for a given irradiation dose were acquired by varying the threshold voltage (the latter is used to select fired pixels).*

Note that the effect of these two types of radiation was investigated separately. The different points obtained for a given irradiation dose were acquired by varying the threshold voltage. For example, lowering this threshold (going from the left-end to the right-end side of the lines in the figure) has two effects: it increases the detection efficiency, but at the same time enhances the fake hit rate. The required detection efficiency is commonly of 99.5%. It is reached for an average fake hit rate of around $1 \times 10^{-6}$ ($3 \times 10^{-6}$), after an irradiation of $10^{13} n_{eq}/cm^2$ (300 kRad).

We assumed an average fake hit rate (per pixel and per read-out cycle) for MIMOSIS-1 of $10^{-4}$. This is 2 orders of magnitude higher than the one measured in the irradiated MIMOSA-26 AHR sensor. This choice was motivated by the fact that this sensor has been irradiated with non-ionizing and ionizing radiation doses separately. Thus, the results presented in Figure 5.4 do not account for combined radiation damages (see ref. [94] for details). Note also that this fake hit rate corresponds to the tolerable one, with respect to the expected rate of real hits in MVD sensors (as mentioned above).

### 5.4.4 On-chip data sparsification

We assumed that the on-chip electronics of MIMOSIS-1 will employ the same data sparsification strategy (see Section 4.4) as used by the one of MIMOSA-26. This data processing is meant to reduce the volume of data generated in the sensor, and which has to be transmitted.

Figure 5.5 shows the functionality blocks of the read-out electronics embedded in the MIMOSA-26 sensor. Each column of pixels is terminated by a discriminator (A/D), which provides a binary information of the type fired/unfired pixels. The matrix of pixels is scanned row by row (or column parallel), and groups of up to 4 consecutive fired pixels in a row are formed. Unfired pixels are thus suppressed from the data stream. This processing is referred to as zero-suppression. It is performed by a $\mu$-circuit referred to as SUZE-01 [98], located on the periphery of the sensor. Hereafter, groups of up to 4 consecutive fired pixels in a row are referred to as states (a more technical definition will be given later).

Each row of pixels is read every 200 ns (this comes from the pixel read-out frequency, of 5 MHz in MIMOSA-26). Due to this time constraint, the number of states which can be formed is limited. As one can see in Figure 5.5, the part of SUZE-01 which forms the states is divided into separate "Sparse Data Scan" modules [97]. Each of these modules processes a sub-group of the row of pixels, typically of 64 pixels (referred to as bank), and can form up to N states (per row and per bank). There are 18 banks in MIMOSA-26 (which features rows of 1152 pixels), while there will be 24 of them in MIMOSIS-1 (which will feature rows of 1536 pixels). The multiplexing stage then selects up to M states among the ones formed by all banks.

As seen in Section 5.4.2, we assumed an average cluster size of 4 fired pixels in MIMOSIS-1. As a conservative approach, we assumed these fired pixels to be systematically located in 3 different rows, i.e. given the row number r where the seed pixel (pixel showing the highest charge in the cluster) is located, 3 states per hit are thus created, at row number r-1, r and r+1 (see Figure 5.6).

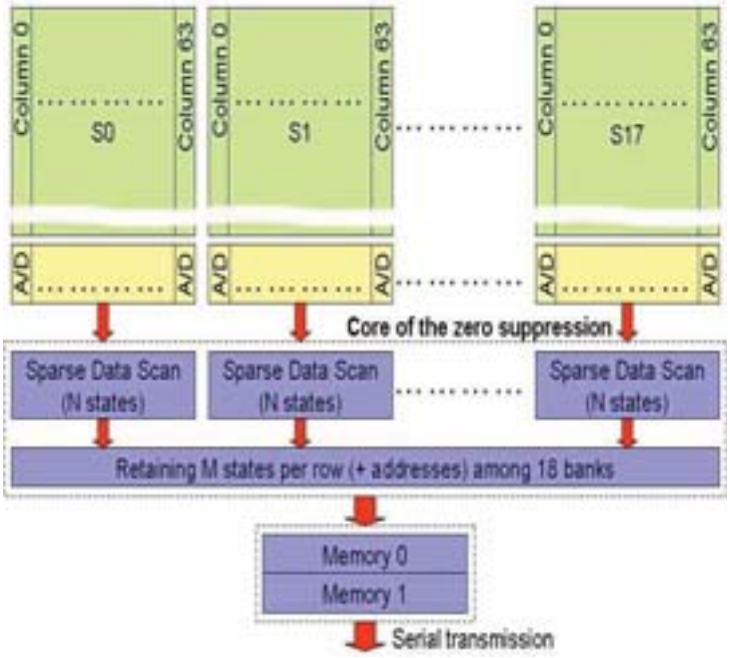


**Figure 5.5:** *Functionality blocks of the read-out electronics embedded in the MIMOSA-26 sensor (taken from Ref. [97]).*

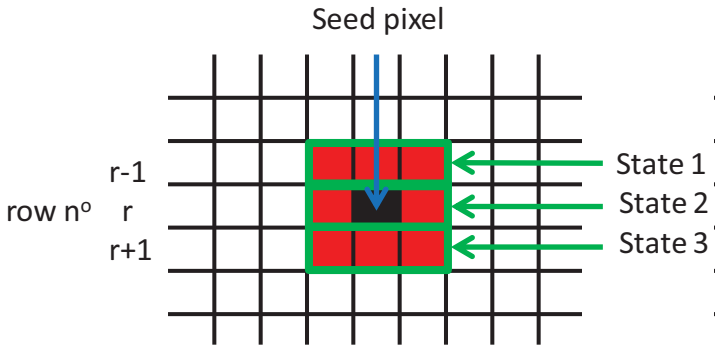


**Figure 5.6:** *Sketch showing the seed pixel (black), the first corona of pixels around it (red), and the 3 states which are assumed to be formed for each hit (green).*

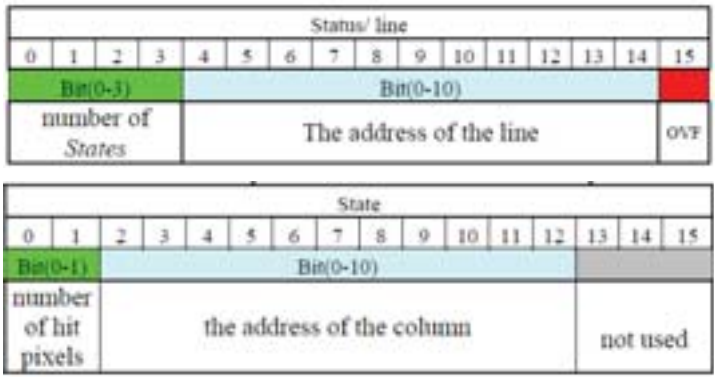


**Figure 5.7:** *Data format delivered by the sensor MIMOSA-26 (taken from Ref. [97]). It contains the address of the first fired pixel within a row and the number of consecutive fired neighbor pixels, in the form of a so-called "state". Every state within one row shares the same row address, encoded in the form of a so-called "status/line" (see text for details).*

In MIMOSA-26, N = 6 states and M = 9 states. Based on such performances, current predictions for MIMOSIS-1 are: N = 6 states and M = 40 states. This corresponds to a tolerable hit occupancy (per pixel and per read-out cycle) above 2.6% within a full row of pixels, and above 9.4% within a bank. Note that the tolerance of the sensor to the hit rate is locally higher. This is meant to account for the fact that the fluctuations of the hit rate is higher at smaller area scales. Given the expectingly large and highly fluctuating hit rates that MVD sensors will have to handle, it is crucial to determine the required number of states (N and M) that the sparsification circuits of MIMOSIS-1 must be able to form.

### Data format

Figure 5.7 shows the data format delivered by MIMOSA-26 [97]. It contains the information related to fired pixels in the form of states, as mentioned above (see bottom part of the figure). A state is a 16-bit word containing the address of the first fired pixel within a row (encoded in 11 bits), and the number of consecutive fired neighbor pixels (encoded in 2 bits), plus additional bits made available for the user specific needs. Every states within one row share the same row address. This latter is encoded in a header (status/line), in 11 bits (see upper part of the figure). The number of states formed in the row is encoded by the first four bits of this header, while the last bit is just a termination.

We assumed that the same data format will be provided by MIMOSIS-1.

### Sensor data transmission

The states (see above) are stored in an embedded memory, to be transfered serially to the front-end electronics. Note in Figure 5.5 the presence of two memory banks: "Memory 0" is meant

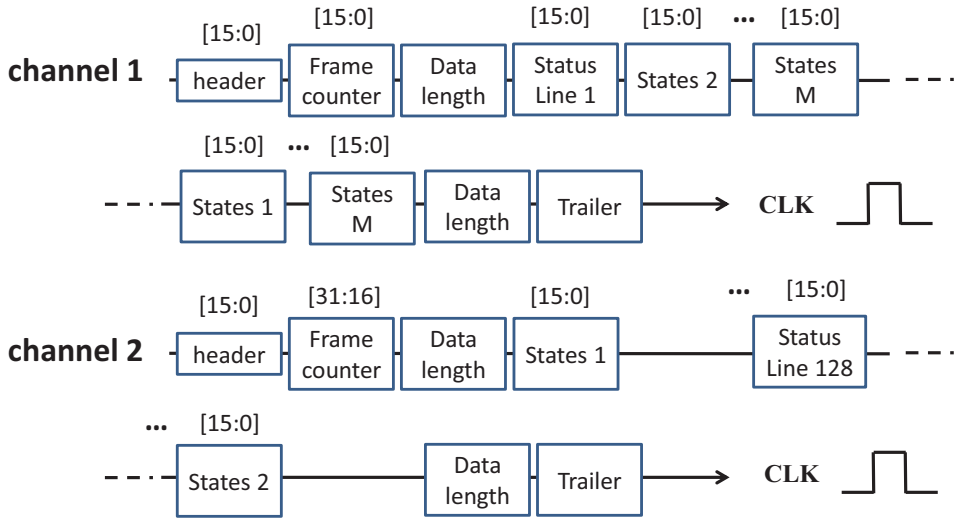


**Figure 5.8:** *Data flow delivered by the two output channels of the sensor MIMOSA-26 (taken from Ref. [97]).*

to register the state information of the current frame*, while "Memory 1" is used to transmit the state information of the previous frame.

MIMOSA-26 delivers its data via two serial output channels. Figure 5.8 shows the data flow delivered by them. The words "header", "frame counter", "data length", "status line", "states" and "trailer" are delivered serially. Header contains markers meant essentially to detect the beginning and the end of a frame. This information is repeated identically in both output channels. Frame counter is the number of frames since the chip was reset. To allow for an unique identification for more than four billion consecutive frames, this information is encoded into 32 bits, the LSB† and MSB‡ being transmitted by channel 1 and 2, respectively. Data length is the number of useful data words of 16 bits. For the sake of synchronizing the data stream provided by different sensors (thus receiving different amount of hits), the volume of data delivered by them is fixed. This data volume is constrained by the necessary information that the sensors located in the maximal hit density region have to deliver. Zero's are added for those located in low hit density regions, or because of beam intensity fluctuations. Data length is encoded in 32 bits, the LSB and MSB being transmitted by channel 1 and 2, respectively. Finally, status lines and states contain hit information, as explained earlier. They are transmitted by both output channels in a $1 \rightarrow 2 \rightarrow 1 \rightarrow 2$ mode. We assumed the same structure of the output data flow of MIMOSIS-1.

Each output line of MIMOSA-26 can transmit up to 80 Mbits/s of information, which leads to a total acceptable data flow of 160 Mbits/s [97]. Two output lines are also expected for MIMOSIS-1. Each is predicted to be able to transmit either 200 or 400 Mbits/s of information (mostly

*A frame is a two-dimensional map of the charge collected by all pixels in the sensor. It takes one read-out cycle for the sensor to read one frame

†Less Significant Bit

‡More Significant Bit

depending on the performance of the on-chip output drivers). This leads to a total acceptable data flow of 400 - 800 Mbits/s. It is crucial to determine whether this output bandwidth allows tolerating the rate of hits received by the MVD. It is also essential to evaluate the data volume that the MIMOSIS-1 sensors accumulate during one read-out cycle. This constrains the minimal capacity required for its embedded memory cells (Memory 0 and Memory 1).

## 5.5 Read-out system of MVD sensors

The read-out system of MVD sensors is currently being designed and prototyped at the Institut fuer Kernphysik in Frankfurt. It is a free-streaming system: given the read-out cycle of MAPS sensors, the latter will deliver frames (containing real hits) continuously. A detailed description can be found in References [113] and [112]. The current design for the MVD detector which will operate at SIS100 is the following:

- the read-out system is constituted of several identical read-out chains (see Figure 5.10), shipping the data from a flexible amount of sensors;

- one read-out chain is connected to MVD sensors through a thin Flex-Print Cables (FPC). FPC cables are present in the acceptance of CBM (see Figure 5.9). The requirement of low material budget in the CBM acceptance imposes a constraint on the affordable amount of metal layers implemented in these cables for signal transmission. In the current design of the read-out system, FPC cables incorporate two metal layers, which represent a material budget of around 0.2% of the radiation length (including the contribution of insulating layers, etc) [113, 80]. Besides, the width of FPC cables is limited by the size of the MIMOSIS-1 sensors (see Figure 5.9). This limits in turn the affordable amount of metal lines embedded in each metal layer for data transmission. It is planned to develop FPC cables featuring 10 read-out channels (each provided by a pair a metal lines for LVDS* transmission). Given that MIMOSIS-1 will feature two output channels, FPC will be able to read up to 5 MIMOSIS-1 sensors. Figure 5.9 shows the connectivity between MIMOSIS-1 sensors and FPC cables. The frequency at which FPC can operate will be limited mostly by electrical cross-talk between neighboring channels and signal attenuation effects over the relatively large distance (about 1 meter) over which signals will have to be propagated. The data are then transmitted to the next component, namely the converter board. Which bandwidth FPC cables must feature to read out MVD sensors was one the question addressed in this work;

- the Converter Board (CB) (see Figure 5.10) is aiming mostly at converting electrical signals to optical signals in order to use optical cables for long distance data transmission. It will be placed at about 1 meter from the sensors. This distance can not be too large to limit the effect of electrical cross-talk and signal attenuation in FPC cables. Given its location

*Low-Voltage Differential Signals

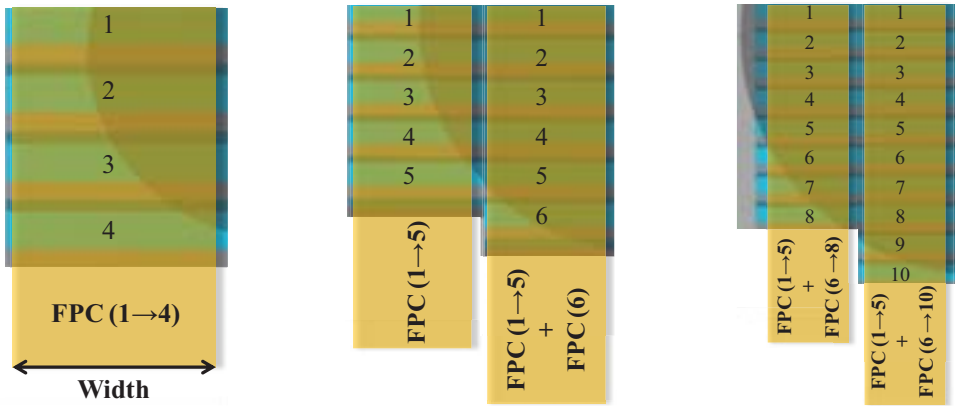


**Figure 5.9:** *Flex-Print Cables (FPC), to which the sensors are bonded (see figure 4.10). The lower-left quadrants constituting the front side of MVD stations at distances of 5, 10 and 15 cm from the target (see figure 4.9) are shown. Note that the layout of MVD stations is symmetric around the beam axis. The numbers in parentheses indicate the sensor numbers (indicated on each sensor) bonded to these FPC cables. The circular shaded areas show the CBM acceptance.*

relatively close to MVD sensors, the CB board will have only simple, radiation tolerant hardware components. Additionally, the size of this board is limited by the space available in the vicinity of the MVD detector, restricting the amount of hardware components implemented on it. Its functionalities are thus limited to data transport (no data processing), in particular 8 bits/10 bits encoding will be performed for data transmission. The detailed data path through the CB will be discussed later (see Figure 5.29). The CB board will have to handle large data rates with limited resources. It is thus crucial to determine the required data rate capability of each of its components. The data is then transmitted to the next component, namely the read-out controller board. The required bandwidth for optical cables was also an issue addressed in this thesis;

- the Read-Out Controller (ROC) board (see Figure 5.10) will be used for slow control (to monitor the MVD sensors), for data processing and as an interface to the CBM data acquisition system. It is thus located at several 10's of meters from the MVD, to operate in a relaxed radiative environment (compared with the CB board). Moreover, its functionalities are not restricted by limited space for their underlying hardware components. Several functionalities will be provided by the ROC board. First, optical/electrical signal conversion and 10 bits/8 bits decoding will be performed. Given the free-streaming data which the system will handle, each event data has to be marked with a precise time stamp for the sake of event building (done at a later stage in the read-out chain). Zero suppression will be performed, aiming at reducing the data flow (an important amount of zero's will be transmitted by MVD sensors, as discussed in Section 5.4.4). The ROC board will feature large memory cells to store several hundreds of sparsified* frames. This will be done to get rid of data flow fluctuations, coming mostly from the beam intensity fluctuations. The

*Containing useful data only

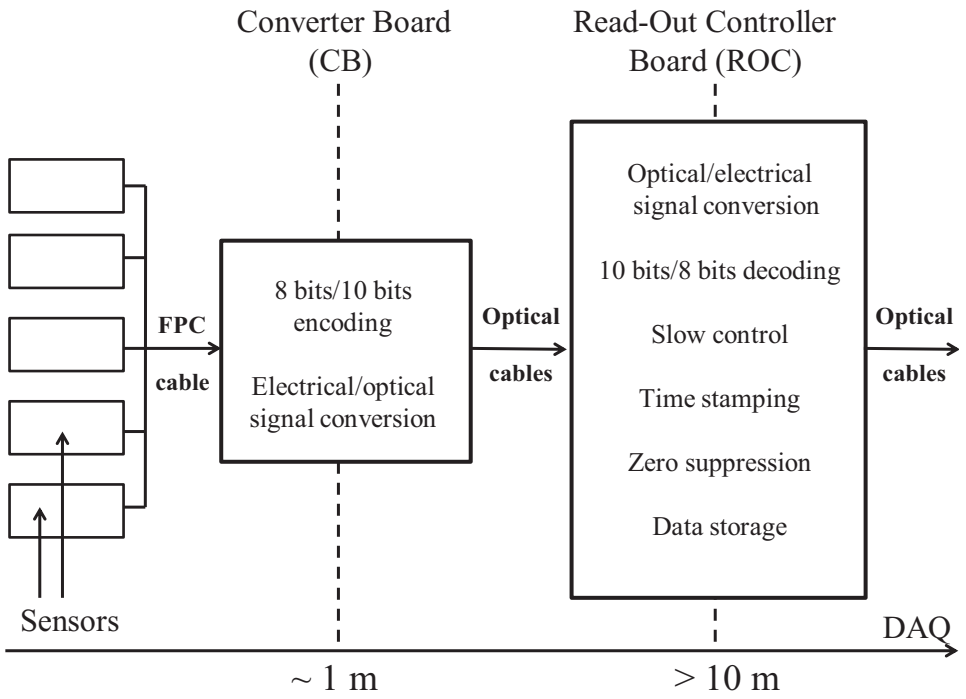


**Figure 5.10:** *Functionality blocks of one read-out chain, shipping the data provided by five MVD sensors [112] (see text). The distance of each component (with respect to MVD sensors) is also shown (bottom axis).*

data transmission to the CBM data acquisition system will be done using optical cables.

## 5.6 Simulation procedure

The simulation studies have been carried out using the simulation environment and analysis framework CbmRoot [106].

### 5.6.1 Event generation

The Ultra-Relativistic Quantum Molecular Dynamics (UrQMD) generator [108] has been used to produce p(30 GeV) + Au and Au(10 AGeV) + Au collisions. The transport of particles through the detector setup is performed using GEANT3 [107]. In addition to particles produced by nuclear collisions, $\delta$-electrons knocked out of the target by beam ions deposit a large amount of hits in the MVD (see Figure 4.3). They were accounted for in the simulations, in the case of Au + Au collisions (see next section).

### 5.6.2 Simulation of $\delta$-electrons

As a particular feature of fixed target experiments, the material budget of the detection setup includes the target material. In the current design, the Au target has a thickness of 250 $\mu$m, which corresponds to a probability of nuclear interaction for a given Au ion of about $1\%$ (see Appendix B). This means that for one Au + Au nuclear collision, 100 Au ions cross the target, on average, and produce $\delta$-electrons. These electrons were generated by shooting Au ions in the Au target using an ion generator and the transport code GEANT3 [107].

#### Yield

$\delta$-electrons are essentially produced in the target by beam Au ions*. The average yield of $\delta$-electrons produced per unit path in the target by relativistic ions is derived in GEANT according to the (integrated) Bethe and Bloch formula ([107], page 270), as follows:

$$\frac{dN}{dX} = \frac{D}{2} \times \rho \times \frac{Z}{A} \times \frac{z^2}{T_{cut}} \tag{5.1}$$

with D = 0.307 MeV $cm^2$ $g^{-1}$, $\rho$ the density of target atoms, (A, Z) the mass number and charge of target atoms ($\rho$ = 19.3 g $cm^{-3}$ and (A, Z) = (197, 79) for Au material), and z the charge of incident ions. $T_{cut}$ is a kinetic energy cut-off below which GEANT stops producing $\delta$-electrons explicitly (they are accounted for in the energy loss of charged particles in matter). This is done to speed up the computation, since their production cross-section increases drastically with

*Bhabha and Moller scatterings contribute only to about $0.5\%$ of the total yield in the simulations

decreasing kinetic energy. In the present simulations, $T_{cut}$ = 1 MeV. According to Equation (5.1), around 185 $\delta$-electrons are produced per Au ion in the 250 $\mu$m thick Au target. This was indeed observed in the simulations, with a small absorption effect in the target material (around 4% of produced $\delta$-electrons are absorbed). This was expected since the range of electrons with kinetic energy of 1 MeV in Au material is of about 400 $\mu$m.

Since the production of $\delta$-electrons scales with the projectile charge squared, this background can be neglected for proton induced reactions.

**Phase space**

In the calculation of the $\delta$-electron spectral distribution, the binding energy of the electrons can be safely neglected. The collision process can therefore be treated as elastic collision and, hence, there is a direct correlation between the momentum of the electron and its emission polar angle, given by [67]:

$$cos(\theta) \quad = \frac{T}{p} \times \frac{p_{max}}{T_{max}} \tag{5.2}$$

with $\theta$, T and p being the polar angle, the kinetic energy and the momentum of $\delta$-electrons, respectively. $p_{max}$ is the maximum momentum of an electron with the maximum possible energy transfer $T_{max}$. For electrons with kinetic energy above 1 MeV, the ratio $p_{max}$/$T_{max}$ is approximately equal to 1, such that:

$$cos(\theta) \quad \sim \frac{T}{p} \tag{5.3}$$

One can see from the last equation, that the higher the momentum of $\delta$-electrons is, the lower the polar angle will be. This is illustrated in Figure 5.11: the dashed blue and full red histograms show the cases of electrons with polar angles above and below 25 degrees, respectively (this polar angle corresponds to the CBM acceptance). We will see (in Section 5.8.2) that this particular feature has a strong impact on the distribution of the hits deposited in MVD stations by $\delta$-electrons.

### 5.6.3 Introduction of the read-out time of MIMOSIS-1 in the simulations

The expected read-out time of MIMOSIS-1 (of 25 $\mu$s) was introduced in the simulations. We explain the simulation procedure in the case of Au + Au collisions. The minor differences for the p + Au case will be discussed at the end of the section. The procedure is the following:

- the hits generated in MVD stations by minimum bias Au + Au collisions and Au ions crossing the target (see previous section) are stored in two-dimensional histograms.
- the number of ions crossing the target per read-out cycle of the sensor ($N_{ion}$) is chosen randomly according to a function featuring a ratio maximum-to-average equal to 3 or 10. This is shown in Figure 5.12 (ratio maximum-to-average equal to 10). The average value of $N_{ion}$ is equal to 50 ions (considering an average beam intensity of 2 $\times$ $10^6$ ion/s). Note that the shape of the distribution is difficult to predict and is chosen arbitrarily (a Landau function).

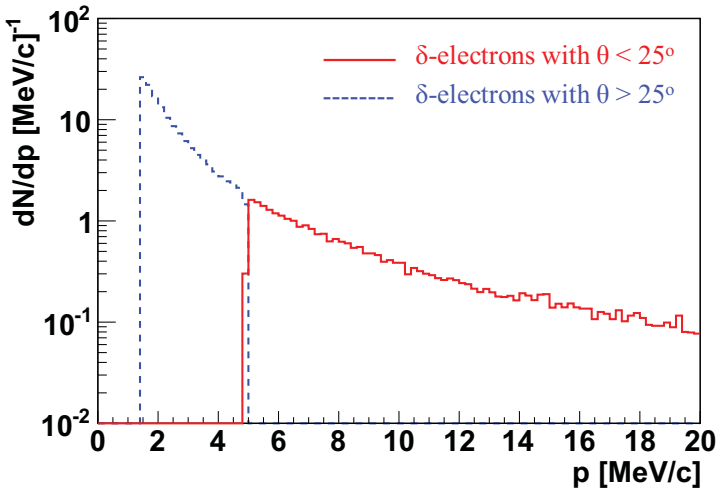


**Figure 5.11:** *Momentum spectrum of $\delta$-electrons produced in the Au target by Au(10 AGeV) ions (normalized to one ion). Two cases are shown: electrons with a polar angle above (blue histogram) and below (red histogram) 25 degrees.*

- the number of Au + Au collisions per read-out cycle of the sensor ($N_{coll}$) is generated randomly according to a Poisson function, with an average value equal to 0.01 $\times$ $N_{ion}$ (accounting for a target with 1% of nuclear interaction probability, see Appendix B)
- a frame is obtained by merging $N_{ion}$ histograms corresponding to "Au ions crossing the target" events and $N_{coll}$ histograms corresponding to Au + Au collisions.

In the p + Au case, the simulation procedure is identical as explained above, except that only $N_{coll}$ histograms corresponding to p + Au collisions are merged (the yield of $\delta$-electrons can be neglected). Additionally, an average collision rate of 2 $\times$ $10^6$ p + Au collisions/s was considered in this system, corresponding to 50 p + Au collisions occurring per sensor read-out time, on average.

### 5.6.4 Introduction of the active area of MIMOSIS-1 in the simulations

MVD stations are modeled by disks (see Section 5.8). The position and active area of MVD sensors are introduced in the simulations as follows: for each frame generated as explained in the previous section, the number of hits received by a sensor covering an area ($X_1$, $X_2$) $\times$ ($Y_1$, $Y_2$) is obtained by counting all hits with transverse coordinates (X, Y) contained in the following intervals: $X_1$ < X < $X_2$ and $Y_1$ < Y < $Y_2$. The set of coordinates ($X_1$, $X_2$, $Y_1$, $Y_2$) is calculated for each MVD sensor, given their layout depicted in Figure 4.9.

For the evaluation of the hit rate on the level of the data sparsification circuits, the hit count is performed as explained above, but based on the area of pixel rows (instead of sensor area), considering a pixel dimension (in the column direction) of 40 $\mu$m. Note that the hit density is

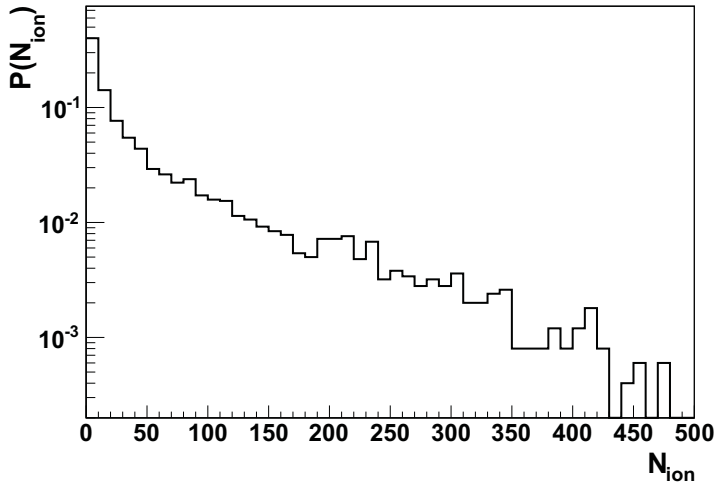


**Figure 5.12:** *Distribution for "Au ions crossing the target" event pile-up ($N_{ion}$) for a 25 $\mu$s read-out cycle and a beam intensity of 2 $\times$ $10^6$ Au ions per second. The ratio maximum-to-average of the beam intensity is assumed to be equal to 10.*

highly inhomogeneous within one sensor, giving rise to different distributions of the number of hits received by different rows of pixels. For a given sensor, these distributions are merged. The procedure is performed, considering either rows of 1536 pixels (full sensor), or rows of 64 pixels (bank)*. The merging of the distributions of hits received by different banks is also done within one sensor.

### 5.6.5 Estimate of the data volume generated in MVD sensors

Based on the information provided by Figures 5.7 and 5.8, one can compute a simple estimate of the data volume ($D_V$) generated per read-out cycle in the sensor as a function of the number of hits, as follows (in unit of Bytes):

$$D_V = (3 \times N_{hits} + N_{status} + N_{fake}) \times 2 + 20 \tag{5.4}$$

with $N_{hits}$ and $N_{fake}$ the number of real and fake hits received by the sensor per read-out cycle, and $N_{status}$ the number of status line headers in the frame. In the formula, the factor 3 comes from the fact that we assumed that one hit generates systematically 3 states (see Section 5.4.4). For $N_{status}$, we assumed that only lines with non-zero states generate a status line header in MIMOSIS-1 (identically as in MIMOSA-26). For $N_{fake}$, we assumed a constant fake hit rate (per pixel and read-out cycle) of $10^{-4}$, as discussed in Section 5.4.3. Given an array of 1536 $\times$ 128 pixels, $N_{fake}$ = 20. Note that if the other MIMOSIS-1 design (an array of 1536 $\times$ 256 pixels) is chosen, there would be two times more pixels in the sensor, and $N_{fake}$ = 40. Additionally, we added 20 Bytes to account for the frame headers (although in most cases this is negligible considering the important hit density reached in MVD sensors).

*Considering a pixel dimension (in the row direction) of 20 $\mu$m

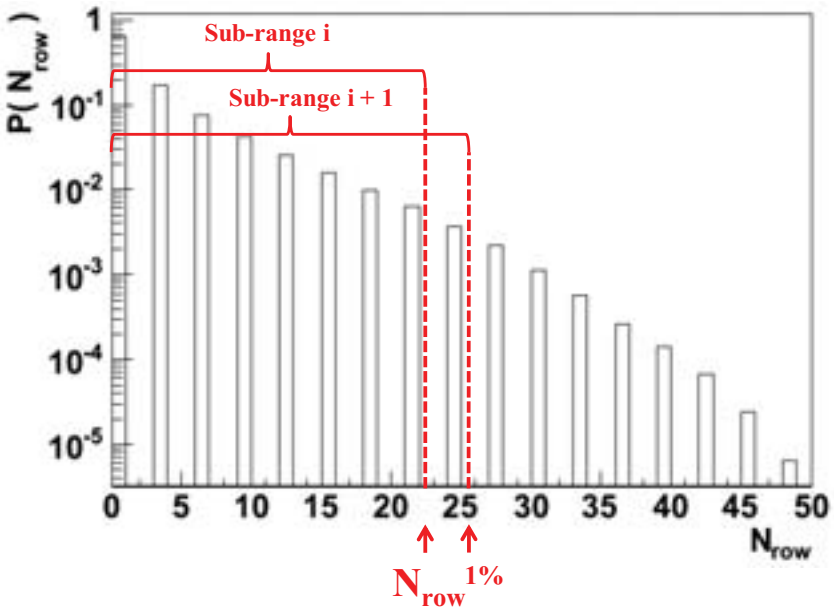


**Figure 5.13:** *Probability distribution of the number of states ($N_{row}$) generated in one sensor within rows of pixels.*

## 5.7 Definition of the observables

The output of the simulation procedure is:

- the probability distribution of the number of states generated in one MIMOSIS-1 sensor, within rows of pixels, all banks included ($N_{row}$) and per bank ($N_{bank}$). Note that $N_{row}$ and $N_{bank}$ include a factor of 3 to account for the fact that we assumed that one hit systematically generates 3 states. This is illustrated in Figure 5.13.
- the probability distribution of the data volume generated in one MIMOSIS-1 sensor ($D_V$), calculated according to Equation (5.4). Note that $D_V$ includes a factor of 2 to account for the fact that MIMOSIS-1 will have 2 memory banks aiming at storing 2 frames (see Section 5.4.4). This is illustrated in Figure 5.14 (in unit of bits). The data flow ($D_F$) is obtained by dividing $D_V$ with the expected read-out time of MIMOSIS-1 (of 25 $\mu$s), and without accounting for the factor of 2 (only one frame is transmitted within one read-out cycle).

Based on these distributions, the observables of the study are defined as follows:

- the number of states that the data sparsification circuits has to record within rows of pixels, all banks included ($N_{row}^{1\%}$) and per bank ($N_{bank}^{1\%}$)
- the data volume that the sensor has to register ($D_V^{1\%}$) and the data flow that it must tolerate ($D_F^{1\%}$)

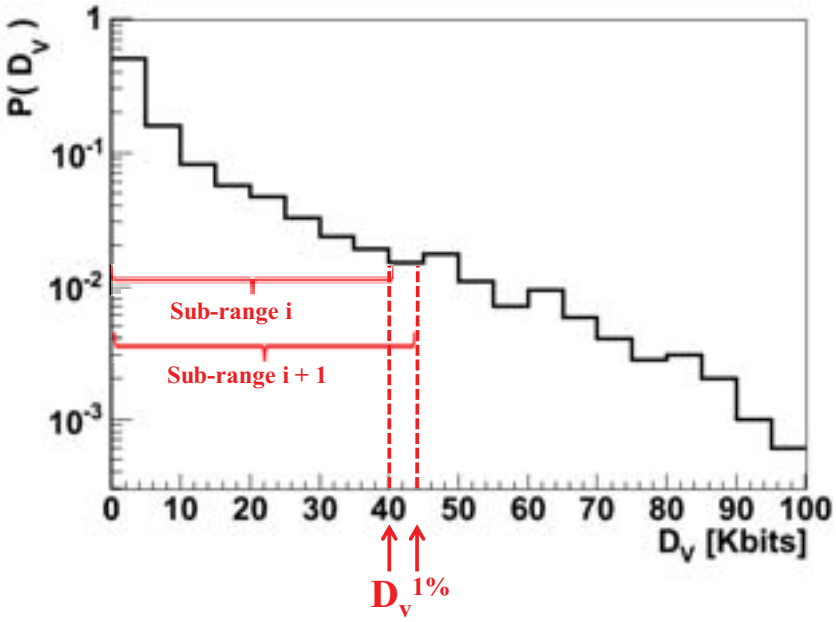


**Figure 5.14:** *Probability distribution of the data volume ($D_V$) generated in one sensor.*

The criteria for these requirements is an average data loss of, typically, a few percents. The data loss is calculated as follows: the average of the distributions shown in Figures 5.13 and 5.14 is calculated on a sub-range ($\mu_{sub}$) and on their full range ($\mu_{tot}$). In the case of $N_{row}$, this is done as follows:

$$\begin{aligned} \mu_{sub} &= \sum_0^{N_{row}^{1\%}} P(N_{row}) \times N_{row} \\ \mu_{tot} &= \sum_0^{MAX} P(N_{row}) \times N_{row} \end{aligned} \tag{5.5}$$

with MAX the upper bound of the full range (set to 50 in this example). The ratio between $\mu_{sub}$ and $\mu_{tot}$ gives an estimate of the average fraction of generated states which are recorded by the sparsification circuits, given that the latter can store up to $N_{row}^{1\%}$ states. This in turn gives the average data loss. As mentioned above, it must be of a few percents. $N_{row}^{1\%}$ is first set to an arbitrarily low value, and then increased gradually, until the following condition is fulfilled:

$$(1 - \tfrac{\mu_{sub}}{\mu_{tot}}) + \delta \leq n \times 0.01 \tag{5.6}$$

with $\delta$ the statistical error on the estimate shown on the left-hand side of the equation, and n an integer. In practice, the calculations shown in Equations (5.5) are carried out considering a sub-range "i", then a sub-range "i+1", and so on as illustrated in Figure 5.13, until the condition shown in Equation (5.6) is satisfied. The same procedure is used for $N_{bank}^{1\%}$, $D_V^{1\%}$, and $D_F^{1\%}$.

## 5.8 Detector setup

Figure 5.15 shows the MVD as introduced in the simulations. We considered stations located at distances of 5, 10 and 15 cm from the target. They are modeled by disks of inner and outer radii

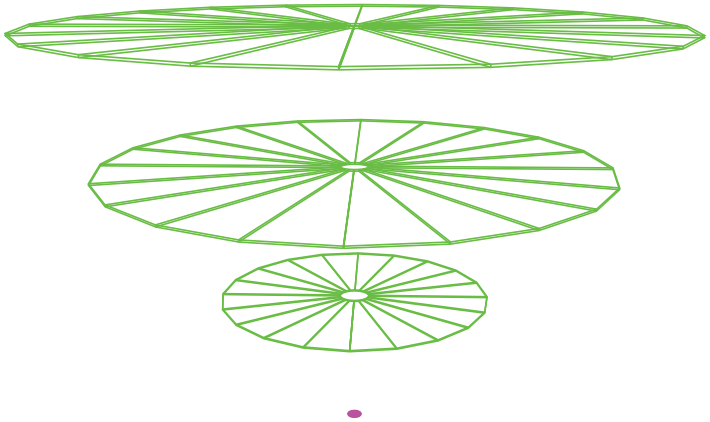

**Figure 5.15:** *MVD detector model in the simulations. Stations located at distances of 5, 10 and 15 cm from the target (red point) are modeled by disks (green), of inner and outer radii corresponding to the CBM acceptance.*

corresponding to the CBM acceptance (see Figure 4.9). Note that their outer radius is slightly increased to cover the active area of MIMOSIS-1 sensors located on the periphery of the stations. Their thickness is set according to realistic estimates, as discussed in Section 4.5. Note also that, for the sake of visibility, the vacuum vessel inside which MVD stations will be placed is not shown.

The target is modeled by a cylinder with a thickness of 250 $\mu$m. This corresponds to probability of nuclear interaction of roughly 1%, as derived in Appendix B. The magnitude of the magnetic dipole field of CBM is shown in Figure 5.16, as a function of the longitudinal coordinate (z). The location of the setup (target + MVD stations) can be varied to change the magnitude of the field in the target region. This will be discussed in the next section.

### 5.8.1 Acceptance for $\delta$-electrons

The MVD acceptance for $\delta$-electrons depends strongly on the magnitude of the magnetic field in the target region. The latter deflects low-momentum electrons away from the detector. This can be seen in Figure 5.17 for Au(10 AGeV) ions crossing the Au target: an integrated field of 1 T.m in the target region results into a low-momentum cut-off for accepted $\delta$-electrons of about 6 GeV/c. Note that this is the maximum available field, as determined by the required performance in experiments with beam from the SIS300 synchrotron. Generally, for operation at SIS100 the field integral can be lowered in favor of an increased acceptance for low-momentum particles. This would also be helpful to improve the measurements of low mass vector mesons decaying into di-electrons, by improving the rejection of background electron-positron pairs with small opening angles. As one can see in Figure 5.17, this has an effect of lowering the low-momentum cut-off for $\delta$-electrons, down to about 2.5 and 1.5 GeV/c for an integrated field of 0.6 and 0.3 T.m, respectively. This in turn increases significantly the number of hits deposited by

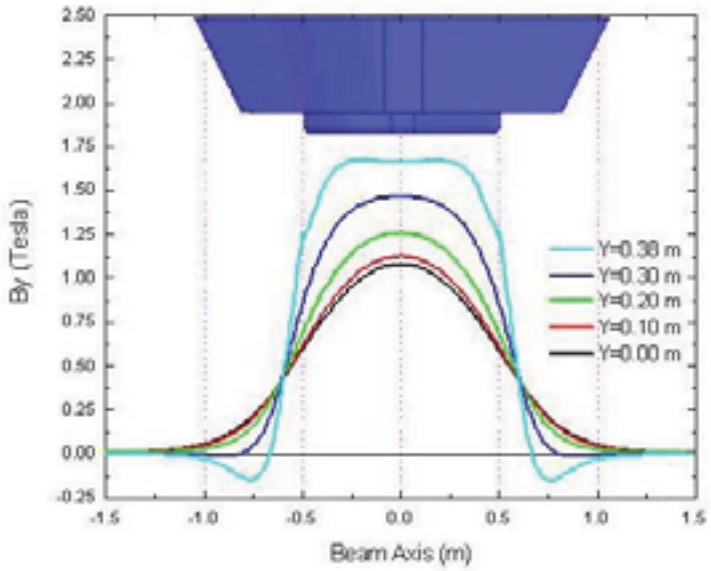


**Figure 5.16:** *Magnitude of the magnetic dipole field (in the Y direction) of CBM as a function of the longitudinal coordinate. This is shown at several distances from the mid-plane (X=0).*

$\delta$-electrons in the MVD stations (see Figure 5.18). As there is no quantitative estimate on how much the field would be decreased, we assumed an extreme case: an integrated field of 0.3 T.m (in the target region) for Au(10 AGeV) + Au collisions. Note that this is likely to deteriorate the bending power for charged particles and the momentum resolution achieved with the STS tracker. Thus, this scenario is to be interpreted only as an extreme case for studying the hit rate received by the MVD detector.

Note also that the low kinetic energy cut-off $T_{cut}$ > 1 MeV set in GEANT, which corresponds to a low-momentum cut-off p > 1.6 MeV/c (black full histogram in Figure 5.17), has no effect on the hit rates received by MVD stations, even considering an integrated field of 0.3 T.m.

### 5.8.2 Shielding against $\delta$-electrons

The hits received by MVD stations are predominately originating from $\delta$-electrons. This can be seen in Figure 5.19 for an integrated field of 0.3 T.m in the target region. Both Au + Au collisions and Au ions crossing the target produce in-homogeneously distributed hits, with a maximal density close to the beam axis. However, while Au + Au collisions are responsible for a maximal density of 0.22 hits/$cm^2$ per collision, the beam ions generate up to 3.5 hits/$cm^2$ per 100 ions (to account for a target with $1\%$ of nuclear interaction probability, see Appendix B). Figure 5.20 shows a cross-section of these distributions. For the case of $\delta$-electrons, the separate contributions of those which deposit hits within or after 0.6 nanoseconds are presented. This time is roughly the one needed for $\delta$-electrons to reach the first MVD station (see Figure 5.21). One can see in Figure 5.20 that the distribution of first hits is sharply peaked at 0. First, this

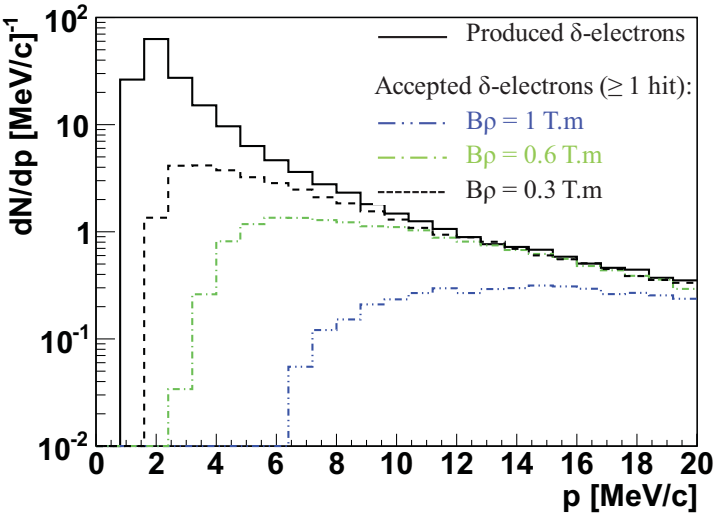


**Figure 5.17:** *Momentum spectrum of δ-electrons produced by Au(10 AGeV) ions crossing the Au target (black full histogram) and of those which enter the CBM acceptance (depositing at least one hit in MVD stations) considering an integrated magnetic field in the target region of 1, 0.6 and 0.3 T.m (double-dotted-dashed blue, dotted-dashed green, and dashed black histograms, respectively). The distributions are normalized to one ion.*

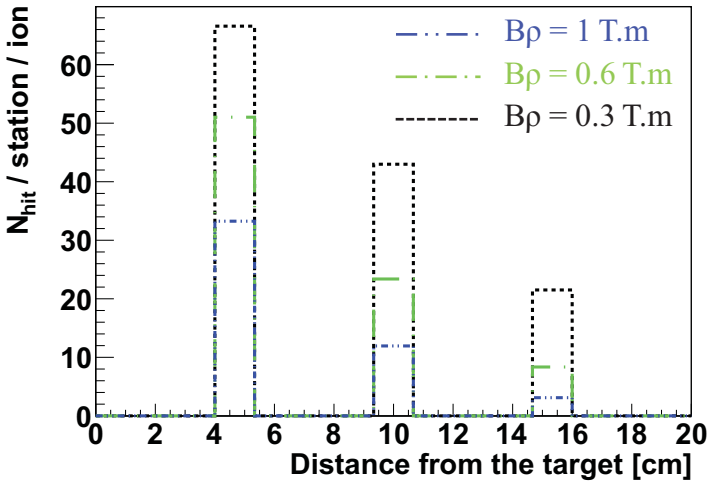


**Figure 5.18:** *Number of hits from δ-electrons received by the MVD stations as a function of the distance to the target (normalized per ion crossing the target). The cases of an integrated magnetic field in the target region of 1, 0.6 and 0.3 T.m are shown (double-dotted-dashed blue, dotted-dashed green, and dashed black histograms, respectively).*

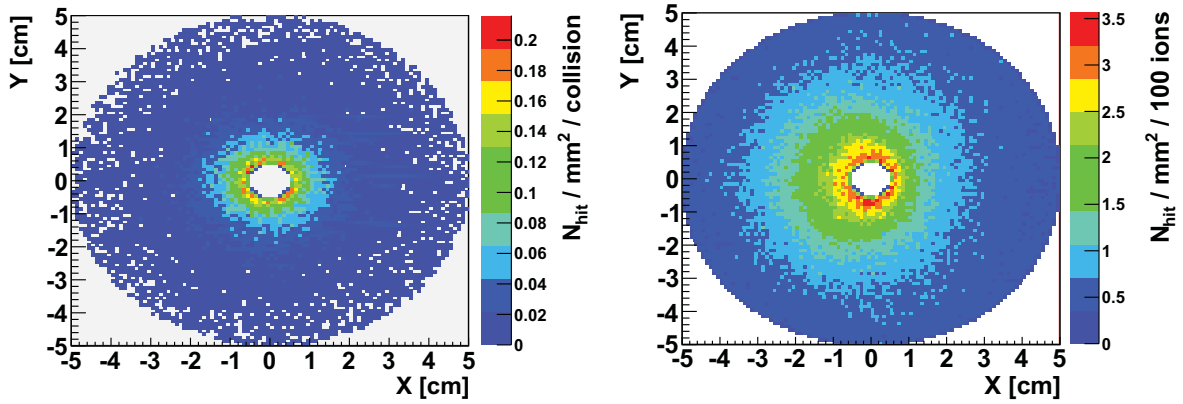


**Figure 5.19:** *Hit densities per $mm^2$ for a MVD station located at 5 cm from the target in minimum bias Au(10 AGeV) + Au collisions. The left-hand and right-hand parts show the separate contributions of Au + Au collisions (normalized to one collision) and of $\delta$-electrons produced by beam ions in the target (normalized to 100 ions crossing the target) respectively. The CBM acceptance is a disk of radius 2.3 cm.*

comes from the Lorentz boost in fixed-target topology: this boost focuses the particle flux within a narrow emission cone around the beam axis. Secondly, $\delta$-electrons with high momenta have small emission polar angles (see Figure 5.11). Additionally, they are only slightly deflected by the magnetic field. In contrast, secondary hits are almost randomly distributed. As seen in Figure 5.21, these hits show a cyclic impact time distribution. This comes from the fact that $\delta$-electrons spiral and accidentally hit the detector several times. The chance to produce secondary hits is more important for low-momentum electrons (since they have smaller deflection radii). This can be seen in Figure 5.22. The momentum of $\delta$-electrons deposing hits after 0.6 ns is softer with respect to the momentum of those which created first hits. Note that the ordinate axis gives the number of hits received by the first MVD station. The two distributions are thus non-exclusive: $\delta$-electrons which deposit hits within the first 0.6 nanoseconds can spiral and deposit hits later on (and vice versa).

The idea to decrease the amount of hits from $\delta$-electrons was to absorb spiraling ones. For this purpose, absorbers have been added to the setup (see Figure 5.23). They are modeled by 1 cm thick disks made of copper and surrounding the MVD stations (the absorber outer radius corresponds to the vacuum vessel boundary). Note that the material budget needed to stop, e.g., 5 MeV electrons is of 27% of $X_0$ in copper, while being of only 5% in polyethylene. To limit the amount of electron-positron conversion pairs created in the absorber, the latter material would rather be used (i.e. a polyethylene 2.5 cm thick absorber).

The absorbers suppress all (low-momentum and spirally) $\delta$-electrons within 2.2 ns (see Figure 5.21). The random component of the hit distribution shown in Figure 5.20 is thus removed. However, first hits can not be avoided using peripheral absorbers. As one can see, the main part of the peak hit density from $\delta$-electrons (about 86%) remains unaffected. This method is very useful, though, to reduce the total amount of hits received by MVD stations, by a factor 1.6 (2)

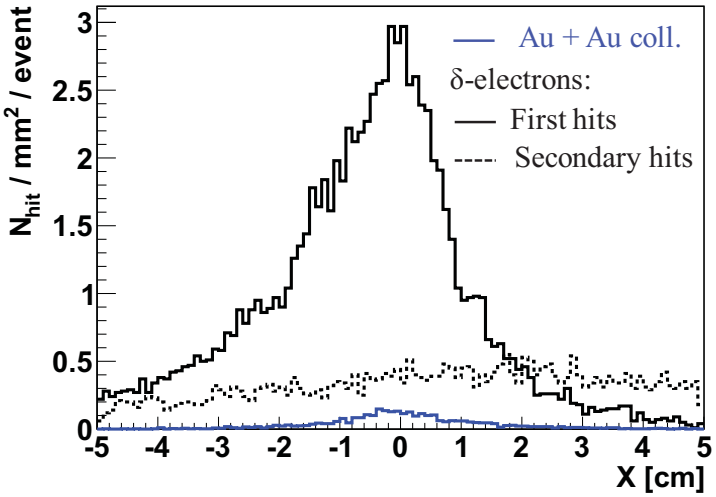


**Figure 5.20:** *Hit densities per $mm^2$ for a MVD station located at 5 cm from the target in minimum bias Au(10 AGeV) + Au collisions, shown for a slice: -0.8 cm < Y < -0.7 cm (see Figure 5.19). The histograms show the contributions of Au + Au collisions (full blue) and of δ-electrons depositing their first hits (full black) and secondary hits after having spiraled (dotted black), as can be seen in Figure 5.21. The distributions are normalized to one event (one Au + Au collision and 100 Au ions crossing the target).*

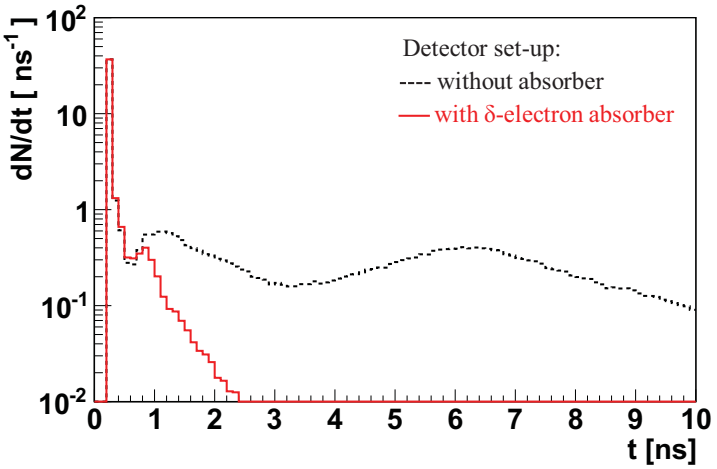


**Figure 5.21:** *Hit impact time distribution (relative to the collision time) for δ-electrons (see previous figure). The dashed black and full red histograms show the case of a setup excluding or including an absorber (see Figure 5.23). Entries at times larger than 0.6 nanoseconds reflect secondary hits of δ-electrons curling in the field. The distributions are normalized to one ion crossing the target.*

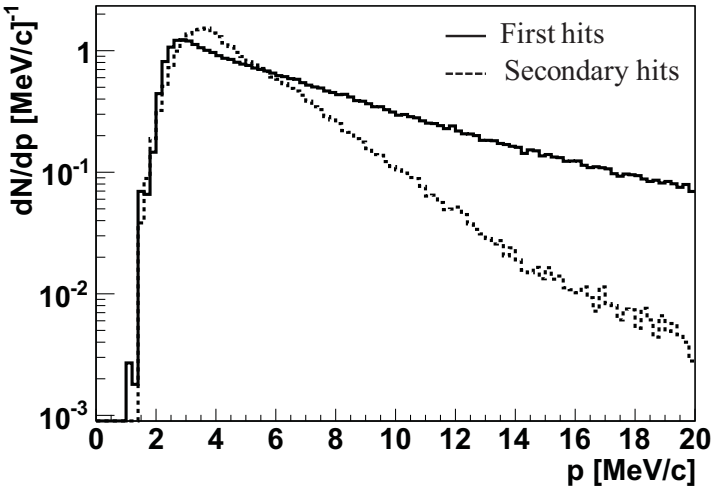


**Figure 5.22:** *Momentum of $\delta$-electrons deposing hits within (full black) or after (dotted black) 0.6 ns (relative to the collision time). The distributions are normalized to one ion crossing the target)*

at 5 cm (10 and 15 cm) from the target, as one can see in Figure 5.24.

Note that there is no significant increase of hits in MVD stations originating from the production of secondary particles in the absorbers. The latter are thus included in the simulated detector setup. In the final design, the components of the read-out electronics and support structure should be designed such that they at the same time properly act as $\delta$-electron absorbers. Special care has to be taken to avoid charging up effects on the support structure.

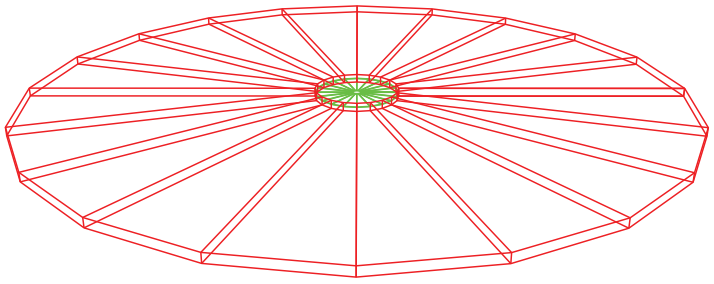

**Figure 5.23:** *Absorber (red disk) in the simulations, shown for a MVD station (green disk) located at 5 cm from the target. Absorbers are modeled by 1 cm thick disks made of copper material and surrounding the MVD stations. Note that in experiment, a polyethylene 2.5 cm thick absorber would rather be used.*

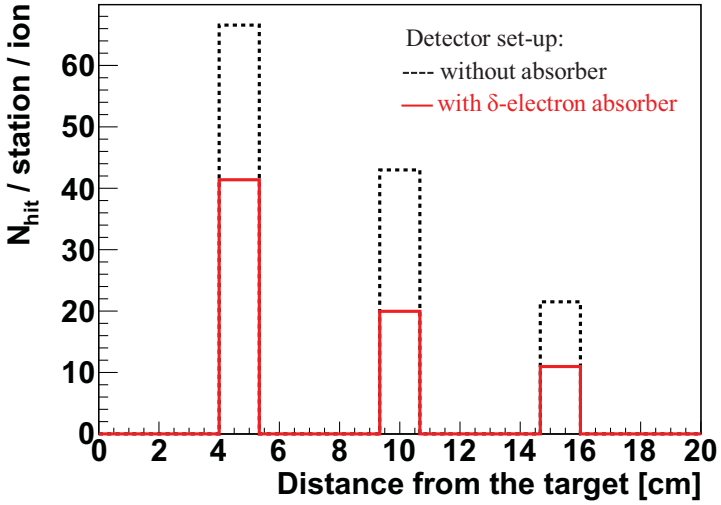


**Figure 5.24:** *Number of hits from $\delta$-electrons received by MVD stations as a function of the distance to the target (normalized per ion crossing the target). The cases of an MVD setup excluding or including absorbers are shown by dotted black and full red histograms, respectively.*

## 5.9 Results

### 5.9.1 Data rate requirements for MIMOSIS-1

#### Focus on the maximal hit density region

Figure 5.25 shows the average hit densities reached in the first MVD station in central p + Au and minimum bias Au + Au collisions. One sees that in both cases, these hit densities are highly inhomogeneous. This comes from the Lorentz boost in fixed-target topology (this boost focuses the particle flux within a narrow emission cone around the beam axis). In Au + Au collisions, the peak hit density also originates from the phase space of $\delta$-electrons (see Section 5.8.2). The maximal hit density reaches up to about 0.012 and 3.2 hits/$mm^2$ per collision in p + Au and Au + Au collisions, respectively.

Figure 5.26 presents the average number of hits collected by MIMOSIS-1 sensors (first MVD station) during one read-out cycle (of 25 $\mu$s), in the case of central p + Au and minimum bias Au + Au collisions. One can see that the number of collected hits varies greatly from one sensor to another. This comes from the highly inhomogeneous hit densities (see Figure 5.25). In p + Au collisions, the most exposed sensor, thus experiencing the highest constraint in terms of hit rate, is located at the bottom of the upper-right quadrant. This sensor accumulates about 30 hits per read-out cycle (on average). In Au + Au collisions, the most exposed sensor, located at the top of the lower-left quadrant, accumulates around 100 hits per read-out cycle (on average). For the sake of determining the requirements for MIMOSIS-1 in terms of hit and date rates, we focused on the most exposed sensor. This is to ensure that the data loss in the sensors located in lower hit density regions is of a few percents as well. Note that the position of the most exposed sensor is

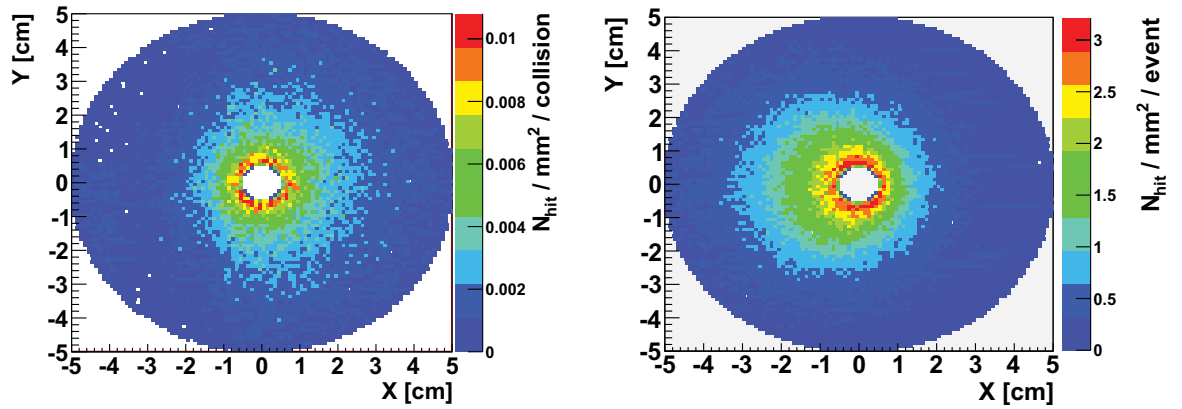


**Figure 5.25:** *Average number of hits ($N_{hits}$) per $mm^2$ created in the MVD station (located at 5 cm from the target) in central p + Au (left-hand side) and minimum bias Au + Au (right-hand side) collisions. These distributions are normalized to, respectively, one p + Au collision and one event, defined as the sum of one Au + Au collision and 100 "Au ions crossing the target" events (see Appendix B). The CBM acceptance is a disk of radius 2.3 cm.*

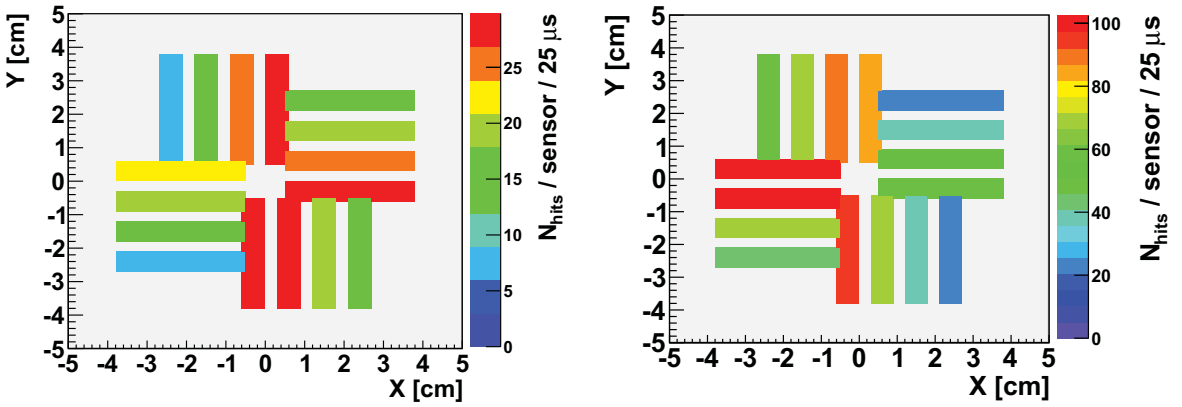


**Figure 5.26:** *Average number of hits ($N_{hits}$) received by MIMOSIS-1 sensors (located at 5 cm from the target) per read-out cycle (of 25 µs), in central p + Au (left-hand side) and minimum bias Au + Au (right-hand side) collisions.*

identical for MVD stations located at 10 and 15 cm from the target.

### Data sparsification circuits

Figure 5.27 presents the number of states that the data sparsification circuits have to handle within rows of pixels, all banks included ($N_{row}^{1\%}$) for the most exposed MIMOSIS-1 sensor. $N_{row}^{1\%}$ increases substantially while going closer to the target, as an effect of increasing particle flux. This effect is particularly strong in the case of Au + Au collisions, due to the sharp rising of the hit density originating from $\delta$-electrons with decreasing distance to the target (see Figure 4.3). $N_{row}^{1\%}$ = 12 and 18 at 5 cm from the target in p + Au and Au + Au collisions, respectively, considering a ratio maximum-to-average of the beam intensity of 3. $N_{row}^{1\%}$ increases substantially with the beam intensity fluctuations: $N_{row}^{1\%}$ = 18 and 36 at 5 cm from the target in p + Au and Au + Au collisions, respectively, considering a ratio maximum-to-average of the beam intensity of 10.

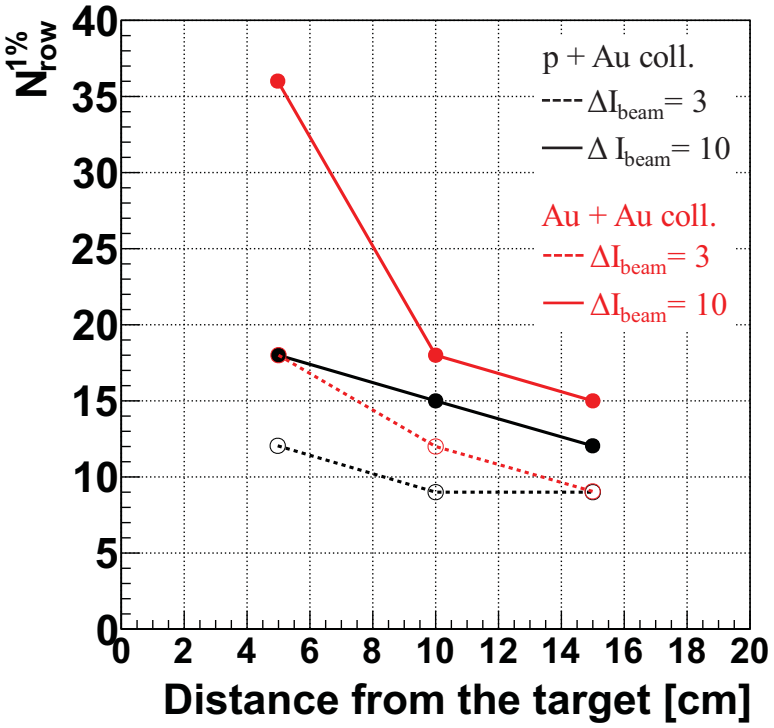


**Figure 5.27:** *Number of states that the data sparsification circuits of MIMOSIS-1 have to handle within rows of pixels ($N_{row}^{1\%}$) as a function of the distance from the target. The black and red points correspond to the cases of p + Au and Au + Au collisions, respectively. The lines are only meant to ease the visibility: the full and dashed ones correspond to a ratio maximum-to-average beam intensity ($\Delta I_{beam}$) of 10 and 3, respectively. The statistical errors ($\delta$ in Equation 5.6) are within 0.2 - 0.7%. The criteria to evaluate $N_{row}^{1\%}$ is thus an affordable hit loss of 1%.*

| Distance from the target [cm] | 5 | 10 | 15 |
|---|---|---|---|
| p + Au coll. | 2.2 (3.3) | 2.7 (4.4) | 3.3 (4.4) |
| Au + Au coll. | 1.1 (2.2) | 2.2 (3.3) | 2.7 (4.4) |

**Table 5.1:** *Ratio between the expected number of states that the data sparsification circuits of MIMOSIS-1 will handle and $N_{row}^{1\%}$ (see Figure 5.27), as a function of the distance between the target and the MVD station, and in the case of p + Au and Au + Au collisions. The first numbers (numbers in parentheses) correspond to the case of a maximum-to-average ratio of the beam intensity of 10 (3).*

These requirements have to be compared with the expected performance of the sparsification circuits of MIMOSIS-1: M = 40 states as discussed in Section 5.4.4. Table 5.1 gives the ratio between the expected performance of MIMOSIS-1 and $N_{row}^{1\%}$. One can see that this ratio is above one in all cases: in both p + Au and Au + Au collisions and at all considered distances, even considering a ratio maximum-to-average of the beam intensity of 10. One can conclude that the expected performance of the sparsification circuits of MIMOSIS-1 are satisfactory for the need of CBM at SIS100.

Let us remind that the first limitation of the data sparsification circuits comes from the restricted number (N) of states that they can handle per row of 64 pixels or bank (see Section 5.4.4). In MIMOSA-26, N = 6 is already achieved. This will be the case also in MIMOSIS-1. The number of states that the sparsification circuits have to handle per bank ($N_{bank}^{1\%}$) is below 6 states in both systems (p + Au and Au + Au collisions), at any distances, and even for a ratio maximum-to-average of the beam intensity of 10 (results not shown). The performance N = 6 is sufficient to sustain the hit rate expected at SIS100. This was expected since this number (N = 6) corresponds to an important hit occupancy (per pixel and per read-out cycle), above 9.4%.

**Output bandwidth and on-chip memory**

Figure 5.28 shows the data volume that the sensor has to register ($D_V^{1\%}$) and the data flow that it must tolerate ($D_F^{1\%}$) for the most exposed MIMOSIS-1 sensor. $D_F^{1\%}$ increases substantially while going closer to the target. At a distance of 5 cm, $D_F^{1\%}$ = 300 Mbits/s and 700 Mbits/s in p + Au and Au + Au collisions, respectively. $D_F^{1\%}$ scales almost linearly with the beam intensity fluctuations (see Appendix C), increasing by a factor of 2-3 while increasing the ratio maximum-to-average of the beam intensity from 3 to 10. This leads to $D_F^{1\%}$ = 700 Mbits/s and 2 Gbits/s in p + Au and Au + Au collisions, respectively (at 5 cm from the target).

These requirements have to be compared with the expected output bandwidth of MIMOSIS-1, of either 400 or 800 MHz, as discussed in Section 5.4.4. In the case MIMOSIS-1 has an output bandwidth of 400 MHz, substantial fluctuations of the beam intensity (a ratio maximum-to-average of 10) would not allow placing the first MVD station at a distance lower than 10 cm from the target in p + Au collisions. Improving the beam temporal homogeneity (a ratio maximum-to-average of 3), would allow approaching it down to 5 cm from the target with a security margin

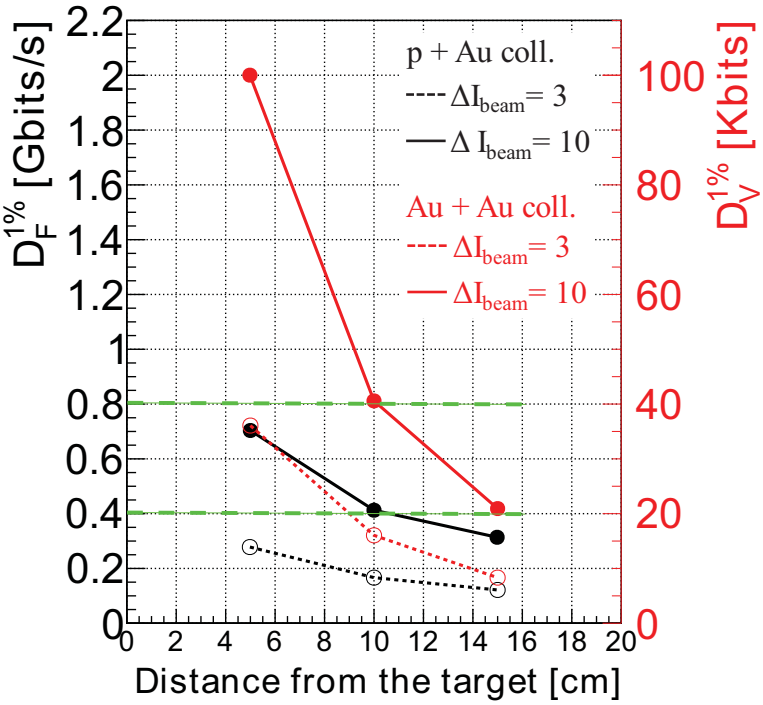


**Figure 5.28:** *Output bandwidth ($D_F^{1\%}$) and embedded memory size ($D_V^{1\%}$) that MIMOSIS-1 has to feature (the memory size is given for a sensor read-out time of 25 $\mu$s), as a function of the distance from the target. The black and red points correspond to the cases of p + Au and Au + Au collisions, respectively. The lines are only meant to ease the visibility: the full and dashed ones correspond to a ratio maximum-to-average of the beam intensity ($\Delta I_{beam}$) of 10 and 3, respectively. The statistical errors ($\delta$ in Equation 5.6) are within 2-3%. The criteria to evaluate $D_F^{1\%}$ (and $D_V^{1\%}$) is thus an affordable data loss of 4%. The horizontal green dashed lines indicate the expected MIMOSIS-1 output bandwidth, of either 400 or 800 MHz.*

| Distance from the target [cm] | 5 | 10 | 15 |
|---|---|---|---|
| p + Au coll. | 0.6 (1.3) | 1 (2) | 1.1 (4) |
| Au + Au coll. | 0.2 (0.6) | 0.5 (1.1) | 1 (2.6) |

**Table 5.2:** *Ratio between the expected output bandwidth of MIMOSIS-1 (of 400 MHz) and $D_F^{1\%}$ (see Figure 5.28), as a function of the distance between the target and the MVD station, and in the case of p + Au and Au + Au collisions. The first numbers (numbers in parentheses) correspond to the case of a ratio maximum-to-average of the beam intensity equal to 10 (3).*

| Distance from the target [cm] | 5 | 10 | 15 |
|---|---|---|---|
| p + Au coll. | 1.1 (2.7) | 2 (4) | 2.3 (8) |
| Au + Au coll. | 0.4 (1.1) | 1 (2.3) | 2 (5.3) |

**Table 5.3:** *Ratio between the expected output bandwidth of MIMOSIS-1 (of 800 MHz) and $D_F^{1\%}$ (see Figure 5.28), as a function of the distance between the target and the MVD station, and in the case of p + Au and Au + Au collisions. The first numbers (numbers in parentheses) correspond to the case of a ratio maximum-to-average of the beam intensity equal to 10 (3).*

of 1.3 (see Table 5.2). Note that a MVD station located from 5 to 10 cm from the target provides the necessary vertexing precision for open charm measurements in p + Au collisions (see [104], and Chapter 6 of the present thesis in the Au + Au case). On can thus conclude that a bandwidth of 400 MHz for MIMOSIS-1 is suitable for the open charm measurement envisaged by CBM at SIS100. In addition, an output bandwidth of 800 MHz would allow MIMOSIS-1 tolerating important beam intensity fluctuations at 5 cm from the target. Alternatively, such a bandwidth would provide a security margin of 2 at 10 cm (see Table 5.3).

In Au + Au collisions, a MVD station located at 10 or 15 cm from the target is very likely to improve the impact parameter resolution for low-mass vector-meson measurements. As for multi-strange hyperons, given their relatively long decay length (with respect to open charm particles), a MVD station located at 15 cm from the target (for example) is also likely to improve their measurements, if needed. A sensor with an output bandwidth of 400 MHz can be placed at 10 cm from the target, if the beam intensity fluctuations are low, or at 15 cm to be able to sustain large fluctuations. One can conclude that a bandwidth of 400 MHz for MIMOSIS-1 is appropriate for low-mass vector-meson and strangeness measurements at SIS100. An output bandwidth of 800 MHz, moreover, would allow MIMOSIS-1 featuring a security margin of 2 at 15 cm from the target (see Table 5.3). This would allow in turn increasing the beam intensity and measure more statistics of these particles if needed. Considering that the data flow delivered by the most exposed sensor scales remarkably well with the beam intensity (see Appendix C), the latter could be increased by a factor of 2. Note that the expected radiation tolerance of MIMOSIS-1 would permit such an increase of the beam intensity (see Section 5.3.1).

It is important to remark that the amount of embedded memory needed to temporarily store hit

information before transmission is sizable: in between 10 and 40 Kbits for the various scenarii mentioned above if MIMOSIS-1 has a read-out time of 25 $\mu$s (see Figure 5.28). These numbers are a factor of two higher if MIMOSIS-1 has a read-out time of 50 $\mu$s. This is an important issue since the area occupied by the peripheral read-out electronics of MIMOSIS-1 (gray area in Figure 4.8) must not exceed 50% of the total area of the sensor.

### 5.9.2 Data rate requirements for the read-out system

In Section 5.9.1, we have demonstrated that an output bandwidth of 400 MHz or 800 MHz for the MIMOSIS-1 sensor allows it transmitting the data with negligible data loss in the highest hit density region of the MVD detector. Since the data volume delivered by MIMOSIS-1 sensors will be fixed (see Section 5.4.4), all sensors will transmit their data at the same frequency (of either 400 or 800 MHz). In this section, the required bandwidths are given for the main parts of the read-out system (described in Section 5.5).

#### Bandwidth for FPC cables

We have seen in Section 5.4.4 that MIMOSIS-1 will feature 2 output channels, each running at a frequency of either 200 or 400 MHz. Let us remind that FPC cables will feature 10 read-out channels, allowing them reading out up to 5 MIMOSIS-1 sensors (see Figure 5.9). These cables must hence feature a total bandwidth of either 2 or 4 GHz.

#### Bandwidth for the Converter board

Figure 5.29 presents the data transport performed on the converter board. Each sensor output is de-serialized into a 16-bit vector. This is useful to concatenate the data from several sensors in the following multiplexing stage, since the data format consists in 16-bit words. A multiplexing of the output channels of the sensors is performed, in two stages: first, the two output channels of each sensor are multiplexed, then the output channels of the five sensors together. Finally, a 8 bits/10 bits encoding is performed (for data transmission), and an electrical/optical conversion unit serializes the data for transmission to the ROC board.

Table 5.4 presents the necessary bandwidth for the components of the converter board. It also shows the amount of them which have to be implemented on this board to read out five MIMOSIS-1 sensors.

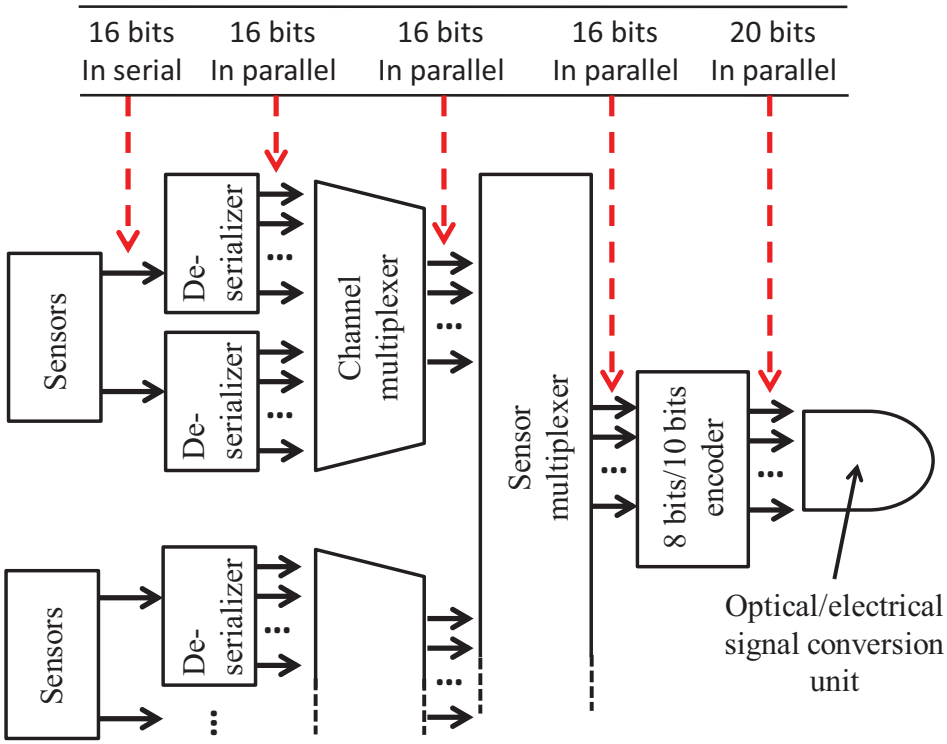


**Figure 5.29:** *Data path through the converter board (see ref. [112])*

| | | CB | | | | |
|---|---|---|---|---|---|---|
| | | De-serializer | Channel multiplex. | Sensor multiplex. | 8bits/10bits encoder | Convers. unit |
| input | bandwidth [MHz] | 200 (400) | 12.5 (25) | 25 (50) | 125 (250) | 125 (250) |
| | channel(s) | 1 | $2 \times 16$ | $5 \times 16$ | 16 | 20 |
| output | bandwidth [MHz] | 12.5 (25) | 25 (50) | 125 (250) | 125 (250) | $2.5\ (5) \times 10^3$ |
| | channel(s) | 16 | 16 | 16 | 20 | 1 |
| | amount | 10 | 5 | 1 | 1 | 1 |

**Table 5.4:** *Bandwidth required for the components of the converter board for SIS100 operation, in the case MIMOSIS-1 features two output channels running at a frequency of 200 MHz (first numbers) or 400 MHz (numbers in parentheses). The number of channels at the input and output of the components, and the amount of these components which have to be implemented to read out five MIMOSIS-1 sensors are also shown.*

| | 5 cm | 10 cm | 15 cm |
|---|---|---|---|
| p + Au collisions | 360 | 420 | 480 |
| Au + Au collisions | 900 | 840 | 660 |

**Table 5.5:** *Average data flow [Mbits/s] that the read-out chain will have to handle to read out the most exposed sensors, in the cases of p + Au and Au + Au collisions as a function of the distance from the target.*

**Bandwidth at the output of the ROC**

Let us remind that only sparsified and average data flow must be transmitted at the output of the ROC board (see Section 5.5). Additionally, the output bandwidth of this board can be increased, if needed, by adding more read-out cables (as there is no spatial limitation for output drivers, connectors, etc).

Table 5.5 gives the zero-suppressed and average data flow that the read-out chain will have to handle to read out the most exposed sensors. Currently, an output bandwidth of 6 Gbits/s is foreseen to ship the data to the data acquisition system, using 6 optical cables with 1 Gbits/s each. In the case of p + Au and Au + Au collisions, the maximal payload (data flow in percentage of the bandwidth at the output of the ROC) does not exceed 8 and 15%, respectively. The envisaged output bandwidth of the ROC thus provides comfortable security margins of 6.7 and 12.5. These security margins are useful to cope with additional information (channel ID, time stamps, etc) which will be added in the data stream (as discussed in Section 5.5) and which is neglected in the present simulations.

## 5.10 Summary

The purpose of this chapter was to determine the data rate requirements for the first generation MVD at the FAIR/SIS100 synchrotron. These requirements were evaluated for the MIMOSIS-1 MAPS sensor, foreseen to equip the MVD detector, as well as for the MVD read-out system.

For MIMOSIS-1, the study was focused on its limitations in terms of data rate capability, in particular, on the restricted number of states (group of neighbor fired pixels) which the internal data sparsification circuits can form within rows of pixels and on the output bandwidth that the sensor can handle.

At SIS100, open charm will be measured in proton-proton and proton-nucleus collisions, at beam energies up to 30 GeV. In nucleus-nucleus collisions, the MVD will also serve to improve the detector performance for low-mass vector meson and multi-strange measurements at beam energies up to 10 GeV (for Au ions). We chose to investigate the cases of p(30 GeV) + Au and Au(10 AGeV) + Au collisions. These conditions (collision system and beam energy) are expected to be the most constraining ones for the MVD detector at SIS100, notably in terms of data rate capability required to handle the expectedly large particle flux. This constraint is

made more stringent by the high collision rates foreseen for the measurements mentioned above, typically $2 \times 10^6$ collisions/s in p + Au and $2 \times 10^4$ collisions/s in Au + Au.

In order to simulate the particle flux in the MVD, detailed Monte Carlo simulations were carried out using the CBMRoot simulation framework and the UrQMD transport model as an event generator. Several aspects of the running conditions, which are relevant for data flow studies, were accounted for: the beam intensity fluctuations, the beam emittance, and the main sources of background particles, in particular, $\delta$-electrons produced in the target material by beam ions.

The contribution of $\delta$-electrons to the hit density reached in the MVD stations has been found to dominate the one from Au + Au collisions. This is particularly the case in the maximal hit density region where Au + Au collisions produce only 0.22 hits/$cm^2$ per event while at the same time $\delta$-electrons are responsible for a hit density of 3.5 hits/$cm^2$. It is therefore important to establish a strategy to shield the MVD stations against $\delta$-electrons. The hits deposited by the latter can be categorized in two parts: "first hits" created by electrons right after their production in the target, and "secondary hits" produced by electrons curling in the CBM magnetic field. It was shown that by adding material around the MVD stations, "secondary" hits can be suppressed due to the absorption of spiraling electrons. This leads to a substantial decrease of the hit rate from $\delta$-electrons in the MVD detector (by a factor of $\sim 2$). However, the maximal hit density, dominated by first hits, can only be moderately decreased (by about $14\%$). The large and highly inhomogeneous particle flux imposes strong constraints on the design of the MVD sensors and on the read-out system, which must provide, locally, very high data rate capability.

The collision pile-up in MIMOSIS-1 sensors was simulated, taking into account their expected read-out time (of 25 $\mu$s), and under two assumptions on the beam intensity fluctuations at SIS100: "low" beam intensity fluctuations, corresponding to a ratio maximum-to-average of the beam intensity equal to 3 as measured at the SIS18 synchrotron, and "large" beam intensity fluctuations, corresponding to a ratio maximum-to-average of the beam intensity equal to 10 as a safe assumption for both proton and Au beams at SIS100. Based on the simulated collision pile-up, a procedure was used to estimate the amount of states that the sparsification circuits of MIMOSIS-1 will have to process, and the data flow that this sensor will have to deliver. These requirements were estimated for the sensor located in the highest hit density region.

In the case of large beam intensity fluctuations, we found that up to 18 and 36 states have to be formed by the sparsification circuits in p + Au and Au + Au collisions, respectively. These numbers are below the 40 states that MIMOSIS-1 will be able to handle. This demonstrates that the projected performances of the sparsification circuits of MIMOSIS-1 are fully satisfactory for the MVD operation at SIS100.

The expected output bandwidth of MIMOSIS-1, of either 400 MHz or 800 MHz, was found to be the leading constraint for the minimal distance to the target at which the first MVD station can be placed. In p + Au collisions, the data flow that MIMOSIS-1 will have to handle amounts to 300 (700) MBits/s at 5 cm from the target, in conditions of low (large) beam intensity fluctuations. A sensor with 400 MHz output bandwidth must be placed at a minimal distance of 10 cm from the target to sustain large beam intensity fluctuations, or at 5 cm if these fluctuations are low. Be reminded that a first MVD station located at distances from 5 to 10 cm provides the necessary

vertexing precision for open charm measurements in p + Au collisions. One can conclude that the projected output bandwidth of MIMOSIS-1 is suitable for open charm measurements at SIS100. In addition, an output bandwidth of 800 MHz would allow MIMOSIS-1 tolerating large beam intensity fluctuations down to 5 cm from the target, or alternatively, with a comfortable security margin of 2 at 10 cm.

In Au + Au collisions, the data flow which MIMOSIS-1 will have to handle amounts to 360 (800) MBits/s at 10 cm from the target in conditions of low (large) beam intensity fluctuations. With an output bandwidth of 400 MHz, MIMOSIS-1 could operate at 10 cm if the beam intensity fluctuations are low, or at 15 cm if they are large. Let us recall that a first MVD stations located at distances from 10 to 15 cm is likely to improve low-mass vector meson and strangeness measurements. One can conclude that the projected output bandwidth of MIMOSIS-1 is suitable for these measurements in Au + Au collisions. Additionally, if MIMOSIS-1 features an output bandwidth of 800 MHz, this would allow this sensor tolerating important beam fluctuations at 15 cm with a comfortable security margin of 2.

Finally, the requirements in terms of bandwidth for the MVD read-out system were addressed based on its current concept for SIS100. The simulations performed for this purpose provided detailed bandwidth requirements for the most sensitive parts of the read-out system, considering an output bandwidth of 400 MHz or 800 MHz for MIMOSIS-1 sensors. The results show that the read-out chain has to feature a total bandwidth of 4 GHz (5 GHz including 8 bits/10 bits encoding). This imposes strong constraints on the design of the different components of the MVD read-out system.

# Chapter 6

# Reconstruction of open charm particles

The purpose of this chapter is to investigate, by means of detailed Monte-Carlo simulations, the expected performance of the CBM detector for the reconstruction of open charm mesons in nucleus-nucleus collisions. Open charm particles decay close to the collision point (or primary vertex). Their average life time is very short, on the order of a picosecond (see Table 4.1, in Chapter 4), which corresponds to a typical decay length of several 100 $\mu$m in the laboratory frame. Thus, the identification of open charm mesons must be done by measuring their daughter particles. One then has to combine all particles produced in nuclear collisions in multiplets, according to the chosen decay channel of the signal, and reconstruct their invariant mass. Due to the very low multiplicity of open charm particles at FAIR energies, and the large multiplicities of hadrons produced in collisions of heavy nuclei, this method leads to a huge combinatorial background of uncorrelated particle multiplets. A strategy aiming at suppressing this background by several orders of magnitude is thus mandatory to extract the signal. This strategy makes use of the displaced decay vertex of open charm mesons with respect to the primary vertex, which results into differences in the topology of the signal and uncorrelated multiplets. The extraction of the signal can be achieved by applying appropriate topological selection cuts.

The simulations presented in this chapter have been carried out for $D^+$ mesons produced in central Au + Au collisions at a beam energy of 25 GeV/nucleon. The $D^+ \rightarrow \pi^+ \, \pi^+ \, K^-$ hadronic decay channel has been chosen for this study. This choice was motivated by the fact that the reconstruction of such decay channel (involving three daughter particles) is particularly challenging.

The chapter is organized as follows. It begins with a brief reminder on the physics related to open charm particles and the experimental challenge imposed by their measurement (Section 6.1). In Section 6.2, the simulation procedure is described in detail step by step. The detector setup is presented in Section 6.3. Then the method used to reconstruct $D^+$-mesons is presented (Section 6.4.1) along with the strategy employed to separate the signal from the combinatorial background (Section 6.4.2). The results are reported in terms of the signal reconstruction efficiency and the signal-to-background ratio (Section 6.5). Finally, an estimate of the expected statistics per running year is given for different D-meson species.

## 6.1 Introduction

As mentioned earlier (Chapter 3), open charm production will be one of the major physics topics addressed by the CBM experiment at the FAIR facility. CBM will measure open charm hadrons for the first time at center-of-mass energies per nucleon pair below 10 GeV (close to their kinematical production threshold). Such measurements are very important for understanding the mechanism of charm production, whose nature is still unclear at these low energies. Furthermore, the relative yields of charmed hadrons in heavy-ion collisions are expected to be sensitive to the deconfinement of nuclear matter. This phenomenon would be reflected for example in changes in the relative abundance of charmonium and D-mesons. The study of open charm hadrons can also provide valuable information on in-medium effects as their effective mass is expected to be modified in the hot and dense nuclear medium, possibly due to the effect of chiral symmetry restoration. Experimental investigations of these effects would thus shed light on fundamental issues like the deconfinement and the restoration of chiral symmetry.

The measurement of open charm hadrons is an experimental challenge at FAIR energies because of their extremely low multiplicities (threshold production), typically on the order of $10^{-5}$ in Au(25 AGeV) + Au collisions. The strategy foreseen to identify these particles is based on the reconstruction of their decay vertex. Due to their very small average proper decay length (see Table 4.1, in Chapter 4), the separation between the collision point and their decay vertex is a very delicate task.

In this chapter, we present detailed simulations aiming at demonstrating the feasibility of open charm measurements in the CBM experiment. We choose to study the reconstruction of $D^+$ mesons decaying into $\pi^+$ $\pi^+$ $K^-$, in the case of central Au + Au collisions at a beam energy of 25 GeV/nucleon. These conditions (system, energy, centrality) are considered to provide a typical environment for open charm reconstruction at FAIR energies.

The identification of $D^+$ mesons will be performed by reconstructing the invariant mass of triplets of charged particles (two positively charged and one negatively charged). This task is particularly challenging in nucleus-nucleus collisions: due to the high charged particle multiplicities (one expects roughly 1000 charged particles in a central Au(25 AGeV) + Au collision), the uncorrelated triplets are expected to create a huge combinatorial background.

The low production multiplicities of open charm particles at FAIR energies call for high collision rate measurements. The FAIR accelerator is designed to provide very high beam intensities, up to $10^9$ ions/s for Au ions. This should allow for measurements at collision rates as high as 10 MHz (assuming an interaction probability of $1\%$ in the target). Open charm measurements will be, however, limited by the collision rate at which the MVD detector will be able to operate. This will be discussed later (see Section 6.5.3).

## 6.2 Simulation procedure

The simulation studies presented in this work were carried out by means of the CbmRoot simulation and analysis framework [106]. In this section, we describe the main steps of the simulation procedure, and we illustrate the performances achieved for the reconstruction of charged particle tracks, for the primary collision vertex and for the secondary $D^+$ decay vertex.

### 6.2.1 Simulation steps

The main simulation steps are displayed in Figure 6.1. The first step consists in generating nuclear collisions, each of them producing a certain number of particles. The latter are transported (second step) through the detector setup using the GEANT3 transport code [107], taking into account the geometry of the MVD and STS stations and their thicknesses. The points of intersection between the particle trajectories and the detector planes (referred as hits) are then smeared to account for the single-point resolution of the tracking stations (i.e. MVD and STS stations). The next step consists in reconstructing the tracks of particles traversing the detector. This is done mainly in 2 steps: the track finding procedure correlates the hits belonging to the same track and the track fitting procedure extracts the parameters of the tracks (e.g. charge and momentum) using a fit of the particle trajectories in the magnetic dipole field. The information on the particle momentum (vector) and track transverse position in the first detector plane is then used to extrapolate the particle trajectories towards the collision point (accounting for their deflection in the magnetic dipole field). This extrapolation allows reconstructing the primary collision point and the secondary decay vertex of open charm mesons using $\chi^2$ minimization procedures. Finally, the reconstructed tracks are used for the identification of open charm mesons using the invariant mass method (see Section 6.4.1).

### 6.2.2 Event generation

The first step of the simulation is to generate events, defined as nuclear collisions between Au nuclei at a beam energy of 25 GeV/nucleon. Due to the low multiplicity expected for $D^+$ mesons at FAIR energies ($4.17 \times 10^{-5}$ in central Au + Au collisions), a large number of central Au + Au collisions (about $2.5 \times 10^5$) should be simulated in order to produce one $D^+$ decaying into $\pi^+$ $\pi^+$ $K^-$ (with branching ratio of $9.51\%$). Since the computation time needed for such a simulation is excessively long, the approach we adopted is to generate $D^+$ signal events separately from the background events. A normalization procedure will be applied later on in the analysis to account for their multiplicity. The UrQMD microscopic transport code [108] has been used to generate background events, i.e. central Au(25 AGeV) + Au collisions. The procedure to produce $D^+$ signal events is explained below.

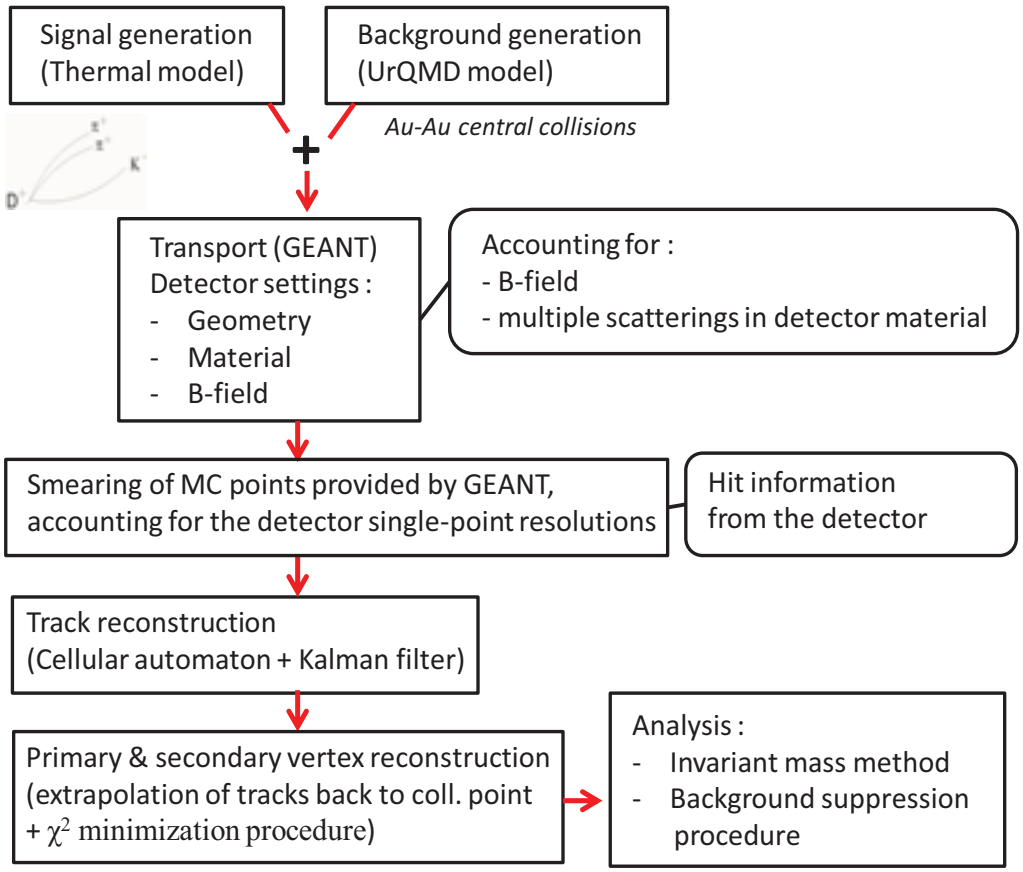


**Figure 6.1:** *Main steps of the simulation procedure.*

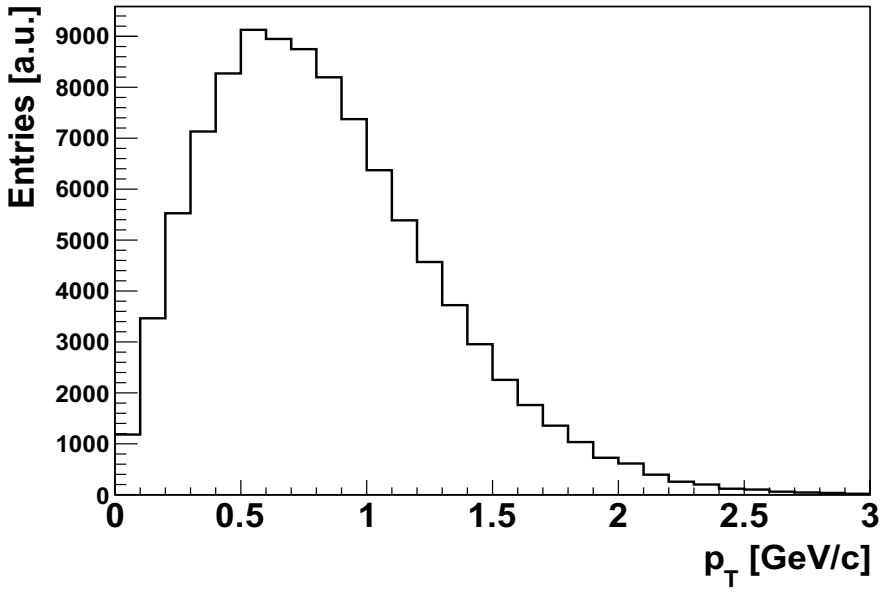


**Figure 6.2:** *Transverse momentum distribution of generated $D^+$ mesons.*

**Generation of $D^+$ mesons**

$D^+$ mesons are generated using a thermal model with a temperature T = 200 MeV. Their transverse momenta ($p_T$) are thus randomly distributed according to the following function:

$$f(p_T) = p_T \times e^{-\frac{m_T}{T}} \tag{6.1}$$

where $m_T$ = $\sqrt{p_T^2 + m_{D^+}^2}$ (with $m_{D^+}$ = 1869.4 MeV/$c^2$ [67]) is the transverse mass, and T the temperature. The transverse momentum distribution of $D^+$ mesons is presented in Figure 6.2. Their rapidity distribution is assumed to follow a Gaussian function with a standard deviation equal to 1 (assumed to be the same as the value predicted by the UrQMD model for pions). This Gaussian function is centered around the center-of-mass rapidity of Au + Au collisions, which is equal to 2 at a bombarding energy of 25 GeV/nucleon.

The decay of $D^+$ mesons into $\pi^+$ $\pi^+$ $K^-$ is done using the Pythia transport code [116]. Their decay length (d) is randomly generated according to the following exponential function:

$$N_{D+}(d) = N_{D+}^0 \times e^{-\frac{|d|}{c\tau}} \tag{6.2}$$

where $N_{D+}^0$ and $N_{D+}$ are the total number of generated $D^+$ mesons and the number of $D^+$ mesons decaying at a distance larger than d, respectively. The decay length of $D^+$ mesons is defined in their rest frame, and $\tau$ is their proper lifetime. For $D^+$ mesons, c$\tau$ equals to 311.8 $\mu$m [67]. The resulting distribution of the number of $D^+$ mesons as a function of the decay length can be seen in Figure 6.3. The red curve shows the result of the fit of this distribution using the function given in Equation 6.2. The parameter of the fit c$\tau$ is found to be approximately equal to 312 $\mu$m. Finally, $D^+$ mesons decay isotropically in their rest frame, giving rise to momenta of the resulting daughter pions and kaons.

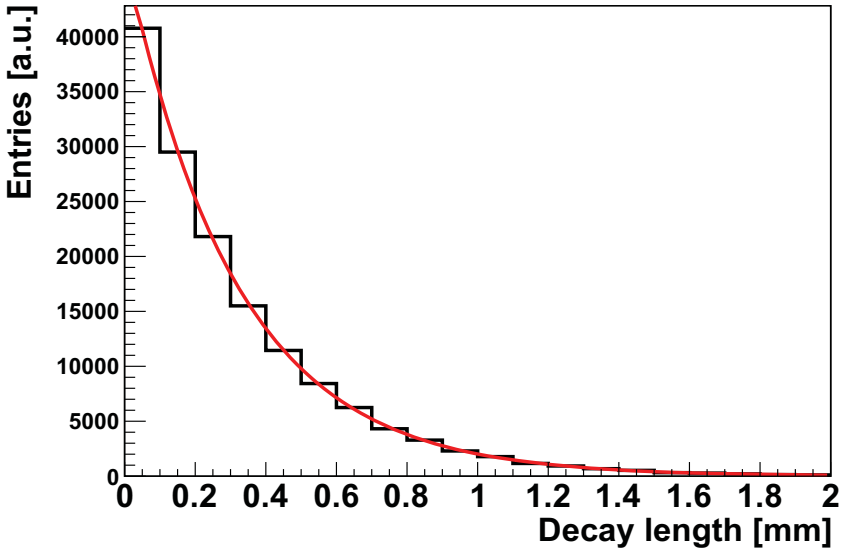


**Figure 6.3:** *Decay length distribution of $D^+$ mesons (histogram) used in the simulations. The red curve shows the result of the fit of this distribution using the exponential function (Equation 6.2).*

In order to simulate the signal in the environment of background hadrons, each signal triplet ($\pi^+$, $\pi^+$, $K^-$ from $D^+$ decay) has been embedded into a central Au + Au collision (generated with UrQMD) to form a signal event.

### 6.2.3 Detector response

The transport of the particles through the CBM detector is done using the GEANT3 transport code [107], developed at CERN for high energy physics. This simulation package treats the interactions of particles with the detector material (including effects such as energy loss, multiple scatterings and secondary particle production) using Monte Carlo procedures. The transport of the particles results in particle hits in the tracking stations. The coordinates of these hits are then randomly smeared using a Gaussian probability distribution. The standard deviation of the latter is taken according to the spatial resolution of the detector stations (given in Table 6.1). This last simulation step is mandatory to provide realistic information on the hit coordinates (taking into account the detector single-point resolutions) to the track reconstruction algorithm.

### 6.2.4 Track reconstruction

The deflection of charged particles due to the presence of the magnetic dipole field of CBM (see Section 6.3) allows their charge and momentum to be determined. It is thus mandatory to

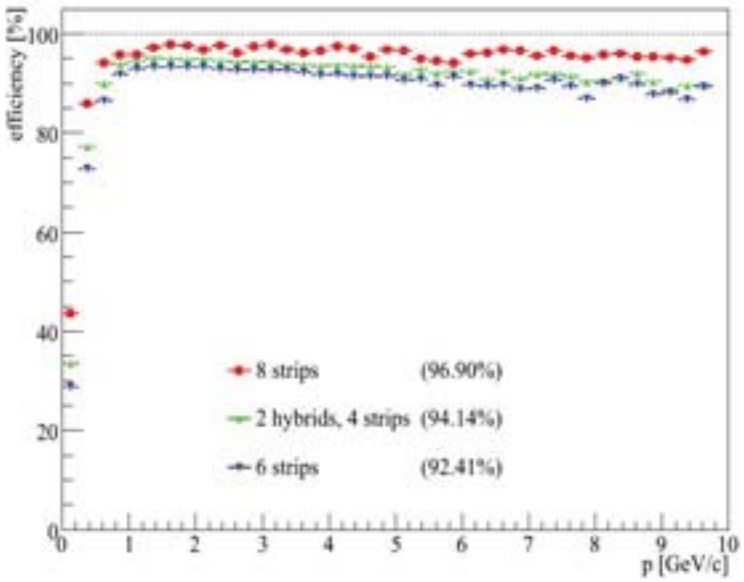


**Figure 6.4:** *Track reconstruction efficiency achieved with the tracking stations (MVD and STS) as a function of the particle momentum for central Au + Au collisions at an incident energy of 25 AGeV [59]. The results are shown for three different STS setups, consisting in: 8 strip stations (red crosses), 2 hybrid and 4 strip stations (green crosses) and 6 strip stations (blue crosses). The second setup configuration (green crosses) is the one used in the present work for the assessment of the performances of open charm particle reconstruction.*

reconstruct each particle trajectory in this field. This procedure consists in two steps. First, the hits belonging to the same particle trajectory are associated with each other, using a Cellular Automaton procedure [117]. Secondly, a Kalman Filter procedure [118] is used to fit the particle trajectory and extract the particle charge and momentum.

Figure 6.4 shows the track reconstruction efficiency achieved with the tracking stations as a function of the particle momentum. The track reconstruction efficiency is defined as the ratio between the number of properly reconstructed particle tracks and the total number of tracks entering the detector acceptance (i.e. with at least four consecutive hits in the tracking stations). A track is properly reconstructed if associated with at least 75% of the true hits (belonging to its original Monte Carlo track). The results are shown for three different STS setups. The green crosses correspond to the setup configuration used in the present work for the assessment of the performances of open charm particle reconstruction (see Table 6.1). The reconstruction efficiency, better than 90% at momenta above 1 GeV/c, is very satisfactory. The degradation observed for particles with momenta below 1 GeV/c (efficiency below 90%) originates from the important diffusion of low-momentum tracks in the detector material. Particles with momentum lower than 200 MeV/c are mostly out of the geometrical acceptance of the tracking detector.

Note that, as we will see later (Figure 6.11), most of the tracks originating from $D^+$ decay have momenta larger than 1 GeV/c and can be, therefore, reconstructed with very high efficiency.

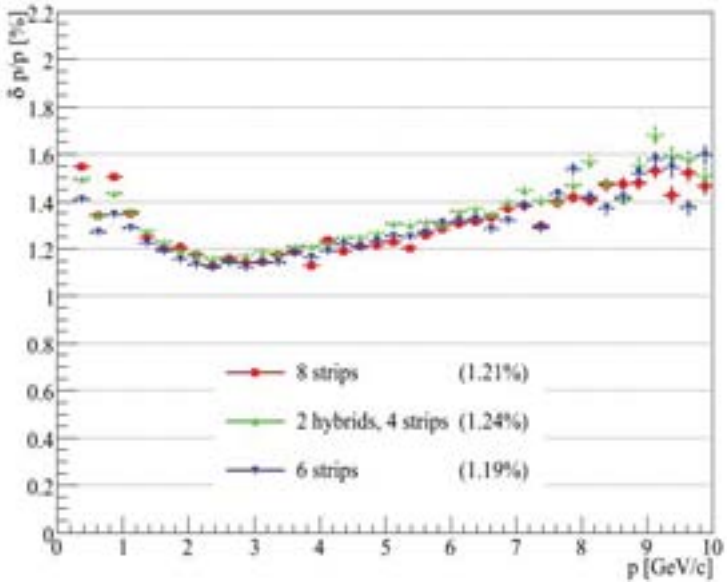


**Figure 6.5:** *Momentum resolution achieved with the tracking stations (MVD and STS) as a function of the particle momentum for central Au + Au collisions at an incident energy of 25 AGeV [59]. The results are shown for three STS setups, consisting in: 8 strip stations (red crosses), 2 hybrid and 4 strip stations (green crosses) and 6 strip stations (blue crosses). The second setup configuration (green crosses) is the one used in the present work for the assessment of the performances of open charm particle reconstruction.*

Figure 6.5 shows the momentum resolution achieved with the tracking stations as a function of the particle momentum for three different STS setups. As in the previous figure, the green crosses correspond to the setup configuration used in the present work. The resolution is found to be very good. It is comprised in between 1.2% and 1.6% over the whole momentum range (up to 10 GeV/c). The slight degradation observed below 1 GeV/c comes from the important diffusion of low-momentum tracks in the detector material, while the deterioration occurring at high momenta is an effect of the poorer bending power provided by the magnetic dipole field.

Finally, one can conclude that the performance of the track reconstruction with the STS detector is very satisfactory for particles with momenta above 1 GeV/c, i.e. a track reconstruction efficiency above 90% and a momentum determination with an accuracy on the order of 1.5%.

### 6.2.5 Primary and secondary decay vertex reconstruction

The information on the particle momentum (vector) and track transverse position in the first detector plane is then used to extrapolate the trajectory of the particles towards the collision point (accounting for their deflection in the magnetic dipole filed). This extrapolation allows reconstructing the primary collision vertex and the secondary decay vertex of open charm mesons using $\chi^2$ minimization procedures. All tracks belonging to a given event are used to reconstruct

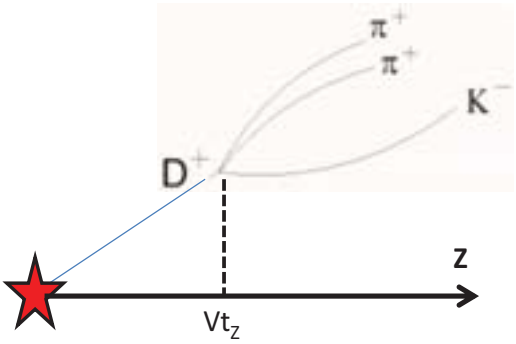


**Figure 6.6:** *Sketch of a $D^+$ meson decaying into $\pi^+$ $\pi^+$ $K^-$. The $vt_Z$ variable is the Z-coordinate of the decay vertex (Z being the beam axis).*

the primary vertex, while in the case of $D^+$ decaying into three particles, the secondary vertex is composed of only three tracks.

Figure 6.7 shows the difference between the z-position of the reconstructed secondary vertex and the z-position of the true (Monte Carlo) vertex. The z-coordinate is defined in the direction of the beam axis (as pictured in Figure 6.6). The secondary vertex resolution is defined as the standard deviation of the Gaussian fit function (red curve) of this distribution.

Typical resolutions on the secondary decay vertex, using realistic detector setups, are below 100 $\mu$m. This resolution depends primarily on the pointing power (momentum vector and position of tracks) provided by the first detector planes, i.e. by the MVD detector. Considering the MVD configuration setup presented in Table 6.1, with a spatial resolution equal to 3 $\mu$m and a thickness equal to 150 $\mu$m silicon equivalent (including the MAPS sensors, their mechanical and cooling support, and their read-out cables), a resolution of the secondary vertex of 72 $\mu$m is achieved, as shown in Figure 6.7.

The achieved resolution on the primary collision vertex is less than a micrometer in the transverse plane, and of a few micrometers along the beam axis. It is much better than the resolution achieved for the open charm decay vertex due to the fact that there are a few hundreds charged particles pointing to the primary vertex per central Au(25 AGeV) + Au collision.

## 6.3 Detector setup

The detector setup used to evaluate the performances of open charm reconstruction is shown in Figure 6.8. As one can see on the left panel, it consists of a MVD detector composed of two silicon stations located at distances of 10 and 20 cm from the target (indicated in red color), and a STS detector constituted of 6 silicon stations located at 30, 40, 50, 60, 75 and 100 cm (magenta and blue). Their transverse dimensions cover polar angles ranging from 2.5 to 25

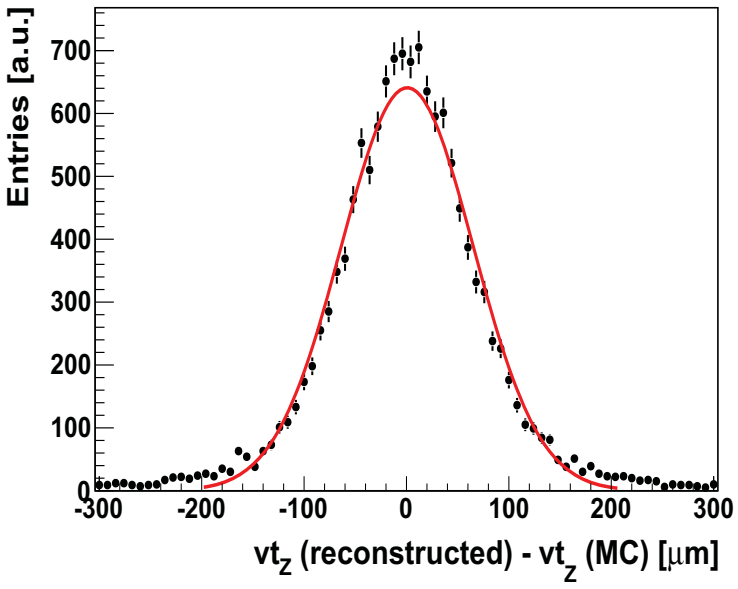


**Figure 6.7:** *Resolution on the z-position (along the direction of the beam axis) of the decay vertex of $D^+ \rightarrow \pi^+ \pi^+ K^-$ embedded into simulated central Au(25 AGeV) + Au collisions. The distribution is fitted with a Gaussian function (red curve).*

degrees (corresponding to the acceptance of CBM). The MVD and STS are placed inside the dipole magnet. The two stations of the MVD are located inside the beam pipe (shown in blue color in the right-hand side of Figure 6.8), which is a carbon tube of 0.5 mm thickness. As can be seen in the figure, the shape of the beam pipe is modified around the MVD in order to allow for the later to be located in the vacuum.

The main features of the MVD and STS stations, as used in the present simulations, are indicated in Table 6.1. The MVD stations are equipped with MAPS pixels. The two first STS stations are made of silicon hybrid pixels (see Section 3.3.2), while the last four stations are constituted of silicon strip sensors. Each station is represented in the simulations as a silicon disk oriented perpendicular to the beam axis. The material budget is assumed to correspond to 150 $\mu$m, 400 $\mu$m and 750 $\mu$m, respectively, for MAPS pixel, silicon strip and hybrid pixel stations.

The magnet is represented in the simulations by an iron structure enclosing the target, MVD and STS stations (details on the magnet can be found in Chapter 3). It provides a magnetic dipole field with a strength of 1 Tesla in the target region, which allows for a very good momentum resolution. The target is assumed to be a Au plate with a radius of 0.25 mm and a thickness of 250 $\mu$m. This thickness corresponds to an interaction probability of 1% for a Au beam at 25 GeV/nucleon.

The Time Of Flight (TOF) detector is not included in the present simulations. However, it is assumed that all protons are identified and rejected. This assumption is based on the excellent identification capabilities of the TOF [71]. In particular, it is justified for momenta below 6 GeV/c (see Figure 3.7, in Chapter 3). The rate of particles with momenta above 6 GeV/c is rela-

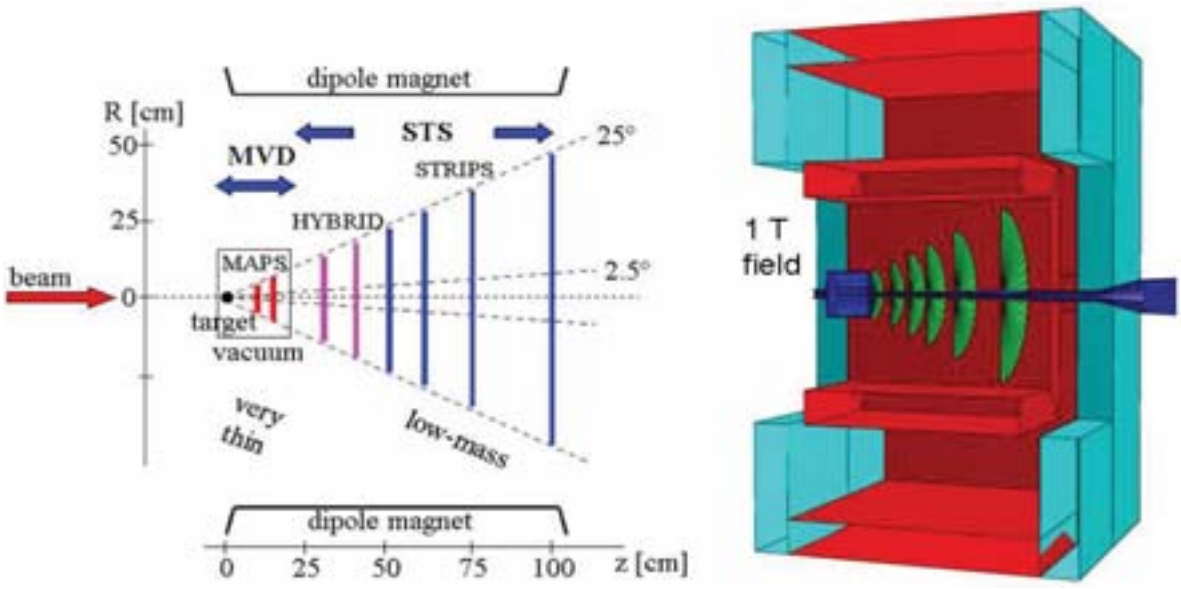


**Figure 6.8:** *The left side shows a schematic side view of the target (black circle), MVD (red) and STS stations (magenta and blue). The MVD stations are located in a vacuum vessel. The transverse dimensions of the stations are indicated, as well as the polar angular coverage (2.5-25 degrees). The right panel shows the complete geometry as used in the simulations. One can see the beam pipe (blue), inside which the MVD stations are located, the STS stations (green), and the magnet (red and light blue).*

| Station | z [cm] | $R_{inner}$ [mm] | $R_{outer}$ [mm] | Technology | spat. resolution [$\mu$m] | Thickness [$\mu$m] |
|---|---|---|---|---|---|---|
| 1 | 10 | 5.5 | 50 | MAPS | 3 | 150 |
| 2 | 20 | 10.5 | 100 | MAPS | 3 | 150 |
| 3 | 30 | 13.1 | 139.9 | HYBRID | 30 | 750 |
| 4 | 40 | 17.5 | 186.5 | HYBRID | 30 | 750 |
| 5 | 50 | 21.8 | 233.2 | STRIPS | 17 | 400 |
| 6 | 60 | 26.2 | 279.8 | STRIPS | 17 | 400 |
| 7 | 75 | 32.7 | 349.7 | STRIPS | 17 | 400 |
| 8 | 100 | 43.7 | 466.3 | STRIPS | 17 | 400 |

**Table 6.1:** *Main features of the detector setup used in the simulations. The second column indicates the distance of the station to the target and the second (third) gives the inner (outer) radius of the station. The thickness of the stations includes the contribution of the mechanical and colling support for the sensors, of servicing and read-out cables. They are given in $\mu$m silicon equivalent.*

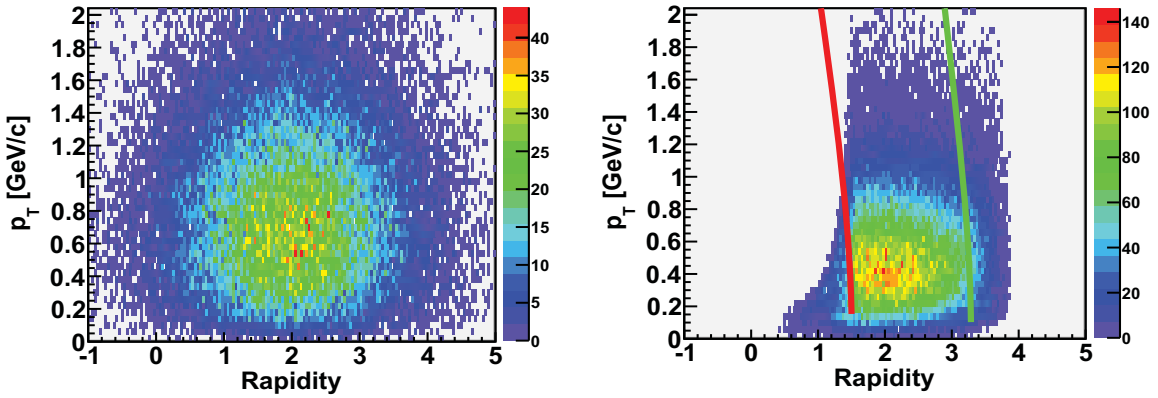


**Figure 6.9:** *Detector acceptance (MVD and STS) for $D^+ \rightarrow K^-\pi^+\pi^+$ in central Au(25 AGeV) + Au collisions, illustrated in the transverse momentum-rapidity plane. Left panel: the initial $4\pi$ distribution. The center-of-mass rapidity is Y = 2. Right panel: the distribution obtained for accepted $D^+$ particles (see text). The red and green curves correspond to constant momenta of 4 and 25 GeV/c, respectively.*

tively low in Au + Au collisions at FAIR energies (see Figure 6.11).

### Detector acceptance for $D^+$ mesons

Figure 6.9 shows the detector acceptance (MVD and STS) for $D^+$ mesons decaying into $K^-\pi^+\pi^+$ in central Au + Au collisions at an incident energy of 25 GeV/nucleon. The left panel corresponds to the initial $4\pi$ distribution, while the right panel shows the distribution of accepted $D^+$ particles. An accepted $D^+ \rightarrow K^-\pi^+\pi^+$ particle is defined here by requiring its three daughter particles to enter the detector acceptance. As one can see in the figure, the detector acceptance covers the region of the mid-rapidity (around Y=2) and a large fraction of the forward hemisphere in the center-of-mass frame (Y $\geq$ 2). The backward region of the distribution can be obtained by symmetry around the center-of-mass point in symmetric systems as Au + Au. The acceptance of $D^+ \rightarrow K^-\pi^+\pi^+$ in the forward hemisphere is satisfactory, of about 58%.

## 6.4 Reconstruction of $D^+$ mesons decaying into $K^-\pi^+\pi^+$

The identification of $D^+$ mesons in their decay channel leading to ($\pi^+$, $\pi^+$, $K^-$), is done via the measurement of their daughter particles and is based on the invariant mass method. As mentioned earlier in this chapter, the identification of the $D^+$ signal requires a very efficient rejection of the combinatorial background due to uncorrelated particle triplets. In this section, we will first present the invariant mass method (Section 6.4.1), and then we will describe the procedure we have used to reduce the contribution of the combinatorial background (Section 6.4.2).

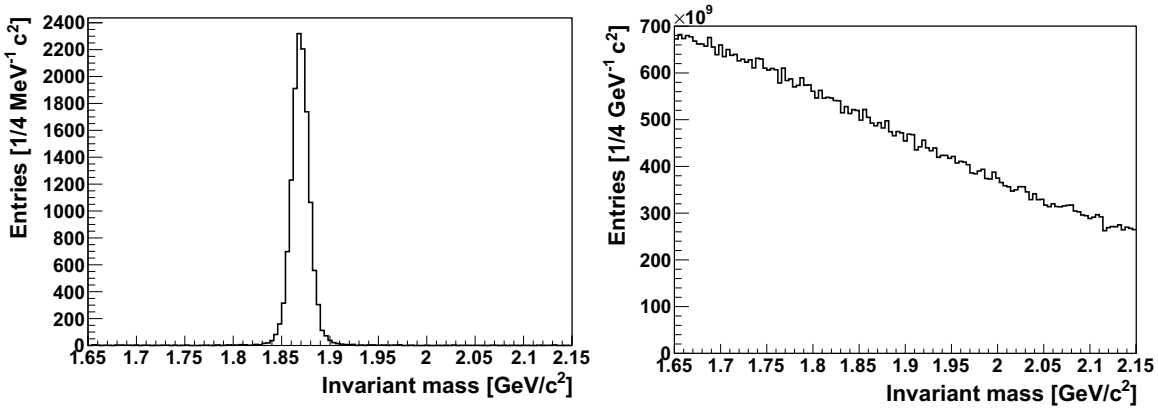


**Figure 6.10:** *Invariant mass distribution of the signal daughter particles (left part) and of uncorrelated charged particle triplets (right part). Note that the latter distribution is shown in the $D^+$ mass region only.*

### 6.4.1 Invariant mass reconstruction

The reconstruction of $D^+$ mesons in their hadronic decay channel into $K^-\pi^+\pi^+$ is based on the invariant mass method. The latter consists in combining event-by-event the measured charged particles into triplets and in determining the invariant mass of those triplets. To do so, one needs the energy and the momentum of the particles. The particle momentum is provided by the STS detector. The particle energy is calculated assuming the pion mass for positively charged particles and the kaon mass for negatively charged ones: $E^2 = m^2 + p^2$, where m is the particle mass. This assumption is needed as no information on the particle identification is available (the TOF detector is not included in the present simulations). The invariant mass of the triplets is then obtained according to the following equation:

$$M_{inv} = \sqrt{(E_{\pi^+} + E_{\pi^+} + E_{K^-})^2 - (\vec{p}_{\pi^+} + \vec{p}_{\pi^+} + \vec{p}_{K^-})^2} \tag{6.3}$$

where E and p are the energy and momentum of particles.

By combining all triplets of charged particles as explained above, one produces a huge combinatorial background. The latter mostly originates from abundant particles like pions, and amounts to about $10^7$ uncorrelated triplets per nuclear collision. Figure 6.10 presents the invariant mass of $D^+$ daughter triplets (left part) and of uncorrelated charged particle triplets (right part). The $D^+$ distribution is obtained for a statistics of 50 000 $D^+$ decaying into $K^-\pi^+\pi^+$, while the background distribution corresponds to 1000 Au(25 AGeV) + Au central events. The latter distribution is normalized in order to be compared to the one of the $D^+$ signal. The normalization factor (F) takes into account the multiplicity of the signal in central Au(25 AGeV) + Au collisions (M), taken from the HSD model [60], and the branching ratio (BR) of the $D^+ \rightarrow K^-\pi^+\pi^+$ decay channel, as follows:

$$F = \frac{50000}{1000 \times M \times BR} \tag{6.4}$$

with M = 4.17 $\times$ $10^{-5}$ and BR = 0.0951.

One can see the that the yield of signal triplets is 8 - 9 orders of magnitude lower than the combinatorial background in the region of the mass of the $D^+$ meson. Clearly, to be able to identify the signal, the combinatorial background must be decreased by several orders of magnitude while keeping, at the same time, the $D^+$ reconstruction efficiency as high as possible.

### 6.4.2 Background suppression strategy

In order to identify the $D^+$ signal, one has to apply selection criteria allowing rejecting a large fraction of the combinatorial background without affecting significantly the signal. In our study, we have used two classes of such selection criteria (or cuts): a first pre-selection based on single track cuts and then a selection based on cuts which are applied to the track triplets.

#### Pre-selection of track candidates

The first step in the selection procedure consists in imposing conditions on individual tracks. The goal here, is to select only tracks that are likely to originate from decay particles of $D^+$ mesons. This first step is very important for reducing the combinatorial background as it reduces the number of candidate tracks that form triplets. The following selection cuts are introduced:

- *Momentum cut (p-cut)*: Track candidates are selected according to their momentum. The average momentum of background particles (of about 2.2 GeV/c) is lower than that of $D^+$ daughter particles (of around 3.9 GeV/c), as illustrated on the left side of Figure 6.11. It is thus possible to introduce a low momentum cut in order to reduce the contribution of background particles. The optimal value of this cut has been determined by maximizing the statistical significance $S/\sqrt{S+B}$. As can be seen in the right panel of Figure 6.11, the maximum of the distribution of the significance lies at a value of p = 1.2 GeV/c. A rejection of particles with momentum less than 1.2 GeV/c allows suppressing 36.5$\%$ of background particles while rejecting only 12.4$\%$ of $D^+$ daughter particles.

- *Transverse momentum cut ($p_T$-cut)*: Track candidates are selected according to their transverse momentum. This cut is based on the fact that the mass of $D^+$ is significantly higher than the one of its daughter particles. Therefore, a significant amount of energy is released in the decay. Due to this effect, it is likely that the decay particles have a higher transverse momentum than many background particles. This is observed on their respective transverse momentum distributions shown in Figure 6.12: the average transverse momentum of background particles (of about 0.32 GeV/c) is lower than that of $D^+$ daughter particles (of around 0.55 GeV/c). One can hence apply a low transverse momentum cut in order to reduce the contribution of background particles. To find the optimal value of this cut, we used the same method as explained for the p-cut. The maximum of significance is found at $p_T$ = 0.3 GeV/c. A suppression of particles with transverse momentum less than 0.3 GeV/c allows suppressing 58.5$\%$ of background particles while rejecting only 21.5$\%$ of $D^+$ daughter particles.

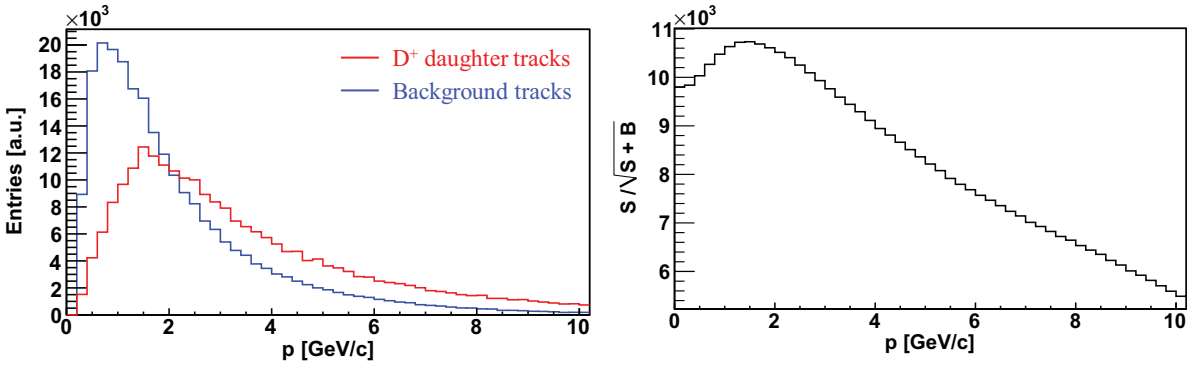


**Figure 6.11:** *Left: Momentum distribution for $D^+$ daughters (red histogram) and background tracks (blue histogram). Right: Statistical significance ($S/\sqrt{S+B}$) as a function of the value used for the p-cut (the significance is obtained by integrating signal and background entries from $+\infty$ down to the value used for the p-cut).*

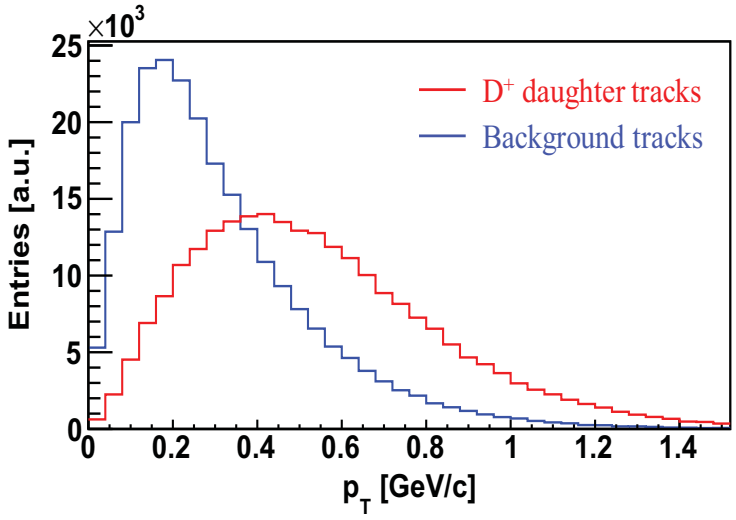


**Figure 6.12:** *Transverse momentum distribution for $D^+$ daughters (red histogram) and background tracks (blue histogram).*

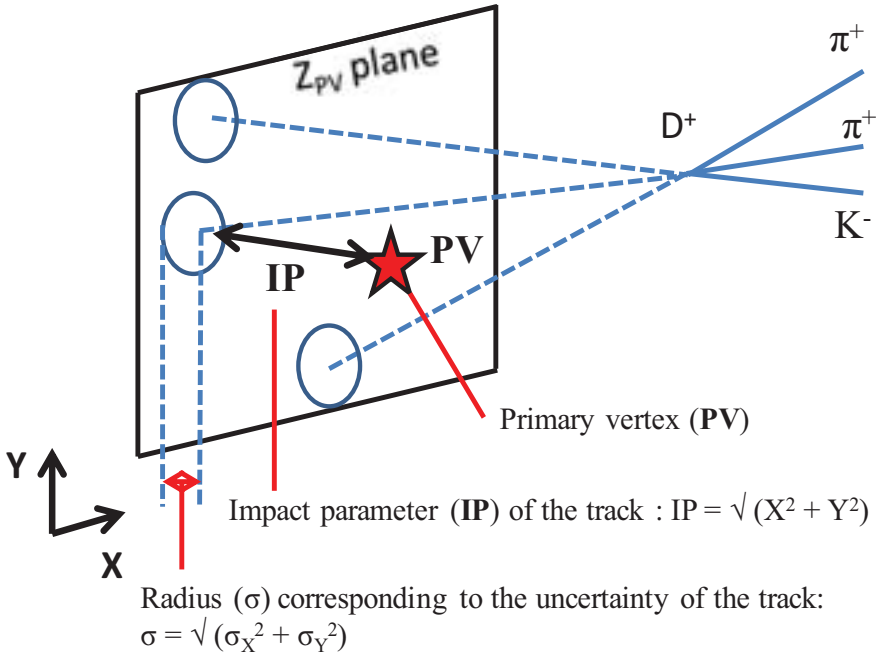


**Figure 6.13:** *Sketch of the topological cuts based on the impact parameter of the tracks.*

The next criteria to select track candidates are based on their impact parameter, defined as the distance between the primary vertex and the impact point of the extrapolated track to the $Z_{PV}$ plane. The latter is the plane perpendicular to the beam axis and containing the primary vertex. One can define three selection cuts related to the impact parameter of the tracks. These topological cuts are illustrated in Figures 6.13 and 6.14. They are the following:

- *Maximum impact parameter cut (IP-cut)*: This cut consists in rejecting tracks with high impact parameter values. It is particularly suited to suppress secondary particles originating from the decay of long-lived particles (compared to $D^+$ mesons), such as $K^0_S$ and hyperons.

- $\chi^2_{prim}$*-cut*: $\chi^2_{prim}$ is the impact parameter of the tracks divided by the extrapolation uncertainty of these tracks. It is obtained as follows:

$$\chi^2_{prim} = (\frac{X}{\sigma_X})^2 + (\frac{Y}{\sigma_Y})^2 \tag{6.5}$$

  with (X,Y) the transverse coordinates of the impact parameter of the track and ($\sigma_X$, $\sigma_Y$) the track extrapolation uncertainties. Note that the $\chi^2_{prim}$ variable is given in units of these uncertainties ($\sigma$ in Figure 6.13). The trajectory of pions and kaons coming from the decay of $D^+$ mesons should not intersect with the primary collision vertex. This cut thus consists in rejecting tracks which have low values of $\chi^2_{prim}$.

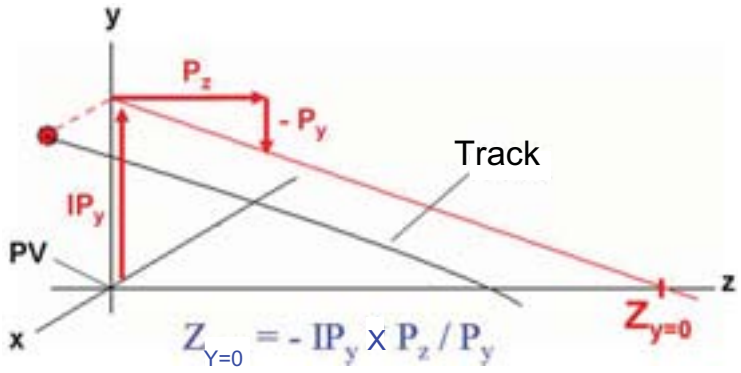


**Figure 6.14:** *Sketch of the topological parameter $Z_{Y=0}$ (see text).*

- $Z_{Y=0}$*-cut*: The variable $Z_{Y=0}$ (see Appendix D) is defined as:

$$Z_{Y=0} = -IP_Y \times \frac{P_Z}{P_Y} \tag{6.6}$$

  where $IP_Y$ is the Y-component of the track impact parameter, and $P_Y/P_Z$ is the Y/Z-component of the momentum of the track extrapolated back to the $Z_{PV}$ plane. This variable is closely related to the track impact parameter (IP). This redundancy is used to insure a more efficient suppression of secondary particles originating from the decay of long-lived strange particles.

In what follows, we will illustrate the effect of each of the three selection criteria defined above.

Figure 6.15 shows the distribution of the $\chi^2_{prim}$ values for primary particles (blue histogram), daughter particles from $D^+$ decay (red histogram), and secondary particles (green histogram) from the decay of long-lived particles like hyperons and $K^0_S$ or produced through interactions with the detector material. As can be seen, all three distributions are peaked close to 0. This means that, to a certain extend, most of particle tracks point back to the primary vertex. This is more pronounced for background (primary and secondary) particles. This effect is trivial for primary particles. For secondary particles, the reason of this effect is that particles created in the detection setup mostly originate from the interaction of primary particles with the target material. Note that the distribution for secondary particles has a relatively long tail towards high $\chi^2_{prim}$ values, which is explained by the contribution of particles originating from the decay of long-lived strange hadrons.

The observation of a maximum close to 0 in the $\chi^2_{prim}$ distribution of $D^+$ daughters is due to the exponential decay distribution of $D^+$ mesons (see Figure 6.3), which makes most of them decay close to the primary vertex. Note that here, the displaced decay vertex topology of $D^+$ mesons shifts the $\chi^2_{prim}$ distribution to higher values compared to background particles. This offers the possibility to introduce a low $\chi^2_{prim}$-cut to reduce the contribution of background particles. The maximum of significance is found at $\chi^2_{prim}$ = 5 $\sigma$. By excluding the tracks associated with a $\chi^2_{prim}$ value below 5 $\sigma$, 94.3% of background particles are suppressed while only 52.8% of $D^+$ daughter particles are rejected.

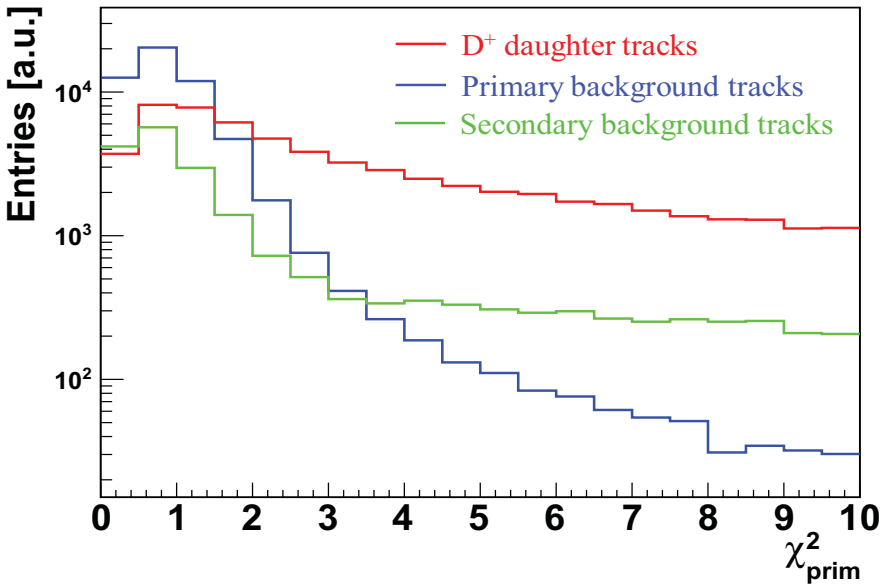


**Figure 6.15:** *Distribution of the $\chi^2_{prim}$ variable (see text), for $D^+$ daughter particles (red histogram), primary (blue histogram) and secondary (green histogram) background tracks. This variable is given in units of the track extrapolation uncertainties (see Equation 6.5).*

After having applied the $\chi^2_{prim}$-cut, the combinatorial background at this stage is mostly due to the contribution of secondary particles ($\sim 50\%$). Note that the latter is mostly composed of charged decay products originating from long-lived strange particles ($\sim 74\%$). Let us remind that the impact parameter IP and $Z_{Y=0}$ variables allow distinguishing $D^+$ daughter particles from secondary particles originating from long-lived strange hadrons. Table 6.2 presents long-lived strange hadrons whose main decay channel contains at least one charged particle (except protons, which are suppressed using the information provided by the TOF detector). The first five particles are strange baryons, whose charged daughter particles constitute about $7\%$ of the background secondary tracks at this stage (after application of the cuts in p, $p_T$ and $\chi^2_{prim}$). The last particle is the $K^0_S$ meson whose daughter charged pions constitute around $67\%$ of the background secondary tracks at this stage. The mean decay length of long-lived strange particles is on the order of 10 cm in the laboratory frame, e.g. 10.3 cm in the case of the $K^0_s$ meson. These particles will, therefore, decay far from the primary vertex as compared to $D^+$ mesons, which makes the impact parameter IP and $Z_{Y=0}$ suitable topological variables to suppress background tracks while preserving $D^+$ daughters.

Figures 6.16 and 6.17 show the distributions of the impact parameter IP and of the $Z_{Y=0}$ variable for $D^+$ daughters and background tracks, obtained after the application of the cuts in p, $p_T$ and $\chi^2_{prim}$. As one can see in Figure 6.16, the impact parameter distribution of background secondary particles (green histogram) is almost constant in the IP range plotted in the figure (0 to 0.14 cm), which is explained by the long decay length of long-lived strange particles. This also explains the relatively constant distribution of the $Z_{Y=0}$ variable (for $Z_{Y=0} > 0$) for background secondary

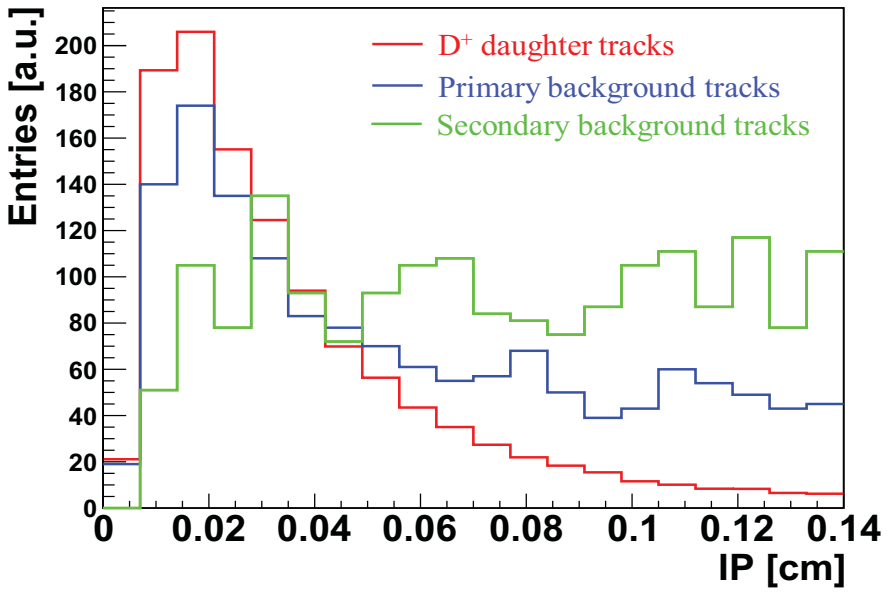


**Figure 6.16:** *Distribution of the track impact parameter for $D^+$ daughter tracks (red histogram), primary (blue histogram) and secondary (green histogram) background tracks. For the sake of visibility, the range plotted on the abscissa only goes up to 0.14 cm.*

| Long-lived strange particles | $\Lambda$ | $\Xi^0$ | $\Xi^-$ | $\Sigma^+$ | $\Sigma^-$ | $K^0_S$ |
|---|---|---|---|---|---|---|
| $\gamma \times \beta \times c\tau$ [cm] | 30 | 33 | 18.6 | 9 | 16.7 | 10.3 |
| Main decay channel | p $\pi^-$ | $\Lambda$ $\pi^0$ | $\Lambda$ $\pi^-$ | n $\pi^+$ | n $\pi^-$ | $\pi^+$ $\pi^-$ |

**Table 6.2:** *Long-lived strange particles whose main decay channel includes at least one charged daughter particle. Their mean decay length in the laboratory frame at a beam energy of 25 GeV/nucleon is also indicated [67].*

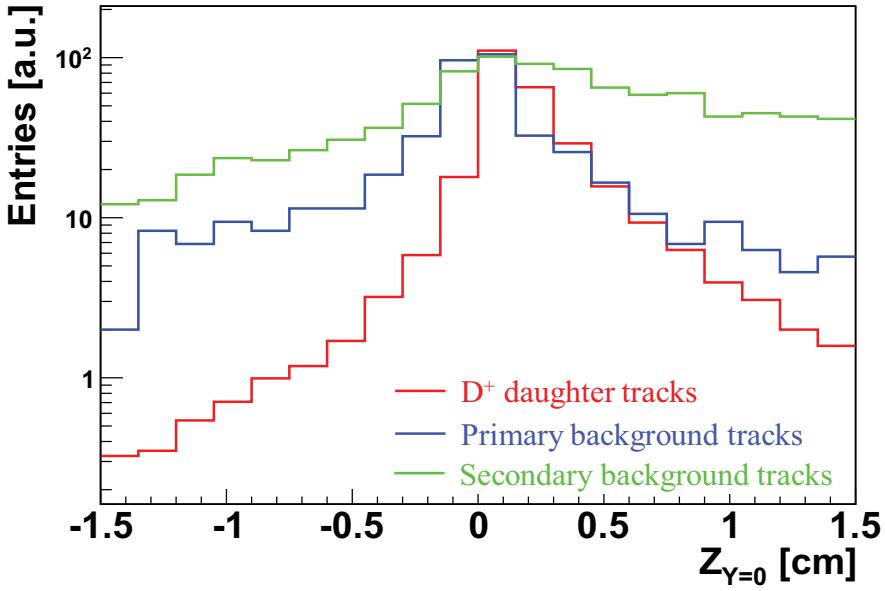


**Figure 6.17:** *Distribution of the $Z_{Y=0}$ variable (see text), for signal daughters (red histogram), primary (blue histogram) and secondary (green histogram) background tracks.*

| Cuts on tracks | p < 1.2 GeV/c | $p_T$ < 0.3 GeV/c | $\chi^2_{prim} < 5\ \sigma$ | Total |
|---|---|---|---|---|
| Background rejection (%) | 36.5 | 58.5 | 94.3 | 98 |
| Signal loss (%) | 12.4 | 21.5 | 52.8 | 59 |

**Table 6.3:** *Effect of the application of each individual cut ($p$, $p_T$ and $\chi^2_{prim}$) on background tracks and on $D^+$ daughter particles. The last column indicates the overall effect of the application of all three cuts.*

particles (green histogram in Figure 6.17). Figures 6.16 and 6.17 show that, in the case of $D^+$ daughter particles (red histograms), both IP and $Z_{Y=0}$ distributions are peaked at a value close to zero, as expected since most of $D^+$ mesons decay close to the primary vertex. As a consequence, one can select tracks by applying an upper cut on these two topological variables. The maximum of significance is found at IP = 0.08 cm and $Z_{Y=0}$ = 1 cm. A rejection of tracks with an impact parameter IP above 0.08 cm and a $Z_{Y=0}$ variable above 1 cm is performed. The IP and $Z_{Y=0}$ cuts allow suppressing, respectively, 66.8 and 30% of background particles, while rejecting only 11.7 and 5.6% of $D^+$ daughter particles (these percentages are given on the basis of the tracks surviving the previous three cuts).

Tables 6.3 and 6.4 give a summary of the effect of the selection cuts. The three cuts in $p$, $p_T$ and $\chi^2_{prim}$ together reject 98% of the background tracks (mainly as an effect of the $\chi^2_{prim}$-cut) while suppressing only 59% of $D^+$ daughter particles. The application, in addition, of the other two cuts (IP and $Z_{Y=0}$) allows removing 72.7% of the background tracks and only 14% of $D^+$ daughter particles surviving the first three cuts.

| Cuts on tracks | IP > 0.08 cm | $Z_{Y=0}$ > 1 cm | Total |
|---|---|---|---|
| Background rejection (%) | 66.8 | 30 | 72.7 |
| Signal loss (%) | 11.7 | 5.6 | 14 |

**Table 6.4:** *Effect of the application of each individual cut (IP, $Z_{Y=0}$) on background tracks and on $D^+$ daughter particles. The percentages are given on the basis of the tracks which survive the three previous cuts (in p, $p_T$ and $\chi^2_{prim}$). The last column indicates the overall effect of the application of both cuts.*

Note that the above pre-selection step allows reducing substantially the computing time needed for the next step of the reconstruction procedure.

### Selection of signal candidates

The second step of the reconstruction procedure consists in combining the selected particle tracks from the first reconstruction step into triplets to form $D^+ \rightarrow K^-\pi^+\pi^+$ signal candidates. This is done by combining particles into triplets of two positively charged particles and one negatively charged particle. Then one must apply additional selection criteria to those triplets in order to extract the $D^+$ signal.

As mentioned earlier in this chapter, one would need to generate about 2.5 $\times$ $10^5$ (central) Au + Au collisions to produce one $D^+$ meson decaying into $K^-\pi^+\pi^+$. Under these conditions, in order to achieve sufficient statistics for open charm studies, one would have to simulate a very large number of collisions (on the order of several hundreds of millions), which is not possible due to computation time constraints. To overcome this problem, we have used the so-called "Super-Event" technique. The latter is inspired from the mixed-event technique used to estimate the combinatorial background in the analysis of experimental data.

In order to identify $D^+$ particles on the basis of their invariant mass distribution, two positively charged tracks are combined with a negatively charged one. In the conventional analysis, this operation is performed using the tracks from the same collision. The number of track triplets ($N_{trip}$) for the combinatorial background is then equal to:

$$N_{trip} = n \times p \times p \times N \tag{6.7}$$

with p and n, respectively, the number of positively charged and negatively charged particles per central Au + Au collision, and N the number of collisions.

In the Super-Event technique, one combines the tracks belonging to different collisions. The number of charged particle triplet combinations ($N^{SE}_{trip}$) is then equal to:

$$N^{SE}_{trip} = (n \times N) \times (p \times N) \times (p \times N) = n \times p \times p \times N^3 \tag{6.8}$$

This corresponds to $N^3$ equivalent events. With this approach, it is possible to raise the statistics of the combinatorial background by a factor of $N^2$ ($N^{SE}_{trip}$ = $N_{trip} \times N^2$), which allows us over-

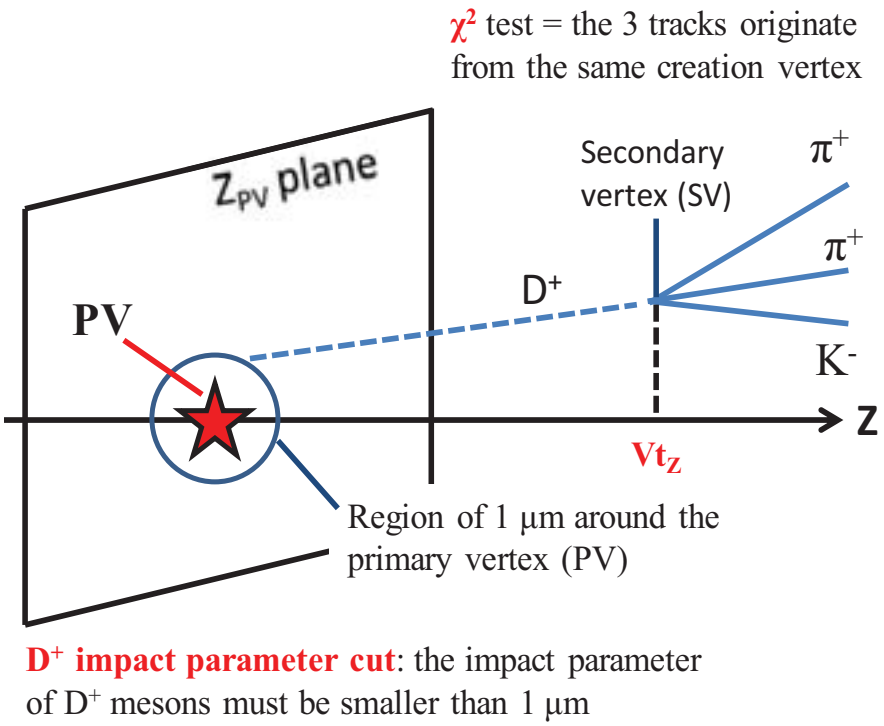


**Figure 6.18:** *Sketch of the topological cuts applied to the triplet candidates (see text).*

coming the CPU time limitation. In this work, N = 1000 central Au + Au collisions were used, which corresponds to $10^9$ equivalent events.

The strategy to reduce the number of background track triplets is based on the selection of displaced-vertex topologies: the selection criteria make use of the separation between the primary collision vertex and the decay vertex of $D^+$ mesons. These selection criteria are illustrated in Figure 6.18.

They are the following:

- $vt_Z$*-cut*: $vt_Z$ is the distance between the reconstructed vertex of $D^+$ decay candidates and the primary collision vertex projected on the beam axis. This selection criterion consists in a lower cut to select triplets which have a displaced-vertex topology. Figure 6.19 (left side) shows the $vt_Z$ distributions for signal (red histogram) and background (blue histogram) triplets. As expected, these distributions differ from each other: background triplets have an almost symmetric $vt_Z$ distribution, while signal triplets have a $vt_Z$ distribution which reflects the exponential decay of $D^+$ mesons (see Figure 6.3). Both the shift of the background distribution towards positive values and the abrupt drop of the signal distribution at a value close to zero originate from the $\chi^2_{prim}$-cut in the track candidate pre-selection stage: it suppresses a large fraction of primary particles, but also particles originating from $D^+$ mesons decaying close to the primary vertex. A lower cut on this variable is thus introduced to suppress the background. The value of this cut has been obtained by maxi-

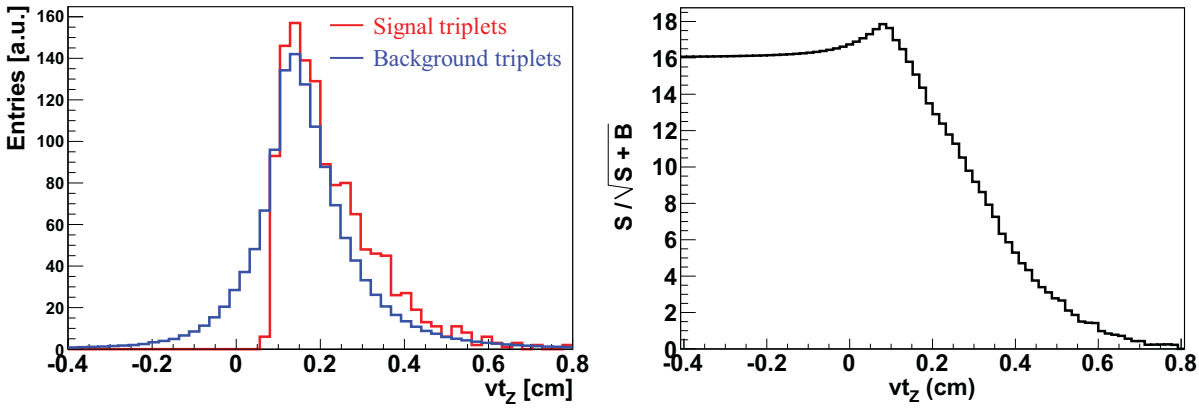


**Figure 6.19:** *Left panel: Distribution of the $vt_Z$ variable for signal (red histogram) and background (blue histogram) triplets. Right panel: Statistical significance ($S/\sqrt{S+B}$) as a function of the value used for the $vt_Z$-cut (the significance is obtained by integrating signal and background entries from $+\infty$ down to the value used for the $vt_Z$-cut).*

mizing the significance. This is illustrated in the right panel of 6.19. One can see that the maximum of significance is obtained by rejecting triplets with $vt_Z < 0.085$ cm.

- $\chi^2$*-cut*: The $\chi^2$ is the distance of closest approach between the reconstructed vertex and the tracks in the triplets, divided by the extrapolation uncertainty of the tracks. It is thus given in units of these uncertainties. It is defined as follows:

$$\chi^2 = \sum_{i=1}^{3} \left(\frac{X_i - X_{vertex}}{\sigma_{i,X}}\right)^2 + \left(\frac{Y_i - Y_{vertex}}{\sigma_{i,Y}}\right)^2 + \left(\frac{Z_i - Z_{vertex}}{\sigma_{i,Z}}\right)^2 \tag{6.9}$$

where $(X, Y, Z)_i$ are the coordinates of the point of closest approach (to the vertex) along the tracks i. $(\sigma_X, \sigma_Y, \sigma_Z)_i$ are the extrapolation uncertainties of the track i on this point, and $(X, Y, Z)_{vertex}$ are the coordinates of the reconstructed vertex. Since for signal triplets, the three tracks originate from the same creation vertex, one expects lower $\chi^2$ values for signal triplets than for background triplets. This can be seen in Figure 6.20 (left side), which shows the $\chi^2$ distributions for signal (red histogram) and background (blue histogram) triplets. For most of signal triplets, the $\chi^2$ values are below 6 $\sigma$. This is due to the excellent secondary decay vertex resolution provided by the MVD detector. As a result of the suppression of primary particles and secondaries originating from the decay of long-lived strange particles, the vertices associated with most of background triplets have relatively high values of $\chi^2$. An upper cut on this variable is thus introduced to reduce the combinatorial background. The value of this cut has been obtained by maximizing the significance. This is illustrated in the right panel of Figure 6.20. One can see that the maximum of significance is obtained by rejecting triplets with $\chi^2 > 1.6\ \sigma$.

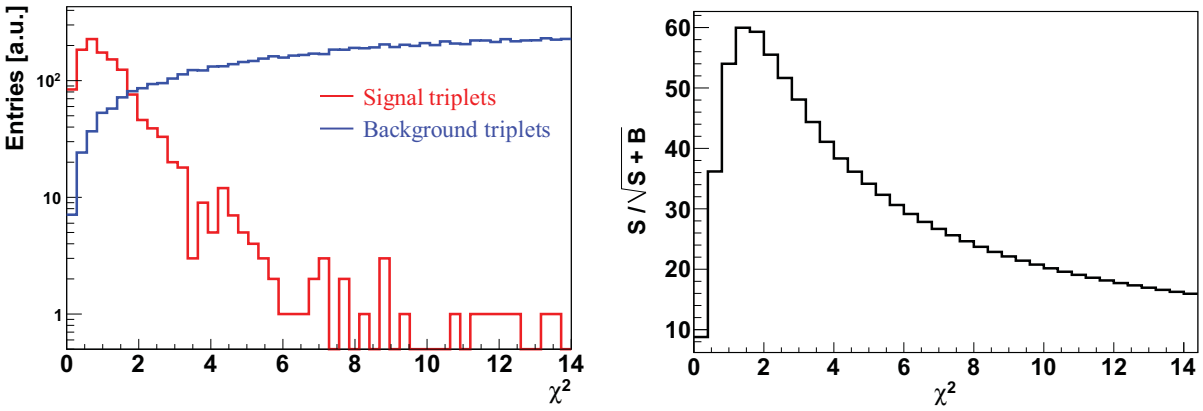


**Figure 6.20:** *Left panel: Distribution of the $\chi^2$ associated with the vertex of signal (red histogram) and background (blue histogram) triplets. $\chi^2$ is given in units of the track extrapolation uncertainties. Right panel: Statistical significance ($S/\sqrt{S+B}$) as a function of the value used for the $\chi^2$-cut (the significance is obtained by integrating signal and background entries from 0 up to the value used for the $\chi^2$-cut).*

| Cuts on triplets | $vt_Z$ < 0.085 cm | $\chi^2 > 1.6\ \sigma$ | Total |
|---|---|---|---|
| Background rejection (%) | 23.3 | 99.8 | 99.82 |
| Signal loss (%) | 1.5 | 27 | 27.6 |

**Table 6.5:** *Effect of the application of each individual cut ($vt_Z$, $\chi^2$) on background and signal triplets. The percentages are given on the basis of the triplets which survive the track preselection stage. The last column indicates the overall effect of the application of both cuts.*

- *$D^+$ impact parameter cut*: A topological constraint is used when reconstructing the vertex of the track triplets (see Figure 6.18). $D^+$ candidates must originate from the primary (collision) vertex. In practice, the momentum vector of triplets (equal to the sum of the momentum vectors of the three particles) must have an impact parameter lower than 1 $\mu$m. This value is set considering the uncertainty achieved for the primary vertex position, of less than a micrometer in the transverse plane.

Table 6.5 gives a summary of the effect of the $vt_Z$ and $\chi^2$ cuts on the signal and on the combinatorial background. The $\chi^2$-cut is by far the most efficient: it rejects 99.8% of background triplets, while sacrificing only 27% of signal triplets. The $vt_Z$-cut is also useful: it rejects 23.3% of background triplets, while sacrificing only 1.5% of signal triplets. As indicated in the last column, the combined effect of both cuts allows rejecting 99.82% of the background triplets while suppressing only 27.6% of signal triplets.

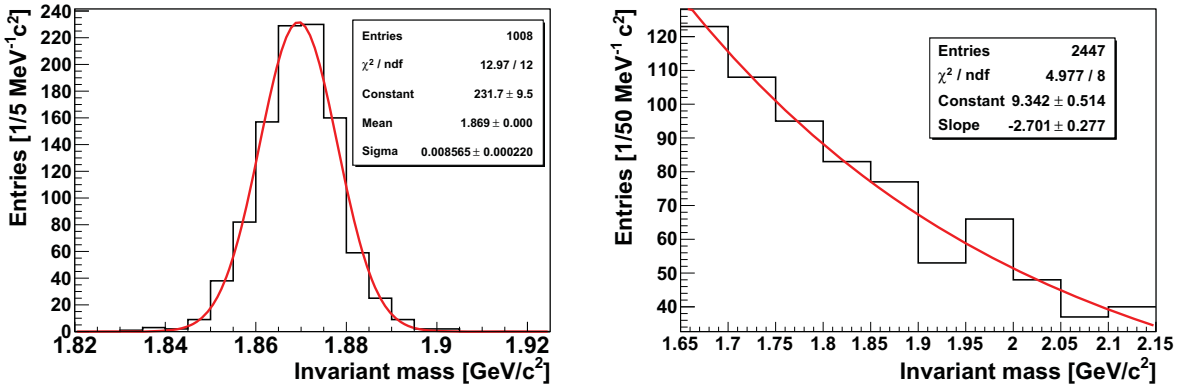


**Figure 6.21:** *Invariant mass distribution for signal triplets (left side) and for background triplets (right side) remaining after the selection procedure. We used* $10^9$ *events for the background and* $5 \times 10^4$ *($K^-$, $\pi^+$, $\pi^+$) triplets for the signal. The signal distribution is fitted with a Gaussian function, while the background distribution is fitted with an exponential function (red curves on both figures).*

## 6.5 Results

Figure 6.21 shows the invariant mass distributions of signal triplets (left panel) and background triplets (right panel) obtained after applying all selection cuts defined in the previous section.

We recall that these distributions were simulated separately (see Section 6.2.2): the signal distribution was obtained on the basis of $5 \times 10^4$ $D^+$ mesons decaying into $K^-\pi^+\pi^+$, while the background distribution corresponds to a sample of $10^9$ equivalent events (see Section 6.4.2 for the definition of an equivalent event). They must, therefore, be normalized to the same number of events in order to evaluate the reconstruction performances. The normalization procedure we have used in our simulations will be presented later in Section 6.5.3.

As seen in Figure 6.21, the simulated invariant mass distributions can be fitted with a Gaussian function and an exponential function, respectively, for the signal and for the combinatorial background. These two functions will be hereafter referred to as $F_S$ (for the signal) and $F_B$ (for the background).

### 6.5.1 Invariant mass resolution

The Gaussian fit of the reconstructed invariant mass distribution of the signal (left panel of Figure 6.21) was used to obtain the mean value ($\mu$) and the standard deviation ($\sigma$). The first parameter ($\mu$) corresponds to the reconstructed invariant mass of $D^+$ mesons decaying into $K^-\pi^+\pi^+$, while the second ($\sigma$) gives an indication on the invariant mass resolution which can be expected in the experiment. Following this procedure, the mass of $D^+$ is found to be ($\mu \pm \sigma$) = (1869.16 $\pm$ 8.56 MeV/$c^2$). This value is consistent, within the uncertainties, with the one used as an input in the

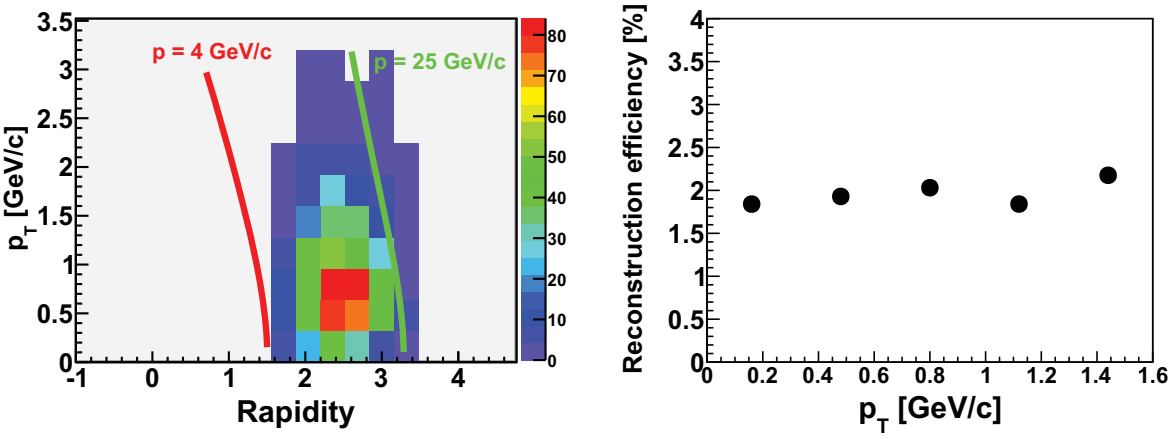


**Figure 6.22:** *Left panel: Phase space coverage for $D^+ \rightarrow \pi^+ \pi^+ K^-$ in the transverse momentum-rapidity plane after applying all selection criteria. The center-of-mass rapidity is equal to 2 for Au + Au collisions at an incident energy of 25 GeV/nucleon. The red and green lines correspond to constant momenta of 4 and 25 GeV/c, respectively. Right panel: reconstruction efficiency as a function of transverse momentum.*

simulations (of 1869.4 MeV/$c^2$).

Note that the width of the resonance mass of the $D^+$ meson is not taken into account in the present study. Because of its very small value, one expects its effect on the invariant mass distribution to be negligible.

The results of our simulation show that the invariant mass distribution of $D^+ \rightarrow K^-\pi^+\pi^+$ can be reconstructed with a resolution of $\sigma$ = 8.56 MeV/$c^2$. This very good resolution is explained by the excellent performances of the STS detector and of the tracking software. This is important for the discrimination of the signal from the combinatorial background.

### 6.5.2 Reconstruction efficiency

The reconstruction efficiency is defined as the number of signal triplets surviving the selection procedure divided by the number of signal triplets initially generated in the simulation. The number of the reconstructed signal triplets was obtained by integrating the Gaussian fit function $F_S$ (see left panel of Figure 6.21) within the invariant mass region: [$\mu$ - 2$\sigma$, $\mu$ + 2$\sigma$]. This was motivated by the fact that about 95.5% of all signal entries lie within this range. The reconstruction efficiency is found to be equal to 2%. Note that this number includes the effect of the detector acceptance.

The expected phase space coverage for $D^+ \rightarrow \pi^+ \pi^+ K^-$ mesons in the transverse momentum-rapidity plane representation is illustrated in the left panel of Figure 6.22. The distribution is obtained after applying all selection cuts. By comparing this distribution to the one shown in the right panel of Figure 6.9, one can see that the selection procedure (used to reduce the combina-

torial background) does not affect significantly the phase space coverage within the limits of the detector acceptance. This is illustrated in the right panel of Figure 6.22, which shows the signal reconstruction efficiency as a function of transverse momentum. As one can see, the reconstruction efficiency, of around $2\%$ (including the effect of the detector acceptance), is fairly constant at least for transverse momenta up to $p_T$ = 1.6 GeV/c. Above this value, the statistics becomes too poor to obtain a reliable estimate of the efficiency.

### 6.5.3 Invariant mass distribution expected per CBM run period

As mentioned earlier, the invariant mass distributions of the signal and of the combinatorial background (shown in Figure 6.21) were simulated separately. In order to estimate the invariant mass distribution of signal candidates expected per CBM run period, each of these distributions must be scaled to the number of central Au + Au collisions (called hereafter $N_{coll}^{cent}$) that can be measured within the duration of the run. This number depends on the collision rate and on the duration of the measurements.

#### Typical CBM run period

Due to the anticipated high availability of FAIR beams (through parallel operation of several experiments), CBM will benefit from a long time of measurement, of typically 4 months per year. To evaluate the expected run period, a $50\%$ operating efficiency will be assumed in the simulations, which corresponds to an effective data taking time of approximately 2 months per year, i.e. $5 \times 10^6$ seconds per year.

#### Collision rate

In the present simulations, we assumed that open charm measurements in Au + Au collisions will be performed at a collision rate of 400 kHz. We recall that, the anticipated time resolution of MAPS sensors, which will equip the MVD detector at SIS300, is 10 $\mu$s (see Table 4.4). This implies a pile-up of 4 collisions in the MVD. Previous studies within the collaboration have shown that such a low rate of pile-up events is tolerable thanks to the high granularity of the MVD [76].

We have verified that at this collision rate, MAPS will be able to sustain the radiation doses they will receive during the whole duration of the run. It is worth recalling here that the most exposed MAPS sensors could be replaced after each CBM run period. At a collision rate of 400 kHz, one expects to collect $2 \times 10^{12}$ Au + Au collisions per run. According to [102], a non-ionizing (ionizing) dose of about 14.7 $n_{eq}/cm^2$ (1.6 $\mu$rad) per Au(25 AGeV) + Au collision is expected at the location of the first MVD station (10 cm downstream the target). MAPS will tolerate a non-ionizing radiation dose of about $3 \times 10^{13}$ $n_{eq}/cm^2$, and an ionizing dose above 3 MRad (see Table 4.4). These numbers indicate that the radiation doses per run remain below the limits of the sensors.

### Number of central Au + Au collisions per CBM run

Knowing the duration of the run and the collision rate, and assuming that central collisions represent 10% of the total number of collisions, one can estimate the number of central collisions which can be measured per run: $N_{coll}^{cent}$ = 2 $\times$ $10^{11}$ central collisions.

### Normalization of the signal and background

The normalization factors, denoted as $\alpha_S$ and $\alpha_B$ for the signal and combinatorial background respectively, are the following:

$$\alpha_S = \frac{N_{coll}^{cent} \times M \times BR}{N_S^{gen}} \tag{6.10}$$

$$\alpha_B = \frac{N_{coll}^{cent}}{N_B^{gen}} \tag{6.11}$$

where $N_S^{gen}$ and $N_B^{gen}$ are the number of simulated $D^+ \rightarrow K^-\pi^+\pi^+$ and background events respectively. In this study, $N_S^{gen}$ = 50 000 and $N_B^{gen}$ = $10^9$ central Au + Au collisions. As mentioned in the previous section, $N_{coll}^{cent}$ equals to 2 $\times$ $10^{11}$ central Au + Au collisions and BR is the branching ratio of the $D^+ \rightarrow K^-\pi^+\pi^+$ decay channel (of 9.51%). The normalization factor $\alpha_S$ also depends on the $D^+$ production multiplicity (M) in central Au(25 AGeV) + Au collisions. In the absence of available experimental data, the value of M is taken from theoretical models. Two models were used for this purpose: HSD and SHM. As we will see, their predictions differ by a factor of about 2 for $D^+$ mesons.

These normalization factors cannot be applied directly to the histograms of Figure 6.21. Indeed, this would result into biased statistical uncertainties on the number of entries in each bin: if N is the number of entries in a given bin, a normalization by a factor $\alpha$ would result into a statistical error on this bin equal to $\alpha \times \sqrt{N}$, while it must be equal to $\sqrt{\alpha \times N}$. For the sake of properly estimating the expected statistical uncertainties on the $D^+$ candidate invariant mass distribution expected per CBM run period, we have done the following. We applied the normalization factors $\alpha_S$ and $\alpha_B$ to the fit functions $F_S$ and $F_B$ defined at the beginning of this section. Then, the normalized fit functions, referred to as $F_S^{norm}$ and $F_B^{norm}$, were added together. Note that the normalization of the signal was done based on the $D^+$ multiplicity predicted by the HSD transport model [60] in central Au(25 AGeV) + Au collisions. The resulting function is referred as $F_{SB}$. This function is then used to fill a histogram: the number of entries in each bin is set to the value of $F_{SB}$. The expected statistical errors are then obtained by assuming Gaussian fluctuations on the content of each bin. The resulting histogram is presented in Figure 6.23. This histogram corresponds to the invariant mass distribution that one could measure per CBM year run for $D^+$ mesons via their decay channel to $K^-\pi^+\pi^+$ in central Au(25 AGeV) + Au collisions.

The amounts of $D^+ \rightarrow K^-\pi^+\pi^+$ signal triplets (S) and of background triplets (B) are obtained as follows. One fills two histograms using the fit functions $F_S^{norm}$ (for the signal) and $F_B^{norm}$ (for the background) separately, using the same procedure as explained above. S and B are obtained by integrating these histograms in the invariant mass region [$\mu$ - 2$\sigma$, $\mu$ + 2$\sigma$] (see Section 6.5.1).

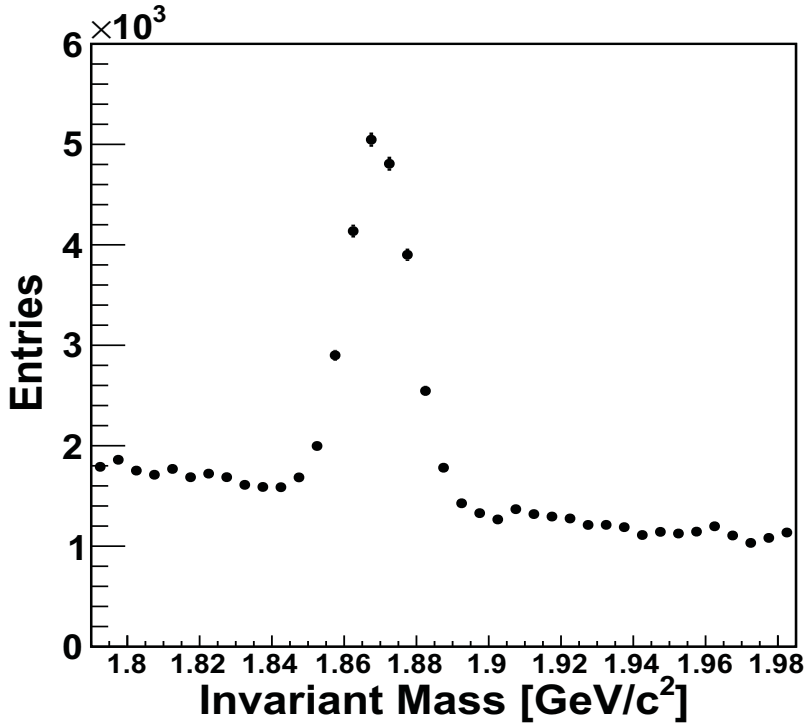


**Figure 6.23:** *Invariant mass distribution of particles surviving the selection procedure (signal daughter particles and background particle triplets). The distribution is normalized to 2 $\times$ $10^{11}$ central Au(25 AGeV) + Au collisions. See text for details of the normalization procedure.*

The signal to background ratio (S/B) is simply the ratio between S and B. As for the significance (Sign), it is defined as follows (see Appendix E):

$$Sign = \frac{S}{\sqrt{S+B}} \tag{6.12}$$

The expected reconstruction performance for $D^+$ mesons is summarized in Table 6.6 (second column). They are expressed in terms of the secondary vertex and invariant mass resolutions, the signal reconstruction efficiency (including the effect of the detector acceptance), the signal to background ratio, the significance of the signal, and the expected statistics per CBM run period. The last three depends on the multiplicity considered for $D^+$ mesons. Assuming the multiplicity predicted by the HSD transport model, the achieved signal to background ratio is about 1.5. As one can see in Figure 6.23, this allows the signal to be clearly extracted from the combinatorial background. This satisfactory signal to background ratio comes from the excellent vertexing precision provided by the MVD detector, i.e. a secondary decay vertex resolution of 72 $\mu$m for $D^+$ mesons. This allows suppressing most of background triplets while preserving a sufficient amount of signal triplets. Considering that $2 \times 10^{11}$ central collisions can be measured per CBM run period, the significance of the signal is about 95. Note that if one considers the multiplicity predicted by the SHM model [49], the achieved signal to background ratio and significance are higher, respectively of 3.0 and 151.

The feasibility study of the reconstruction of $D^-$ mesons via the hadronic decay channel $D^- \rightarrow \pi^- \pi^- K^+$ has also been carried out in the present study, under the same conditions as for the simulations presented above for $D^+$ mesons. The results of these simulation studies are given in Table 6.6 (third column). They indicate that $D^-$ mesons can be reconstructed with an efficiency of $1.4\%$. Assuming their production multiplicity predicted by the HSD (SHM) model, the achieved signal to background ratio is of 3.7 (12.0).

The amount of signal triplets (S) gives an estimation of the expected statistics of $D^+$ mesons which can be measured per CBM run period: assuming the multiplicity predicted by the HSD model, S $\sim 1.5 \times 10^4$ $D^+$ particles. If one assumes the multiplicity predicted by the SHM model, the expected statistics of $D^+$ mesons is higher: about $3.0 \times 10^4$ particles per run are expected. As for $D^-$ mesons, a statistics of $2.3 \times 10^4$ ($7.5 \times 10^4$) particles are expected per CBM run period, assuming the production multiplicity predicted by the HSD and SHM models, respectively.

The expected statistics is higher for $D^-$ mesons compared to $D^+$ mesons. This is due to the larger $D^-$ production multiplicities. In the HSD and SHM models, the production multiplicity of $D^-$ is roughly 2 and 3.5 times higher than for $D^+$, respectively. In HSD, which is a purely hadronic model, the $D^-$ ($\bar{c}d$) is more frequently produced at low energies, due to the associated production with $\Lambda_c$, $\Sigma_c$ baryons. In SHM, which assumes the formation of a thermalized quark-gluon plasma, this difference in multiplicity is due to the fact that the net baryon density is high at FAIR energies. This means that the number of d quarks is higher than the number of $\bar{d}$ quarks, although the number of c quarks is equal to the number of $\bar{c}$ quarks, as they are produced in pairs. Therefore, the production of $D^-$ ($\bar{c}d$) is favored over the production of $D^+$ ($c\bar{d}$).

| | | $D^+$ | $D^-$ | $D^+$ + $D^-$ |
|---|---|---|---|---|
| Decay channel | | $\pi^+ \pi^+ K^-$ | $\pi^- \pi^- K^+$ | |
| Branching ratio [%] | | 9.5 | 9.5 | |
| Multiplicity | HSD | $4.2 \times 10^{-5}$ | $8.9 \times 10^{-5}$ | $1.3 \times 10^{-4}$ |
| | SHM | $8.4 \times 10^{-5}$ | $2.9 \times 10^{-4}$ | $3.7 \times 10^{-4}$ |
| Decay length c$\tau$ [$\mu$m] | | 311.8 | 311.8 | |
| Sec. vertex resol. [$\mu$m] | | 72 | | |
| Inv. mass resol. [MeV/$c^2$] | | $8.56 \pm 0.22$ | $8.41 \pm 0.23$ | |
| Reco. efficiency [%] | | 2.0 | 1.4 | |
| S/B | HSD | 1.5 | 3.7 | |
| | SHM | 3.0 | 12.0 | |
| Significance | HSD | 95 | 134 | |
| | SHM | 151 | 262 | |
| Particles/year | HSD | $1.5 \times 10^4$ | $2.3 \times 10^4$ | $3.8 \times 10^4$ |
| | SHM | $3.0 \times 10^4$ | $7.5 \times 10^4$ | $1.1 \times 10^5$ |

**Table 6.6:** *Invariant mass resolution, reconstruction efficiency, signal-to-background ratio, significance and expected number of particles for $D^+$ and $D^-$ measurements in central Au+Au collisions at 25 AGeV beam energy. The normalization is done for $2 \times 10^{11}$ central collisions, corresponding to a collision rate of 400 kHz and to a CBM run period of approximately 2 months. The "Sec. vertex resol." is the secondary vertex resolution along the beam axis. The performances are shown assuming the production multiplicities predicted by the HSD and SHM models.*

| Decay channel | Multiplicity | | BR | Reco. | Particles/year | |
|---|---|---|---|---|---|---|
| | HSD | SHM | [%] | eff. [%] | HSD | SHM |
| $D^+ \to \pi^+ \pi^+ K^-$ | $4.2 \times 10^{-5}$ | $8.4 \times 10^{-5}$ | 9.5 | 2.0 | $1.5 \times 10^4$ | $3.0 \times 10^4$ |
| $D^- \to \pi^- \pi^- K^+$ | $8.9 \times 10^{-5}$ | $2.9 \times 10^{-4}$ | 9.5 | 1.4 | $2.3 \times 10^4$ | $7.5 \times 10^4$ |
| $D^0 \to \pi^+ K^-$ | $3.7 \times 10^{-5}$ | $2.0 \times 10^{-4}$ | 3.9 | 2.0 | $5.8 \times 10^3$ | $3.2 \times 10^4$ |
| $\bar{D^0} \to \pi^- K^+$ | $1.1 \times 10^{-4}$ | $6.1 \times 10^{-4}$ | 3.9 | 2.0 | $1.7 \times 10^4$ | $9.6 \times 10^4$ |
| $D^0 \to \pi^+ \pi^+ \pi^- K^-$ | $3.7 \times 10^{-5}$ | $2.0 \times 10^{-4}$ | 7.7 | 0.4 | $2.1 \times 10^3$ | $1.2 \times 10^4$ |
| $\bar{D^0} \to \pi^- \pi^- \pi^+ K^+$ | $1.1 \times 10^{-4}$ | $6.1 \times 10^{-4}$ | 7.7 | 0.4 | $6.4 \times 10^3$ | $3.5 \times 10^4$ |
| $D_s^+ \to \pi^+ K^+ K^-$ | $5.4 \times 10^{-6}$ | $1.4 \times 10^{-4}$ | 5.3 | 1.0 | $5.8 \times 10^2$ | $1.5 \times 10^4$ |
| Sum | | | | | $6.9 \times 10^4$ | $3.0 \times 10^5$ |

**Table 6.7:** *Expected statistics for D-mesons [76, 77, 78], corresponding to 2 $\times$ $10^{11}$ central Au(25 AGeV )-Au collisions.*

### 6.5.4 Expected annual yields of other D-mesons

In order to investigate the mechanism of charm production with CBM, it is important to measure all open charm species, in particular D-mesons which are the most abundant charm particles. The reconstruction of other open charm particles was studied in other works [76, 77, 78] within the collaboration. This was done for central Au + Au collisions at an incident energy of 25 GeV/nucleon. Table 6.7 indicates the reconstruction efficiency and the expected statistics per year run obtained for $D^+$ and $D^-$ (present work), $D^0$ and $\bar{D^0}$ [76, 77] and $D_s^+$ [78]. Note that all these results were obtained assuming the same detection setup as in the present work, except for $D^0 \to \pi^+ K^-$ and $\bar{D^0} \to \pi^- K^+$ where the two stations of the MVD detector were located closer to the target (at 5 and 10 cm instead of 10 and 15 cm in this work).

The CBM experiment will allow measuring D-mesons via different hadronic decay channels. For example, the decay of the $D^0$ meson into four hadrons ($D^0 \to \pi^+ \pi^+ \pi^- K^-$) can also be reconstructed. It was found in [77] that the detection efficiency for this channel ($\sim 0.4\%$) is about 5 times lower than for the $D^0 \to \pi^+ K^-$ decay channel. This is mainly due to geometrical acceptance effects. The requirement that all four hadrons issued from a $D^0$ decay are within the acceptance, is more difficult to fulfill.

The results presented in Table 6.7 demonstrate the feasibility of the measurement of open charm mesons in the CBM experiment. The expected reconstruction performances for different D-meson species are very satisfactory. The number of open charm mesons that can be measured during a typical CBM run period (i.e. two months beam on target) has been estimated for two assumptions on the particle multiplicities based on the predictions of the HSD and SHM models (see Table 6.7). We found that at least 6.9 $\times$ $10^4$ (3.0 $\times$ $10^5$) D-mesons are expected to be measured per CBM run period assuming, respectively, HSD and SHM particle multiplicities.

## 6.6 Summary

The goal of this chapter was to study the feasibility of measuring open charm mesons in nucleus-nucleus collisions with the CBM detector at the FAIR accelerator facility. $D^+$ mesons decaying into $\pi^+ \pi^+ K^-$ were chosen to benchmark the detector performance. This choice was motivated by the fact that the reconstruction of such a decay channel, involving three daughter particles, is particularly challenging as the signal must be extracted from a very large (many orders of magnitude higher) combinatorial background due to uncorrelated charged particle triplets. The MVD detector plays a crucial role in the reconstruction of these mesons as it allows a good separation between their secondary decay vertex and the primary collision vertex.

Detailed Monte Carlo simulations were carried out, within the CBMRoot simulation framework, using a realistic MVD detector geometry and taking into account the performances of MAPS sensors: a single-point resolution of 3 $\mu$m, a read-out time of 10 $\mu$s, and a tolerance to radiation doses up to 3 MRad and $3 \times 10^{13}\ n_{eq}/cm^2$ for ionizing and non-ionizing radiations, respectively. The particle identification was taken into account by assuming that the information provided by the TOF detector allows rejecting all protons. We studied the case of central Au(25 AGeV) + Au collisions (generated with the UrQMD transport model), which represent a typical environment for open charm reconstruction in nucleus-nucleus collisions at FAIR energies.

We assumed that open charm will be measured in Au + Au collisions at a collision rate of 400 kHz. This was motivated by previous studies, which demonstrated that the MVD detector, thanks to its high granularity, can tolerate the low rate of collision pile-up (of 4 collisions) expected at this collision rate. Also, we have verified that at such a rate, MAPS will be able to sustain the radiation doses they will receive per CBM run period (corresponding to 2 months beam on target per year), after which it is planned to replace those that are most exposed to radiation.

The reconstruction of $D^+$ mesons was based on the determination of the invariant mass of their decay products among other particles produced in the collision. Several selection criteria were used to reduce the high combinatorial background due to uncorrelated charged particle triplets. These criteria were mainly based on the different topology of $D^+$ meson decay and, in particular, its characteristic displaced decay vertex relative to the interaction point. After optimization of the underlying selection cuts used to extract the signal, we found a reconstruction efficiency of $2\%$ (including the effect of the detector acceptance). Based on the multiplicity of $D^+$ mesons predicted by the HSD (SHM) model, we found that a statistics of $1.5 \times 10^4$ ($3.0 \times 10^4$) $D^+$ particles can be measured per CBM run period at a collision rate of 400 kHz with a quite good purity, i.e. a signal to background ratio of 1.5 (3.0). These good performances are mainly due to the excellent vertexing accuracy provided by the MAPS based MVD detector of CBM, i.e. a secondary decay vertex resolution of 72 $\mu$m for $D^+$ mesons decaying into $\pi^+ \pi^+ K^-$.

The reconstruction performances have also been determined for $D^- \rightarrow \pi^- \pi^- K^+$ under the same conditions (collision system, energy, centrality and collision rate) as for $D^+$ mesons. We found a reconstruction efficiency of $1.4\%$. Assuming the multiplicity of $D^-$ mesons predicted by the HSD (SHM) model, a statistics of $2.3 \times 10^4$ ($7.5 \times 10^4$) $D^-$ particles can be measured per CBM run period with a good purity, i.e. a signal to background ratio of 3.7 (12.0).

Combining our results with those from other studies performed within the collaboration, we found that at least $6.9 \times 10^4$ ($3.0 \times 10^5$) D-mesons are expected to be measured per run period assuming, respectively, HSD and SHM particle multiplicities.

The above results demonstrate the feasibility of open charm particle measurements in nucleus-nucleus collisions with the CBM detector. The expected performances should allow for the extraction of different observables required by the physics program of CBM for open charm (yields, yield ratios, transverse mass spectra, etc). In the next chapter, we will focus on the elliptic flow of D-mesons, which is one of the most challenging observables, in particular regarding the requirements in terms of statistics.

# Chapter 7

# Evaluation of CBM capabilities for open charm elliptic flow measurements

In this chapter, we present a simulation study to investigate the capabilities of the CBM experiment for measuring the elliptic flow of D-mesons. It starts with a brief introduction on the anisotropic flow and the importance of studying this phenomenon in the FAIR energy range, in particular for open charm particles (Section 7.1). Then, the procedure used to simulate the D-meson elliptic flow is described (Section 7.2). This is followed by a detailed evaluation of the resolution with which the reaction plane can be determined in CBM (Section 7.3). Finally, the expected performances of CBM for D-meson elliptic flow measurements are presented and their implications and limitations are discussed (Section 7.4).

## 7.1 Introduction

The anisotropic flow phenomenon, illustrated in Figure 7.1, refers to an anisotropy in the azimuthal distribution with respect to the reaction plane of the particles emitted in non-central heavy ion collisions. This anisotropy is built up during the hot and dense early stage of the collision. It is driven by the initial coordinate-space anisotropy of the overlap region between the two colliding nuclei, which is converted by multiple secondary interactions among the produced particles into the final momentum-space as illustrated in Figure 7.2. The anisotropic flow introduces a correlation between the azimuthal angle of emitted particles and the azimuthal orientation of the reaction plane. The latter is defined by the impact parameter vector and the beam direction (see Figure 7.1).

Anisotropic flow is commonly parametrized by a Fourier expansion of the invariant differential distribution of the particles emitted in non-central collisions:

$$E\,\frac{d^3N}{d^3p} = \frac{1}{2\pi}\frac{d^2N}{p_T dp_T dY}\,(1 + \sum_{n=0}^{\infty} 2v_n \cos(n(\phi - \Psi_R))) \tag{7.1}$$

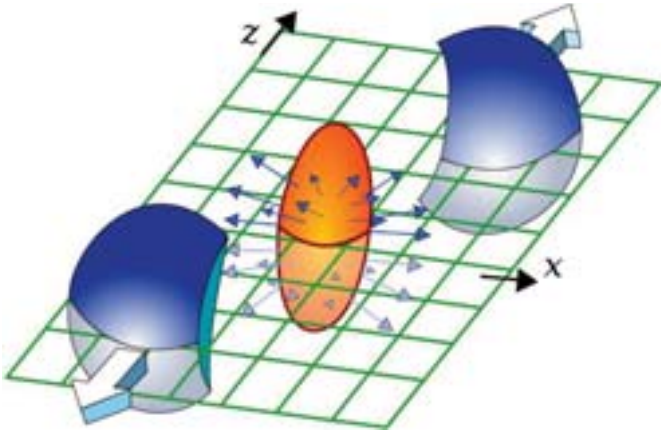


**Figure 7.1:** *Sketch of a heavy ion collision, shown in the case of a finite impact parameter. The reaction plane is defined by the impact parameter vector (x-axis) and the beam direction (z-axis).*

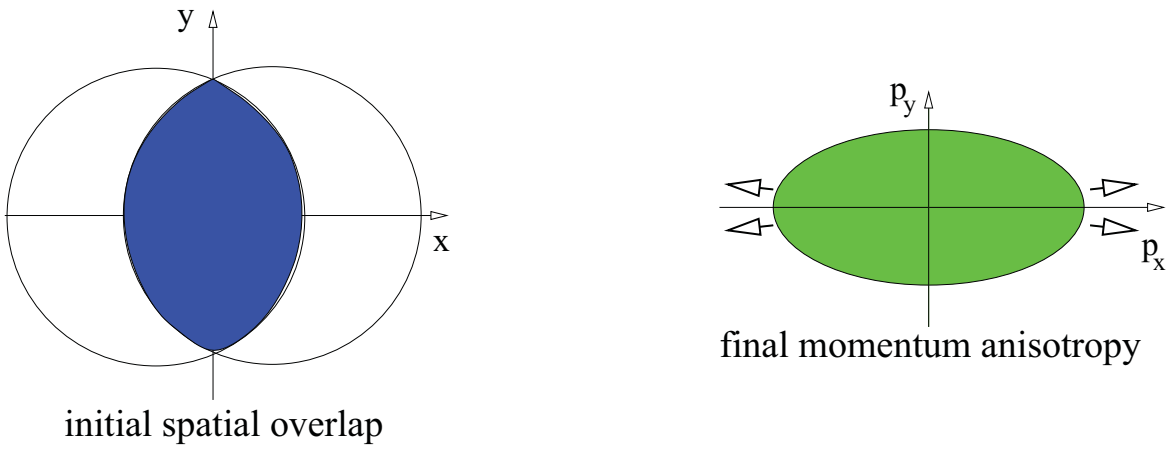


**Figure 7.2:** *Illustration of the development of elliptic flow in heavy ion reactions at high energies. The initial spatial anisotropy in the overlap region between the two colliding nuclei (left side) is converted, due to the anisotropic pressure gradients, into an anisotropic transverse momentum distribution (right side).*

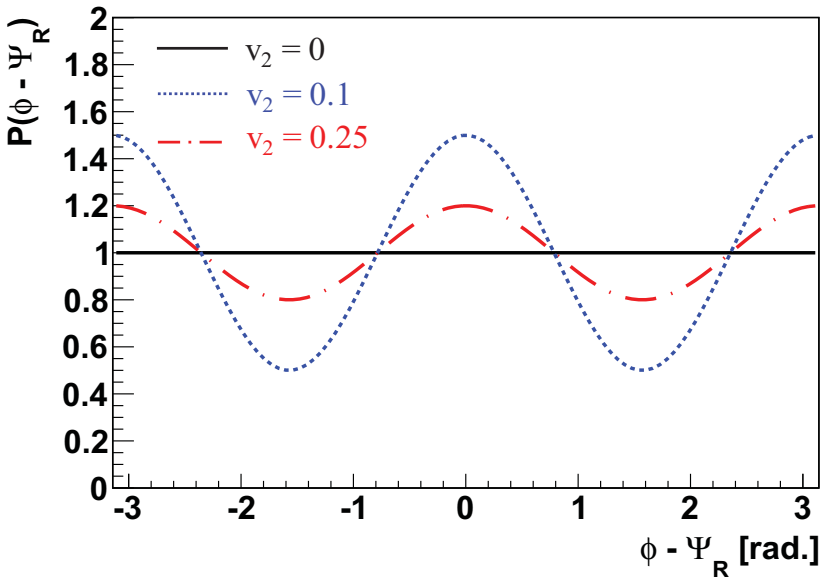


**Figure 7.3:** *Azimuthal distribution relative to the reaction plane corresponding to 3 different assumptions on the elliptic flow coefficient $v_2$ (see Equation 7.1): $v_2$ = 0 (black curve), 0.1 (red dashed-dotted curve) and 0.25 (blue dotted curve).*

where E, p, $p_T$, Y and $\phi$ denote, respectively, the energy, the momentum, the transverse momentum, the rapidity and the azimuthal angle of the particle. $\Psi_R$ is the reaction plane angle. $v_n$ are the Fourier coefficients, which depend on the rapidity and on the transverse momentum. Note the absence of the sine terms in Equation (7.1), which vanish due to the reflection symmetry with respect to the reaction plane.

The lower order terms of the Fourier expansion in Equation (7.1) are the so-called directed flow and elliptic flow components, which are characterized by, respectively, the $v_1$ and $v_2$ anisotropy coefficients. Flow components associated to higher Fourier harmonics are much weaker than $v_1$ (for odd harmonics) and $v_2$ (for even harmonics) at FAIR energies [132] where their magnitude is expected to be very low. The term "directed flow" (also called "sideward flow") comes from the fact that this effect acts as a bounce-off of spectator remnants (blue color in Figure 7.1) in the reaction plane. The elliptic flow parameter $v_2$ characterizes the ellipticity of the azimuthal distribution of the emitted particles (see Figure 7.2). This is the reason why this phenomenon is called "elliptic flow". It corresponds to the amplitude of the oscillation in the azimuthal distribution with respect to the reaction plane. This is illustrated in Figure 7.3 (we used the function defined in Equation (7.2)) for different values of the $v_2$ anisotropy parameter: $v_2$ = 0 (black curve), 0.1 (red dashed-dotted curve) and 0.25 (blue dotted curve). In the absence of elliptic flow ($v_2$ = 0), there is no azimuthal anisotropy resulting in a flat azimuthal distribution. The latter becomes more and more peaked in the reaction plane (i.e., maxima at $\phi$ - $\Psi_R$ = 0 and $\pi$), as the $v_2$ anisotropy parameter increases.

From a macroscopic point of view, the mechanism which converts the spatial anisotropy of the

reaction volume into the final momentum-space is related to the pressure gradients which develop anisotropically: the pressure and the energy density are maximal in the center of the reaction volume and decrease towards the outside, until they reach a value close to zero at the system boundary. The size of the system being the shortest in the reaction plane, the pressure gradients must then be maximal. This is the reason why the outgoing particles will be emitted preferentially in the reaction plane*.

As mentioned above, the elliptic flow is intimately related to the pressure gradients built up in the evolving nuclear system. Its magnitude is expected, therefore, to be sensitive to the equation of state of nuclear matter [128]. In particular, it is sensitive to the velocity of sound $C_s$† in nuclear matter. $C_s$ determines how much pressure arises from an increase of the energy density. Since the elliptic flow is build-up during the first stages of the collision (the spatial anisotropy of the system decreases rapidly with time during expansion), this observable can be used to probe the properties of the early, hot and dense nuclear matter.

From a microscopic point of view, the building of the flow is driven by multiple re-scatterings among the constituents of the system, which lead to a collective motion: all constituents flow in a common velocity field. This makes the elliptic flow a very sensitive probe of the properties of nuclear matter in the early stage of the collision and, in particular its equation of state and its degree of thermalization.

Elliptic flow is also a very interesting observable for studying the phase transition from hadronic matter to the quark gluon plasma, in particular at FAIR energies where the onset of deconfinement is expected to take place ([47], [119]). A collapse of elliptic flow of protons at mid-rapidity has been suggested as a signature of a first order phase transition [129]. Moreover, the scaling of the elliptic flow parameter $v_2$ with the number of valence quarks (known as the constituent quark number scaling [46]) is an indication for flow generation in a partonic phase. The appearance of this scaling behavior as the beam energy increases would signal a change in the effective degrees of freedom of the system.

Another observable sensitive to the effective degrees of freedom (partonic or hadronic) of the matter produced in the early stage of the collision, is the elliptic flow of open charm particles. In a purely hadronic scenario, open charm hadrons have relatively low interaction cross section and are, therefore, expected to develop a low elliptic flow compared with lighter hadrons. In contrast, in a partonic collision scenario, one expects open charm particles to exhibit a stronger elliptic flow [59]. Detailed measurements of open charm elliptic flow with the CBM detector would reveal the presence of partonic degrees of freedom already at FAIR energies (25 - 45 AGeV) and their relative contribution [61]. That is the main motivation for the simulation studies presented in this chapter. Our goal is to investigate the feasibility of those measurements with the proposed detector setup for the CBM experiment and assess the expected physics performances.

The accuracy on the measurement of the $v_2$ anisotropy parameter will depend strongly on the resolution on the reaction plane that one might expect in CBM. Therefore, a particular emphasis

*Note that at low energies (e.g. at SIS energies), the presence of spectator nucleons in the reaction zone prevents particles to flow in the reaction plane, resulting into an out-of-plane emission (called "squeeze-out").

†$C_s = \frac{\partial P}{\partial E}$

will be placed on this aspect.

Before addressing the issue of the reaction plane reconstruction in CBM, we will first describe how the elliptic flow of D-mesons is introduced in the simulations.

## 7.2 Simulation of $D$-meson elliptic flow

We have seen in Chapter 2 that the elliptic flow parameter $v_2$ is expected to be relatively small in the FAIR energy range (as compared to RHIC and LHC energies). This is particularly the case for open charm particles because of their low hadronic cross section (under the assumption that their flow develops in a purely hadronic phase, e.g. according to the HSD model). Measurements of such small $v_2$ magnitudes for open charm particles, which are extremely rare at FAIR energies (threshold production), are very challenging for the detection system. The accuracy on those measurement will be limited mostly by the available statistics and the reaction plane resolution. The simulations were thus focused on these two issues.

The evaluation of the expected statistics for open charm particles was the object of the previous chapter. We have shown that the CBM experiment will be able, thanks to its highly performant micro-vertex detector, to measure large samples of open charm mesons with a quite good purity: about 1.5 $\times$ $10^4$ $D^+$ particles per CBM run period (i.e., 2 months beam on target) in central Au(25 AGeV) + Au collisions (at a collision rate of 400 kHz) and at least 6.9 $\times$ $10^4$ particles per run if one includes all D-meson species ($D^0$, $\bar{D}^0$, $D^+$, $D^-$ and $D_s^+$). The simulation studies presented in this chapter are based on those numbers. Note that the expected statistics might be even higher (by about a factor of 2 for $D^+$ mesons) if one assumes the production multiplicities predicted by the SHM model instead of those predicted by HSD. But for the purpose of our study we considered the most unfavorable scenario.

In order to investigate the expected accuracy on the D-meson elliptic flow measurements, we have carried out simple (and fast) simulations based on a parametrization of their azimuthal distribution relative to the reaction plane. It is important to notice that the contribution of the combinatorial background to the D-meson elliptic flow was ignored in this study, i.e. we assumed an ideal purity of the D-meson signal. We will come back on this point later in this chapter.

$D$-mesons were generated using the thermal model according to the Monte Carlo procedure described in Section 6.2.2 (assuming the same $p_T$-spectrum for all species). To introduce an azimuthal anisotropy corresponding to the elliptic flow, the azimuthal angle of $D$-mesons was generated randomly according to the following probability distribution, which corresponds to the second harmonic (the $v_2$ term) in Equation (7.1):

$$P(\phi - \Psi_R) = (1 + 2 \times v_2 \cos(2 \times (\phi - \Psi_R))) \tag{7.2}$$

As mentioned earlier (Section 7.1), the $v_2$ parameter depends on the particle rapidity and on its transverse momentum. In the following, we will restrict ourselves to the region of the mid-rapidity, which is the central region of the collision where hot and dense matter (possibly the

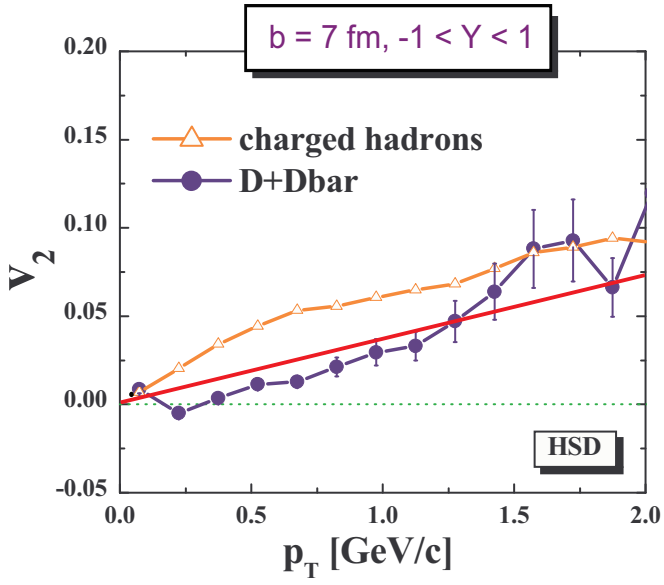


**Figure 7.4:** *Elliptic flow parameter ($v_2$) as a function of transverse momentum ($p_T$), predicted by the HSD transport model for semi-peripheral Au + Au collisions at a beam energy of 25 GeV/nucleon (with an impact parameter equal to 7 fm). The solid lines with full dots and open triangles correspond, respectively, to D-mesons and charged hadrons [61]. The red line shows the assumed $p_T$-dependence of D-meson $v_2$.*

QGP) is produced. This is the region where the elliptic flow is the most pronounced. For the strength of $v_2$ and its $p_T$-dependence, we used the predictions of the HSD transport model for D-meson elliptic flow as an input in the simulations. Figure 7.4 shows the results of HSD calculations for D-mesons and charged hadrons for semi-peripheral Au(25 AGeV) + Au collisions (b = 7 fm), where the elliptic flow is close to its maximum. Recent data from the STAR experiment on charged hadron elliptic flow in Au + Au collisions at similar c.m. energies ($\sqrt{s_{NN}}$ = 7 and 9 GeV) [120] seem to support these predictions.

For mid-rapidity D-mesons, the $p_T$-dependence predicted by the HSD model can be approximated by a linear function: $v_2(p_T) = \alpha \times p_T$, with $\alpha = 0.03$ (red curve on Figure 7.4). This is the parametrization that we have used in our simulations (see e.g. Figure 7.6).

It is important to emphasize that HSD is a purely hadronic model, which does not take into account the partonic degrees of freedom. This explains why the magnitude of the elliptic flow is relatively small in this model, in particular for D-mesons (because of their low hadronic cross-section). The contribution of partonic degrees of freedom which becomes more and more important as the beam energy increases, is expected to enhance the strength of the collective flow as it has been shown recently within the framework of the PHSD (Parton-Hadron-String Dynamics)[120] and AMPT [130] models. The experiment must be able to discriminate between these two collision scnenarii (with and without partonic contributions). That is why the accuracy on the $v_2$ measurement is of crucial importance.

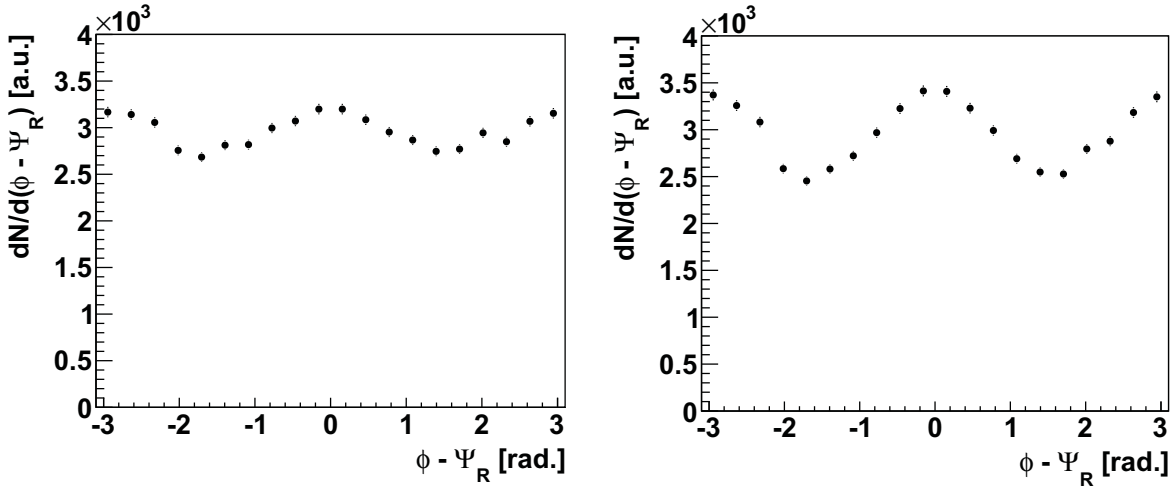


**Figure 7.5:** *Examples of simulated azimuthal distributions of $D$-mesons relative to the reaction plane obtained for two input values of the elliptic flow: $v_2(p_T) = \alpha \times p_T$, with $\alpha$ = 0.03 (left panel) and 0.06 (right panel). These distributions were obtained for a total statistics of, e.g., 2 × $10^5$ $D$-meson particles and for 1 GeV/c < $p_T$ < 2 GeV/c. The vertical bars represent statistical uncertainties. See text for more details.*

Figure 7.5 shows typical azimuthal distributions relative to the reaction plane (dN/d($\phi$ - $\Psi_R$)) simulated as described above for a $p_T$ range: 1 GeV/c < $p_T$ < 2 GeV/c. These distributions are obtained for a total statistics of, e.g., 2 × $10^5$ $D$-meson particles, and assuming two input values of the elliptic flow: $v_2(p_T) = \alpha \times p_T$, with $\alpha$ = 0.03 (left panel) and 0.06 (right panel). The magnitude of the elliptic flow parameter ($v_2$) can be extracted quantitatively from these simulated distributions (see Appendix F) according to:

$$v_2 = < \cos(2 \times (\phi - \Psi_R)) > \tag{7.3}$$

where the angle brackets denote an average over all particles in a sample of events corresponding to the same collision centrality.

The resulting elliptic flow parameter for $D$-mesons is presented in Figure 7.6 as a function of the transverse momentum. The error bars correspond to the statistical uncertainties obtained for a total number of 2 × $10^5$ $D$-meson particles (i.e., the expected statistics per CBM run period). They are obtained, for each $p_T$ bin, as the standard deviation of the $\cos(2\times(\phi-\Psi_R))$ distribution of $D$-mesons divided by the square root of the sample statistics contained in this bin (N):

$$\delta v_2 = \sqrt{\frac{(\sum_{i=1}^{N} \cos(2(\phi - \Psi_R))_i - < \cos(2(\phi - \Psi_R)) >)^2}{N-1}} \; / \; \sqrt{N} \tag{7.4}$$

with the factor (N - 1) accounting for the Bessel correction relevant for small population samples*. From this equation, one can see that the statistical uncertainty depends on the strength of

*Note that this is a biased estimator of the (underlying) population standard deviation, systematically underestimating it. This effect is neglected here.

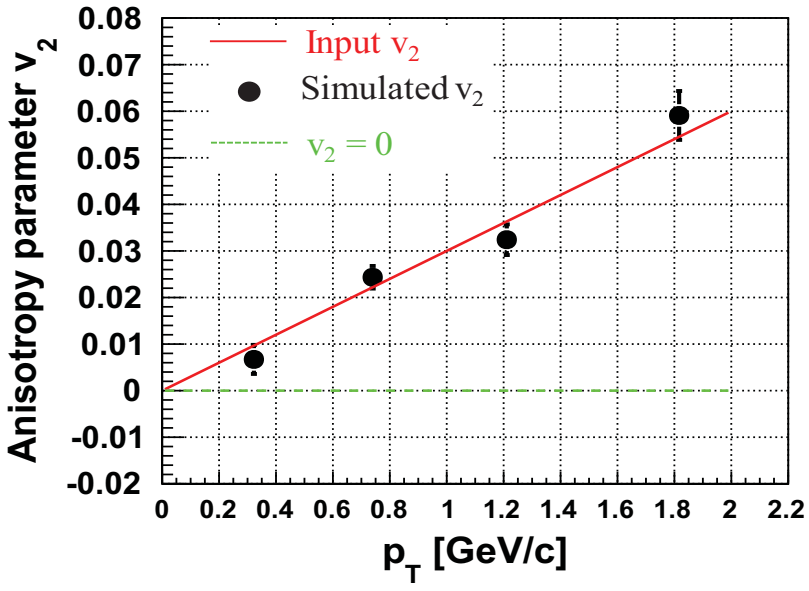


**Figure 7.6:** *Elliptic flow parameter of $D$-mesons versus the transverse momentum, as obtained from the simulations (see text). The error bars correspond to the statistical uncertainties obtained for a sample of $2 \times 10^5$ particles. The red line corresponds to the $v_2$ values used as an input in the simulations (see text).*

the elliptic flow (the stronger the flow is, the lower the standard deviation will be) and on the $D$-meson sample statistics.

The red curve shown in Figure 7.6 corresponds to the generated raw elliptic flow parameter used as an input in the simulations. As it can be seen, the $v_2$ values obtained from the simulations agree well, within statistical uncertainties, with the input values. This agreement is not surprising, since at this stage of the simulations we did not account for the resolution on the reaction plane.

A key feature for measuring of elliptic flow (and more generally anisotropic flow) is the resolution on the reaction plane angle that one can achieve experimentally. The accuracy on $v_2$ measurements of open charm particles will be limited not only by the available statistics (Equation 7.4) but also by the resolution on the reaction plane, since the azimuthal anisotropy must be determined relative to this plane. A finite resolution on the reaction plane angle $\Psi_R$ has as an effect to smear the anisotropy signal leading, therefore, to a reduction of the observed anisotropy parameter ($v_2^{obs}$) with respect to its real strength ($v_2^{real}$):

$$v_2^{obs} = v_2^{real} \times Res(\Psi_R) \tag{7.5}$$

where Res($\Psi_R$) is the resolution on the reaction plane angle. It is a constant factor (for a given collision centrality) and is lower than one. This factor can be evaluated as (see Appendix G):

$$Res(\Psi_R) = < \cos(2(\Psi_n - \Psi_R)) > \tag{7.6}$$

where the angle brackets denote an average over a large sample of events corresponding to the same centrality, and $\Psi_n$ and $\Psi_R$ are the measured and true reaction plane azimuthal angles.

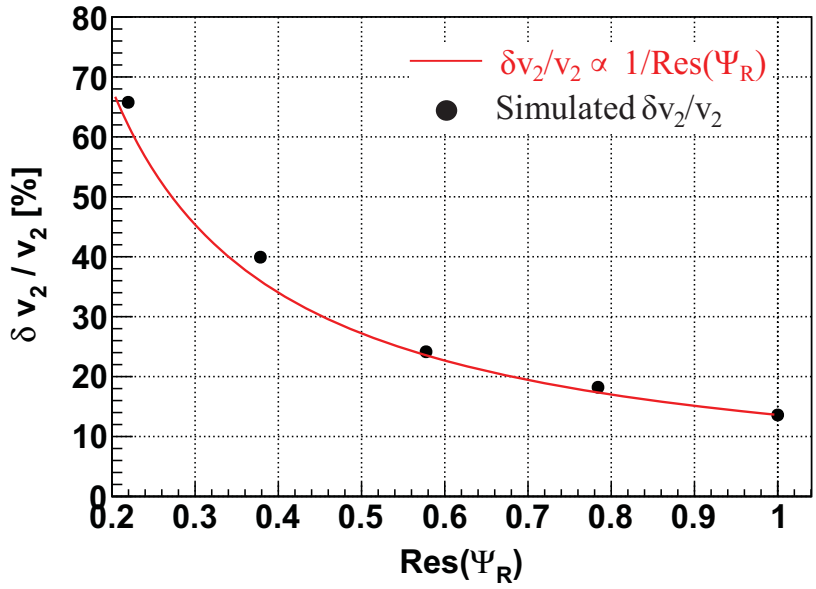


**Figure 7.7:** *Relative uncertainty on the $D$-meson elliptic flow parameter $v_2$ for 1 GeV/c < $p_T$ < 1.5 GeV/c as a function of the reaction plane resolution (see text).*

It can be shown that the relative statistical uncertainty on $v_2$ is proportional to:

$$\frac{\delta v_2}{v_2} \propto \frac{1}{Res(\Psi_R) \times \sqrt{N}} \tag{7.7}$$

The effect of the resolution on the reaction plane on the uncertainty of $v_2$ is illustrated in Figure 7.7 for $D$-mesons particles in the transverse momentum bin 1 GeV/c < $p_T$ < 1.5 GeV/c. The points show the calculated values of the relative statistical uncertainties ($\delta v_2/v_2$), while the curve shows the dependence of these uncertainties on the reaction plane resolution Res($\Psi_R$). The case Res($\Psi_R$) = 1 corresponds to an ideal resolution on the reaction plane (i.e., $\phi$ is determined relative to the true reaction plane angle). As it can be seen, a finite resolution of the reaction plane worsens the uncertainty on the measurement of the $v_2$ parameter. This effect can be quite substantial: a resolution factor of Res($\Psi_R$) = 0.2, for example, would affect the uncertainty on $v_2$ by a factor of 5.

The considerations discussed above show that accurate measurements of elliptic flow require the reconstruction of the reaction plane with a good resolution. This is particularly important for open charm particles at FAIR energies because their flow might be very small (in particular, in a purely hadronic scenario) in addition to their very low production yields which limit the statistics that one could achieve in the experiment. It is, therefore, of crucial importance to ensure that the CBM experiment will be able to provide the necessary resolution on the reaction plane azimuthal angle. This is the object of the next section.

## 7.3 Reaction plane determination in the CBM experiment

In the CBM experiment, the reaction plane will be measured from the sidewards deflection of spectator particles (see Figure 7.1) using the Projectile Spectator Detector (PSD). The design of this detector has been particularly optimized for this purpose.

The Silicon Tracking System (STS) can also provide another independent and complementary measurement of the reaction plane in CBM. This is possible, in particular, thanks to its large acceptance and high granularity.

In this section, we present detailed realistic simulation studies to investigate the capabilities of each of the two above mentioned detectors for reconstructing the reaction plane, and we discuss their respective performances. Although the main motivation behind these studies is to evaluate the accuracy on the elliptic flow (which is the purpose of the present work), the obtained results can be also useful for the study of other flow harmonics (in particular $v_1$) as well as for the reconstruction of other observables requiring the determination of the reaction plane, such as HBT correlations [121], the nuclear modification factor [121] and observables related to the CP violation [122].

### 7.3.1 The event plane method

Experimentally, one can estimate the reaction plane of each event from the azimuthal correlations between emitted particles. Hereafter, the estimated reaction plane will be referred to as the "Event Plane". Its azimuthal angle can deviate from the true reaction plane angle due to the fluctuations originating from finite particle number effects and from the different biases introduced by the detection system.

The most commonly used procedure to reconstruct the angle of this plane is the so-called "event plane method" [123]. The latter uses the anisotropic flow itself to determine the azimuthal orientation of the event plane. This can be done for each harmonic (n) of the Fourier expansion (Equation (7.1)) by evaluating, for each event, the flow vector $\vec{Q_n}$, which is defined as a 2-d vector in the transverse plane:

$$\vec{Q_n} = Q_n \begin{pmatrix} \cos(n\Psi_n) \\ \sin(n\Psi_n) \end{pmatrix} = \begin{pmatrix} \sum_i w_i \times \cos(n\phi_i) \\ \sum_i w_i \times \sin(n\phi_i) \end{pmatrix} \tag{7.8}$$

where the sum runs over all particles in a given event, $\phi_i$ is the azimuthal angle of particle i and $w_i$ is a weight factor assigned to this particle. For odd harmonics $w_i$ must have opposite signs in forward and backward rapidity ($w_i$(-y) = - $w_i$(y)) in the center-of-mass frame. This is a consequence of the reflection symmetry in symmetric collisions, like Au + Au (which is under consideration in the present work).

Finally, the event plane azimuthal angle ($\Psi_n$) can be obtained independently for each harmonic

as the azimuthal angle of $\vec{Q_n}$:

$$\Psi_n = \frac{1}{n}\arctan(\frac{Q_n^y}{Q_n^x}) \tag{7.9}$$

with $Q_n^x$ and $Q_n^y$ the X and Y components of $\vec{Q_n}$. By construction $\Psi_n$ lies in the range $[-\pi/n; \pi/n]$.

The weight factors $w_i$ in Equation (7.8) can be adjusted to achieve the best accuracy on the event plane angle. The optimal choice of these factors depends on the detector used for the reaction plane determination. The weight factors can be also useful to remove correlations due to azimuthal anisotropies caused by the biases of the detection system. We will come back on these two points later (see Sections 7.3.3.3 and 7.3.3.4).

The resolution on the event plane azimuthal angle depends on the strength of the flow and the event multiplicity. One expects a good resolution for high multiplicity and strong anisotropic flow and a poor resolution for low multiplicity and week anisotropic flow. In addition, as we will see later (Section 7.3.3.3), the biases introduced by the detector used to reconstruct the reaction plane can deteriorate significantly this resolution.

## 7.3.2 Simulation procedure

In order to assess the expected accuracy on the determination of the reaction plane in the CBM experiment, we have carried out a detailed and realistic simulation study for Au + Au collisions at an incident energy of 25 AGeV. The resolution of the event plane is expected to be different depending on the collision centrality. We therefore performed a systematic study as a function of the collision impact parameter.

The simulations have been carried-out using the CbmRoot simulation and analysis framework [106].

### 7.3.2.1 Event generation

Au + Au collisions were generated using the Ultra-Relativistic Quantum Molecular Dynamics (UrQMD) transport code [108]. The latter describes most of the observables measured so far in heavy-ion collisions at the CERN-SPS (NA49) and RHIC (STAR, PHENIX) at c.m. energies ($\sqrt{s_{NN}}$ = 7 and 9 GeV) similar to those of FAIR. In particular, this model reproduces reasonably well the overall hadron production multiplicities and the magnitude of the collective flow [124], which is very important in the context of our study since, as mentioned earlier, the accuracy on the event plane depends quite strongly on those two features of the collision. Note also that the magnitude of the elliptic flow in UrQMD is very similar to that predicted by the HSD transport model.

Samples of typically $10^5$ UrQMD events with impact parameters from 0 to 16 fm were used in the simulations presented hereafter.

#### 7.3.2.2 Transport through the detectors

Particles emerging from Au + Au collisions are propagated along the direction of their momenta. The GEANT3 transport code [107] is used to simulate the interactions of those particles with the detector material (particle decays, particle scattering, energy deposition, etc), taking into account the magnetic dipole field of the CBM experiment. Further details specific to each of the two reaction plane detectors (the PSD and the STS) will be given in the two following sections.

### 7.3.3 Reconstruction of the reaction plane with the PSD detector

#### 7.3.3.1 The PSD detector

In the CBM experiment, the Projectile Spectator Detector [125] is the main sub-detector dedicated to the event characterization: the determination of the collision centrality and of the azimuthal orientation of the reaction plane. The latter features are of crucial importance for the analysis of event-by-event observables and in particular those related to the collective flow.

The PSD is a hadronic compensated modular calorimeter which will measure the energy carried by projectile spectator nucleons and fragments. It consists of 12 $\times$ 9 individual modules, each composed of 60 lead-scintillator layers. A sketch of one of those modules is depicted in Figure 7.8. The PSD detector is located in the forward rapidity region. It thus measures the energy of projectile spectators (deposited in the scintillator material). This allows in turn determining the number of participant particles and, therefore, the centrality of the collision. In the current design, the detector is placed at a distance of 15 m from the target. It has a hole to prevent the beam from hitting the detector. This hole is not placed around the beam axis, but shifted in the X-direction (X = + 10 cm) due to the deflection of beam ions in the magnetic field of CBM.

The transverse granularity of the calorimeter (12 $\times$ 9 modules), as illustrated in Figure 7.9, gives access to the azimuthal dependence of the energy carried by projectile spectators. Its energy resolution in conjunction with its granularity are important features for the determination of the orientation of the reaction plane angle.

**Detector acceptance**

Figure 7.10 shows the rapidity distribution of particles produced in Au + Au collisions at a beam energy of 25 GeV/nucleon with impact parameters from 0 to 16 fm. Y and $Y_{proj}$ are, respectively, the particle rapidity and the projectile rapidity in the center-of-mass frame. The black dashed histogram shows the distribution over the full phase space. Produced particles are located in the central (mid-rapidity) region of this distribution, while spectator (non interacting) particles are emitted at forward/backward rapidities. This explains the presence of the two structures around Y = |$Y_{proj}$|. The red full histogram corresponds to the rapidity distribution of particles entering the PSD detector acceptance. As one can see, the PSD calorimeter covers the region of the projectile rapidities (Y around $Y_{proj}$).

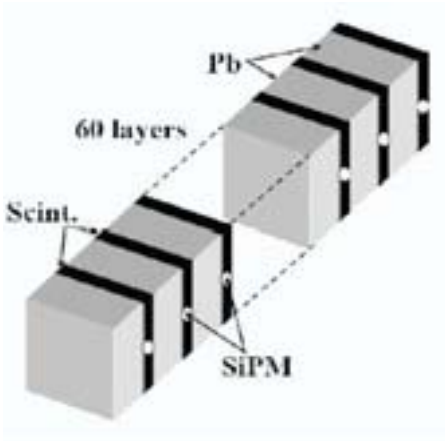


**Figure 7.8:** *Sketch of one PSD module made of a superposition of 60 layers of 4 mm thick scintillator plates and 16 mm thick lead absorbers. This module has an area of 10 × 10 $cm^2$. The Silicon Photo-Multipliers (SiPM) used for light readout are also shown [125].*

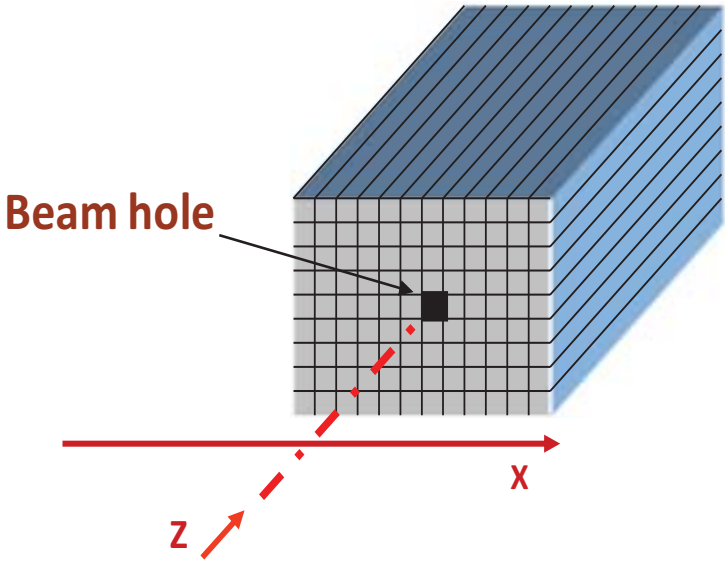


**Figure 7.9:** *Sketch of the overall PSD calorimeter [125]. The detector is segmented into 12 × 9 squared modules of 10 × 10 $cm^2$ (see Figure 7.8). The beam passes through it. The central hole prevents the beam from hitting the calorimeter.*

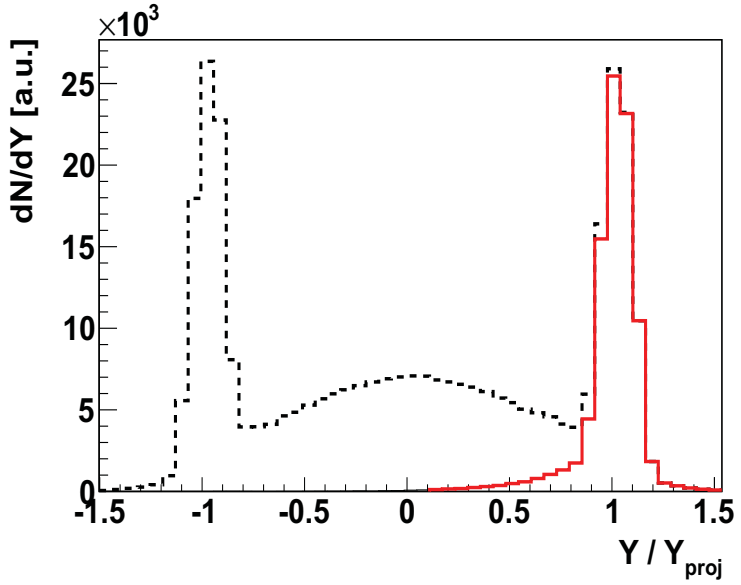


**Figure 7.10:** *Rapidity distribution of particles produced in Au + Au collisions at a beam energy of 25 GeV/nucleon with impact parameters from 0 to 16 fm. The particle rapidity Y and the projectile rapidity $Y_{proj}$ are in the center-of-mass frame. The black dashed histogram shows the distribution over the full phase space. The red full histogram corresponds to the rapidity distribution of particles entering the PSD detector acceptance.*

#### 7.3.3.2 Detector response

The interaction of particles with the PSD detector has been simulated using the GEANT3 transport code [107]. Note that GEANT simulates the energy loss of charged particles via electromagnetic interactions only. Hadronic interactions in the PSD detector are thus simulated using, in addition, the GCALOR simulation package [134].

The concept of compensated calorimetry allows the PSD detector measuring the energy of projectile spectators with high accuracy. The expected relative energy resolution is:

$$\frac{\sigma_E}{E} < \frac{50\%}{\sqrt{E(GeV)}} \tag{7.10}$$

in the energy range [15, 3000] GeV. Note that this resolution allows for a centrality selection with a collision impact parameter accuracy of around $10\%$ [125]

#### 7.3.3.3 Evaluation of the flow vector

As seen in Figure 7.10, the PSD covers the forward rapidity region around the beam rapidity, where the directed flow is dominant. We will, therefore, consider here only the first order event plane corresponding to the first harmonic (n = 1) in Equation (7.8).

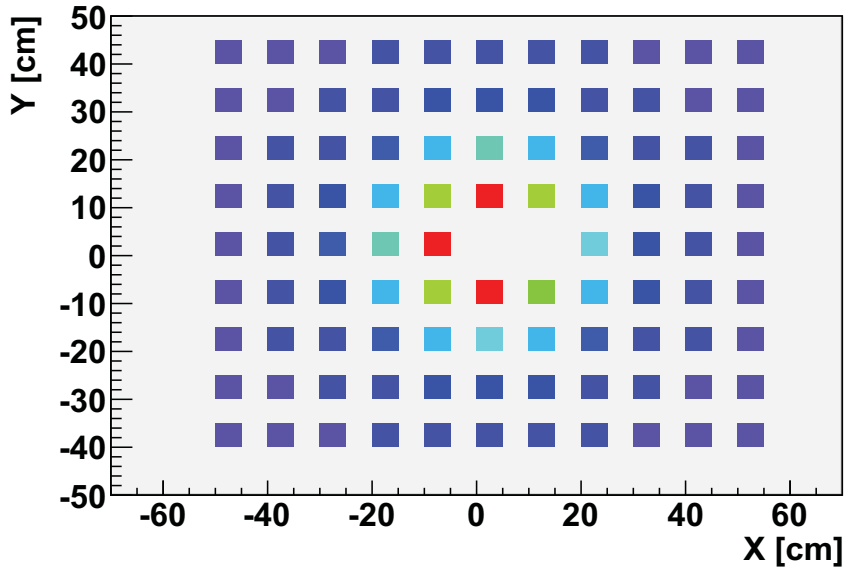


**Figure 7.11:** *Energy deposited into the PSD modules versus the location of the modules in the transverse plane (X, Y). Different colors correspond to different amounts of the energy deposition. The maximum is shown in red, followed by green, light blue and dark blue.*

The determination of the flow vector (see Section 7.3.1) has to be adapted to use the information provided by the PSD. The energy deposited into each of its 108 modules is shown in Figure 7.11. Because of the limited granularity, the energy deposited in a given module might include the contributions of several particles. Thus, in contrast with Equation (7.8), the calculation of the event flow vector is performed based on modules rather than particles, as follows:

$$\begin{aligned} Q_x &= \sum_i R_i \times E_{dep,i} \times \cos(\phi_i) \\ Q_y &= \sum_i R_i \times E_{dep,i} \times \sin(\phi_i) \end{aligned} \tag{7.11}$$

with $E_{dep,i}$ the energy deposited in the module i (i = 0 to 108), $\phi_i$ the azimuthal angle corresponding to the center of the module i, and $R_i$ its transverse distance to the beam axis. This distance is introduced as a weight factor ($w_i$ in Equation (7.8)). This is somehow equivalent to a transverse momentum weight: the further the module is from the beam axis, the bigger chance it has to intercept particles with high transverse momenta. The factor $R_i$ is used to put more weight on particles with high transverse momenta, which allows for a better determination of the reaction plane.

The energy deposited in the PSD modules is shown in Figure 7.11 as a function of the location of the modules in the transverse plane. As expected, the maximum (red and green colors) is observed in the most inner modules. Note the azimuthal asymmetry effect introduced by the beam hole, which affects mainly the central region of the calorimeter where the detector occupancy is the highest.

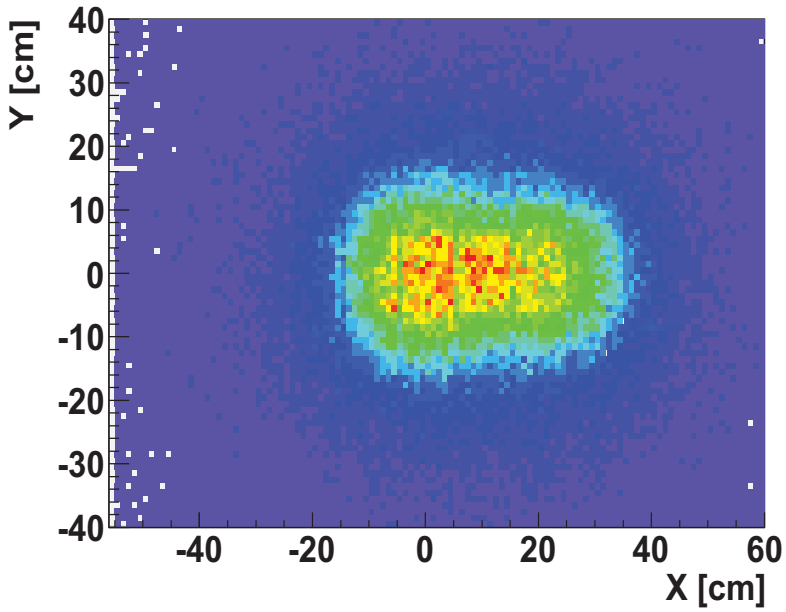


**Figure 7.12:** *Hit occupancy distribution in the first layer of the PSD detector for Au + Au collisions at a beam energy of 25 GeV/nucleon. The magnetic dipole field of CBM deflects the spectator protons in the direction X > 0 (the Z-axis being the beam axis).*

The presence of a magnetic field in the CBM experiment biases also the azimuthal symmetry of the energy deposited in the PSD modules. This is illustrated in Figure 7.12 by the hit occupancy distribution in the first PSD layer. The magnetic dipole field deflects the spectator protons along the X > 0 direction resulting in a strong azimuthal asymmetry effect.

The azimuthal asymmetries caused by the above mentioned detector biases affect severely the reconstruction of the reaction plane using the event plane method. This is clearly visible in the left panel of Figure 7.13, where the black histogram represents the distribution of the event plane angle for Au(25 AGeV) + Au collisions with an impact parameter 6 fm < b < 8 fm, obtained using Equation (7.9). This distribution exhibits a very pronounced maximum at $\Psi_1 = 0$. Such a trend departs substantially from the flat dependence expected in the absence of detector biases. This effect is also seen as a shift of the X-component ($Q_x$) of the event flow vector towards positive X-values (black histogram in the right panel of Figure 7.13).

Several methods have been proposed to overcome this problem [123] by flattening the event plane distribution. The simplest one among them is the so-called “re-centering” method. The latter is described in the next sub-section.

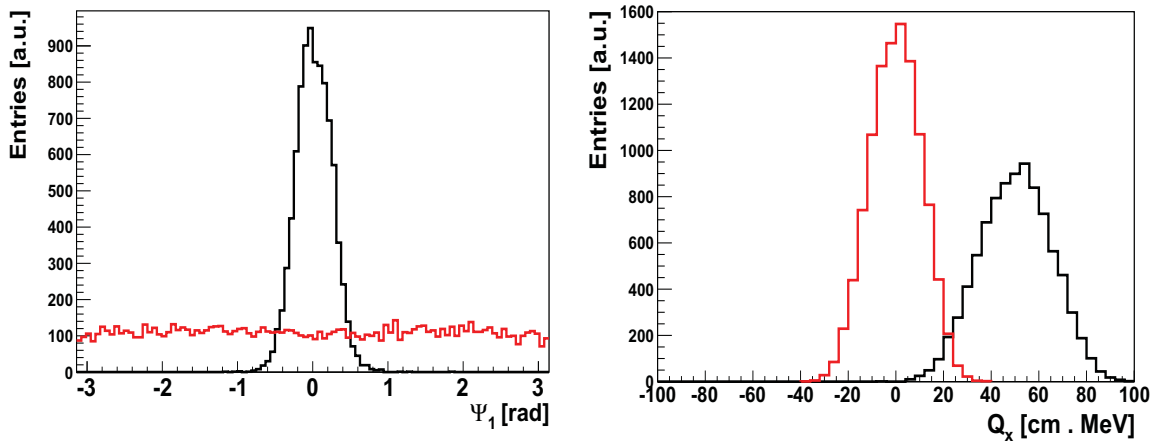


**Figure 7.13:** *Left panel: Event plane azimuthal angle distribution. Right panel: Distribution of the X-component ($Q_x$) of the event flow vector. The distributions are the results of the simulations for Au(25 AGeV) + Au collisions with an impact parameter 6 fm < b < 8 fm. They are shown before (black histogram) and after (red histogram) applying the re-centering procedure (see text).*

#### 7.3.3.4 Event plane flattening

We have used the re-centering procedure mentioned above to remove the detector biases due to the central beam hole in the PSD and the effect of the magnetic dipole field of CBM. In this method, the flow vector components of a given event are shifted by subtracting the ($Q_x$, $Q_y$) values averaged over all events (for a given centrality class) and divided by the standard deviation ($\sigma_x$, $\sigma_y$) of their distribution. With this correction, the components of the flow vector $\vec{Q}_1$ become:

$$Q_x^{corr} = \frac{Q_x - < Q_x >}{\sigma_x}$$
$$Q_y^{corr} = \frac{Q_y - < Q_y >}{\sigma_y} \tag{7.12}$$

In practice, one calculates (<$Q_x$>, <$Q_y$>) and ($\sigma_x$, $\sigma_y$) in a first pass through all simulated events belonging to the same centrality class, and then uses in a second pass the obtained shift and standard deviation values to recenter and normalize the flow vector components. The application of this method makes the distribution of the flow vector components centered around 0, as it can be seen in the right panel of Figure 7.13 (red histogram).

After applying the re-centering method, the event plane orientation angle can then be caculated from the above equations:

$$\Psi_1^{corr} = \arctan(\frac{Q_y^{corr}}{Q_x^{corr}}) \tag{7.13}$$

The resulting $\Psi_1^{corr}$ distribution, plotted as a red histogram in the left panel of Figure 7.13, is indeed fairly uniform, which illustrates the ability of the re-centering method to remove the

detector biases. Our simulations show the importance of applying such corrections in the case of the PSD detector of CBM before determining the event plane.

As already mentioned, other methods can also be used to remove non-uniformity effects of the experimental apparatus in the determination of the event plane, such as the "$\phi$ weighting method" and the "shifting method" [123]. In the first method, the distribution of the particles themselves is used as a measure of the detector acceptance. One accumulates the laboratory azimuthal distribution of the particles for all events and uses the inverse of this as weights in the calculation of the event planes ($w_i$ in Equation 7.8).

The application of these two methods in the case of the PSD of CBM did not result into a significant improvement with respect to the re-centering procedure. Therefore, only the latter method is used in the results which will be presented in the next section.

#### 7.3.3.5 Reaction plane resolution with the PSD detector

It is worth recalling here that the reconstruction of the reaction plane is mandatory for the analysis of many physics observables and in particular those related to the anisotropic collective flow. The latter must be corrected by the resolution factor due to the fluctuations of the reconstructed reaction plane. It is therefore important to evaluate the expected resolution in the CBM experiment. For this purpose, we compared the azimuthal angle $\Psi_1$ reconstructed with the PSD detector to the true reaction plane angle ($\Psi_R$), which is known in the model (UrQMD) used for event generation. Figure 7.14 shows the distribution of the difference between the reconstructed and generated azimuthal angles of the reaction plane, obtained for semi-peripheral (6 fm < b < 8 fm) Au(25 AGeV) + Au collisions. The resolution of the reaction plane can be evaluated from the standard deviation of this distribution. This is done by fitting a Gaussian function to the distribution (red line in 7.14). The obtained standard deviation, $\sigma$, is of about 38 degrees, which indicates that in this case the reaction plane can be determined with a good accuracy.

Figure 7.15 exhibits the impact parameter (b) dependence of the expected resolution $\sigma$ for Au(25 AGeV) + Au collisions. As can be seen, the best performance is achieved for semi-peripheral collisions: a resolution $\sigma$ of about 40 degrees in the b-range from 5 to 9 fm. This is not surprising, since it is in this impact parameter range that the magnitude of the sideward flow is the highest. In this case, the reaction plane is well defined and easier to determine using the event plane method. One has to keep in mind that in the event plane procedure, the reaction plane is determined from the anisotropic flow itself and, therefore, the resolution $\sigma$ must depend on the magnitude of this effect.

The worsening of the reaction plane resolution seen in the low b-side (Figure 7.15) is explained by the gradual vanishing of the directed flow towards highly central collisions (due to the absence of spectators). Moreover, the reaction plane resolution depends on the multiplicity of measured particles, or equivalently on the amount of energy carried by projectile spectators and measured by the PSD detector. The acceptance of the PSD detector being located at forward rapidities, the measured amount of energy decreases in central collisions where the forward rapidity region gets depleted. On the high b-side (i.e., peripheral collisions), the resolution $\sigma$ also deteriorates.

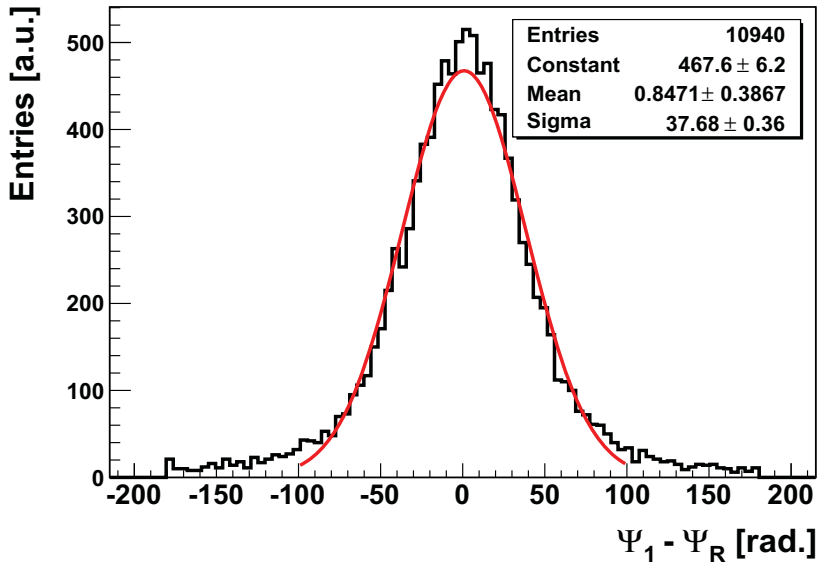


**Figure 7.14:** *Distribution of the difference between the reconstructed event plane ($\Psi_1$) and the true reaction plane ($\Psi_R$) in semi-peripheral Au + Au events (6 < b < 8 fm) at a beam energy of 25 GeV/nucleon. The red line is a Gaussian fit to the distribution.*

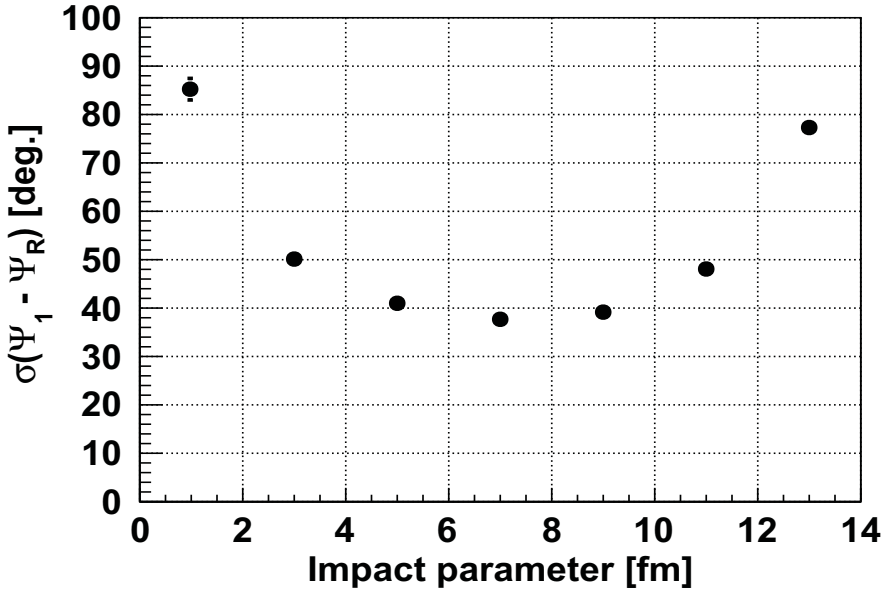


**Figure 7.15:** *Reaction plane resolution achieved with the PSD detector for Au(25 AGeV) + Au collisions as a function of the collision impact parameter. The error bars represent the statistical uncertainties.*

This is due to the fact that the magnitude of the directed flow becomes smaller and smaller as the collision centrality decreases (no directed flow in the absence of participant matter).

The resolution on the reaction plane azimuthal angle can be also expressed in terms of the Res($\Psi_R$) factor defined in Equation (7.6), where n is the flow harmonics. The knowledge of this factor is of crucial importance in the analysis of anisotropic flow observables since the magnitude of the observed anisotropic flow must be corrected by this factor (see Appendix G). Using the first order event plane (n = 1), the observed directed flow ($v_1^{obs}$) and elliptic flow ($v_2^{obs}$) must be corrected, respectively, as follows:

$$\begin{aligned} v_1^{corr} &= \frac{v_1^{obs}}{< cos(\Psi_1 - \Psi_R) >} \\ v_2^{corr} &= \frac{v_2^{obs}}{< cos(2 \times (\Psi_1 - \Psi_R)) >} \end{aligned} \tag{7.14}$$

where the vector brackets denote an average over a sample of events with the same centrality.

Figure 7.16 shows the $< cos(\Psi_1 - \Psi_R) >$ (blue circles) and $< cos(2 \times (\Psi_1 - \Psi_R)) >$ (red squares) resolution factors as a function of the collision impact parameter. Here again, one sees that the best resolutions (i.e. highest values of the resolution factor) are obtained in semi-peripheral collisions, for the same reasons as explained above regarding the trend observed in Figure 7.15. These results demonstrate the capability of the PSD detector for accurately measuring the event plane. This will allow for detailed measurements of both the directed flow ($v_1$) and the elliptic flow ($v_2$) over a quite broad range in impact parameter (from about 3 fm to 11 fm).

### 7.3.4 Reconstruction of the reaction plane with the STS detector

The STS tracker, due to its large acceptance and high granularity, can be also used as a reaction plane detector.

#### 7.3.4.1 Detector set-up

The STS detector setup used in the simulations presented in this section consists in 8 silicon planar stations placed at distances of 30, 35, 40, 50, 60, 75, 95 and 100 cm from the target. We considered a realistic geometry and thickness of the detector planes, as presented in Table 6.1 of the previous chapter. Note that we considered here a slightly different set-up, i.e. two additional detector planes located at 35 and 95 cm from the target, and assumed that the detector stations are all made of silicon strips (as described in Section 3.3.2).

**Detector acceptance**

Figure 7.17 presents the rapidity distribution of particles produced in Au + Au collisions at a beam energy of 25 GeV/nucleon with impact parameters from 0 to 16 fm. The black dashed

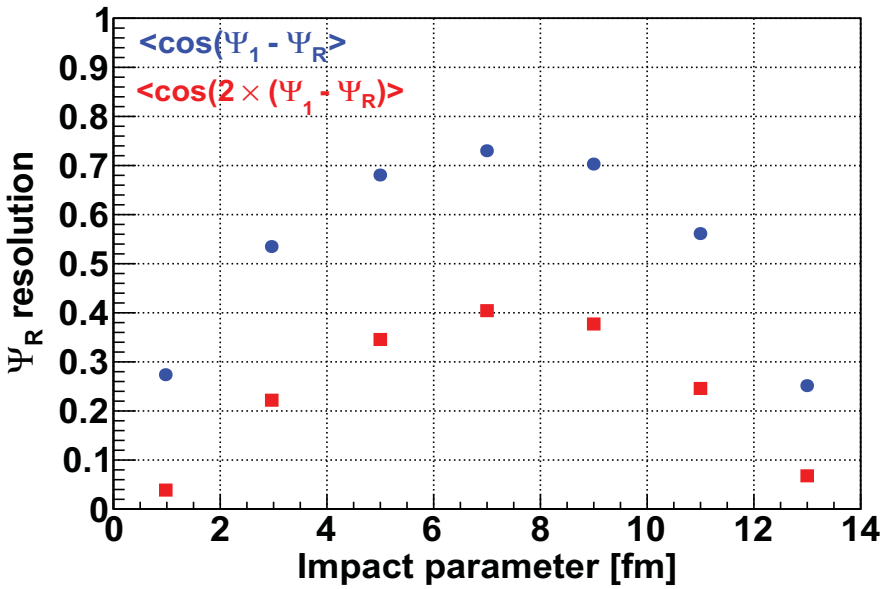


**Figure 7.16:** *Reaction plane resolution expressed in terms of the correction factors* $<cos(\Psi_1 - \Psi_R)>$ *(blue circles) and* $<cos(2 \times (\Psi_1 - \Psi_R))>$ *(red squares) for Au(25 AGeV) + Au collisions as a function of the collision impact parameter. The statistical uncertainties are smaller than the symbol sizes.*

histogram shows the distribution over the full phase space. The red full histogram corresponds to the rapidity distribution of charged particles entering the STS detector. Accepted particles are defined as those producing hits in at least 4 STS detector planes. As one can see, the STS tracker covers a large region of the phase space including the mid-rapidity region (Y around 0).

#### 7.3.4.2 Detector response

Detailed GEANT simulations have been performed taking into account the single point resolution of the STS detector stations as explained in Section 6.2.3. The track reconstruction procedure (track finding and track fitting) used in the simulations is described in Section 6.2.4.

#### 7.3.4.3 Evaluation of the second order event plane

Because of its large acceptance of participant particles (mid-rapidity region in Figure 7.17), the STS is most suited for the reconstruction of the second order event plane (corresponding to the second harmonic n = 2 in Equation (7.8)). The components of the flow vector can be written as:

$$\begin{aligned} Q_x &= \sum_i w_i \times \cos(2 \times \phi_i) \\ Q_y &= \sum_i w_i \times \sin(2 \times \phi_i) \end{aligned} \tag{7.15}$$

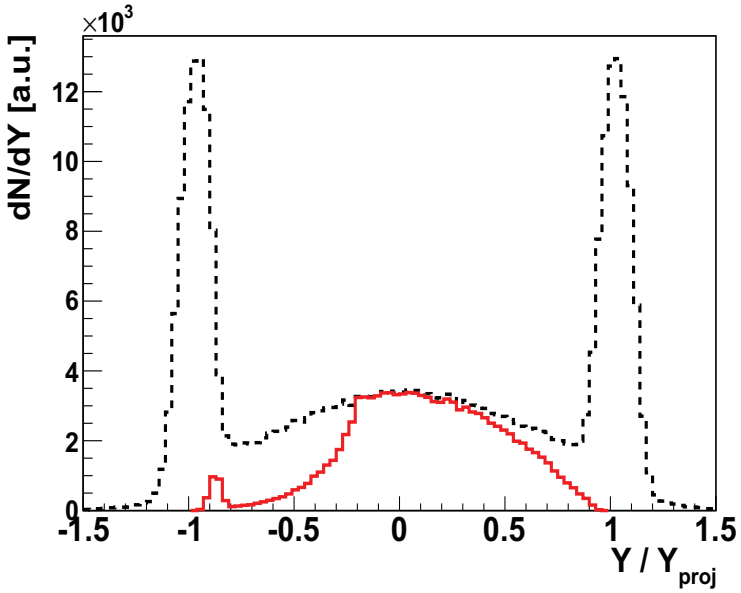


**Figure 7.17:** *Rapidity distribution of particles produced in Au + Au collisions at a beam energy of 25 GeV/nucleon with impact parameters from 0 to 16 fm. The particle rapidity Y and the projectile rapidity $Y_{proj}$ are in the center-of-mass frame. The black dashed histogram shows the distribution over the full phase space. The red full histogram corresponds to the rapidity distribution of charged particles entering the STS detector acceptance, i.e. particles producing hits in at least 4 STS stations.*

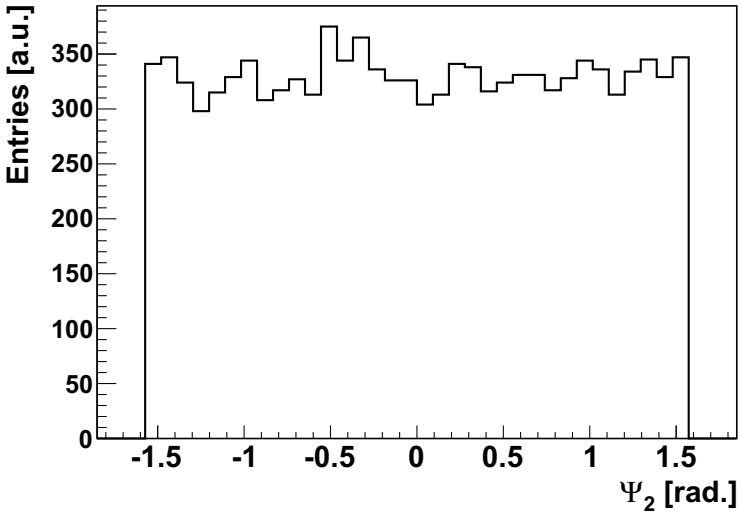


**Figure 7.18:** *Event plane azimuthal angle ($\Psi_2$) distribution in semi-peripheral Au(25 AGeV) + Au collisions (impact parameter range from 6 to 8 fm).*

The weight factors $w_i$ are taken here as the transverse momentum of particles. This choice is motivated by the fact that the elliptic flow increases with the particle transverse momentum. In this way, the contribution of the particles participating to a stronger flow is enhanced. The event plane orientation angle can then be obtained as:

$$\Psi_2 = \frac{1}{2}\arctan(\frac{Q_y}{Q_x}) \tag{7.16}$$

The distribution of the event plane azimuthal angle is shown in Figure 7.18.

#### 7.3.4.4 Reaction plane resolution with the STS detector

We have evaluated the expected resolution on the reaction plane azimuthal angle with the STS detector for Au + Au collisions at an incident energy of 25 AGeV. To do that, we have performed full Monte Carlo simulations: propagation of the produced particles through the STS detector stations taking into account the magnetic dipole field and the reconstruction of the charged particle tracks from the produced hits in the stations (see Section 6.2). Note that additional criteria were applied on the quality of the reconstructed tracks, by excluding tracks with $\chi^2_{prim}$ > 2 and IP > 500 $\mu$m (those variables are defined in Section 6.4.2).

For each simulated event, the reaction plane has been reconstructed by evaluating the second order event flow vector, as described in the previous section. The contribution of secondary decay particles which are less well correlated to the reaction plane has been significantly reduced by imposing the cuts mentioned above. Note in passing that this contribution amounts on the average to 15 - 20% of the total number of particles, its effect on the resolution of the reaction plane was thus found to be very small. It is worth noting that due to the excellent tracking performances

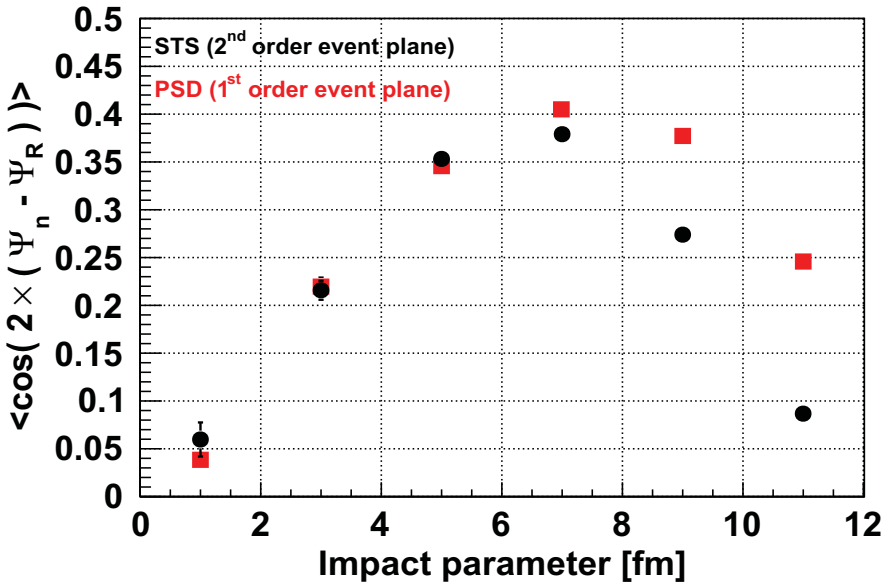


**Figure 7.19:** *Reaction plane resolution, expressed in terms of the* $<cos(2\times(\Psi_n-\Psi_R))>$ *factor as a function of the collision centrality for Au + Au collisions at a beam energy of 25 GeV/nucleon. The black circles correspond to the resolutions obtained using the second order event event plane (n = 2) reconstructed with the STS detector. They are compared to those obtained in Section 7.3.3.5 using the first order event plane (n = 1) with the PSD calorimeter (red squares). The error bars represent the statistical uncertainties.*

in CBM, the use of reconstructed tracks (instead of Monte Carlo tracks) did not lead to any significant degradation in the reconstruction of the reaction plane. Note also that the azimuthal asymmetry of the STS detector due to its elongated (ovoid-like) shape (see Figure 3.6) and the presence of the magnetic dipole field (which deflects charged particles mostly along the X-axis), were found to have a negligible effect on the accuracy of the determination of the reaction plane. Therefore, in contrast to the case of the PSD (Section 7.3.3.4), the flattening of the event plane distribution was not necessary here. Nonetheless, the track selection criteria mentioned earlier and the event plane flattening are mandatory to properly estimate the reaction plane resolution experimentally (see Section 7.4.2). For consistency, the distributions shown in Figures 7.18 and 7.19 are obtained after the application of these two procedures.

Figure 7.19 presents the reaction plane resolution, expressed in terms of the $<cos(2 \times (\Psi_n - \Psi_R))>$ correction factor, as a function of the collision impact parameter. The results obtained here using the second order event plane (n = 2) reconstructed with the STS detector are indicated with the black circles. They are compared to those obtained in Section 7.3.3.5 using the first order event plane (n = 1) with the forward PSD calorimeter (red squares). It should be reminded here that, by definition, larger (smaller) $<cos(2 \times (\Psi_n - \Psi_R))>$ values correspond to better (worse) resolutions of the reaction plane. As can be seen in the figure, the centrality dependence of the resolution factor exhibits a maximum for semi-peripheral collisions. This trend is very

similar to the one found for the PSD detector. This is due to the fact that the resolution of the reaction plane depends on the event particle multiplicity and on the magnitude of the elliptic flow: this gives a good resolution for high multiplicity and strong elliptic flow (which is the case of semi-peripheral collisions) and a poor resolution for weak elliptic flow (central events) and low multiplicity (peripheral events). The best event plane resolutions obtained with the STS detector are for collisions in the impact parameter range from 6 to 8 fm, i.e. a correction factor of about 0.38.

It is interesting to notice that both the STS and the PSD, although they cover two different phase space regions, give similar event plane resolution factors for central and semi-peripheral collisions (for impact parameters below 9 fm). The PSD calorimeter gives, however, a better resolution for very peripheral collisions thanks to its coverage of the forward phase space region. These results show that the PSD and the STS will provide two independent and complementary measurements of the event plane in CBM. They will be both used in the analysis of the elliptic flow. This will be very important for controlling the systematic errors due to the uncertainty on the experimental evaluation of the resolution of the reaction plane. We will come back on this point at the end of this chapter.

In the sequel, we will exploit the information provided here on the expected resolution of the reaction plane for investigating the capabilities of the CBM experiment in measuring the elliptic flow of open charm mesons. For this purpose, we will consider semi-peripheral collisions where the magnitude of elliptic flow is the largest. This corresponds to a resolution factor $<cos(2 \times (\Psi_n - \Psi_R))>$ of about 0.4 and a standard deviation $\sigma(\Psi_1 - \Psi_R)$ of approximately 40 degrees (as shown in Section 7.3.3.5). It is this latter value that we will use in the simulations presented in the following section.

## 7.4 Expected performances of CBM for open charm elliptic flow measurements

It is important to remind that our primary aim in this chapter is to investigate the sensitivity of the CBM experiment for the measurement of open charm elliptic flow. For this purpose, we need to evaluate the statistical accuracy with which this observable could be measured, taking into account the expected resolution of the reaction plane. That is the object of this section. We will estimate the expected statistical errors on the magnitude of the elliptic flow of D-mesons and will also discuss the main systematic uncertainties.

### 7.4.1 Evaluation of the expected statistical accuracy for D-meson elliptic flow measurements

This work represents the first simulation study of D-meson elliptic flow in CBM. For this reason and in order to allow performing fast simulations, we adopted a very simple Monte Carlo pro-

cedure based mainly on the random generation of azimuthal angles (according to Equation 7.2). The way the elliptic flow signal is introduced in this procedure has been described in Section 7.2 for mid-rapidity D mesons in semi-peripheral Au + Au collisions at an incident energy of 25 AGeV. In this procedure, one assumes an ideal reconstruction of D-mesons at mid-rapidity. This can be justified by the good performances of CBM in reconstructing open charm particles: a quite good signal to background ratio (S/B), e.g. S/B = 1.5 for $D^+$ mesons, and almost the same reconstruction efficiency over a $p_T$ range up to $\sim$ 2 GeV/c (see Chapter 6). The contribution of the combinatorial background to the systematic uncertainties will be discussed at the end of this section.

Examples of simulated azimuthal distributions were given in Figures 7.5. Those distributions were obtained assuming the knowledge of the true reaction plane of each event. To take into account the fluctuations of this plane due to the finite number of particles and to detector biases, D-meson azimuthal angles were smeared with the resolution of the reaction plane, $\sigma(\Psi_R)$ = 40 degrees, as determined in the previous section. The resulting azimuthal distribution (dN/d($\phi$ - $\Psi_R$)) for D-mesons with 1 GeV/c < $p_T$ < 2 GeV/c is shown in Figure 7.20 for two input values of the elliptic flow: $v_2(p_T) = \alpha \times p_T$, with $\alpha$ = 0.03 (left panel) and 0.06 (right panel). These distributions are obtained for an event sample of $N_D$ = 6.2 $\times$ $10^4$, corresponding to one CBM run period (i.e., 8 weeks beam on target at a collision rate of 400 kHz) for semi-peripheral Au(25 AGeV) + Au collisions. This number ($N_D$) has been estimated by rescaling the yield of D-mesons from the results of our simulations for central Au + Au collisions (Chapter 6) as follows:

- We assumed that semi-peripheral collisions represent a fraction of about 23% of the total number of collisions (instead of 10% for central collisions). This would correspond typically to an impact parameter range from 5 to 9 fm. Note that the elliptic flow is maximal in this range and that is also where the best resolutions on the event plane are obtained (see Figure 7.19).

- We assumed that the D-meson multiplicity scales with the number of binary collisions. The latter was found to decrease by about a factor of 2.6 [133] from central to semi-peripheral collisions (as defined in the previous item).

- We assumed that the D-meson reconstruction efficiency in semi-peripheral collisions is the same as the one we have evaluated in Chapter 6 for central collisions (see Table 6.6). This can be considered as a conservative assumption. In fact, one expects a higher reconstruction efficiency in semi-peripheral collisions due to the much lower combinatorial background. The latter scales with the number of participants squared (e.g., for $D^0 \rightarrow \pi^+$ $K^-$) or cubed (e.g., for $D^+ \rightarrow \pi^+$ $\pi^+$ $K^-$). A realistic estimate of this efficiency would require detailed simulations similar to those we have performed in the case of central collisions. This will have to be done in the future.

The azimuthal distribution shown in the left side of Figure 7.20 (for $v_2(p_T) = 0.03 \times p_T$) has been used to derive the magnitude of the elliptic flow (the $v_2$ parameter) in the same way as we have done in Section 7.2 (using Equation 7.3). The $v_2$ values obtained for different D-meson transverse

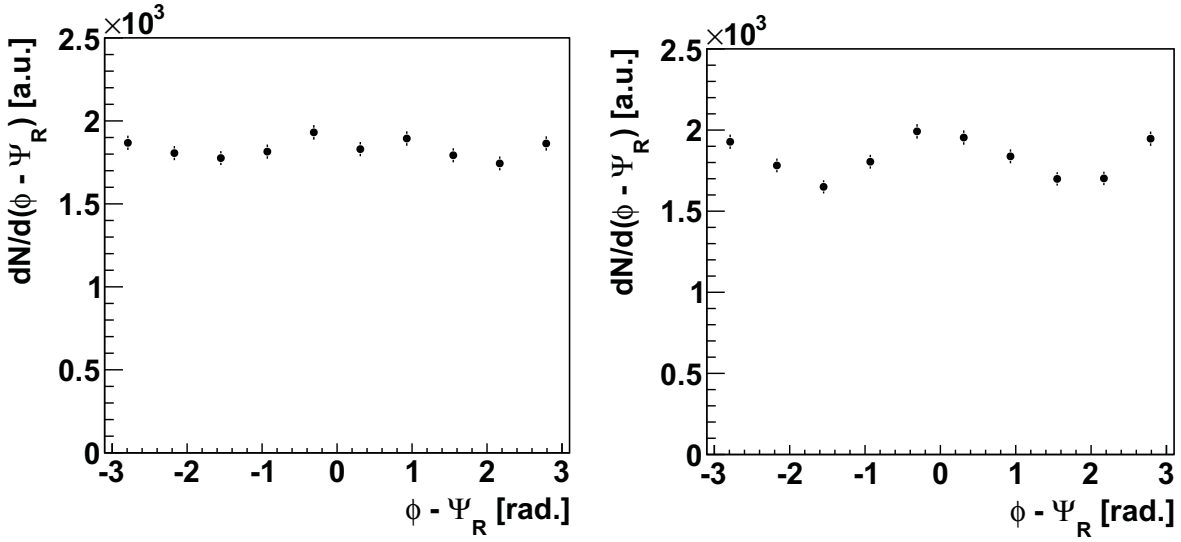


**Figure 7.20:** *Azimuthal distributions relative to the reaction plane for mid-rapidity D-mesons with 1 GeV/c < $p_T$ < 2 GeV/c, produced in semi-peripheral Au(25 AGeV) + Au collisions. These distributions were obtained for an event sample of 6.2 $\times$ $10^4$ D-mesons, corresponding to a single CBM run period (i.e. 8 weeks beam on target at a collision rate of 400 kHz) and for two input values of the elliptic flow: $v_2(p_T) = \alpha \times p_T$, with $\alpha$ = 0.03 (left panel) and 0.06 (right panel). The vertical bars correspond to the statistical uncertainties.*

momentum bins are shown by the open circles in Figure 7.21 and compared to the $v_2$ values used as an input in the simulations (indicated by the solid red line). They are termed "$v_2^{obs}$" because they correspond to what would be observed in the experiment. As can be seen in the figure, the "observed" magnitude of D-meson elliptic flow is systematically and significantly lower than the input $v_2$ values, an effect which is due to the fluctuations of the event plane azimuthal angle around the true reaction plane angle. This effect can be corrected for by dividing the observed $v_2$ by the resolution factor Res($\Psi_R$), as explained in Section 7.2 (see Equation 7.5). The corrected $v_2$ values (termed hereafter as "measured" $v_2$) are indicated by the full circles in Figure 7.21. This correction is satisfactory, since the measured $v_2$ values are indeed consistent, within error bars, with the input $v_2$ values (red curve).

We give in Table 7.1 the value of the $v_2$ parameter obtained by integrating over the transverse momentum (i.e., $p_T$-integrated $v_2$) and by correcting for the resolution of the reaction plane. The error bars are the statistical uncertainties. The first line corresponds to all D-mesons that could be measured per run with CBM ($N_D$ = 6.2 $\times$ $10^4$) and the following lines to individual D-meson species. The relative yield contributions of the latter were taken from Table 6.7 (Chapter 6), including in addition the scaling from central to peripheral collisions (as explained above). The results show that the measurement of the $p_T$-integrated elliptic flow of open charm mesons should be feasible but with only a modest statistical accuracy: a relative uncertainty of about 41% for all D-mesons and from 54 to 110% for individual species. These uncertainties would be even larger for more detailed $p_T$-differential measurements, as can be seen in Figure 7.21.

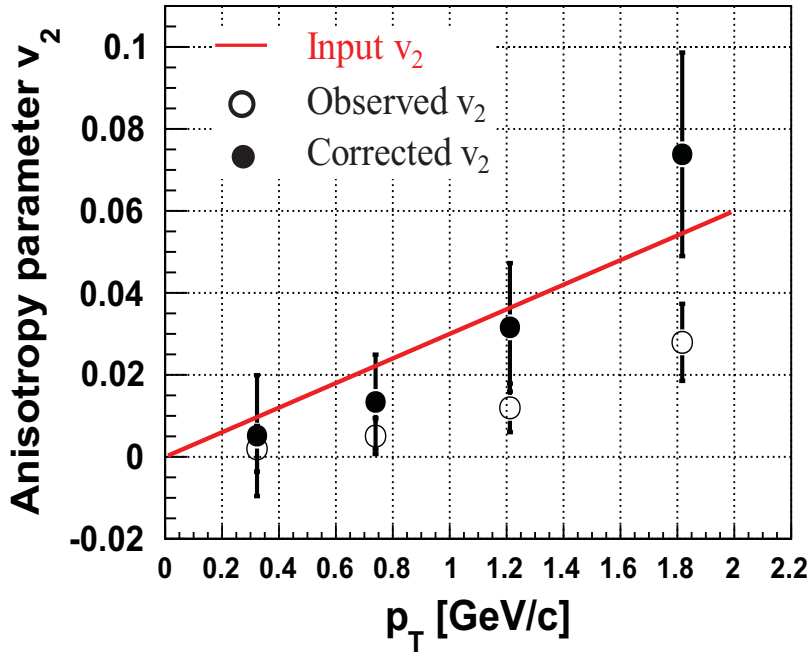


**Figure 7.21:** *Elliptic flow parameter of D-mesons as a function of their transverse momentum in semi-peripheral Au(25 AGeV) + Au collisions. Open circles (full circles) are the values obtained before (after) applying the correction for the resolution of the reaction plane (see text). They are obtained for an event sample of 6.2 $\times$ $10^4$ D-mesons, corresponding to a single CBM run period (i.e. 8 weeks beam on target at a collision rate of 400 kHz). The error bars correspond to the statistical uncertainties. The red line corresponds to the $v_2$ values used as an input in the simulations.*

| particles | yield/year | $v_2$ | $\frac{\delta v_2}{v_2}$ |
|---|---|---|---|
| $N_D$ | $6.2 \times 10^4$ | $0.018 \pm 0.0075$ | 41 % |
| $D^+$ | $1.3 \times 10^4$ | $0.022 \pm 0.016$ | 73 % |
| $D^-$ | $2 \times 10^4$ | $0.024 \pm 0.013$ | 54 % |
| $D^0$ | $7 \times 10^3$ | $0.02 \pm 0.022$ | 110 % |
| $\bar{D^0}$ | $2 \times 10^4$ | $0.024 \pm 0.013$ | 54 % |

**Table 7.1:** *$p_T$-integrated elliptic flow ($v_2$-integrated) of D-mesons in semi-peripheral Au(25 AGeV) + Au collisions. The results have been obtained for an event sample corresponding to one CBM run period (i.e., 8 weeks beam on target at a collision rate of 400 kHz). The errors correspond to the statistical uncertainties.*

The large statistical uncertainties on the D-meson elliptic flow measurements are due to the limited statistics that one can accumulate during a CBM run period, but also to the very weak $v_2$ magnitude of D-mesons used as an input in the simulations ($v_2(p_T)$ = 0.03 $\times$ $p_T$). It has to be reminded that the elliptic flow was introduced in our simulations (Section 7.2) on the basis of the predictions of the HSD transport model, which is a purely hadronic model and where the elliptic flow of D-mesons is very low because of their low hadronic cross-section.

In fact, at FAIR energies one expects the partonic degrees of freedom to play a non-negligible role (see Chapter 2). This is supported by recent predictions from the PHSD (Parton-Hadron String Dynamics) model [131], which is an extension of the HSD model that includes also the dynamics of explicit partonic degrees of freedom as well as dynamical local transition rates from partons to hadrons. In this model, the relative contribution of partonic interactions in Au + Au collisions is quite substantial at top FAIR energies: it represents about 25-30$\%$ in the central region of the collision at $\sqrt{s_{NN}}$ = 9 GeV [132]. It has been shown that this important partonic activity has an effect to enhance the strength of the elliptic flow at this energy, by about a factor of 1.7 (as compared to HSD predictions) for mid-rapidity charged hadrons with 0.75 GeV/c < $p_T$ < 1 GeV/c in peripheral collisions [132]. Similar predictions were also made within the AMPT (A Multi Phase Transport model) transport code [130], which has the possibility to include a partonic phase (by including "string melting") before hadronization. The inclusion of "string melting" in this model leads to an increase of the elliptic flow of mid-rapidity charged hadrons by about a factor of 2 in peripheral Au(25 AGeV) + Au collisions (see Figure 2.21 in Chapter 2), which results from a longer phase of partonic interactions during the early stage of the reaction.

In Reference [132], it has been suggested that the observation of a strong collective flow (i.e., sizeably larger than in a purely hadronic scenario) for charm mesons at FAIR would indicate the presence of partonic degrees of freedom already at bombarding energies of 25-35 AGeV. Quantitative predictions for D-meson elliptic flow in PHSD are, however, not available yet. In the meanwhile and in order to illustrate the capabilities of the CBM experiment in the case of a strong D-meson flow, we made the 2 following assumptions:

- We increased the $v_2$ input in our simulations by a factor of 2: $v_2(p_T)$ = 0.06 $\times$ $p_T$ instead of $v_2(p_T)$ = 0.03 $\times$ $p_T$.
- We used an angular resolution of the reaction plane of $\sigma(\Psi_R)$ = 30 degrees (instead of 40 degrees), which is motivated by the fact that $\sigma(\Psi_R)$ is expected to be better if the flow of produced hadrons is stronger. This is important, as statistical accuracy on the determination of the elliptic flow depends also on the resolution of the reaction plane (see Equation 7.7).

Note that the D-meson production yield may be also higher if partonic degrees of freedom are included, which would translate into higher statistics and better statistical accuracy for the D-meson elliptic flow. This was, however, not considered in the current study.

Results under the two above assumptions are given in Figure 7.22 and Table 7.2 for the same event sample as previously ($N_D$ = 6.2 $\times$ $10^4$). The statistical accuracy on the D-meson elliptic flow is clearly much better than in the case of weaker flow (Figure 7.21 and Table 7.1). For the

| particles | yield/year | $v_2$ | $\frac{\delta v_2}{v_2}$ |
|---|---|---|---|
| $N_D$ | $6 \times 10^4$ | $0.049 \pm 0.0049$ | 10 % |
| $D^+$ | $1.3 \times 10^4$ | $0.054 \pm 0.01$ | 18 % |
| $D^-$ | $2 \times 10^4$ | $0.055 \pm 0.009$ | 16 % |
| $D^0$ | $7 \times 10^3$ | $0.062 \pm 0.015$ | 24 % |
| $\bar{D}^0$ | $2 \times 10^4$ | $0.055 \pm 0.009$ | 16 % |

**Table 7.2:** *$p_T$-integrated elliptic flow of D-mesons in semi-peripheral Au(25 AGeV) + Au collisions, assuming that the elliptic flow is stronger by a factor of 2 and a better resolution of the reaction plane (Res($\Psi_R$) = 30 degrees instead of 40 degrees). The results have been obtained for an event sample corresponding to one CBM run period (i.e. 8 weeks beam on target at a collision rate of 400 kHz). The errors correspond to the statistical uncertainties.*

$p_T$-integrated flow, the relative statistical uncertainty is about 10% for all D-mesons and from 16% to 24% for individual D-meson species. The $p_T$-differential flow would be also measurable in this case, although with a modest accuracy. From this, one can conclude that if the flow is strong, which is likely to be the case at the highest FAIR energies (25-35 AGeV), then the CBM experiment will be able to perform detailed measurements of the integrated elliptic flow of open charm. This could be readily done as a function of the incident energy (at least above 25 AGeV).

The other conclusions that one can draw from the present study, is that even very small magnitudes of D-meson elliptic flow in Au(25 AGeV) + Au collisions could be measured, although with a limited statistical accuracy, and that the sensitivity of the experiment should be sufficient to discriminate purely hadronic models (e.g. HSD) and models including partonic degrees of freedom (e.g. PHSD) from one another. The latter point is illustrated in Figure 7.22, where one compares the results obtained for "low flow" and "strong flow" simulations for the same event sample (i.e., corresponding to one year of data taking at a collision rate of 400 kHz). Measurements significantly higher than the "low flow" points would indicate an important rescattering at the partonic level, which may induce collectivity also for the charm quarks. Such measurements may provide also information about the extent of thermalization of light quarks through partonic interactions.

### 7.4.2 Comments on the expected systematic errors

In the present study, we focused on the evaluation of the statistical accuracy that one can expect for the measurements of D-meson elliptic flow with the CBM experiment. This was extremely important to ensure that the proposed detection system, in particular its sub-detectors needed for open charm reconstruction and for the reaction plane determination, will provide the necessary accuracy to allow detailed studies of this observable. In the experiment, such measurements will also be subject to systematic uncertainties. Below, we discuss briefly some of their main sources:

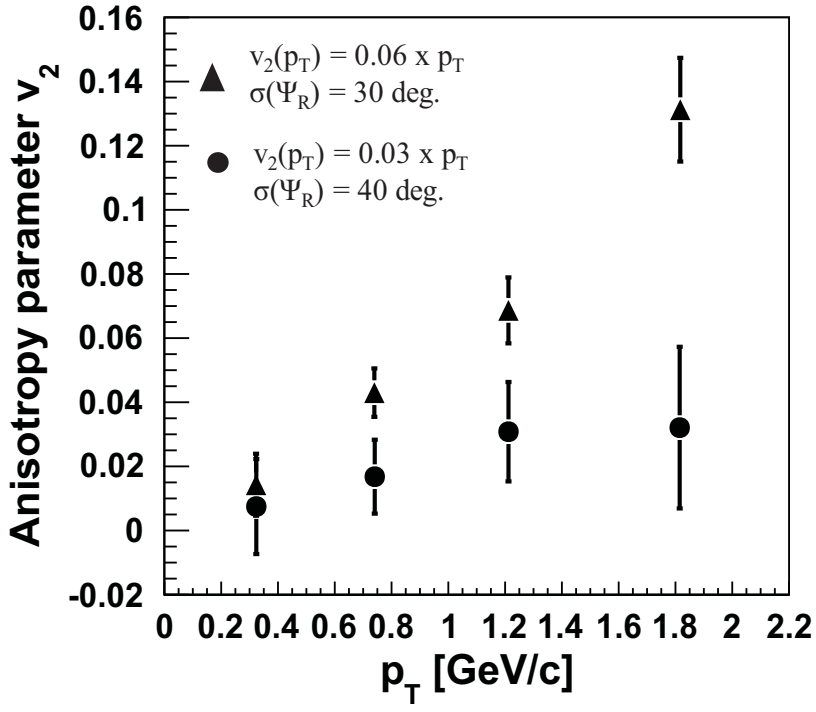


**Figure 7.22:** *Elliptic flow parameter of D-mesons as a function of their transverse momentum in semi-peripheral Au(25 AGeV) + Au collisions. Full circles are the same as in Figure 7.21. Full triangles are obtained assuming that the elliptic flow is stronger by a factor of 2 and a better resolution of the reaction plane (Res($\Psi_R$) = 30 degrees instead of 40 degrees). The results are shown for an event sample of 6.2 $\times$ $10^4$ D-mesons, corresponding to a single CBM run period (i.e., 8 weeks beam on target at a collision rate of 400 kHz). The error bars correspond to the statistical uncertainties.*

- The uncertainty due to the subtraction of the combinatorial background in the reconstruction of open charm mesons through their decay daughter particles. The background subtraction must be done for each ($\phi$ - $\Psi_R$) bin in order to obtain the azimuthal distributions relative to the reaction plane required for the extraction of the $v_2$ signal. Considering the good S/B-ratio expected in semi-peripheral Au(25 AGeV) + Au collisions (which should be at least on the same order as those reported in Table 6.7 for central collisions, due to the much lower combinatorial background expected in semi-peripheral collisions), one expects that the systematic error on $v_2$ due the background subtraction procedure will be small.

- The uncertainty on the evaluation of the event plane resolution. The latter is required to correct the observed $v_2$ values for the fluctuations of the estimated reaction plane due to finite multiplicity effects and to detector biases (see Section 7.3). In our simulations, we evaluated this resolution based on the knowledge of the true reaction plane angle. This will not be the case in the experiment, where only an estimate of this resolution can be obtained. The method generally used for this purpose is the so-called sub-event procedure [123]. It consists in splitting each event into two separated sub-events equal in multiplicity. The event plane resolution can be estimated from the correlation between the azimuthal angles of the two sub-events. A more detailed description of this method can be found in Appendix H. As an example, we show in Figure 7.23 the results obtained by applying this method to simulated events in the case where the reaction plane is determined by means of the STS detector. The resolution estimated with the sub-event procedure (red open crosses) is compared to the one (black full circles) obtained in Section 7.3.4.4 on the basis of the knowledge of the true reaction plane angle. Note that additional criteria were applied on the quality of the reconstructed tracks: this was done by excluding tracks with $\chi^2_{prim} > 2$ and IP > 500 $\mu$m (those variables are defined in Section 6.4.2). The flattening of the two sub-event planes using the re-centering technique was also effective in improving the precision of the method in central collisions (impact parameter below 5 fm). As can be seen, the two set of points are in agreement within the statistical accuracy of the simulation, except for the most peripheral collision bins (from 9 to 12 fm). The latter discrepancy is an effect of the finite number of particles. This effect becomes important in peripheral collisions and impacts the two methods differently.

- The possible systematic uncertainty due to non-flow correlations, i.e. azimuthal correlations not related to the reaction plane orientation. Several physical effects can give rise to those non-flow correlations at FAIR energies. Among them are short-range correlations (e.g., HBT), Coulomb effects, momentum conservation, correlations caused by resonance decays and initial eccentricity fluctuations. The event plane method is known to be particularly sensitive to these effects [123]. This can affect both the evaluation of the resolution on the reaction plane (previous item) and the observed magnitude of the elliptic flow. The contamination arising from these non-flow correlations can be accounted for and corrected quite accurately using different methods (e.g., based on the cumulant procedure [126] or the Lee-Yang Zero method [127]) recently developed for this purpose. This will be partic-

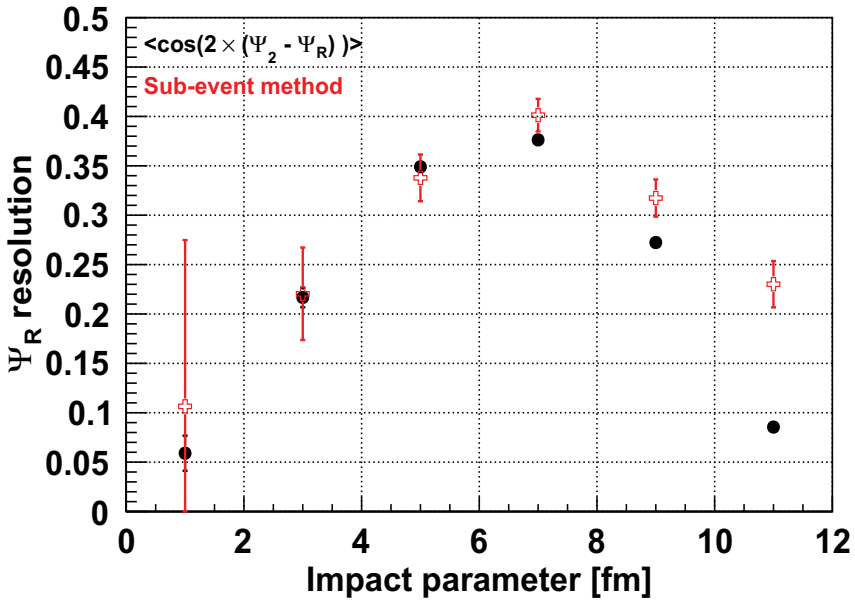


**Figure 7.23:** *Resolution of the reaction plane obtained in Au(25 AGeV) + Au collisions using the second order event plane reconstructed by means of the STS detector (using reconstructed tracks). The results are expressed in terms of the correction factor associated with the elliptic flow coefficient ($\upsilon_2$). The resolution estimated with the sub-event procedure (red open crosses) is compared to the one (<cos (2 × ($\Psi_2 - \Psi_R$))>) obtained in Section 7.3.4.4 on the basis of the knowledge of the true reaction plane angle (black full circles). The error bars represent the statistical uncertainties.*

ularly important in the case of the event plane reconstruction with the STS detector. This is due to the fact that, in this case, particles of interest (for the extraction of the $v_2$ signal) will tend to correlate with particles used in the flow vector determination because of short-range correlations. The analysis of the elliptic flow using the event plane method with the PSD detector is much less sensitive to non-flow effects: short-range correlations are expected to be substantially suppressed due to the large gap between the rapidity region covered by the PSD and the one covered by the STS tracker (which provides the azimuthal angle of the particle of interest).

## 7.5 Summary

This chapter dealt with the elliptic flow of open charm mesons in heavy ion collisions. The study of this phenomenon at FAIR energies is particularly interesting for the investigation of a possible phase transition from hadronic matter to a deconfined quark gluon plasma. Our purpose was to evaluate the potential of the CBM experiment for studying this important physics topic. The measurements of D-meson elliptic flow at FAIR, close to the charm production threshold, are very challenging. They are not only limited by the maximum collision rate that can be achieved in the experiment (in particular, with regard to the read-out time of the MVD detector and its radiation tolerance) but also rely on the possibility to accurately measure the azimuthal orientation of the reaction plane.

Our study focused on the assessment of the statistical accuracy with which the D-meson elliptic flow can be measured in CBM. This was done by means of Monte Carlo simulations performed for Au + Au collisions at an incident energy of 25 AGeV. The study was carried out for semi-peripheral collisions where the magnitude of the elliptic flow is expected to be the strongest.

In a first step, we evaluated the expected resolution of the reaction plane, using the CBMRoot simulation framework and the UrQMD transport model as an event generator for simulating Au + Au collisions. In CBM, the reaction plane can be determined independently by two different detector sub-systems (covering different rapidity regions), namely the PSD calorimeter and the STS tracker. The performance of each of those sub-detectors was investigated in our study. Based on the event plane method, we evaluated the resolution of the reaction plane as a function of the collision centrality. We found that the analysis of the elliptic flow in CBM can be performed quite accurately, using either the first order (n = 1) event plane from the PSD or the second order (n = 2) event plane from the STS. Both detectors were found to provide similar accuracy on the reconstruction of the reaction plane, in particular for semi-peripheral collisions (in the impact parameter range from 5 to 9 fm) where the best resolution was obtained. The resolution expressed in terms of the $<cos(2 \times (\Psi_n - \Psi_R))>$ factor (needed to correct the observed $v_2$ for the fluctuations of the estimated reaction plane) was evaluated to about 0.4 in semi-peripheral events, which corresponds to an azimuthal angular resolution of about 40 degrees.

For the study of the D-meson elliptic flow, we adopted a very simple Monte Carlo procedure where a $p_T$-dependent azimuthal anisotropy was added to the generated (uniform) azimuthal dis-

tributions. To take into account the fluctuations of the estimated reaction plane due to the finite number of particles and to detector biases, D-meson azimuthal angles were smeared with the estimated resolution of the reaction plane ($\sigma(\Psi_R)$= 40 degrees). The resulting azimuthal distributions relative to the reaction plane were then analyzed to extract the elliptic flow parameter $v_2$ as a function of the transverse momentum. The obtained $v_2$ values, after being corrected for the resolution of the reaction plane, have been found to be in good agreement with the anisotropy values used as an input in the simulations. The statistical uncertainties on $v_2$ were evaluated for a sample of events corresponding to the anticipated annual statistics for D-mesons in semi-peripheral Au(25 AGeV) + Au collisions (estimated on the basis of the results presented in Chapter 6). This was done for two assumptions on the magnitude of the D-meson flow: i) a "weak flow" as predicted by the HSD model (due the small hadronic interaction cross-section of D-mesons) and ii) a "strong flow" scenario, which is expected in the case where partonic interactions occur frequently enough. The statistical uncertainty was found to be, as expected, better in the case of strong flow. Assuming that the effect is higher by a factor of two than predicted by HSD, we found a relative statistical uncertainty of about $10\%$ for the integrated elliptic flow of all D-mesons and from $16\%$ to $24\%$ for individual D-meson species.

From the present study, one can conclude that even very small magnitudes of D-meson elliptic flow would be measurable in one year of data taking with the CBM detector and that the sensitivity of the experiment should be sufficient to discriminate between purely hadronic models (e.g. HSD) and models including partonic degrees of freedom (e.g., PHSD or AMPT). If the elliptic flow of D-mesons is strong, which is likely to be the case at the highest FAIR energies (25-35 AGeV), then the CBM experiment will be able to measure accurately its integrated magnitude as a function of the beam energy. More detailed $p_T$-differential measurements would, however, be feasible (with moderate statistical precision) only if all reconstructed D-mesons are included. Performing such measurements for individual D-meson species would require higher statistics and hence higher collision rates, beyond the limit tolerable by the MAPS sensors.

# Chapter 8

# Summary and conclusion

The present thesis is a contribution to the design and development of the Micro Vertex Detector (MVD) of the CBM experiment planned at the future FAIR accelerator facility. The MVD detector is one of the major components of CBM. It aims at providing the high vertexing precision necessary for the measurement of short-lived open charm particles through their weak hadronic decay in the high hadron multiplicity environment characterizing heavy ion collisions. Open charm is one the major physics topics which will be addressed by the CBM experiment. According to theoretical models, measurements of observables related to open charm particles in heavy ion collisions at FAIR energies will provide important information on the deconfinement phase transition and on the in-medium effects expected in dense baryonic matter (related to a chiral symmetry restoration).

The research work reported in this thesis consisted of three main parts. The first part deals with Monte Carlo simulations carried out in order to define the design requirements for the first generation MVD which will operate at the FAIR/SIS100 synchrotron. This includes, in particular, the determination of the data rate requirements for the proposed MAPS sensor, namely MIMOSIS-1, and the evaluation of the bandwidth requirements for the MVD read-out system. The second part is a detailed simulation study aiming at assessing the expected performances of the CBM experiment for the reconstruction of open charm particles in nucleus-nucleus collisions. Finally, the third part is a feasibility study of open charm elliptic flow measurements in CBM.

At the SIS100 synchrotron, open charm will be measured in proton-proton and proton-nucleus collisions, at beam energies up to 30 GeV. In nucleus-nucleus collisions, the MVD will also serve to improve the detector performance for low-mass vector meson and multi-strange hyperon measurements, up to 10 AGeV for incident Au ions. High collision rates are foreseen for these measurements, typically on the order of $2 \times 10^6$ collisions/second in p(30 GeV) + Au collisions and $2 \times 10^4$ collisions/second in Au(10 AGeV) + Au collisions.

In order to simulate the data rate expected in MIMOSIS-1 sensors, detailed Monte Carlo simulations were carried out within the CBMRoot simulation framework. Two aspects of the running conditions, which were absent in previous studies, were included in the simulations: the beam intensity fluctuations and the beam emittance. The latter, extrapolated from the beam emittance

in SIS18, was found to have little effect on the hit density in the MVD stations. The collision pile-up in MIMOSIS-1 sensors were simulated, taking into account their expected read-out time (of 25 $\mu$s), and under two assumptions on the beam intensity fluctuations at SIS100: a ratio maximum-to-average of the beam intensity equal to 3 (based on measurements at the SIS18 synchrotron) and 10 as a safe assumption for both proton and Au beams at SIS100. The beam intensity fluctuations resulted into important fluctuations of the hit rates in the MIMOSIS-1 sensors. This is particularly critical for those located in the region of the MVD stations where the hit density is maximal. In Au + Au collisions, this region is dominated by the contribution of $\delta$-electrons produced in the target material by Au beam ions. It has been shown that the contribution of $\delta$-electrons to the total number of hits created in the MVD can be substantially reduced by adding absorbing material outside the detector acceptance. However, this strategy was found to have little effect on the maximal hit density, as the latter is dominated by the contribution of $\delta$-electrons which impact the detector before reaching the absorber material.

The data rate requirements were given for the MVD sensors located in the maximal hit density region for different assumptions on the distance between the MVD station and the CBM target. By comparing these requirements with the expected performances of the sparsification circuits of MIMOSIS-1, we found that this sensor can tolerate important beam intensity fluctuations while being placed close to the target, down to 5 cm away from it, in both p + Au and Au + Au collisions. The expected output bandwidth of MIMOSIS-1, of either 400 MHz or 800 MHz, was found to be the leading constraint for the minimal distance at which the first MVD station can be placed. A sensor with 400 MHz output bandwidth can be placed at distances from 5 to 10 cm (from 10 to 15 cm) from the target in p + Au (Au + Au collisions), depending on the beam intensity fluctuations. Feasibility studies within the collaboration have demonstrated that such distances are suitable for the different measurements foreseen at SIS100. In addition, an output bandwidth of 800 MHz for the sensor would allow it operating in conditions of large beam intensity fluctuations with security margins. From this, one can conclude that the projected performances of MIMOSIS-1 (in terms of data rate capability) fully satisfy the data rate requirements at SIS100.

The present work also allowed evaluating the bandwidth requirements for the different components of the MVD read-out system, taking into account its current design for operation at the SIS100 synchrotron. These requirements were based on the output bandwidth that MIMOSIS-1 has to feature (of either 400 MHz or 800 MHz). We concluded that the read-out system has to feature a total bandwidth of 5 GHz, which imposes strong constraints on the design of its different components.

The aim of the second part of this thesis was to investigate the expected performances of CBM for the reconstruction of open charm particles through their weak hadronic decay. For this purpose, simulations were carried out using a realistic MVD detector geometry and taking into account the expected performances of MAPS sensors: a spatial resolution of 3 $\mu$m, a read-out time of 10 $\mu$s and a tolerance to radiation doses up to 3 Mrad and $3 \times 10^{13}\ n_{eq}/cm^2$ for ionizing and non-ionizing radiations, respectively. The particle identification was taken into account by assuming that the information provided by the TOF detector allows rejecting all protons. The simulations

were performed in the case of central Au + Au collisions at an incident energy of 25 AGeV, which represent a typical environment for open charm reconstruction in nucleus-nucleus collisions at FAIR energies. $D^+$ mesons decaying into $\pi^+$ $\pi^+$ $K^-$ were chosen to benchmark the detector performance. This choice was motivated by the fact that the reconstruction of this decay channel, involving three daughter particles, is particularly challenging as the signal must be extracted from a very large (many orders of magnitude) combinatorial background.

The resolution of the secondary vertex was found to be 72 $\mu$m, mostly as a result of the excellent spatial resolution and low material budget of the MVD detector. The momentum resolution was found to be between 1.2% and 1.6% for particles with momenta above 1 GeV/c. To reconstruct $D^+$ mesons through their decay into ($\pi^+$, $\pi^+$, $K^-$) triplets, several selection criteria were used to reduce the combinatorial background due to uncorrelated charged particle triplets. These criteria were mainly based on the different topology of $D^+$ meson decay and, in particular, its characteristic decay vertex relative to the interaction point. After optimization of the underlying selection cuts used to extract the signal, we found a signal to background ratio of 1.5 (3.0) in the mass region of the $D^+$ meson, depending on whether we used the HSD model or the SHM model to estimate the $D^+$ production multiplicity. This was achieved with a fairly good total reconstruction efficiency (including the geometrical acceptance) of 2%. The reconstruction performances have also been determined for $D^- \rightarrow \pi^-$ $\pi^-$ $K^+$ under the same conditions (collision system, energy and centrality) as for $D^+$ mesons: a signal to background ratio of 3.7 (based on the HSD production multiplicity) and a reconstruction efficiency of 1.4% were achieved.

The expected statistics per CBM running year (about 4 months of data taking at 50% efficiency) was evaluated at a collision rate of 400 kHz. We found that the experiment will be able to measure $1.5 \times 10^4$ $D^+$ and $2.3 \times 10^4$ $D^-$ particles per year (assuming their production multiplicities predicted by HSD). Combining our results with those from other studies performed within the collaboration, we estimated the total number of D-mesons than can be measured per year to be at least $6.9 \times 10^4$. Such statistics should allow for the extraction of several observables (e.g. production multiplicities, particle yield ratios, $p_T$-spectra at mid-rapidity) of interest for open charm physics at FAIR energies.

In the third part of the thesis, we investigated the capabilities of the CBM experiment for measuring the elliptic flow of open charm D-mesons. Such measurements are very challenging at FAIR energies (close to the charm production threshold). They are not only very demanding in terms of statistics but also rely on the possibility to accurately measure the azimuthal orientation of the reaction plane.

Our study focused on the assessment of the statistical accuracy with which the D-meson elliptic flow can be measured in CBM. This was done by means of Monte Carlo simulations performed for Au + Au collisions at an incident energy of 25 AGeV. The study was carried out for semi-peripheral collisions where the magnitude of the elliptic flow is expected to be the strongest.

In a first step, we evaluated the expected resolution of the reaction plane, using the CBMRoot simulation framerwork and the UrQMD transport model as an event generator for simulating Au + Au collisions. In CBM, the reaction plane can be determined independently by two different detector sub-systems (covering different rapidity regions), namely the PSD calorimeter and the

STS tracker. The performances of each of those sub-detectors were investigated in our study. Based on the event plane method, we evaluated the resolution of the reaction plane as a function of the collision centrality. We found that the analysis of the elliptic flow in CBM can be performed quite accurately, using either the first order (n = 1) event plane from the PSD or the second order (n = 2) event plane from the STS. Both detectors were found to provide similar accuracy on the reconstruction of the reaction plane, in particular for semi-peripheral collisions (in the b-range from 5 to 9 fm) where the best resolutions were obtained. The resolution expressed in terms of the $<\cos(2 \times (\Psi_n - \Psi_R))>$ factor (needed to correct the observed $v_2$ for the fluctuations of the estimated reaction plane) was evaluated to about 0.4 in semi-peripheral events, which corresponds to an azimuthal angular resolution of about 40 degrees.

For the study of the D-meson elliptic flow, we adopted a very simple Monte Carlo procedure where a $p_T$-dependent azimuthal anisotropy was added to the generated (uniform) azimuthal distributions. To take into account the fluctuations of the reaction plane due to finite number of particles and to detector biases, D-meson azimuthal angles were smeared with the estimated resolution of the reaction plane ($\sigma(\Psi_R)$= 40 degrees). The resulting azimuthal distributions relative to the reaction plane were then analyzed to extract the elliptic flow parameter $v_2$ as a function of the transverse momentum. The obtained $v_2$ values, after being corrected for the resolution of the reaction plane, have been found to be in good agreement with the anisotropy values used as an input in the simulations.

The statistical uncertainties on $v_2$ were evaluated for a sample of events corresponding to the anticipated annual statistics for D-mesons in semi-central Au(25 AGeV) + Au collisions (estimated on the basis of the results obtained in the second part of the thesis). This was done for two assumptions on the magnitude of the D-meson flow: i) a "weak flow" as predicted by the HSD model (due the small hadronic interaction cross section of D-mesons) and ii) a "strong flow" scenario, which is expected in the case where partonic interactions occur frequently enough. The statistical uncertainty was found to be, as expected, better in the case of "strong flow". Assuming that the effect is higher by a factor of two than predicted by HSD, we found a relative statistical uncertainty of about $10\%$ for the integrated elliptic flow of all D-mesons and from $16\%$ to $24\%$ for individual D-meson species.

The results of this study show that even very small magnitudes of D-meson elliptic flow can be measured in one year of data taking with CBM and that the sensitivity of the experiment should be sufficient to discriminate between purely hadronic models (e.g. HSD) and models including partonic degrees of freedom (e.g., PHSD or AMPT). If the elliptic flow of D-mesons is strong, which is likely to be the case at the highest FAIR energies (25-35 AGeV), then the CBM experiment will be able to measure accurately its integrated magnitude as a function of the beam energy. More detailed $p_T$-differential measurements would, however, be feasible (with moderate statistical precision) only if all reconstructed D-mesons are included. Performing such measurements for individual D-meson species would require higher statistics, and hence higher collision rates, which would be possible only with faster and more radiation tolerant MAPS sensors.

In conclusion the present thesis provides important contributions to the development of the MVD

detector. It has been established that the expected data rate capability of the electronics circuits of the MAPS sensor proposed for equipping the first generation MVD is suitable to carry out the physics program foreseen by the CBM experiment at the SIS100 synchrotron. The bandwidth requirements for the different components of the MVD read-out system have been determined. These specifications are now included in the technical design of the MVD read-out system. This is an important step towards the realization of this detector.

Furthermore, detailed simulation studies were carried out to evaluate the expected capability of the CBM experiment for open charm particle measurements in nucleus-nucleus collisions. It was demonstrated that the reconstruction of these particles through their hadronic decays in Au(25 AGeV) + Au collisions is feasible with a good purity. The expected statistics per running year at a collision rate of 400 kHz was estimated to be 1.5 $\times$ $10^4$ for $D^+ \rightarrow \pi^+ \pi^+ K^-$ and at least 6.9 $\times$ $10^4$ if one sums up the yields of all reconstructible D-meson decay channels. Based on these results, the possibility of measuring the D-meson elliptic flow was investigated, taking into account a realistic estimate of the expected resolution of the reaction plane. It was shown that the integrated elliptic flow parameter can be accurately determined for several D-meson species. However, more detailed $p_T$-differential measurements would require higher statistics and hence higher collision rates, beyond the limit tolerable by the MAPS sensors.

It is worthwhile to note that the development of MAPS sensors is progressing well and faster than anticipated. It is, therefore, reasonable to expect that by the time the construction of the MVD detector for SIS300 begins, more performing sensors (as compared to those considered in the simulations carried-out in this work) might be available. In particular, the recent emergence of 3D integrated architectures promises substantial improvements in the rate capability of the sensor: a read-out time down to a few microseconds and a tolerance to a non-ionizing radiation dose higher than $10^{14}$ $n_{eq}/cm^2$ and to an ionizing radiation dose above 30 Mrad. This would greatly enhance the capabilities of the experiment for D-meson measurements and might offer, in addition, the possibility to measure also the $\Lambda_c$ baryon, which is more challenging due to its extremely short lifetime ($c\tau$ = 59.9 fm).

# Appendix A

# Beam emittance

The emittance represents the position-momentum phase space volume occupied by beam particles. This phase space has 6 dimensions, and consists in the spatial coordinates (X, Y, Z) and the momenta ($p_X$, $p_Y$, $p_Z$) of particles, z being the direction of the beam propagation. Since we are not interested in the beam longitudinal motion in our case, this phase space is examined here in the transverse plane only. The horizontal (X) and vertical (Y) phase space dimensions are not coupled and can be treated independently, i.e. (X, $p_X$), (Y, $p_Y$). Instead of using the momentum of particles, e.g. $p_Y$, the following variable is usually defined:

$$Y' = \arctan(\frac{p_Y}{p_Z}) \sim \frac{p_Y}{p_Z} = \frac{v_Y}{v_Z} = \frac{dY}{dZ} \tag{A.1}$$

where we assumed $p_Y$ to be much smaller than $p_Z$*, which is justified for relativistic beams. Each particle is represented by a point in the phase space (X, X') and (Y, Y'). This can be seen in Figure A.1 which shows the (Y, Y') phase space of beam particles. The emittance of the beam characterizes the maximal spread of beam particles in this phase space. This maximal spread is referred to as the beam width ($\Delta$Y) in spatial coordinates, and as the beam divergence in momentum coordinates ($\Delta$Y'). For example, in the figure, $\Delta$Y = 0.4 mm and $\Delta$Y' = 2 mrad. The emittance is usually defined as the product of $\Delta$Y' and $\Delta$Y, and given in unit of mrad $\times$ mm.

In real conditions, there is no clear boundary between beam particles and the vacuum. The beam emittance is thus usually defined as the area (in the (Y, Y') plane in Figure A.1) containing a large fraction of beam particles. In the simulation, we assumed that the beam emittance contains all particles: their phase space density is assumed finite and uniform (nul) inside (outside) the boundary defined by the emittance.

To estimate the beam emittance, we assumed that it scales with the inverse of the magnetic rigidity from the injection into SIS18 to the SIS100 synchrotron [109]. One can thus write:

$$\epsilon_{ex} = \epsilon_{in} \times \frac{(B \times \rho)_{in}}{(B \times \rho)_{ex}} \tag{A.2}$$

*Momenta are expressed in the laboratory reference system

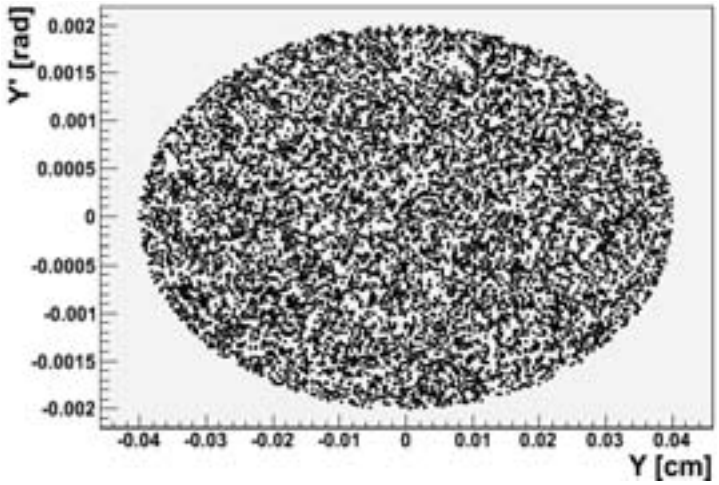


**Figure A.1:** *Distribution of beam particles in the YY' plane (perpendicular to the beam axis). The beam emittance is assumed to be equal to (2, 0.4) mrad × mm in this example. The particle phase space density is assumed finite and uniform (nul) inside (outside) the beam boundary defined by this emittance.*

where $\epsilon_{in}$ and $(B \times \rho)_{in}$ are, respectively, the beam emittance and rigidity at the injection into the SIS18 ring, and $\epsilon_{out}$ and $(B \times \rho)_{out}$ are those at the SIS100 synchrotron. Such scaling suggests that the damping of the beam is adiabatic. Note that this is a reasonable assumption if the emittance is not deteriorated by:

- non-linear space charge forces inside the beam
- the interactions between the beam particles and the gas inside the beam pipe. These interactions are expected to be important in the case of a beam of partially stripped ions (ex: $U^{28+}$) since these ions may loose electrons by scattering with the gas molecules inside the beam pipe. However, the effect of such interactions on the beam emittance is less important in the case of bare ions (ex: $Au^{79}_{197}$), which will be used in the CBM experiment.

These effects are indeed expected to be very small at SIS100 [109].

The magnetic rigidity is determined as follows:

$$B \times \rho[T.m] = \frac{p}{q} = \frac{A}{Z} \times \frac{1}{c} \times \sqrt{(2 \times u + E_{kin}) \times E_{kin}} \tag{A.3}$$

where A and Z are, respectively, the atomic mass number and the charge of beam particles, c is the speed of light in vacuum (equal to 300 Mm/s), u is the atomic mass unit (equal to 931.494 MeV), and $E_{kin}$ is the kinetic energy of beam particles (in units of MeV/u).

At the injection into SIS18, the beam emittance is fixed by the SIS18 geometrical acceptance, to a value $\epsilon_{in}$ = 150 (X-direction) and 50 (Y-direction) mrad × mm. At this point, the beam

| | $(B \times \rho)_{in}$ [T.m] | $(B \times \rho)_{out}$ [T.m] | $\epsilon_{ex}$ [mrad × mm] | $\Delta X_{ex}/\Delta Y_{ex}$ mm |
|---|---|---|---|---|
| Proton beam | 0.49 | 103 | 0.71 (X) / 0.24 (Y) | 0.35 (X) / 0.12 (Y) |
| Au ion beam | 1.18 | 88.2 | 2 (X) / 0.67 (Y) | 1 (X) / 0.33 (Y) |

**Table A.1:** *Beam rigidity at the injection into SIS18 ($(B \times \rho)_{in}$) and in SIS100 ($(B \times \rho)_{out}$), beam emittance expected in SIS100 ($\epsilon_{ex}$) assuming adiabatic damping of the beam (X and Y-directions are specified in parentheses), and the corresponding beam width ($\Delta X_{ex}/\Delta Y_{ex}$) if the beam divergence is fixed (to about 2 mrad). The cases of a beam of protons and Au ions are shown, considering a bombarding energy at SIS100 of 30 GeV and 10 GeV/nucleon respectively.*

energy is fixed and equal to 11.4 MeV/nucleon, such that $(B \times \rho)_{in}$ depends on the ratio A/Z exclusively (see Equation (A.3)). $(B \times \rho)_{out}$ also depends on the energy of the beam reached in SIS100. $(B \times \rho)_{in}$ and $(B \times \rho)_{out}$ are given in Table A.1 for a beam of Au ions * and of protons, considering that a beam energy of, respectively, 10 AGeV and 30 GeV is reached in SIS100. The table also gives the emittance expected in SIS100 ($\epsilon_{ex}$).

For geometrical reasons, the beam divergence at the CBM target will be constant and roughly equal to 2 mrad in both X and Y directions. This comes from the fact that the open aperture of the focusing quadrupole in front of the CBM target has a radius of 80 mm, and that the distance between both elements is of about 25 m (see Figure A.2). Note that the whole aperture of the focusing quadrupole cannot be filled with the beam, as otherwise particles scratching the beam pipe in the quadrupole would lead to background particles at the target. We assumed that 70% of its aperture can safely be filled with the beam. The beam width is thus of 56 mm inside the quadrupole. These geometrical considerations lead to a constant beam divergence of 2 mrad, resulting into a beam width $\Delta$X ($\Delta$Y) of about 1 (0.33) mm in the case of a Au ion beam (for which we expect $\epsilon_{ex}$ = 2 (0.67) mrad × mm in X (Y) direction). Table A.1 also gives the expected beam width at the CBM target (last column).

It is to be noted that the effect of the extraction process of the beam (from the SIS100 synchrotron to the CBM beam line) on the beam emittance is not known quantitatively. However, the emittance in the Y dimension will not be affected, since only the emittance in the X dimension will be used for the slow extraction process foreseen at SIS100. It is believed that the slow extraction process may reduce the beam emittance in the X dimension. As a conservative approach, this effect has been neglected here, such that the beam emittance in the SIS100 ring and at the CBM target are assumed to be equal.

**Effect of the beam emittance on the number of hits created in the MVD**

Figure A.3 shows the number of hits created in the MVD detector in Au(10 AGeV) + Au collisions as a function of the beam width in the X direction. These hits are summed over the three stations (see Section 4.5). Let us remind that, the beam divergence being fixed, the beam width

*(A, Z) = (197, 79)

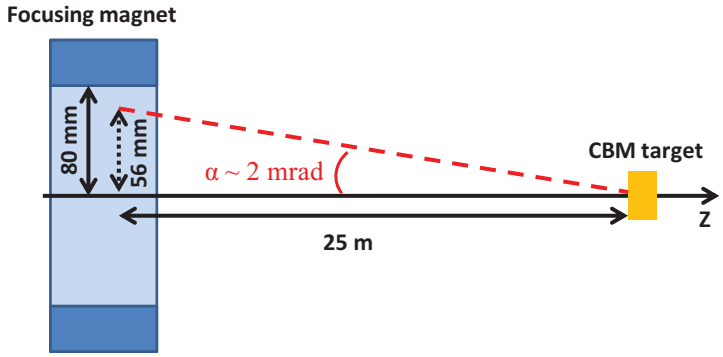


**Figure A.2:** *Simplified sketch of the focusing quadrupole in front of the CBM target. The open aperture of the first element has a radius of 80 mm. 70% of this aperture is assumed to be filled with beam particles (see text). The radius of the beam spot is thus of 56 mm inside the quadrupole. The distance between the quadrupole and the CBM target is of 25 meters. The last two facts impose a fixed beam divergence at the CBM target, of about 2 mrad.*

is proportional to the beam emittance. Two contributions are shown: the hits originating from Au + Au collisions (normalized to one collision), and those created by $\delta$-electrons produced by Au ions traversing the Au target (normalized to 100 "ion crossing the target" events). The normalizations are meant to account for a target with 1% of nuclear interaction probability, i.e. one nuclear collision occurs per 100 ions crossing the target, on average (see Appendix B).

As one can see in the figure, the number of hits created by Au + Au collisions (red squares) is not significantly affected by the beam width. The number of hits originating from $\delta$-electrons (blue triangles) decreases slightly with the beam width due to the rejection of those with low-momenta (thus emitted with high polar angles, see Fig. 5.11). As one can see, the expected width of a Au(10 AGeV) ion beam (of 1 mm) does not affect significantly the number of hits deposited over the whole MVD stations. The same conclusion can be drawn in the case of a proton(30 GeV) beam, for which the emittance is even smaller.

Note that no hits coming from the beam ions is observed for a beam width below 5.5 mm. This was expected since MVD stations have a beam hole with an inner radius of 5.5 mm (in the simulation, beam ions have straight trajectories, almost parallel to the beam axis).

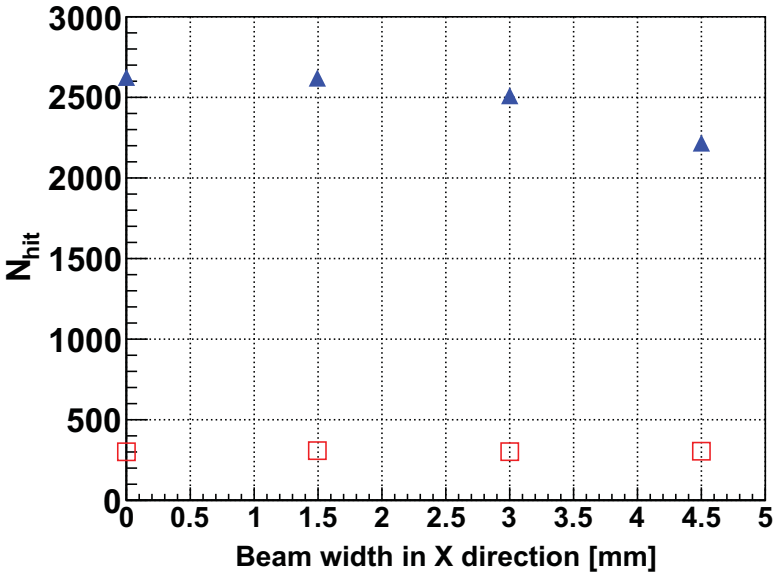


**Figure A.3:** *Number of hits accumulated in the MVD detector (with 3 stations, see text) as a function of the beam width in X-direction. Two contributions are shown: the hits originating from particles produced in Au(10 AGeV) + Au collisions (red square) and those created by $\delta$ electrons (blue triangles). The latter are produced by beam ions in the target. Both contributions are normalized to account for a target with 1% of nuclear interaction probability (see text).*

# Appendix B

# Thickness of the CBM target

The target of the CBM experiment must be very thin (typically a few hundreds of micrometers) for several reasons. For example, this condition is important to prevent beam particles from experiencing several nuclear reactions. The detector would be unable to differentiate in time these collisions from one another and any measurements would be severely biased. Also, a thick target would be responsible for the production of a large amount of electron-positron pairs (originating from the conversion of $\gamma$'s, mostly from $\pi^0$ decays, in its material). This would create an important source of background for measurements of di-leptonic decay channels (e.g. low-mass vector mesons). Furthermore, the material budget of the target has to be minimized to limit multiple scatterings of charged particles, which is important for accurate measurements of the particle impact parameter. The consequence of such a limitation is that the probability for beam particles to undergo a nuclear collision with a target atom is typical of the order of $1\%$.

The target thickness corresponding to an interaction probability of $1\%$ can be obtained by first writing the interaction rates (R) between beam particles and the target. Figure B.1 shows a sketch depicting a flux of particles $\Phi$ with a cross-sectional area S. Given the probability P for particles to interact, R is given by:

$$R = \Phi \times S \times P \tag{B.1}$$

Assuming n atoms are contained in the volume crossed by the beam in the target, P is given by:

$$P = \frac{n \times \sigma}{S} \tag{B.2}$$

with $\sigma$ the inelastic interaction cross-section between beam particles and target atoms (see Figure B.1). Combining Equations (B.1) and (B.2), one can write:

$$\begin{aligned} R &= \Phi \times S \times \frac{n \times \sigma}{S} \\ &= \Phi \times S \times \rho_S \times \sigma \end{aligned} \tag{B.3}$$

with $\rho_S$ = n/S the area density of target atoms. According to Equation (B.1), P can be re-expressed as follows:

$$P = \frac{R}{\Phi \times S} = \rho_S \times \sigma \tag{B.4}$$

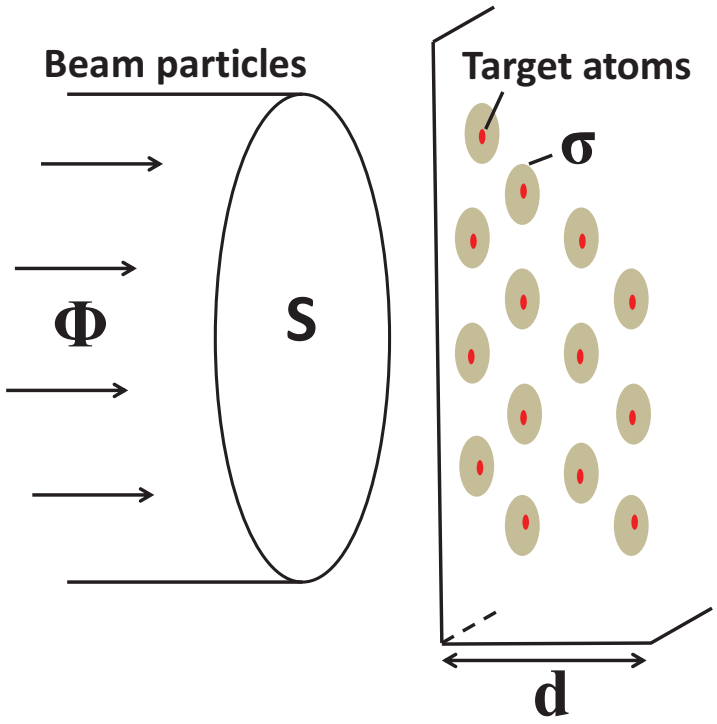


**Figure B.1:** *Flux ($\Phi$) of particles impinging an area ($S$) of the target. The latter has a thickness $d$. Beam particles and target atoms (red points) have an inelastic interaction cross-section ($\sigma$) depicted by gray disks surrounding the latter.*

It follows that the interaction probability per unit length ($P_L$) is:

$$P_L = \frac{P}{d} = \rho \times \sigma \tag{B.5}$$

with d the target thickness and $\rho$ the volume density of target atoms. We can now calculate the variation of the flux of particles through a slice dz of the target:

$$d\Phi = -\Phi \times P_L \times dz \tag{B.6}$$

The solution of this equation is:

$$\begin{aligned} \Phi(z) &= \Phi_0 \times e^{-P_L \times z} \\ &= \Phi_0 \times e^{-\rho \times \sigma \times z} \\ &= \Phi_0 \times e^{-\frac{z}{\lambda}} \end{aligned} \tag{B.7}$$

with $\Phi_0$ the flux of particles before they reach the target, and $\lambda$ = 1/($\rho \times \sigma$) the inelastic interaction length. Finally, the thickness ($Z_{1\%}$) of the target corresponding to a nuclear interaction probability of $1\%$ can be derived by requiring that $\Phi$ = 0.99 $\Phi_0$ in the last equation. This gives:

$$\begin{aligned} 0.99 \times \Phi_0 &= \Phi_0 \times e^{-\frac{Z_{1\%}}{\lambda}} \\ &\leftrightarrow \\ Z_{1\%} &= -\lambda \ln(0.99) \end{aligned} \tag{B.8}$$

Let us now define $\lambda_p$ and $\lambda_{Au}$ the inelastic interaction length of protons and Au ions, respectively, in Au material. $\lambda_p$ = 10.16 cm, it follows that $Z_{1\%}$ = 1020 $\mu$m for protons in Au material. $\lambda_{Au}$ can be extrapolated based on $\lambda_p$ using for example the Sihver parametrization formula [115]:

$$\sigma = \pi r_0^2 (A_p^{1/3} + A_t^{1/3} - b_0 \times (A_p^{-1/3} + A_t^{-1/3}))^2 \tag{B.9}$$

with $r_0$ = 1.36 fm, $b_0$ = 1.581 - 0.876 $\times$ ($A_p^{-1/3} + A_t^{-1/3}$), and with $A_p$ and $A_t$ the atomic mass number of projectile particles and target atoms, respectively. For proton and Au ion beams, $A_p$ = 1 and 197, respectively. In both p + Au and Au + Au systems, $A_t$ = 197. The last equation allows estimating the ratio between the inelastic interaction cross-section in Au material of protons ($\sigma_p$) and the one of Au ions ($\sigma_{Au}$). Since $\lambda$ goes with the inverse of the interaction cross-section, one can write:

$$\lambda_{Au} = \frac{\sigma_p}{\sigma_{Au}} \times \lambda_p \tag{B.10}$$

The last equation leads to $\lambda_{Au} \sim$ 2.3 cm. According to Equation (B.8), $Z_{1\%} \sim$ 230 $\mu$m for Au ions in Au material.

For simplicity, we assumed in this work a target thickness of 250 $\mu$m for both Au ion and proton beams. According to Equation (B.7), this corresponds to a nuclear interaction probability of $1.1\%$ ($0.25\%$) for a beam of Au ions (protons). Note that, for the sake of our present study, the target thickness is of minor importance in the case of a proton beam. Indeed, when estimating the hit rates in the MVD, this parameter affects essentially the production of $\delta$-electrons in the target material. The amount of these last is negligible in the case of a proton beam (with respect to the hadron multiplicity in p-Au collisions).

# Appendix C

# Scaling of the data flow delivered by MIMOSIS-1 with the beam intensity

Figure C.1 shows the number of hits ($N_{hits}$) received by the most exposed MIMOSIS-1 sensor as a function of the number of Au ions ($N_{ions}$) crossing the Au target per read-out cycle (25 $\mu$s). An approximate scaling of $N_{hits}$ with $N_{ions}$ is observed:

$$N_{hits} \sim 2 \times N_{ions} \tag{C.1}$$

Using equation (5.4) to convert the number of hits into a data volume, and by dividing both sides of the equation by the read-out cycle of the sensor, it follows that the data flow scales approximately linearly with the beam intensity.

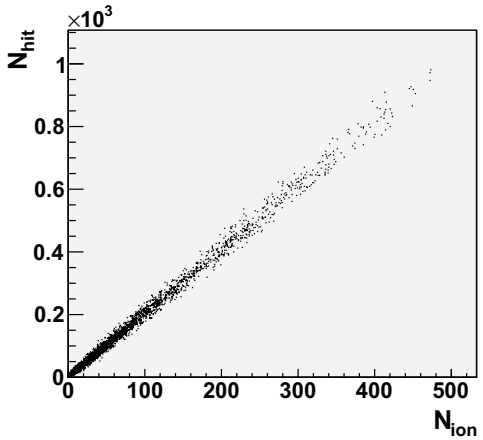


**Figure C.1:** *Number of hits ($N_{hits}$) received by the most exposed MIMOSIS-1 sensor as a function of the number of Au ions ($N_{ions}$) crossing the Au target per read-out cycle (25 $\mu$s). The average beam intensity is of 2 $\times$ $10^6$ ions/s. These results are shown in the case of a MVD station located at a distance of 5 cm from the target.*

# Appendix D

# $Z_{Y=0}$ variable

The $Z_{Y=0}$ variable is defined as the (approximative) Z-position of the point where a particle trajectory crosses the $(Y = 0)$ plane. Assuming that the particle trajectory is a straight line (see Figure 6.14), its projection on the $(X = 0)$ plane is given by the following equation:

$$Y = IP_Y + \frac{\partial Y}{\partial Z} \times Z \Leftrightarrow Y = IP_Y + \frac{P_Y}{P_Z} \times Z \tag{D.1}$$

The condition Y = 0 leads to:

$$Z = -IP_Y \times \frac{P_Z}{P_Y} \tag{D.2}$$

# Appendix E

# Significance

The significance is a measure of the confidence one has on the estimated number of measured signal particles (S). S depends on the number of nuclear collisions ($N_{coll}$), on the signal multiplicity (M), on the branching ratio of the channel under study (BR) in case signal particles are measured through their decay daughters, and on the signal reconstruction efficiency ($\epsilon_S$), as follows:

$$S = N_{coll} \times M \times BR \times \epsilon_S \tag{E.1}$$

Since M = $\sigma_S/\sigma_{coll}$, $\sigma_S$ and $\sigma_{coll}$ being the production cross-section of signal particles and the nuclear collision cross-section, respectively, Equation (E.1) can be written as follows:

$$\begin{aligned} S &= N_{coll} \times \frac{\sigma_S}{\sigma_{coll}} \times BR \times \epsilon_S \\ &= \sigma_S \times I \times T \times BR \times \epsilon_S \end{aligned} \tag{E.2}$$

with I the beam intensity and T the "beam on target" duration. In the last equation, we used the fact that $N_{coll}/\sigma_{coll}$ equals to I $\times$ T. S is derived from the data, by subtracting the estimated amount of background entries (B) from the total amount of entries selected ($N_{sel}$): S = $N_{sel}$ - B. According to Equation (E.2), the production cross-section of signal particles is thus equal to:

$$\sigma_S = \frac{N_{sel} - B}{I \times T \times BR \times \epsilon_S} \tag{E.3}$$

To estimate the uncertainty on $\sigma_S$ ($\Delta\sigma_S$), we assume that the resolutions on the beam intensity, the branching ratio and the detection efficiency are sufficiently good, such that they can be neglected with respect to those on $N_{sel}$ and B. Using Equation (E.3), this leads to:

$$\Delta\sigma_S = \frac{1}{I \times T \times BR \times \epsilon_S} \sqrt{(\sqrt{N_{sel}})^2 + (\Delta B)^2} \tag{E.4}$$

Here we assume that $N_{sel}$ has a Gaussian distribution, which is justified for high values of $N_{sel}$. Equation (E.4) can be simplified by neglecting the error on B, as follows:

$$\Delta\sigma_S = \frac{1}{I \times T \times BR \times \epsilon_S} \sqrt{N_{sel}} \tag{E.5}$$

The relative uncertainty on the production cross-section of signal particles is obtained by dividing Equation (E.5) by Equation (E.3), which leads to:

$$\frac{\Delta\sigma_S}{\sigma_S} = \frac{\sqrt{N_{sel}}}{N_{sel} - B} = \frac{\sqrt{S+B}}{S} \tag{E.6}$$

Inverting both sides of this relation allows defining the significance (Sign), as follows:

$$Sign = \frac{S}{\sqrt{S+B}} = (\frac{\Delta\sigma_S}{\sigma_S})^{-1} \tag{E.7}$$

As one can see, the higher the significance is, the smaller the relative uncertainty on the estimated production cross-section of signal particles will be.

# Appendix F

# Calculation of the flow parameter $v_n$

It follows from equation (7.1) that:

$$\begin{aligned} < \cos(n\phi) > &= \frac{\int_{-\pi}^{\pi} \cos(n\phi) \times E\frac{d^3N}{d^3p} d\phi}{\int_{-\pi}^{\pi} E\frac{d^3N}{d^3p} d\phi} \\ &= \frac{\int_{-\pi}^{\pi} \cos(n\phi) \times (1 + \sum_{m=1}^{\infty} 2v_m \cos(m\phi)) d\phi}{\int_{-\pi}^{\pi} (1 + \sum_{m=1}^{\infty} 2v_m \cos(m\phi)) d\phi} \\ &= \frac{\int_{-\pi}^{\pi} 2v_n \cos^2(n\phi) d\phi}{2\pi} \\ &= v_n \end{aligned} \tag{F.1}$$

where the angle brackets denote an average over all particles in a sample of events corresponding to the same collision centrality. Note that the orthogonality relation between Fourier coefficients $\int_{-\pi}^{\pi}[\cos(n\phi) \times \cos(m\phi)]_{n\neq m}$ = 0 and the trigonometric identity $\cos^2(n\phi)$ = $(1 + \cos(2n\phi))$/2 have been used in this calculation.

# Appendix G

# Effect of the reaction plane resolution on the observed flow parameter $v_n$

The measured reaction plane azimuthal angle ($\Psi_n$) fluctuates around the true reaction plane angle ($\Psi_R$). This is caused mostly by the finite number of measured particles used in the estimation of $\Psi_n$. Such fluctuations have the effect of attenuating the observed flow coefficients $v_n^{obs*}$ with respect to their real strength ($v_n^{real}$). $v_n^{obs}$ is evaluated similarly as described in (7.3), by replacing $\Psi_R$ with ${\Psi_n}^{\dagger}$, as follows:

$$v_n^{obs} =< \cos(n \times (\phi - \Psi_n)) > \tag{G.1}$$

To relate $v_n^{obs}$ and $v_n^{real}$, one can write the following trigonometric relation:

$$\begin{aligned} \cos(n \times (\phi - \Psi_n)) &= \cos(n \times (\phi - \Psi_R) - n \times (\Psi_n - \Psi_R)) \\ &= \cos(n \times (\phi - \Psi_R)) \times \cos(n \times (\Psi_n - \Psi_R)) \\ &+ \sin(n \times (\phi - \Psi_R)) \times \sin(n \times (\Psi_n - \Psi_R)) \end{aligned} \tag{G.2}$$

By averaging over a large number of events, the sin terms vanish due to a reflection symmetry of $\phi$ and $\Psi_n$ with respect to $\Psi_R$, leading to the following relation:

$$< \cos(n \times (\phi - \Psi_n)) >=< \cos(n \times (\phi - \Psi_R)) > \times < \cos(n \times (\Psi_n - \Psi_R)) > \tag{G.3}$$

Note that the cos terms in the product on the right-hand side of the equation are assumed to be independent. By using the equations (7.3) and (G.1), the relation (G.3) can be written as:

$$v_n^{obs} = v_n^{real} \times < \cos(n \times (\Psi_n - \Psi_R)) > \tag{G.4}$$

One can see that indeed $v_n^{obs}$ is lower than $v_n^{real}$ by a factor $< \cos(n \times (\Psi_n - \Psi_R)) >$. This factor corresponds to the reaction plane resolution, and is referred to as Res($\Psi_R$). The value of the $v_n^{real}$ flow parameter can be obtained as follows:

$$v_n^{real} = v_n^{obs} / Res(\Psi_R) \tag{G.5}$$

*The index n is the order of the flow, see Equation 7.1

†The index n indicates that the flow of order n is used to estimate the reaction plane angle

# Appendix H

# Event plane method: the sub-event technique

The sub-event technique [123] consists in randomly dividing each event into sub-events of equal multiplicity. One then evaluates an event plane (see Section 7.3.1) for each of these sub-events. These event planes are now on designated as sub-event planes. The reaction plane resolution can be determined from the correlation between the two sub-event planes. One can write a relation between the azimuthal correlation between the sub-event planes and their respective deviation from the true reaction plane angle ($\Psi_R$):

$$< \cos(n(\Psi_n^a - \Psi_n^b)) >=< \cos(n(\Psi_n^a - \Psi_R)) > \times < \cos(n(\Psi_n^b - \Psi_R)) > \quad \text{(H.1)}$$

where the angle brackets denote an average performed over a large event sample. $\Psi_n^a$ and $\Psi_n^b$ are the azimuthal angles of the sub-event planes a and b.

As mentioned above, the sub-events are build with equal multiplicity. This is done to ensure that the reaction plane resolutions from the two sub-events are nearly equal, i.e. $< \cos(n(\Psi_n^a - \Psi_R)) >\sim< \cos(n(\Psi_n^b - \Psi_R)) >$. Equation (H.1) can then be simplified in this way:

$$< \cos(n(\Psi_n^a - \Psi_R)) >\sim \sqrt{< \cos(n(\Psi_n^a - \Psi_n^b)) >} \quad \text{(H.2)}$$

Next, one has to relate the reaction plane resolution obtained by using the full event multiplicity with the one obtained by using sub-events. This can be done as follows [123]:

$$< \cos(k\ m\ (\Psi_m - \Psi_R)) >= \frac{\pi}{2\sqrt{2}}\ \chi_m\ e^{-\chi_m^2/4}(I_{\frac{k-1}{2}}(\chi_m^2/4) + I_{\frac{k+1}{2}}(\chi_m^2/4)) \quad \text{(H.3)}$$

where $I_p$ is the modified Bessel function of order p, and $\chi_m$ is the number flow, equal to the flow magnitude $v_m$ multiplied by $\sqrt{2\ M}$ (M being the event multiplicity). Note that a flow coefficient of order n can be estimated based on an event plane determined using a lower order harmonic (m) of the flow. In practice, one replaces $\Psi_n$ by $\Psi_m$ and n by k $\times$ m (with k a positive integer) in Equations (G.1) and (G.4). The harmonic of the event plane, m, is explicitly written in Equation

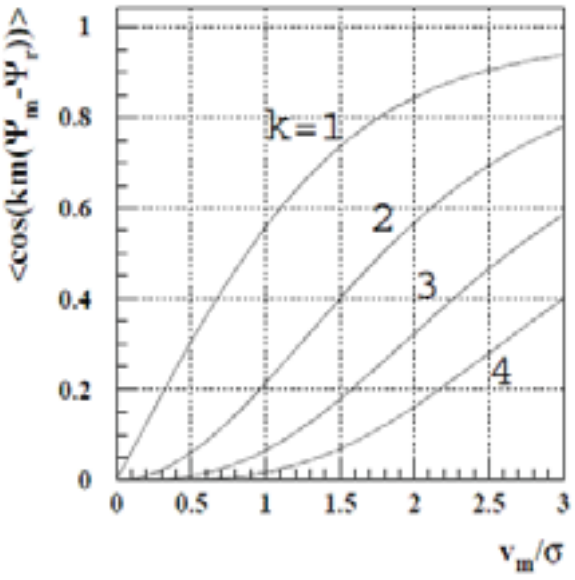


**Figure H.1:** *Reaction plane resolution as a function of the number flow* $\chi_m = \frac{v_m}{\sigma} = v_m \sqrt{2\,M}$*, with M the event multiplicity and m the harmonic of the flow used to evaluate the event plane [123]. The resolutions for the correction of the flow component of order n = k* $\times$ *m are shown, for k ranging from 1 to 4.*

(H.3). The reaction plane resolution ($< \cos(k\ m(\Psi_m - \Psi_R)) >$) derived from this equation is plotted as a function of the number flow in Figure H.1 [123] for several values of k (from 1 to 4). The best resolutions are obtained if the event plane and the flow coefficient have the same order, i.e. k = 1 $\leftrightarrow$ m = n. In such a case, one can see the approximate linear dependence of $< \cos(n(\Psi_n - \Psi_R)) >$ with $\sqrt{M}$ for $\chi_n \leq 1$ (or equivalently for $< \cos(n(\Psi_n - \Psi_R)) > \leq 0.6$). Because M in the sub-events is equal to one half of the full event multiplicity, we have:

$$< \cos(n(\Psi_n - \Psi_R)) > \sim \sqrt{2}\ < \cos(n(\Psi_n^a - \Psi_R)) > \tag{H.4}$$

Combining equations (H.2) and (H.4), we can estimate the reaction plane resolution from the correlation between the two sub-event planes, as follows:

$$< \cos(n(\Psi_n - \Psi_R)) > \sim \sqrt{2}\ \sqrt{< \cos(n(\Psi_n^a - \Psi_n^b)) >} \tag{H.5}$$

The reaction plane resolution presented in Figure 7.23 (red open crosses) are obtained using Equation (H.5) with n = 2.

Note that Equations (H.1) and (H.3) are valid only when non-flow effects are negligible. As one can see in Figure 7.23, non-flow effects are small using the sub-event procedure with the STS detector over a broad range of collision impact parameters (below 9 fm), if additional criteria are applied on the quality of the reconstructed tracks (see Section 7.3.4.4).

# Bibliography

[1] F. Wilczek, Physics Today 53, Issue 8, p. 22 (2000); D. E. Kharzeev and J. Raufeisen, nucl-th/0206073 (2002)

[2] A. W. Hendry and D. B. Lichtenberg, Rep. Prog. Phys., Vol. 41 (1978)

[3] B. Andersson, G. Gustafson, G. Ingelman and T. Sjostrand, Phys. Rep., Vol. 97, Issue 2-3, p. 31-145 (1983)

[4] A. Casher, H. Neuberger, and S. Nussinov, Phys. Rev. D 20, 179 (1979)

[5] V. Koch, Int. J. Mod. Phys. E6, 203-250 (1997)

[6] Y. Nambu and G. Jona-Lasinio, Phys. Rev. 122, 345-358 (1961)

[7] S. Bethke, J. Phys. G 26:R27 (2000)

[8] D. J. Gross and F. Wilczek, Phys. Rev. Lett. 30, 1343-1346 (1973)

[9] M. Gyulassy and X. N. Wang, Nucl. Phys. B 420, 583-614 (1994)

[10] J. Pochodzalla et al., Phys. Rev. Lett. 75, 1040-1043 (1995)

[11] J. Randrup, Nucl. Phys. A 752, 384-393 (2005)

[12] C. Kuhn, Proceedings of "Plasma de quarks et de gluons et matière étrange du SPS au LHC", Ecole Joliot-Curie de Physique Nucléaire, Maubuisson, France, 7-12 septembre 1998

[13] P. Braun-Munzinger et al., arXiv:nucl-th/0304013v1 (2003)

[14] Z. Fodor and S. D. Katz, JHEP, 03:014 (2002)

[15] P. de Forcrand, S. Kim and O. Philipsen, PoSLAT2007:178 (2007)

[16] L. McLerran, arXiv:0808.1057v1 [hep-ph] (2008); L. McLerran, C. Sasaki and K. Redlich, Nucl. Phys. A 824, 86-100 (2009); L. McLerran and R. Pisarski, Nucl. Phys. A 796, 83-100 (2007)

[17] M. G. Alford, A. Schmitt et al., Rev. Mod. Phys. 80, 1455-1515 (2008)

[18] M. Müller-Preussker and M. Creutz, Cambridge University Press, Cambridge (1983), doi: 10.1002/zamm.19870670104

[19] T. Blum, L. Kärkkäinen, D. Toussaint and S. Gottlieb, Phys. Rev. D 51, 5153-5164 (1995)

[20] F. Karsch and E. Laermann, Quark-gluon plasma. Vol. 3, eds. R. C Hwa and Xin-Nian Wang, World Scientific (2004), arXiv:hep-lat/0305025v1 (2003)

[21] F. Karsch, E. Laermann and A. Peikert, Nuclear Physics B 605, 579-599 (2001)

[22] Z. Fodor and S. D. Katz, JHEP 0404, 050 (2004)

[23] A. Bazavov et al., Phys. Rev. D 80, 014504 (2009)

[24] G. S. Bali, Phys. Rept. 343, 1-136 (2001)

[25] M. Stephanov, Journal of Physics: Conference Series 27, 144-153 (2005)

[26] M. Stephanov, Prog. Theor. Phys. Suppl. 153, 139-156 (2004)

[27] S. Salur, Dissertation Thesis, Yale (2006)

[28] J. D. Bjorken, Phys. Rev. D 27, 140-151 (1983)

[29] A. Andronic and P. Braun-Munzinger, arXiv:hep-ph/0402291v1 (2004)

[30] A. Toia et al., arXiv:1107.1973v1 [nucl-ex] (2011)

[31] Yu. B. Ivanov et al., Phys. Rev. C 73, 044904 (2006)

[32] L. V. Bravina et al., Phys. Rev. C 60, 044905 (1999)

[33] I. C. Arsene et al., Phys. Rev. C 75, 034902 (2007)

[34] `http://press.web.cern.ch/press/pressreleases/Releases2000/PR01.00EQuarkGluonMatter.html`

[35] T. Matsui and H. Satz, Phys. Lett. B 178, 416 (1986)

[36] M.C. Abreu et al., NA50 Collaboration, Phys. Lett. B 477, 28-36 (2000)

[37] M.C. Abreu et al., NA38 Collaboration, Phys. Lett. B 466, 408 (1999)

[38] A. Foerster et al., NA60 Collaboration, J. Phys. G 32, S51-S60 (2006)

[39] O. Linnyk, E.L. Bratkovskaya, W. Cassing and H. Stoecker, Nucl. Phys. A 786, 183-200 (2007)

[40] S. Gavin, M. Gyulassy and A. Jackson, Phys. Lett. B 207, 257-262 (1988)

[41] J. Adams et al., STAR Collaboration, Nucl. Phys. A 757, 102-183 (2005)

[42] K. Adcox et al., PHENIX Collaboration, Nucl. Phys. A 757, 184-283 (2005)

[43] B. B. Back et al., PHOBOS Collaboration, Nucl. Phys. A 757, 28-101 (2005)

[44] J. Adams et al., STAR Collaboration, Phys. Rev. Lett. 91, 072304 (2003)

[45] K. Aamodt et al., ALICE Collaboration, Phys. Rev. Lett. 105, 252302 (2010)

[46] R. A. Lacey, A. Taranenko et al., PoSCFRNC2006, 021 (2006)

[47] C. Alt et al., NA49 collaboration, Phys. Rev. C 77, 024903 (2008)

[48] B. I. Abelev et al., STAR Collaboration, Phys. Rev. C 81, 024911 (2010)

[49] A. Andronic, P. Braun-Munzinger and J. Stachel, Phys. Lett. B 678, 516 (2009); A. Andronic, P. Braun-Munzinger, K. Redlich and J. Stachel, Phys. Lett. B 659, 149-155 (2008); F. Becattini, arXiv:0901.3643v1 [hep-ph] (2009)

[50] S. Shi, STAR collaboration, arXiv:1201.3959v1 [nucl-ex] (2012)

[51] R. Vogt, Int. J. Mod. Phys. E12, 211-270 (2003)

[52] P. Shukla, arXiv:nucl-th/0112039v1 (2001)

[53] M. C. Abreu et al., NA38 and NA50 Collaborations, Eur. Phys. J. C14, 443-455 (2000)

[54] J. W. Cronin et al., Phys. Rev. D 11 3105 (1975)

[55] M. Arneodo, Phys. Rept. 240, 301-393 (1994)

[56] Y. Zhang, J. Phys. G 35, 104022 (2008)

[57] ALICE Collaboration, arXiv:1205.4007v2 [hep-ex] (2012)

[58] P. Braun-Munzinger et al., Eur. Phys. J. C1, 123-130 (1998); R. Gavai et al., Int. J. Mod. Phys. A 10, 3043-3070 (1995); S. S. Adler et al., PHENIX Collaboration, Phys. Rev. Lett. 92, 051802 (2004); H. Sato, Mem. Fac. Sci. Kyoto 44, 89-193 (2003)

[59] B. Friman, C. Hoehne, J. Knoll, S. Leupold, J. Randrup, R. Rapp, (editors), The CBM Physics Book: Compressed Baryonic Matter in Laboratory Experiments, Springer Verlag, 2011

[60] W. Ehehalt and W. Cassing, Nucl. Phys. A 602, 449-486 (1996)

[61] O. Linnik, E.L. Bratkovskaya and W. Cassing, Int. J. Mod. Phys. E 17, 1367-1439 (2008)

[62] W. Cassing, E.L. Bratkovskaya and A. Sibirtsev, Nucl. Phys. A 691, 753-778 (2001)

[63] H. van Hees and R. Rapp, Phys. Rev. C 71, 034907 (2005)

[64] FAIR Baseline Technical Report, `http://www.gsi.de/documents/DOC-2006-Dec-94-1.pdf` (2006)

[65] J. Randrup and J. Cleymans, Phys. Rev. C 74, 047901 (2006)

[66] J. Cleymans, H. Oeschler, K. Redlich, and S. Wheaton, Phys. Rev. C 73, 034905 (2006)

[67] S. Eidelman et al. (Particle Data Group), Phys. Lett. B 592, 1 (2004)

[68] Technical Status Report of the CBM Collaboration, https://www-alt.gsi.de/documents/DOC-2005-Feb-447-1.pdf (2005)

[69] Johann M. Heuser, M. Deveaux et al., Nucl. Instr. & Meth. in Phys. Res. A 568, 258-262 (2006)

[70] D. Gonzalez-Diaz et al., CBM Progress Report 2006, p. 39 (2007)

[71] D. Kresan and C. Höhne, CBM Progress Report 2008, p. 63 (2009)

[72] C. Hoehne et al., Nucl. Instrum. Meth. A 595, 187-189 (2008)

[73] A. Dubey et al., CBM Progress Report 2007, p. 39 (2008)

[74] C. Trageser, Master thesis, Frankfurt University

[75] I. Vassiliev et al., CBM Progress Report 2008, p. 60 and p. 61 (2009)

[76] C. Dritsa, PhD thesis, Frankfurt/Strasbourg (2011)

[77] I. Vassiliev et al., CBM Progress Report 2007, p. 12 (2008)

[78] I. Vassiliev et al., CBM Progress Report 2007, p. 13 (2008)

[79] A. Senger, private communication

[80] S. Amar-Youcef, PhD thesis, Frankfurt (2011)

[81] T. Sluka et al., Nucl. Instr. & Meth. in Phys. Res. A 607, 27-30 (2009)

[82] G. Casse, Nucl. Instr. & Meth. in Phys. Res. A 598, 54-60 (2009)

[83] E. Cabruja et al., Nucl. Instr. & Meth. in Phys. Res. A 574, 392-400 (2007)

[84] K. Stefanov, Nucl. Instr. & Meth. in Phys. Res. A, 501, 245-250 (2003)

[85] N. B. Sinev et al., Nucl. Instr. & Meth. in Phys. Res. A 549, 117-121 (2005)

[86] Y. Banda et al., Nucl. Instr. & Meth. in Phys. Res. A 621, 192-204 (2010)

[87] R. Turchetta et al., Nucl. Instr. & Meth. A 458, 677-689 (2001)

[88] M. Koziel, PhD thesis, Strasbourg (2011)

[89] M.Winter, Nucl. Instr. & Meth. A 623, 192-194 (2010)

[90] C. Hu-Guo et al., "A ten thousand frames per second readout MAPS for the EUDET beam telescope", TWEPP 2009 (CERN-2009-008)

[91] J. Baudot, IEEE Nuclear Science Symposium, Orlando (25-31 October 2009)

[92] M. Deveaux et al., Nucl. Instr. & Meth. A 512, 71-76 (2003)

[93] M. Deveaux et al., 2011 JINST 6 C02004 (2011)

[94] G. Voutsinas et al., Nucl. Phys. B (Proc. Suppl.) 215, 48-50 (2011)

[95] T. Haas., Nucl. Instr. & Meth. in Phys. Res. A 569, 53-56 (2006)

[96] M. Winter for the IPHC team, CBM Progress Report 2011, p. 6 (2012)

[97] A. Himmi et al., Mimosa 26 UserManual, V.1.0 (2008)

[98] A. Himmi et al., Proc. of TWEPP-09, CERN-2009-006, p. 426 (21-25 sept. 2009)

[99] A. Dorokhov et al., Nucl. Instr. & Meth. A 650, 174-177 (2011)

[100] TOWER/JAZZ semiconductor (`http://www.towerjazz.com/index.html`)

[101] R. Yarema, PoS (Vertex 2007) 017 (2007)

[102] M. Deveaux, PhD thesis, Frankfurt/Strasbourg (2007)

[103] T. Tischler, GSI Scientific Report 2010, p. 19 (2011)

[104] Nuclear matter physics at SIS-100, The CBM Collaboration, CBM Report 2012-01 (2012)

[105] T. Galatyuk et al., GSI Scientific Report 2006, p. 10 (2007)

[106] `http://fairroot.gsi.de/`; `http://cbmroot.gsi.de/`

[107] GEANT, Detector Description and Simulation Tool, `http://wwwasd.web.cern.ch/wwwasd/geant/`

[108] S. A. Bass, M. Belkacem et al., Prog. Part. Nucl. Phys. 41, 225-370 (1998); `http://urqmd.org/`

[109] S. Ratschow, Internal note, 2010 (private communication)

[110] P. Forck et al., GSI Scientific Report 2005, p. 129 (2006)

[111] J. Pietraszko, private communication

[112] C. Schrader et al., CBM Progress Report 2010, p. 6 (2011)

[113] C. Schrader, PhD thesis, Frankfurt (2011)

[114] C. Schrader, private communication

[115] `http://wwwasd.web.cern.ch/geant4/G4UsersDocuments/UsersGuides/PhysicsReferenceManual/html70/node80.html`

[116] http://home.thep.lu.se/~torbjorn/Pythia.html

[117] I. Kisel et al., Nucl. Instr. & Meth. A 489, 389 (2002)

[118] R.E. Kalman, Journal of Basic Engineering 82, 35-45 (1960)

[119] C. Alt et al., NA49 Collaboration, Phys. Rev. C 68, 034903 (2003)

[120] V. P. Konchakovski et al., Phys. Rev. C 85, 044922 (2012)

[121] E. Richardson et al., Nucl. Instr. & Meth. in Phys. Res. A 636, 99-107 (2011)

[122] B.I. Abelev et al, STAR collaboration, Phys. Rev. Lett. 103, 251601 (2009)

[123] A. M. Poskanzer, S.A. Voloshin et al., Phys. Rev. C 58, 1671-1678 (1998)

[124] H. Petersen et al., Phys. Rev. C 74, 064908 (2006)

[125] F. Guber, A. Ivashkin, et al., https://www.gsi.de/documents/DOC-2006-Jan-140-1.pdf (2006)

[126] N. Borghini, P. M. Dinh and J.-Y. Ollitrault, Phys. Rev. C 63, 054906 (2001)

[127] R. S. Bhalerao, N. Borghini and J.-Y. Ollitrault, Nucl. Phys. A 727, 373-426 (2003)

[128] H. Sorge, Phys. Rev. Lett. 78, 2309-2312 (1997)

[129] H. Stoecker, arXiv:0710.5089v1 [hep-ph] (2007); H. Stoecker, Nucl. Phys. A 750, 121-147 (2005)

[130] Z.W. Lin and C.M. Ko, Phys. Rev. C 65, 034904 (2002); Z.W. Lin, C.M. Ko, B.A. Li, B. Zhang and S. Pal, Phys. Rev. C 72, 064901 (2005)

[131] E. L. Bratkovskaya et al., Nucl. Phys. A 856, 162-182 (2011)

[132] V. P. Konchakovski et al., Proceedings of 28th Winter Workshop on Nuclear Dynamics in Dorado del Mar, Puerto Rico, 7-14 April, 2012, arXiv:1201.3320v1 [nucl-th] (2012)

[133] R. L. Ray and M. Daugherity, J. Phys. G 35, 125106 (2008); M.C. Abreu et al., NA50 Collaboration, Phys. Lett. B 530, 43-55 (2002)

[134] http://www.staff.uni-mainz.de/zeitnitz/Gcalor/gcalor.html